DEVELOPMENT OF
TEMPORAL PHASE ANALYSIS TECHNIQUES
IN OPTICAL MEASUREMENT

BY

FU   YU

(M. Eng., NUS)

A THESIS SUBMITTED

FOR THE DEGREE OF DOCTOR OF PHILOSOPHY

DEPARTMENT OF MECHANICAL ENGINEERING

NATIONAL UNIVERSITY OF SINGAPORE

2005

ACKNOWLEDGEMENTS

TABLE OF CONTENTS

SUMMARY

In this thesis, different temporal phase analysis methods are studied. Temporal phase analysis techniques allow accurate measurements on non-static objects, using whole-field optical methods, such as classical interferometry, electronic speckle pattern interferometry (ESPI), shearography as well as fringe projection and moiré techniques. They cover a large domain of resolutions and range for measurement of instantaneous shape and displacement of rough and smooth objects. In temporal phase analysis, a series of fringe or speckle patterns is captured during the deformation or vibration of the tested specimen. The intensity variation on each pixel is analyzed along time axis. Based on two existing temporal phase analysis methods, temporal Fourier analysis and phase scanning method, a new technique is proposed in this study. It uses a robust mathematic tool — continuous wavelet transform as the processing algorithm.

An analytic wavelet is selected for analysis of phase related properties of real functions. The complex Morlet wavelet is used as a mother wavelet because it gives the smallest Heisenberg box so that better temporal and frequency resolutions are obtained. Selection of a suitable central frequency of a Morlet wavelet is discussed. The instantaneous frequency of intensity variation of a pixel, which is the first derivative of a temporal phase, can be extracted by the maximum modulus — the ridge of a wavelet coefficient. The temporal phase can then be calculated by two methods, integration or unwrapping methods. The system errors involved in these two methods are evaluated, especially when the signal frequencies are non-uniform. To avoid phase ambiguity problem in the wavelet technique, temporal carrier technique is applied when vibrating objects are measured.

To demonstrate the validity of the proposed temporal wavelet analysis technique, several experiments based on various optical techniques are designed for different applications. These include the profiling of surface with height step using shadow moiré technique; instantaneous velocity, displacement and shape measurement on continuously deforming objects using ESPI and shadow moiré, absolute displacement measurement on vibrating objects using temporal carrier technique and displacement derivatives measurement using digital shearography. The results generated by temporal Fourier analysis are also presented for comparison. It is observed that wavelet analysis generates better results. As wavelet analysis calculates the optimum frequency at each instant, it performs an adaptive band-pass filtering of the measured signal, thus limits the influence of various noise sources and increases the resolution of measurement significantly. However, it requires longer computing time, higher speed and larger memory.

The wavelet processing as proposed in this work demonstrates a high potential for robust processing of continuous sequencing of images. The study on different temporal phase analysis techniques will broaden the applications in optical, non-destructive testing area, and offer more precise results and bring forward a wealth of possible research directions.

NOMENCLATURE

a Scaling in wavelet transform

a_f Background in Fourier transform

a_{rb} Scaling on the ridge at position b

A_S Sensitivity factor in shearography

b shifting parameter

B_S Sensitivity factor in shearography

C Fourier transform of c_f

c_f Complex function in Fourier transform

C_S Sensitivity factor in shearography

d_F Distance between the projector and camera axis

d_S Distance between the camera axis and the light source in shadow moiré set up

f_0 Spatial frequency of the projected fringes on the reference plane

H Parameter related to profile in shadow moiré

h_F Relative height of object to reference plane in fringe projection technique

h_S Distance between the grating plane and object

I_0 Background of intensity variation

I_M Modulation factor of intensity variation

I_{max} Maximum gray value

I_{min} Minimum gray value

I_n Intensity at phase step n

k_F Optical coefficient related to the configuration of the system in fringe projection technique

k_S Constant related to the shadow moiré set up

L_F Distance between the LCD projector and the reference plane

l_S Distance between the light source and the grating plane in shadow moiré set up

m Adjustable coefficients

N Total number of step in phase shifting technique

s Signal

S Adjustable coefficients

u Horizontal spatial frequency

v Vertical spatial frequency

V Visibility of speckle pattern

w Window function

W_S Wavelet coefficients

α_n Phase step in phase shifting technique

β Rotating angle of the moiré grating

$\Delta\varphi$ Phase change

φ_i Initial random phase

λ Wavelength of light source

ϕ_p Phase value at point P

ϕ Phase

φ_0 Initial phase at $T_0 = 0$

φ Phase

ω Frequency in spectrum

Δt Temporal duration

$\Delta \omega$ Frequency bandwidth

σ Square root of variance of the Gaussian window

Ψ Mother wavelet

Ψ_{ab} Daughter wavelet

ω_0 Central (or mother) frequency of Complex Morlet wavelet

ζ Frequency variable

ε Corrective term

LIST OF FIGURES

LIST OF TABLES

CHAPTER ONE

INTRODUCTION

1.1   Background

In the last several decades, the drive for higher performance and reliability of devices, structures, and processes in engineering has placed stringent demands on the methods used in their development and operation. Optical metrology is a major and inseparable part of these methods. The field of optical metrology is arguably more than one century old. However, major advances have resulted from the invention of laser only about fifty years ago. This new light source opened a realm of new techniques to both the physicist and the engineer. With the advent of the laser, coherent optics has been brought into measurement techniques such as moiré method which resulted in the rapid development of moiré interferometry and the adaptation of optical spatial filtering schemes; and holographic interferometry became practicable at the same time. In 1970's, the genesis and evolution of speckle interferometry, speckle photography and shearography were observed. The maturing of all these techniques occured in the 1980's. Due to the rapid development of computer and charged couple device (CCD) camera, automation becomes the major theme of research during the 1990's.

The transition of such methods into industrial area is a slow but accelerating process. As usual, high-technology domains such as space and aeronautical industries were the first to employ them, since there is a genuine need to understand the behavior of new materials and structures before sending them into space. The automotive industry has also used holography and shearography to detect defects in

tires or to study the vibration modes of car components, in order to detect potential failure points and reduce acoustic noise sources. Some manufacturers started using shape measurement methods to better control the complex shapes of car body parts that are assembled automatically by robots. Optical techniques, such as shadow moiré and moiré interferometry, also gained recognition in electronics industry in the measurement of thermally-induced deformation of electronic package and PCB board.

Optical interferometry techniques are usually applied on precision measurement of tiny deformation or unevenness of objects. Generally, they are non-contacting and whole-field techniques. The results obtained by the aforesaid methods are usually in the form of fringe patterns that represent different physical quantities, such as distance, in-plane or out-of-plane displacements, or stresses. Although a fringe pattern representing distance, deformation or distortion is readily obtained, expert interpretation is necessary to convert these fringes into desired information. For accurate mapping of these physical quantities, which will thus permit numerical differentiation, various fringe processing algorithms, notably the Fourier transform and phase shifting, have been used.

Phase shifting technique is a predominant method to retrieve accurate phase values from sinusoidal fringe patterns. However, it requires several, normally three, four or five images to be captured with prescribed phase steps. Due to this reason, normal phase-shifting approach also limits optical techniques to the measurement of static objects. Furthermore, in order to remove the 2π phase discontinuities, spatial phase unwrapping is compulsory. However, two dimensional spatial phase unwrapping is usually a difficult step, especially in processing of speckle patterns, because of the noise effect and low modulated pixels may produce breaks in wrapped phase map and generate large phase errors when unwrapping process is performed.

Optical interferometry can also be applied to the determination of vibration modes of objects. For high-frequency linear vibration, any vibration state can be considered as the superposition of all the vibration modes. Thus determining the vibration modes of the objects is fundamental for vibration analysis. Time averaged methods, based on holography, moiré or electronic speckle pattern interferometry (ESPI), possess many advantages over the other techniques: they directly acquire a spatially dense, full-field, real-time image of the mode shape, while other techniques require the reconstruction of the mode shape from single point measurements. Furthermore, with optical techniques, there is no physical contact with the structure, thus eliminating mass loading and local stiffening issues associated with contact sensors.

In some cases, high resolution 3-D displacement or surface profiling of objects under vibration or continuous profile changing can give useful information of dynamic response and deformation of the objects concerned. However, it is very difficult to be achieved with phase shifting technique and with time averaged method. Due to the rapid development of high-speed digital recording devices, it is now possible to record fringe patterns with rates exceeding 10,000 frames per second (fps). Retrieving precise instantaneous spatial phase maps from those fringe patterns along the time-axis enables instantaneous 3-D profile and deformation as well as dynamic response to be studied. Generally, two methods are used to analyze the instantaneous fringe patterns, namely, spatial phase analysis and temporal phase analysis. Spatial phase analysis is a method to retrieve an instantaneous phase map from one fringe pattern. In late 1990's, a new phase evaluation method based on temporal analysis has been introduced. It analyzes the phase point-wisely along time axis, so that the disadvantages of spatial phase evaluation techniques mentioned above are avoided. This advantage is more obvious in the processing of speckle patterns, as the temporal

intensity variation on each pixel is much less noisy than spatial distribution of a modulated random speckle pattern. One dimensional Fourier transform became a predominant method in temporal phase analysis.

1.2   Scope of work

Figure 1.1 shows a flow chart of various fringe analyzing techniques being applied on different problems. The scope of this dissertation work is focused on the temporal phase analysis techniques and applying them to measurement of continuously-deforming objects or low-frequency vibrating objects indicated in Fig. 1.1 in red colour. The objectives of this thesis include: (1) studying two existing temporal phase analysis methods, i.e. temporal Fourier transform (Huntely and Saldner, 1997) and phase scanning (Li et al. 2001), and their advantages and weaknesses; and (2) developing a new temporal processing technique based on time-frequency analysis and wavelet transform to overcome problems encountered in existing methods. The outcome will be a robust technique that would process a series of fringe patterns and reconstruct temporal phase evolution precisely. The objectives of this thesis also include (3) introducing a new experimental technique, temporal carrier, to overcome the phase ambiguity problem involved in temporal phase analysis methods, and (4) applying those temporal phase analysis methods, especially the new temporal wavelet analysis on different static and dynamic problems with various optical techniques. Applications include surface profiling on objects with step changes; measurement on continuously-deforming objects; measurement on low-frequency vibrating objects and displacement derivative measurement on a continuously-deforming plate.

1.3 Thesis outline

An outline of the thesis is as follows:

Chapter 1 provides an introduction of this dissertation.

Chapter 2 provides a literature survey in three parts: In the first part, an overview of whole-field optical techniques used in dynamic phase evaluation is presented, followed by shadow moiré, ESPI ,digital shearography and fringe projection techniques that are used to demonstrate the temporal phase analysis algorithms; and examples using these techniques are also presented. Different spatial fringe analysis techniques are also reviewed. The second part describes the state-of-the-art in the field of temporal phase analysis and two temporal phase analysis methods are included (temporal Fourier transform and phase scanning method). The last part introduces the concept of wavelet and includes a literature survey on wavelet applications in optical interferometry.

Chapter 3 focuses on temporal phase analysis algorithms. It includes selection of complex Morlet wavelet as a mother wavelet, the selection of central frequency of the Morlet wavelet, and applying Morlet wavelet on phase extraction. Different properties of this new technique are characterized through simulations and examples. The method provides us with a very efficient method of evaluating the phase of interferograms temporally. Some problems involved in this new technique are also discussed. In the second part of this chapter, a phase scanning method is discussed and applied on vibrating objects.

Chapter 4 describes the practical aspects of a dynamic phase measurement. The setup of fringe projection, shadow moiré, ESPI and digital shearography are described.

Chapter 5 presents the results of different temporal phase analysis techniques, especially temporal wavelet analysis. In Section 5.1, temporal wavelet analysis is applied to surface profiling with a height step by rotating a moiré grating. In Section 5.2, temporal wavelet analysis and Fourier analysis are applied on continuously deforming objects using shadow moiré and ESPI. The results from these methods are compared. In section 5.3, the main focus is on vibrating objects. Two techniques are presented. One is the temporal carrier technique and the other is the phase scanning method. In the last section, displacement derivatives are measured using temporal carrier with digital shearography. In addition, Haar wavelet transform is introduced to obtained the transient curvature and twist of a plate.

Chapter 6 emphasizes the contribution of this project work and shows potential development on dynamic measurements.
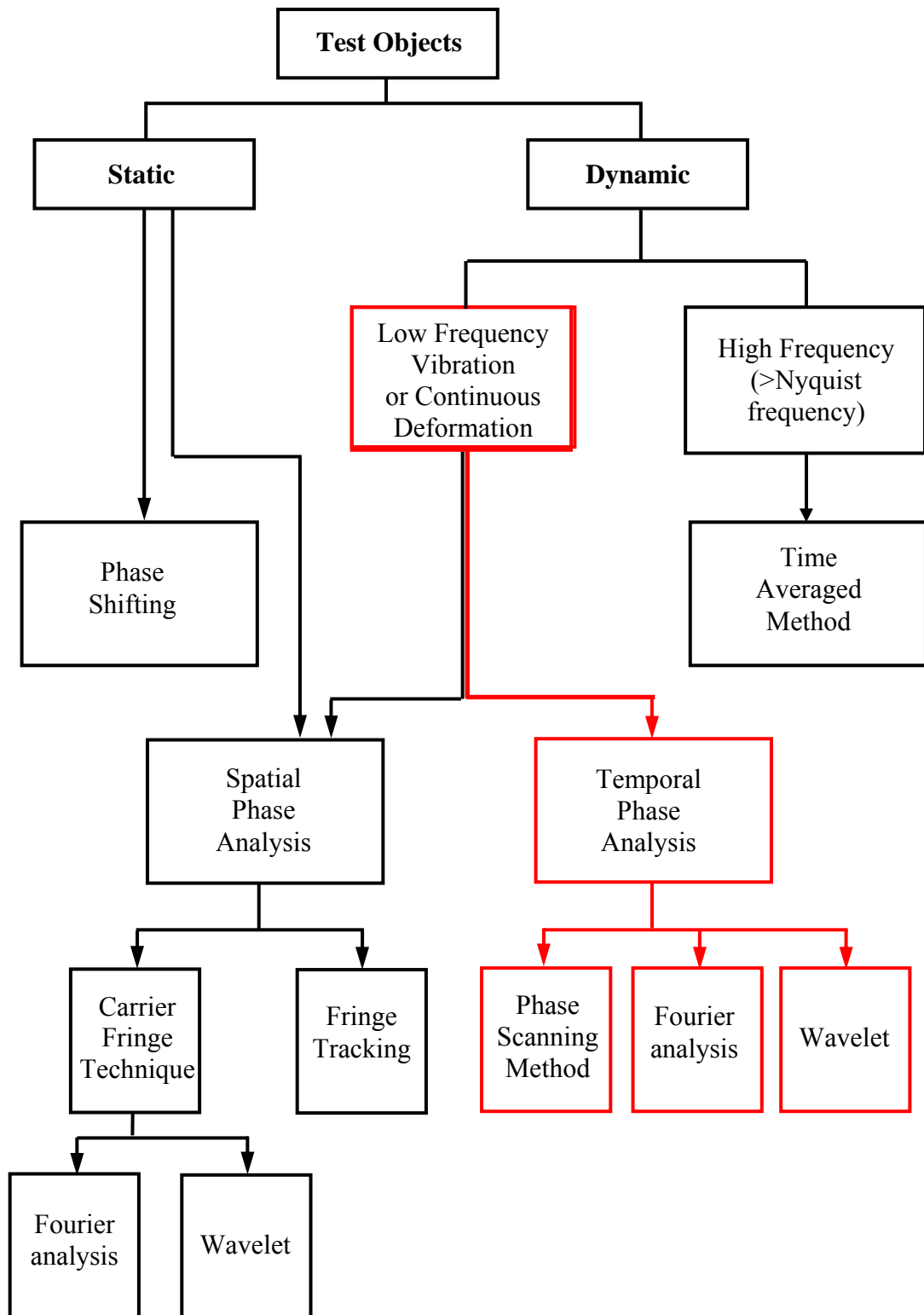
Figure 1.1 Fringe analysis techniques applied on different types of object

CHAPTER TWO

LITERATURE REVIEW

2.1 Review of whole-field optical techniques

Optical metrology (Cloud, 1995) encompasses a large number of techniques allowing direct or indirect measurement of diverse physical quantities. The developments presented in this dissertation are conducted in the framework of "fringe-based" methods where information are coded as an intensity modulation of light. Such techniques can be temporal or spatial and usually rely on the use of an interference phenomenon or a specific structuring of light.

A particular focus here is the so-called "whole-field" techniques, which provide direct measurement on a large number of points in a limited number of steps. Examples of application include measurement of shape, deformation, strain, refractive index, etc. Typically, an image of the object under study is obtained with superimposed alternately dark and bright fringes which are directly related to the measured quantity. When it is imaged on a two-dimensional spatial detector such as CCD camera, the intensity distribution of light is coded in a digital form. This digital image can be processed by a computer to extract the useful information.

The optical techniques mentioned in this section are suitable tools for shape or deformation measurements on rough or smooth objects that can be opaque or transparent. They offer sensitivities ranging from decimeter to sub-micrometer. Some of them are more suitable for evaluating shape while others are better suited for

displacement or deformation evaluation. In shape measurement, classical interferometry (Steel, 1986), such as Michelson interferometer and Newton ring are usually used for high precision measurements, while shadow moiré (Meadows et al., 1970), projection moiré (Takasaki, 1970) and fringe projection (Suganuma and Yoshizawa, 1991) are less sensitive and thus more suitable for three-dimensional measurement of large unevenness of surfaces. Large deformations can be evaluated by comparing of two shapes while small deformations or displacements can be assessed with sensitive techniques such as holography (Vest, 1979), moiré interferometry (Post et al. 1994) and electronic speckle pattern interferometry (Vikhagen, 1990). Shearing techniques used conjointly with speckle interferometry provide a method to evaluate directly the out-of-plane displacement derivatives (Hung, 1982).

2.1.1 Review of techniques for shape and displacement measurement

In this section, the techniques used in this dissertation are reviewed in detail. They are fringe projection technique, shadow moiré, electronic speckle pattern interferometry (ESPI) and digital shearography.

2.1.1.1 Fringe Projection Technique

Fringe projection technique (Sirnivasan et al. 1984) is not an interferometric technique in essence, but it provides fringe patterns very similar to two wavefront interferograms. Hence, fringe analysis methods can be used to obtain quantitative information. In the fringe projection technique, a known fringe pattern, in our case a linear grating with sinusoidal wave configuration, is projected onto a surface of interest at a certain angle; the distribution of the fringe pattern on the surface is

perturbed in accordance with the profile of a test surface when it is observed from a different angle, thereby a three-dimensional feature of the object is converted into a two-dimensional image.
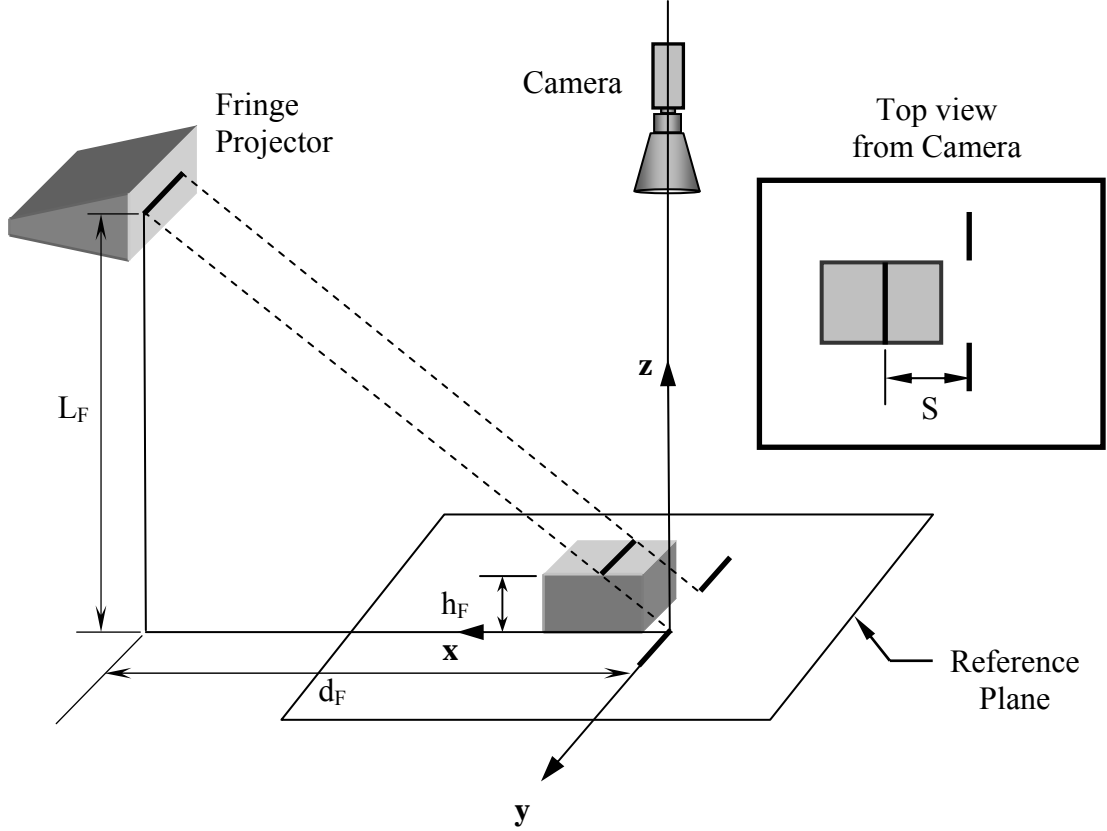
Figure 2.1 Schematic layout of the projection and imaging system

Figure 2.1 shows the schematic layout of the projection and imaging system. With normal viewing, the phase change φ due to height h_F is given by (Quan, et al. 2000)

$$h_F = \frac{L_F}{d_F} \frac{\varphi}{2\pi f_0} = k_F \varphi \tag{2.1}$$

where L_F is the distance between the Liquid Crystal Display (LCD) projector and the reference plane, d_F is the distance between the projector and camera axis, f_0 is the

spatial frequency of the projected fringes on the reference plane and k_F, which can be

obtained by calibration, is an optical coefficient related to the configuration of the

system. φ is the phase angle change which contains information on the surface height

information.

When a sinusoidal fringe pattern (ie, straight lines parallel to the reference y-

axis in Fig. 2.1) is projected onto an object, the mathematical representation of the

intensity distribution captured by a CCD camera is governed by the following

equation:

$$I(x, y) = I_0(x, y) + I_M(x, y) \cos[2\pi f_0 x + \varphi(x, y)] \tag{2.2}$$

where $I_0(x, y)$ and $I_M(x, y)$ are the background and modulation factor respectively,

and $\varphi(x, y)$ is the phase which contains the shape information.

(a)   (b)
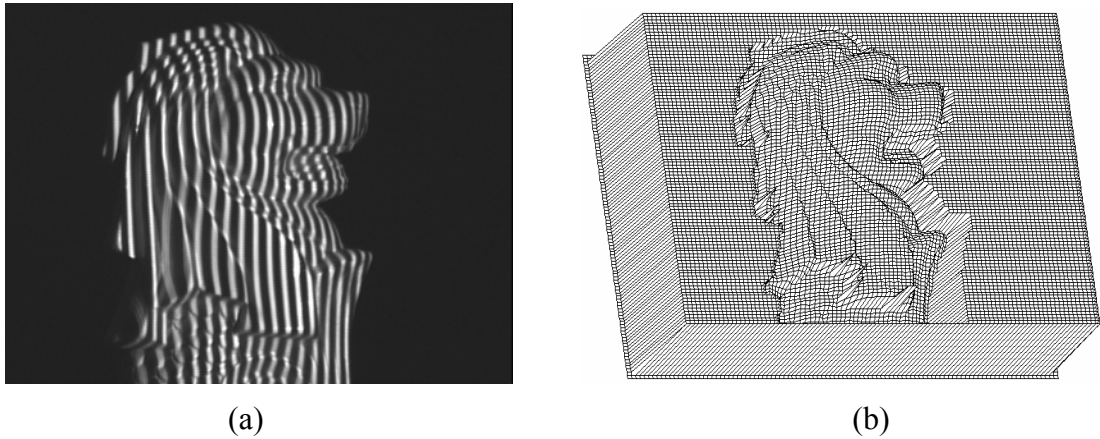
Figure 2.2 (a) Fringe pattern on a merlion paperweight; (b) reconstructed shape of the
merlion

Figure 2.2(a) shows a typical fringe pattern captured using the fringe

projection technique. The phase value $\varphi(x, y)$ in Eq. (2.2) can be extracted by

different algorithms, such as spatial Fourier transform (Takeda et al. 1982), phase

shifting (Quan, et al. 2000), etc. The height of each point can then be reconstructed using Eq. (2.1). Figure 2.2(b) shows the reconstructed profile of the object.

The fringe projection technique has the following merits: (1) easy implementation; (2) phase shifting, fringe density and direction change can be realized with no moving parts if a computer controlled LCD projector is used (Hung, et al. 2002); and (3) fast full field measurement. Because of these advantages, the coordinate measurement and machine vision industries have started to commercialize the fringe projection method and some encouraging applications has been reported by Gartner et al. (1995), Muller (1995) and Sansoni et al. (1997). However, to make this method even more acceptable for industrial use, some issues have to be addressed, including the shading problem, which is inherent to all triangulation techniques. The 360-deg multiple view data registration (Stinik et al. 2002) and defocus with projected gratings or dots (Engelhardt and Hausler, 1988) show some promise.

2.1.1.2 Shadow Moiré

Since Lord Rayleigh first noticed the phenomena of moiré fringes, moiré techniques have been used for a number of testing applications. However, a rigorous theory of moiré fringes did not exist until the mid-fifties when Ligtenberg (1955) and Guild (1956) explained moiré for stress analysis by mapping slope contours and displacement measurement. Excellent historical reviews of the early work in moiré have been presented by Theocaris (1962, 1966). Books on this subject have been written by Guild (1960), Theocaris (1969) and Durelli and Parks (1969) for optical gauging and deformation measurement. Until 1970, advances in moiré techniques were primarily in stress analysis. Some of the first applications of moiré to measure

surface topography were reported by Meadows et al. (1970), Takasaki (1970) and Wasowski (1970).

Similar to the fringe projection technique, Moiré topography is not an interferometric technique, but widely used in shape measurement (Chen, et al. 2000). Depending on the optical arrangement of the system, moiré topography can be classified into: shadow moiré and projection moiré. In projection moiré, the fringes, which contain information of surface profile, are generated by projecting a grating onto the object and viewing through a second grating in front of the viewer. Shadow moiré uses a single grating that is placed close to the object. An oblique light beam passes through the grating and casts a shadow of the grating on the object surface. The shadow is distorted in accordance with the profile of the test surface. When the shadow is viewed from a different direction through the original grating, the grating and its distorted shadow interfere, thus generating fringes which depict loci of the surface depth with respect to the plane of the grating. Compared with projection moiré, shadow moiré is a relatively cheap and simple technique.

In a typical optical arrangement of shadow moiré shown in Fig. 2.3, the light source and the camera are placed at the same distance l_S from the grating with a pitch p. The mathematical representation of the intensity distribution recorded with a CCD camera is given by the following equation (Jin et al. 2001):

$$I(x, y) = I_0(x, y) + I_M(x, y) \cos\left\{\frac{2\pi \cdot d_S \cdot h_S(x, y)}{p[l_S + h_S(x, y)]}\right\} \tag{2.3}$$

where d_S is the distance between the camera axis and the light source, $h_S(x, y)$ is the distance from the grating plane to a point P (x, y). In normal cases, the distance

between the grating and object is very small compared to that between the light source

and object, i.e., $l_S \gg h_S(x, y)$, thus Eq. (2.3) can be simplified as

$$I(x, y) = I_0(x, y) + I_M(x, y) \cos\left[k_S h_S(x, y)\right] \tag{2.4}$$

where $k_S = \dfrac{2\pi d_S}{p l_S}$ is a constant related to the optical setup. Figure 2.4 shows a typical

shadow moiré fringe pattern captured on a spherical cap. The profile of the object can

be reconstructed after image processing. The shortcomings of shadow moiré

topography include: (1) lower resolution of contouring fringes; (2) difficulty in

judging whether a surface is convex or concave from a moiré pattern (Arai et al.

1995).
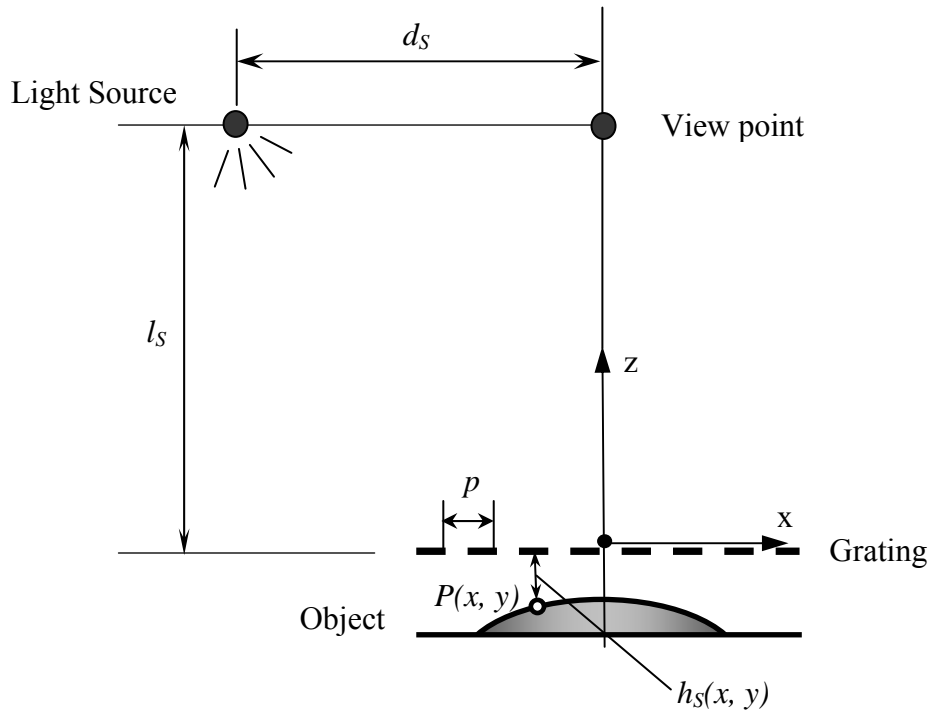
Figure 2.3 Schematic layout of shadow moiré system

Due to the progress of computer capacities and image processing techniques in 1990's, different types of phase-shifting methods were applied in moiré topography to address these shortcomings, i.e., to achieve high resolution measurements and to enable determination of the direction of the curved surface. These methods include combination of shifting the light source and moving grating in z-direction (Yoshizawa and Tomisawa, 1993), combination of rotating the grating in x-y plane and moving it in z-direction (Jin et al. 2000), and rotating the grating in x-z plane (Xie et al. 1997). However, in shadow moiré technique, phase shifting is not easily accomplished (Mauvoisin et al. 1994) and is also limited to measurement of constant surface profile.
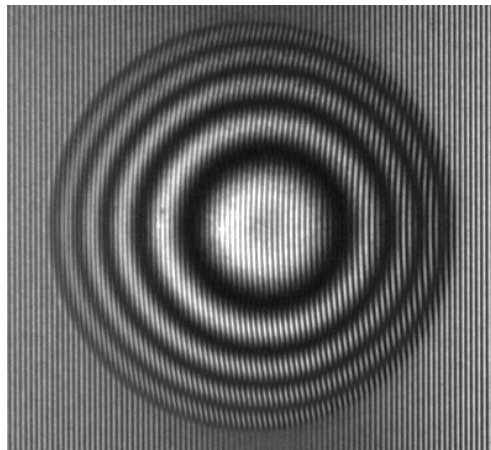
Figure 2.4 Typical moiré fringe patterns on a spherical cap

The moiré technique has also been applied to dynamic problems (Hung et al. 1977a; Hovanesian et al. 1981; Fujimoto, 1982) based on the time-averaged method. These applications generate the object images and superimpose on moiré fringes from which vibration amplitudes are determined. However, the methods cannot be applied to the study of movement and contour of an object as a function of time.

2.1.1.3 Electronic Speckle Pattern Interferometry (ESPI)

Simply speaking, ESPI involves recording two speckle patterns of an object corresponding to two slightly different states. For an object having a diffuse surface, each speckle pattern is the result of two light wave-fronts interfering at the image plane of a CCD camera. The light wave-fronts are the reference wave-front, which is an expanded beam of laser, and the object wave-front, which is scattered from the laser-illuminated object surface. This optical arrangement is similar to conventional film-based holography and is thus often known as Digital Holography.

In spite of similarity in the optical arrangement, wave-front reconstruction for film-based holography is different from that for digital holography. In film-based holography, the two speckle patterns are recorded sequentially and superimposed (image addition) on the same film; and wave-front reconstruction is achieved through viewing the film against the reference wave-front. In digital holography, however, two intensity maps corresponding to the two speckle patterns are separately recorded using a CCD camera and then digitized using a frame grabber; and wave-front reconstruction is achieved through digital subtraction of the two intensity maps on a pixel-by-pixel basis.

The intensity distribution is generally expressed in the following manner, which is also similar to the general expression for fringe projection (Eq. 2.2).

$$I = I_0 + I_M \cos \varphi \qquad\qquad\qquad (2.5)$$

Where I_0 and I_M are the background and modulation intensity, respectively. φ is the phase value which is different for different deformed states.

When the intensity of a reference state and deformed states are recorded, they can be described by

$$I_i = I_0 + I_M \cos\varphi_i$$
$$I_d = I_0 + I_M \cos(\varphi_i + \Delta\varphi)$$

(2.6)

where $\Delta\varphi$ is the phase change due to deformation. Since φ_i is a random variable, both images do not display any fringe patterns. However if these two images are subtracted from each other, we can obtain

$$\Delta I = |I_d - I_i| = 2I_M \left| \sin\left(\varphi_i + \frac{\Delta\varphi}{2}\right)\sin\left(\frac{\Delta\varphi}{2}\right) \right|$$

(2.7)

while the values of φ_i and I_M vary randomly from one point to another, the $\sin\left(\dfrac{\Delta\varphi}{2}\right)$-term is generally a slowly varying modulation of the random intensity difference. Dark and bright areas show up as correlation fringes. Correlation by subtraction can be done electronically in real-time, thus enabling visualization of the evolution of fringe patterns.

ESPI can be used to measure in-plane and out-of-plane displacements depending on the optical arrangement. Figure 2.5 shows a setup for out-of-plane displacement measurement, which is similar to Michelson interferometer. In the z-direction, the sensitivity or amount of deformation that produces one fringe is $\dfrac{\lambda}{2}$, where λ is the wavelength of the laser. As in other optical techniques, it is impossible

to judge the direction of deformation from one ESPI fringe pattern as shown in Fig. 2.5.
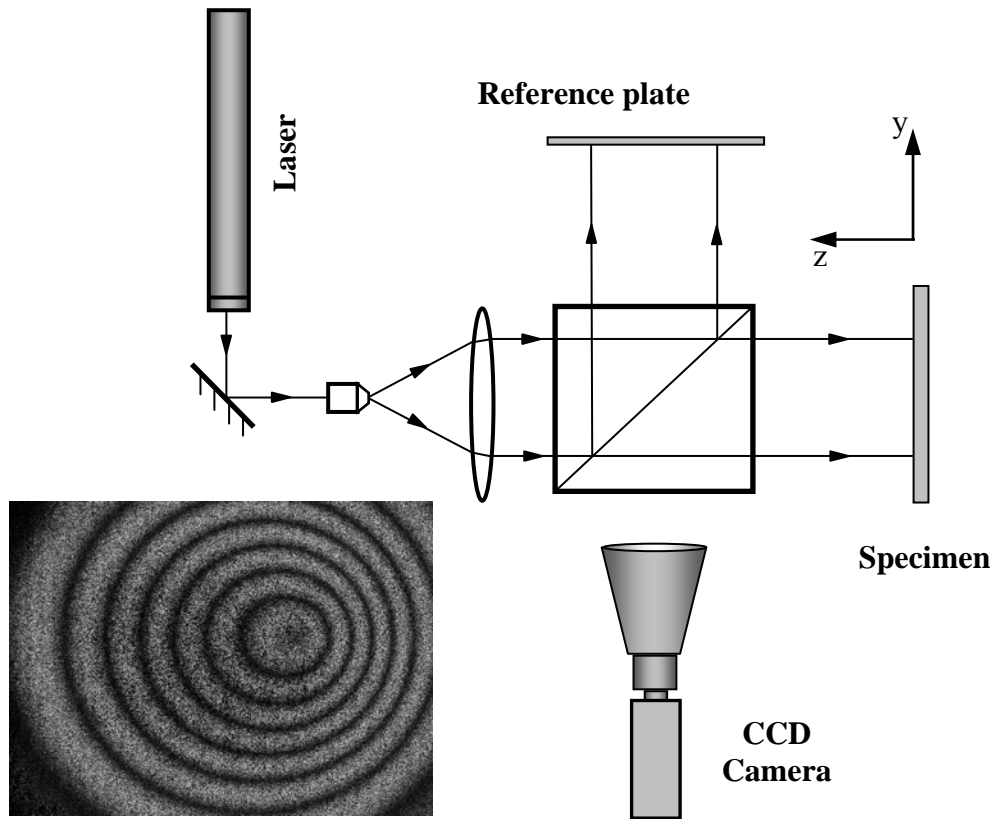
Figure 2.5 ESPI setup for out-of-plane displacement measurement and the typical fringe pattern obtained by image subtraction

2.1.1.4 Shearography

The technique of shearography (Hung, 1982; 1989) requires the use of an image-shearing device placed in front of an ordinary camera so that two laterally displaced images of the object surface are focused at the image plane of the camera, and thus the technique is named as shearography. The shearing device brings two nonparallel beams scattered from two different points on the object surface to become nearly co-linear and interfere with each other. As the angle between the two interfering beams in almost zero, the spatial frequency of the interference fringe pattern is so low that it

is resolvable by a low-resolution image sensor such as a CCD. A typical set-up of

digital shearography is illustrated in Fig. 2.6.
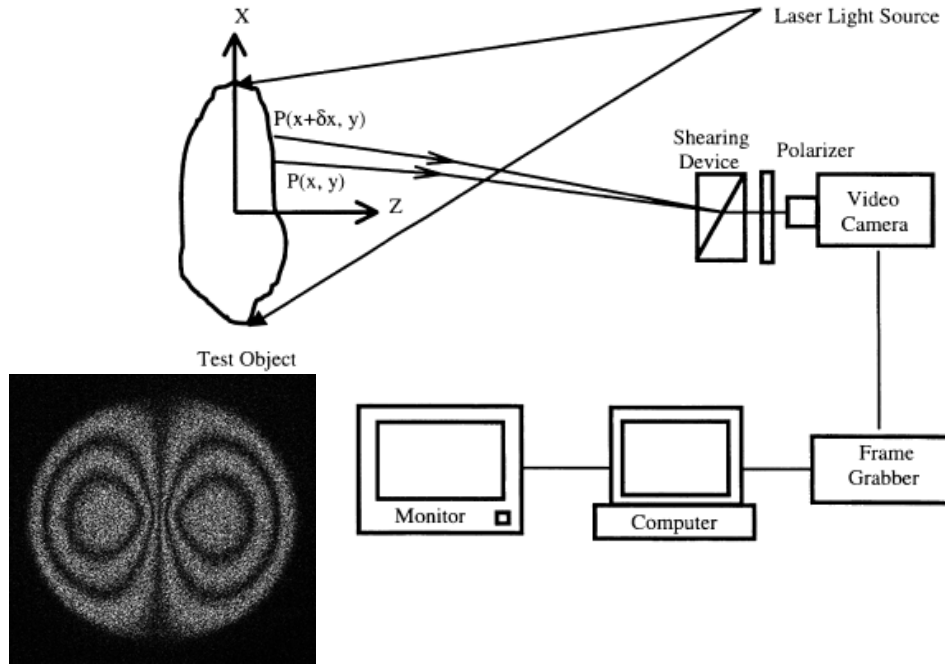
Figure 2.6 Digital shearography set-up and typical fringe pattern obtained by image subtraction.

The phase change $\Delta\varphi$ is induced by the relative optical path length change

between the light scattered from two neighboring points, $P(x, y, z)$ and $P(x + \delta x, y, z)$

on the object surface. In this case the shearing direction is assumed parallel the x-axis,

and the amount of shearing is δx. It can be shown that $\Delta\varphi$ is related to the relative

displacement $(\delta u, \delta v, \delta w)$ of two neighboring points separated by:

$$\Delta\varphi = \frac{2\pi}{\lambda}\left(A_S\,\frac{\delta u}{\delta x} + B_S\,\frac{\delta v}{\delta x} + C_S\,\frac{\delta w}{\delta x}\right)\delta x \tag{2.8}$$

where A_S, B_S and C_S are sensitivity factors related to the position of the

illumination point and the camera position. If the amount of shearing δx is small, the

relative displacement can be approximated as the displacement derivatives respect to x. The direction of shearing determined the direction of the derivative. Should the shearing direction be parallel to the y direction, the derivatives in Eq. (2.8) becomes the displacement derivatives with respect to y. It is possible to employ a multiple image-shearing camera to record the displacement derivatives with respect to both x and y simultaneously (Hung and Durelli, 1979). Compared with holography, shearography does not require a reference light beam. This feature leads to simple optical setups and alleviation of the coherence length requirement of laser and environmental stability demand. With the rapid development of computer and image processing technologies, digital shearography received wide acceptance in the last two decades.

2.1.2 Review of fringe analysis techniques

In previous sections, a set of whole-field optical techniques is briefly presented. These techniques share a common property that the reconstructed intensities encode phase-change that is associated with a corresponding change in displacements, deformations, or other physical quantities. Different types of qualitative diagnostics are possible with a visual analysis of these fringe or speckle patterns. However, more and more applications require that a complete quantitative analysis be performed with high sensitivity. Phase measurements based on digital fringe processing are techniques adopted in this area. These techniques have precisions in the order of one hundredth of the sensitivity of a given interferometer. They can be classified according to the number of images required into two families: the single image techniques which, historically, are the oldest but new refinements still appear every year and the

multiple-image approach which offers additional possibilities that have not yet been fully exploited.

In this section, two single-image based techniques are reviewed, they are (1) skeletonization & fringe tracking and (2) single-image carrier-based method using Fourier transform. Next, the multiple-image phase-shifting algorithms are described briefly. As most of these methods provide a modulo-2π phase map of the interferogram, difficulty in two-dimensional phase unwrapping is also discussed, leading to a possible solution ------- temporal phase analysis.

2.1.2.1 Fringe skeletonization and fringe tracking

Fringe skeletonization techniques use morphological operators (Serra, 1988) that locate the mass center of a pixel cluster using thresholding of the gray level of an image. The fringe skeletons represent a set of points where the phase is an odd or even multiples of π, assuming that I_0 and I_M are locally constant and a continuous phase map can be reconstructed by interpolation (Robinson and Reid, 1993).

Fringe tracking is another method of obtaining a fringe skeleton. Special algorithms are constructed to "follow" paths along the maximum and minimum intensity regions defining bright and dark fringes. The method performs poorly in images where the extremes are loosely defined, as in ESPI fringe patterns.

These methods are adopted when none of the methods mentioned below can be used, as their accuracy is seldom better than a tenth of the measurement sensitivity.

2.1.2.2 Single-image carrier-based method

The second fringe analysis technique is based on the use of "carrier fringe", which basically consists of a set of parallel fringes of constant spacing. These initially straight fringes are distorted by a phase change induced by a deformation (Quan et al. 1996), or by the shape of the object. In effect, a phase wedge is introduced in the interferogram. Sometimes introducing carrier fringes is a complicated process as in shearography (Shang et al. 2001). However, the main advantage of this method is the use of a single image to perform the phase evaluation. The knowledge of phase slope corresponding to the carrier fringes solves the problem of the absolute sign of the phase.

Assuming that the carrier fringes are in *y*-direction (Fig. 2.1) and with spatial frequency f_0, the intensity profile is given by Eq. (2.2). The Fourier technique, proposed by Takeda et al. (1982), has been widely used, particularly in cases where no abrupt fringe discontinuities exist. The intensity distribution can be expressed in a complex form as:

$$I(x, y) = a_f(x, y) + c_f(x, y)\exp(2i\pi f_0 x) + \overline{c}_f(x, y)\exp(-2i\pi f_0 x) \qquad (2.9)$$

where

$$a_f(x, y) = I_0(x, y) \text{ and } c_f(x, y) = \frac{1}{2}I_M(x, y)\exp[i\varphi(x, y)] \qquad (2.10)$$

$c_f(x, y)$ and $\overline{c}_f(x, y)$ are complex functions, and $-$ denotes complex conjugation. The two-dimensional Fourier transform of this image is then computed:

$$I(u,v) = A(u,v) + C(u - f_0, v) + \overline{C}(u + f_0, v) \tag{2.11}$$

where u and v are the horizontal and vertical spatial frequencies and $C(u,v)$ is the 2-D Fourier transform of $c_f(x,y)$.

As $a_f(x,y)$, $c_f(x,y)$ and $\varphi(x,y)$ are slowly varying functions compared to the spatial carrier frequency f_0, using the convolution theorem, $C(u - f_0, v)$ can be isolated with different types of window, such as Hamming and Kaiser (Huang, 1975) and translated by f_0 towards the origin. This removes the carrier and results in a complex image containing $C(u,v)$. The inverse Fourier transform then yields the complex function $c_f(x,y)$. The phase of this function is $\varphi(x,y)$ and can be obtained by

$$\varphi(x,y) = \tan^{-1} \frac{\text{Im}[c_f(x,y)]}{\text{Re}[c_f(x,y)]} \tag{2.12}$$

where Re and Im represent the real and imaginary parts of $c_f(x,y)$, respectively. The phase is numerically obtained as an arctangent function. Taking into account the signs of both the numerator and denominator, this yields a value in the range of $[0, 2\pi)$. The resulting modulo-2π image is often called a "wrapped phase map". The removal of this modulation is discussed in Section 2.1.2.4. Figure 2.7(a) shows a fringe pattern obtained on a curved surface by fringe projection technique. The resulting wrapped phase is shown in Fig. 2.7(b). From a practical point of view, the number of fringes created by the deformation should not be larger than the number of carrier fringes. The width of the peaks in the frequency domain is a function of the pitch variations in

the initial image. If the gradient of the fringes due to deformation becomes too high, the peaks would spread out and overlap, making the selection of a single peak impossible. However, Fourier transform is not the only technique to extract phase from a fringe pattern. Recently, Gabor transform and wavelet transform were used successfully. These algorithms will be discussed in Section 2.3.

(a)   (b)
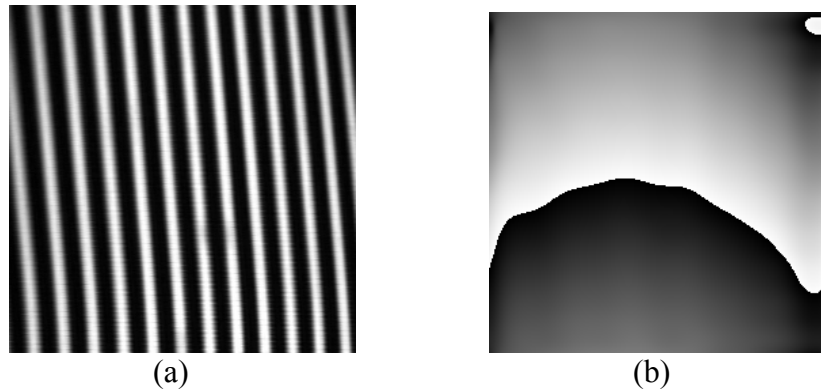
Figure 2.7 (a) Fringe patterns obtained by fringe projection technique; (b) wrapped phase map computed with the carrier-based Fourier transform method

2.1.2.3 Phase-shifting technique

Phase-shifted images are acquired after modification of the optical path length of one of the two interfering light waves-fronts. The result is a movement of the fringes in the image without changing the shape of the phase map. These interferograms lead to a mathematical extraction of the phase φ and permit the determination of its sign.

An ubiquitous device for phase shifting in interferometer is the piezoelectric transducer (PZT), which can translate or rotate optical components, typically a mirror or a reference plate, by a small amount with a resolution close to a few tens of nanometers. This element has proven to be essential for the practical realization of phase-shifting.

With the capability to introduce controlled phase changes α_n in an interferogram, Eq. (2.5) becomes:

$$I(x, y) = I_0(x, y) + I_M(x, y) \cos[\varphi(x, y) + \alpha_n]$$

$$= I_0(x, y) + I_u(x, y) \cos \alpha_n + I_v(x, y) \sin \alpha_n \qquad (2.13)$$

where $I_u(x, y) = I_M(x, y) \cos \varphi(x, y)$ and $I_v(x, y) = -I_M(x, y) \sin \varphi(x, y)$. For the solution of the non-linear system of equations, Gauss least square method is used. $I_0(x, y)$, $I_u(x, y)$ and $I_v(x, y)$ are obtained by minimizing the errors, i.e., the sum of the quadratic errors $\sum_{n=1}^{N} \{I_n(x, y) - [I_0(x, y) + I_u(x, y) \cos \alpha_n + I_v(x, y) \sin \alpha_n]\}^2$ is to be minimized. Obtaining the partial differential of this function with respect to $I_0(x, y)$, $I_u(x, y)$ and $I_v(x, y)$, and equating the derivatives to zero gives a linear system of equations as (Sirohi and Chau, 1999):

$$\begin{pmatrix} N & \sum \cos \alpha_n & \sum \sin \alpha_n \\ \sum \cos \alpha_n & \sum \cos^2 \alpha_n & \sum \sin \alpha_n \cos \alpha_n \\ \sum \sin \alpha_n & \sum \sin \alpha_n \cos \alpha_n & \sum \sin^2 \alpha_n \end{pmatrix} \begin{pmatrix} I_0 \\ I_u \\ I_v \end{pmatrix} = \begin{pmatrix} \sum I_n \\ \sum I_n \cos \alpha_n \\ \sum I_n \sin \alpha_n \end{pmatrix} \qquad (2.14)$$

This system is to be solved pointwise:

$$I_0(x, y) = \frac{1}{N} \sum_{n=1}^{N} I_n \qquad (2.15a)$$

$$I_M(x, y) = \frac{\sqrt{\left(\sum I_n \cos \alpha_n\right)^2 + \left(\sum I_n \sin \alpha_n\right)^2}}{N} \qquad (2.15b)$$

$$\tan\varphi(x,y) = \frac{\sum I_n \sin\alpha_n}{\sum I_n \cos\alpha_n}$$ (2.15c)

This is the general equation (Kong and Kim, 1995) for phase shifting algorithms. A large number of algorithms have been introduced in 1990s. Table 2.1 presents some of these algorithms with three, four or five steps. Similar to Fourier transform, the result obtained is a wrapped phase. Figure 2.8 shows a typical 4-step phase shifting algorithm applied with fringe projection technique. Four fringe patterns with $\pi/2$ shifting are projected by a LCD fringe projector on a 50-cent coin and perturbed fringe patterns are captured by CCD camera as shown in Fig. 2.8(a). Using 4-steps phase-shifting algorithm shown above, a wrapped phase map as shown in Fig. 2.8(b) is obtained. Figure 2.8(c) shows a continuous phase map after unwrapping. It is still a slanted phase distribution, however, an absolute phase value (Fig. 2.8(d)) can be obtained easily by subtracting the phase value of the base plane.

Table 2.1 Algorithms of phase shifting

N	Phase-step α_n	Expression for $\tan\varphi(x,y)$
3	60º (0º, 60º, 120º)	$\tan\varphi(x,y) = \dfrac{2I_1 - 3I_2 + I_3}{\sqrt{3}(I_2 - I_3)}$
3	90º (0º, 90º, 180º)	$\tan\varphi(x,y) = \dfrac{I_1 - 2I_2 + I_3}{I_1 - I_3}$
3	120º (0º, 120º, 240º)	$\tan\varphi(x,y) = \dfrac{\sqrt{3}(I_3 - I_2)}{2I_1 - I_2 - I_3}$
4	90º(0º, 90º, 180º, 270º)	$\tan\varphi(x,y) = \dfrac{I_4 - I_2}{I_1 - I_3}$
4	60º(0º,60º, 120º, 180º)	$\tan\varphi(x,y) = \dfrac{5(I_1 - I_2 - I_3 + I_4)}{\sqrt{3}(2I_1 + I_2 - I_3 - 2I_4)}$
5	90º(0º,90º, 180º, 270º, 360º)	$\tan\varphi(x,y) = \dfrac{7(I_4 - I_2)}{4I_1 - I_2 - 6I_3 - I_4 + 4I_5}$

The limitation of the phase shifting techniques is that they require several, normally three to five, images together with prescribed phase steps. For this reason, it is mainly adopted in measurement of static objects. Generally, it is not suitable for measuring continuous deformation. However, if the rate of the phase shift and recording are sufficiently high, the phase-shifting method can also be used in dynamic measurement. Huntley et al. (1999) adopted Pockels cell instead of traditional PZT phase shifter to generate a four phase-step in a very short time. High-quality phase maps from a vibrating object were extracted. However, the improvement was mainly in hardware rather than in the phase shifting algorithm.

(a)   (b)

(c)   (d)
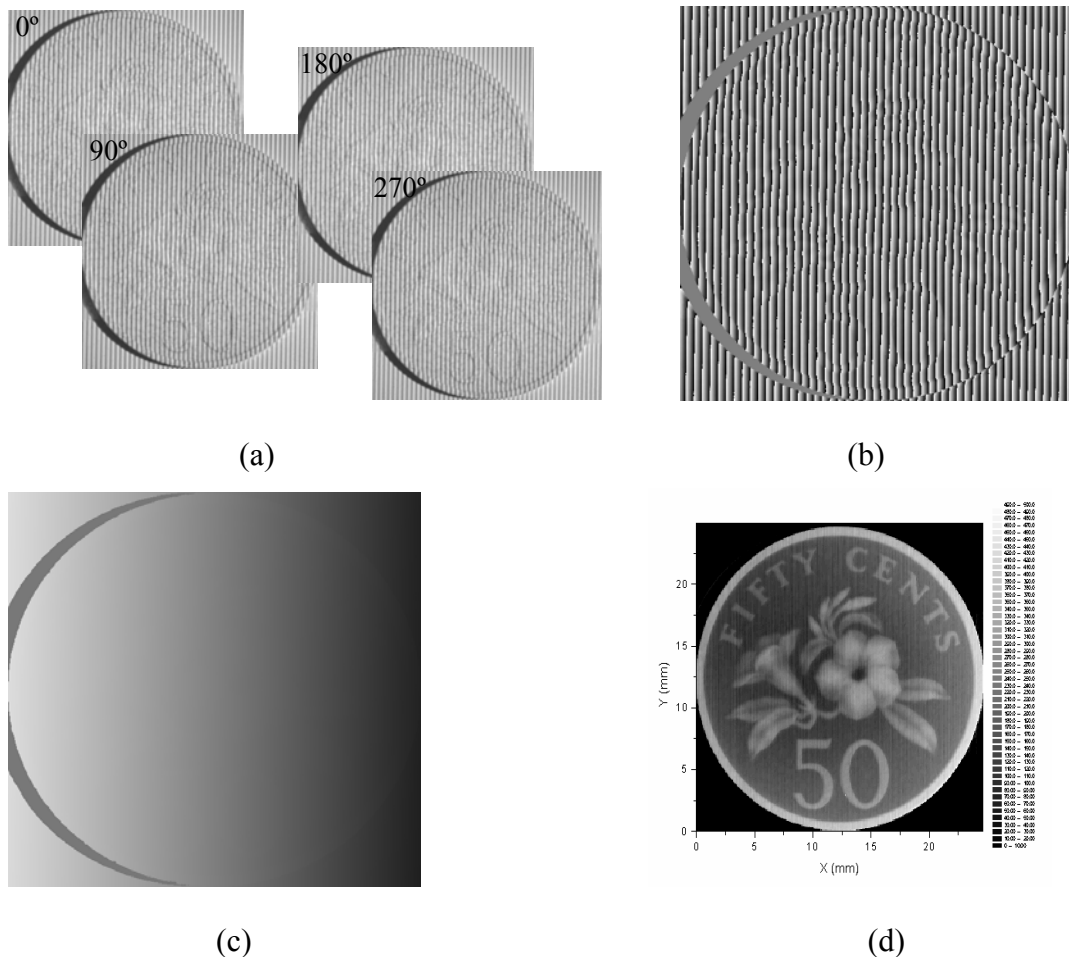
Figure 2.8 (a) Four perturbed fringe patterns with $\pi/2$ phase shifting on a 50-cent coin. (b) wrapped phase map obtained by 4-step phase shifting, (c) continuous phase map after phase unwrapping, (d) gray level map of a 50-cent coin

2.1.2.4 Phase unwrapping

The previous sections show that the results obtained by carrier-based Fourier transform and phase shifting is a modulo-2π phase map. The process of converting the discontinuous phase information into a continuous function which is directly related to the physical parameter measured is called phase unwrapping. This can be defined in the following expression (Creath, et al. 1993):

"Phase unwrapping is the process by which the absolute value of the phase angle of a continuous function that extends over a range of more than 2π (relative to a predefined starting point) is recovered. This absolute value is lost when the phase term is wrapped upon itself with a repeat distance of 2π due to the fundamental sinusoidal nature of the wave function (electromagnetic radiation) used in the measurement of physical properties."

The process of phase unwrapping (Judge and Bryanston-Cross, 1994) is the last but maybe the most difficult step of the quantitative measurement. The unwrapping process consists, in one way or another, of comparing pixels or groups of pixels to detect and remove the 2π phase jumps. Numerous solutions exist to process single wrapped phase images (Ghiglia and Pritt, 1998), based on path dependent or path independent algorithms, such as branch cut method (Just et al. 1995), quality-guided path following algorithm (Bone, 1991), mask cut algorithm (Priti et al. 1990), minimum discontinuity approach (Flynn, 1996), cellular automata (Ghiglia et al. 1987), neural networks and so on. They all present advantages and disadvantages, emphasizing the fact that no single tool can be used to solve all the problems in this field (Robinson and Reid, 1993).

Generally, there are two main difficulties in phase unwrapping. The first is erroneous phase values, often in the case of speckle interferometry. Correct filtering of a wrapped phase map can greatly improve the results, as long as the proportion of

erroneous phase values within the image stays reasonable, say less than 30%. Above this value, the effectiveness of filtering process is limited. Unwrapping algorithms based on group processing instead of individual pixels usually perform better in the presence of noise.

The second difficulty arises from physical discontinuities in the wrapped phase map. They correspond to abrupt step changes on the object in the case of shape measurement, or discontinuities of an object surface in the case of deformation measurement, for example, cracks. The problem also appears when fringes are located in unconnected zones in an image. Different zones in an image can be unwrapped but they do not share a common phase origin.

Once unwrapping process is completed, a phase map has to be transformed into its corresponding physical quantity, such as shape or displacement. This is accomplished using a sensitivity vector. The process is not always easy or accurate as unwanted sensitivities as well as sensitivity variations need to be considered.

The algorithms mentioned above are "spatial" algorithms in the sense that a phase map is unwrapped by comparing adjacent pixels or pixel regions within a single image. A completely different approach was proposed by Huntley and Saldner (1993) where a series of wrapped phase images are used. Each corresponds to a step in the deformation process of an object and unwrapping is conducted along the time axis for each pixel. No spatial relationship is used. The advantages are manifold. First, erroneous phase values do not propagate in the image. Second, physical discontinuities can be dealt with automatically. Third, isolated regions in the interferogram are correctly unwrapped, without any uncertainty concerning their relative phase order. The limitation is that the experiment must be conducted step by

step, which can be a problem when a load has to be controlled precisely. However, the basic idea behind this method is that the phase at each pixel is evaluated as a function of time. This concept leads to a family of phase extraction methods ------ temporal phase analysis techniques, which is very well adapted to the measurement on continuously deformed or vibrating objects.

2.2 Review of temporal phase analysis techniques

Within the field of deformation measurement, the study of the response of objects to impact loading and vibration is a subject of great interest in experimental mechanics and constitutes one of the most appealing applications of optical interferometry. Interesting research describing transient deformation measurement by use of twin-cavity double-pulsed lasers has been published by Fernandez et al. (1998) and Farrant (1998). Provided that both laser pulses effectively freeze the object movement, ESPI will produce a fringe pattern representing an instantaneous deformation field between pulses. However, these techniques have an important limitation. To obtain the evolution of the transient deformation, an experiment must be repeated many times, each time with a different delay between the beginning of the impact loading and the emission of the second laser pulse. This means non-repeatable events such as rapid crack propagation, cannot be studied in detail. A further limitation with such an approach is the inability to record more than one exposure of the deformed state, which means that phase-shifting techniques cannot be employed. Single image carrier-based methods are frequently used, but these have significant drawbacks of reduced phase resolution compared with phase shifting.

One solution to these problems is to record a sequence of interferograms throughout the entire deformation history. If the temporal sampling rate is sufficiently

high, temporal phase analysis can be used to extract high-quality phase maps, and

temporal phase unwrapping allows absolute displacement fields to be obtained

(Brown, 1989; Huntley 1993). The term "absolute" here means the total displacement

from the start of the measurement process, as opposed to displacement relative to a

reference point in the field of view, which is all that can be achieved with spatial

unwrapping.
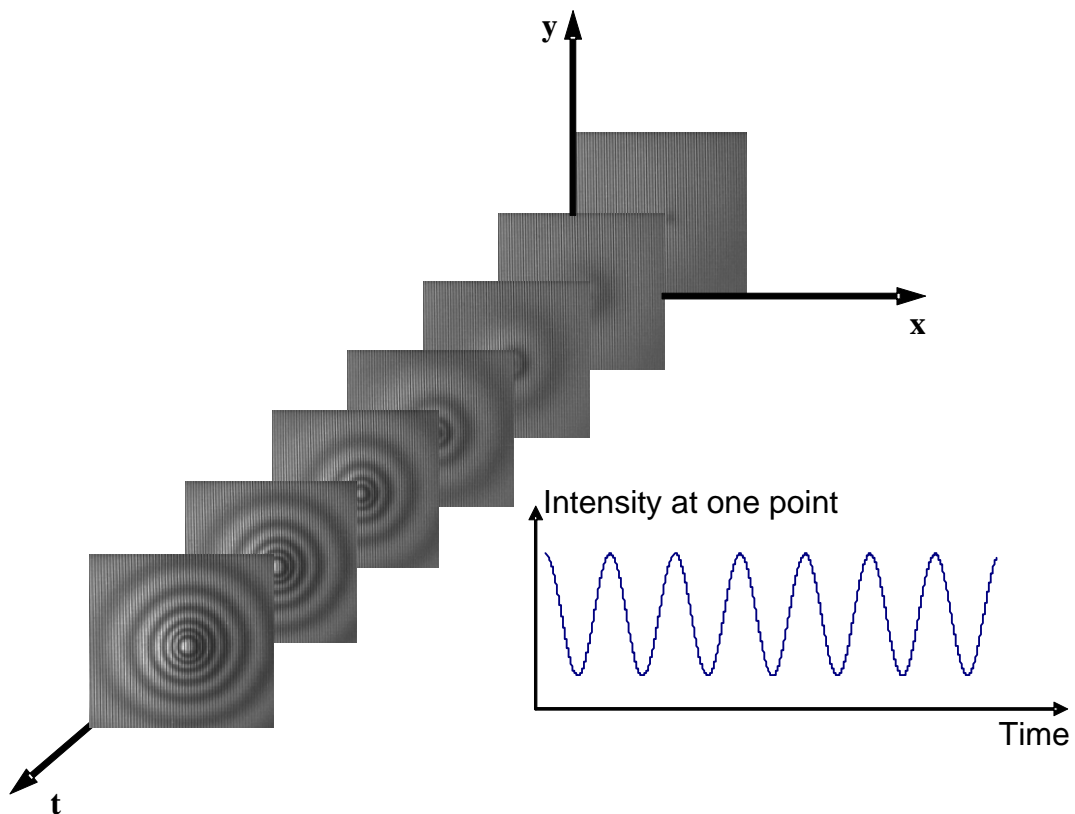
Figure 2.9 Schematic layout of temporal phase analysis technique

Figure 2.9 shows the schematic layout of the temporal phase analysis

technique. During deformation, a series of frames is recorded, from which intensity

variation over time is extracted for each point. Fourier transform is the predominant

method in temporal phase analysis to retrieve the phase. It works by pixelwise Fourier

transforming the data, zeroing everything but a band around a peak frequency, and

transforming back into time domain, thereby effectively performing a bandpass filter. Result of the inverse Fourier transform is the phase of the filter fringe signal, which is then unwrapped. Figure 2.10 shows an example of the Fourier transform process on one pixel.
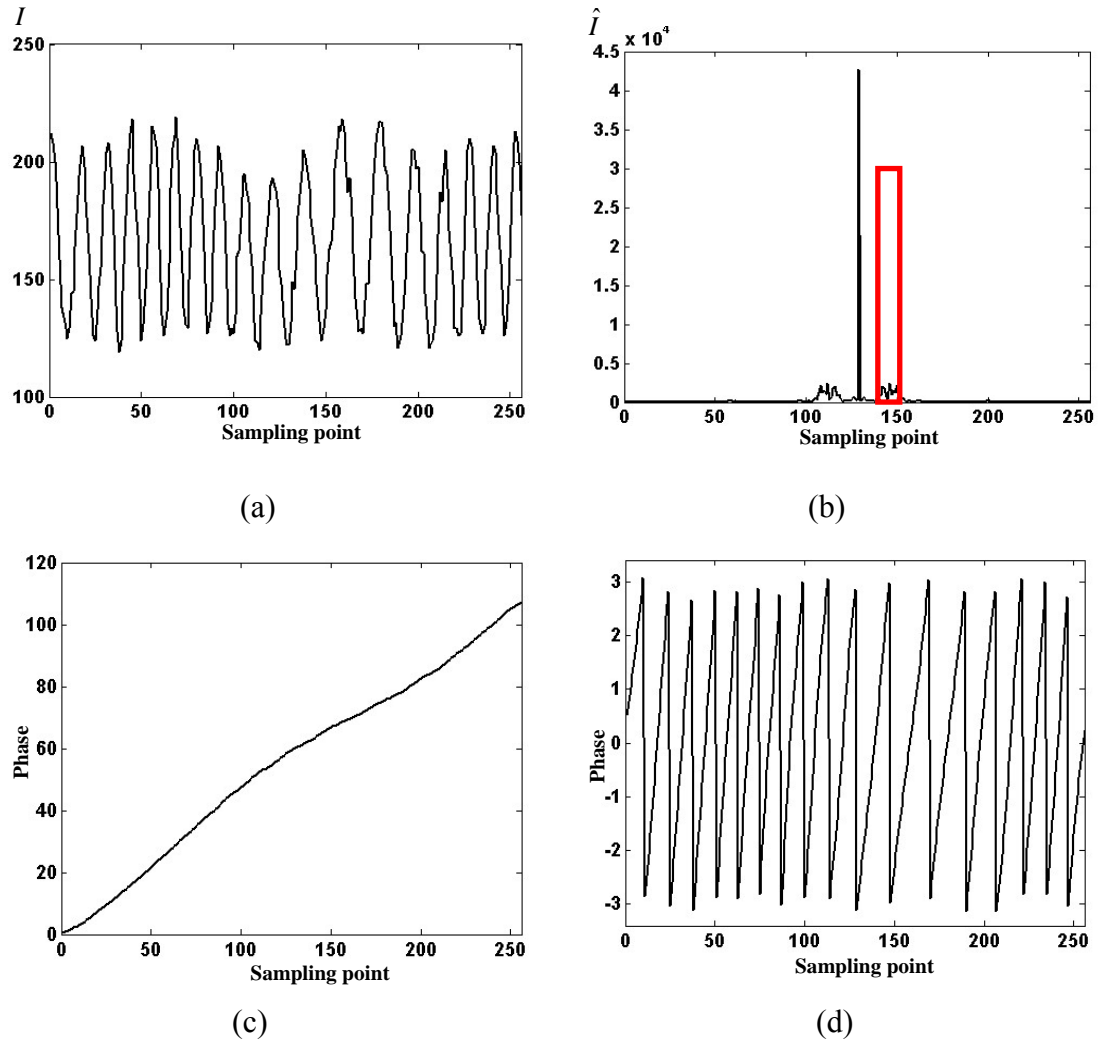
Figure 2.10 (a) Intensity variation of one pixel; (b) frequency spectrum of the signal and bandpass filter; (c) wrapped phase; (d) continuous phase after unwrapping.

Temporal Fourier analysis and temporal phase unwrapping (Huntley and Saldner, 1997) were firstly applied with wavelength-scanning interferometry (Takeda and Yamamoto, 1994) for surface contour with discontinuities. When the object contains discontinuities that are due, for example, to specimen edges or growing

cracks, spatial unwrapping is potentially risky because of the possibility of unwrapping across a boundary which can cause spatial propagation of a large phase error. By contrast, the combination of temporal phase analysis and temporal phase unwrapping means that each pixel in the camera behaves as an independent displacement sensor. For a continuously-varying wavelength (Tiziani et al. 1997, Kuwamura and Yamaguchi 1997), a temporal interference signal is observed at each pixel of the detector array in the image plane. During data acquisition, a series of frames is recorded, from which the intensity variation over time is extracted for each pixel. In this case, the phase value of each pixel varies due to a change of wavelength of the light source instead of displacement. Temporal Fourier analysis and one dimensional phase unwrapping are then applied on each pixel. The height information of each pixel can be extracted independently. Figure 2.11 is a result given by Tiziani (2000). It shows a milled aluminum surface with steps of 0.4 mm and 0.8 mm. The tilt at the top is 8°, and the object itself was tilted by 5°. Measurement of such tilted surfaces would be difficult with classical interferometric methods as the fringe density would become much too high to be analyzed. A similar concept has been applied on shadow moiré profilometry by Jin et al. (2001). Instead of changing the wavelength in interferometry, the frequency of the grating above the object to be measured was changed by in-plane rotation (Hung et. al, 1977b) and a series of fringe patterns was captured at certain intervals. Fourier transform was then applied on each pixel to obtain the height information.

At the end of 1990s, temporal phase evaluation technique (Luo, 2001) has gained wider applications in the measurement of large continuous deformation (Joenathan et al. 1998a). A typical technique is temporal speckle pattern interfeormetry (TSPI). Speckle methods have been used for different deformation

measurements because of several advantages, especially the simplicity of the experimental arrangement. ESPI has enhanced the possibility of real-time and highly quantitative analysis. However, the speckle interferometric methods suffer because of their high sensitivity, which is of the order of half the wavelength of light. For large deformations, the number of fringes that can be observed depends on the size of the CCD array. With a 512×512 array, one can observe about 20 fringes on the monitor for reasonably good quantitative analysis. Therefore the upper limit on an object deformation is around 6-7μm.
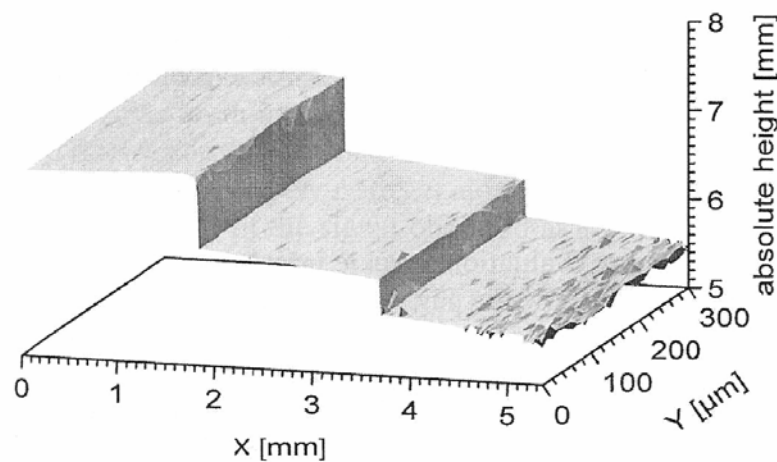
Figure 2.11 Milled steps of 0.4 mm and 0.8 mm (Tiziani, 2000)

Temporal speckle pattern interferometry (TSPI) makes use of the fact that a continuous deformation of the object introduces fluctuations in the phase of the speckles in the image plane of the object. Although the intensity modulation in the speckles occurs over the whole image plane, the individual speckles are analyzed as a function of time. Depending on the optical arrangement used, the phase of the speckles can be related to out-of-plane or in-plane motion (Joenathan et al. 1998b) or the slope of the object deformation (Joenathan et al. 1998c) as well as for shape analysis. Figure 2.12 shows a typical wrapped phase map obtained by TSPI.

Besides speckle methods, temporal phase analysis has also been applied with fringe projection techniques to retrieve the out-of-plane displacement (Pawlowski et al. 2002). In this case, a high quality linear fringe pattern is projected onto the object surface. Similarly, Fourier transform method is used to evaluate the temporal phase value pixel by pixel.
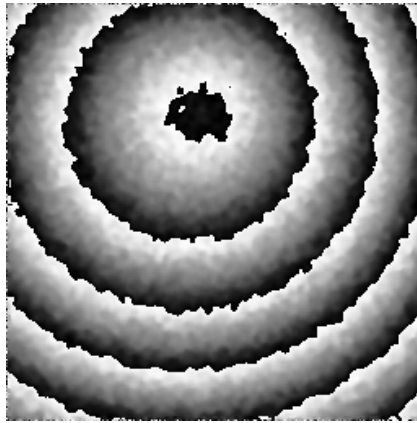
Figure 2.12 Typical wrapped phase difference distribution obtained from TSPI

The temporal Fourier transform has its disadvantages. If the deformation is highly nonlinear then the process of extracting data using Fourier transform method will not be accurate. The width of the side bands in the spectrum therefore increases and overlaps with the central peak. Selecting a proper bandpass filtering window becomes difficult.

To overcome this problem, Li et al. (2001) presented a simple but effective method, called phase scanning method to retrieve the phase from the variation of the gray value. If the amplitude of vibration is large enough, the variation of an instant phase value $\phi_p(x_p, y_p; t)$ of a point P will be higher than 2π, which implies intensity change of more than one period. With this assumption, the phase value at any instant can be calculated by the following equation: (Li, et al. 2001)

$$\phi_p(x_p, y_p; t) = \arccos\left[\frac{2I(x_p, y_p; t) - I_{\max}(x_p, y_p) - I_{\min}(x_p, y_p)}{I_{\max}(x_p, y_p) - I_{\min}(x_p, y_p)}\right]$$
(2.16)

where $I_{\max}(x_p, y_p)$ and $I_{\min}(x_p, y_p)$ denote the maximum and minimum gray value at point P, respectively. $I(x_p, y_p; t)$ is the gray value of point P at instant t. Similarly, unwrapping is executed on the time axis.

The significant drawback of the phase scanning method is that it cannot be applied to a very noisy signal as the accuracy of the method relies on the correct identification of the maximum and minimum values in each cycle of the intensity variation. Although Li also applied this algorithm to speckle fringe patterns, it is found that the method is more suitable for clear patterns obtained by incoherent methods such as fringe projection and shadow moiré. Furthermore, it needs more sampling points in one cycle of gray value variation. Li mentioned at least 6 sampling points; however, according to our experience, it is found that 10 to 16 sampling points per cycle produce the best results. Relatively large errors in the phase profile are also found when the gray value approaches extreme values. The errors are introduced by: (1) maximum or minimum values detected by the camera are slightly different from the actual extreme gray scale values; (2) for a sine-wave configuration, a slight difference in gray level near the extreme values causes a large change in phase value.

2.3 Review of wavelet applications in optical interferometry

Wavelet analysis has become an effective tool in many research areas since the last decade. An interesting historical account by Daubechies (1992) shows that different domains of physics and engineering have developed methods that can all be brought in a larger perspective based on wavelets. The same situation applies in optical metrology. In this section, a brief introduction of wavelet analysis is discussed, followed by reviews of wavelet applications in optical interferometry, in particular its applications in phase retrieval using one fringe pattern; speckle noise reduction; and flow detection.

2.3.1 Fourier analysis and continuous wavelet transform

From the reviews presented above, two types of signals are processed in optical interferometry. One is the spatial distribution of the gray value variation; it could be a one-dimensional or two-dimensional signal. The other is the temporal intensity variation on each pixel, which is obviously a one-dimensional signal. Fourier transform is one of the effective algorithms in this area. It was introduced in 1807 by Fourier. Although rejected by his contemporaries, Fourier's ideas have been developed into one of the cornerstones of contemporary mathematics and engineering. Fourier transform (FT) is a standard tool for obtaining the frequency spectrum of a given signal *s(t)* over its total duration. The definition of FT is expressed as:

$$\hat{s}(\omega) = \int_{-\infty}^{+\infty} s(t)e^{-i\omega t}dt \qquad (2.17)$$

Normally the spectrum $\hat{s}(\omega)$ is complex. The amplitude of the spectrum represents the weight of different frequencies that compose the signal. The signal s can be reconstructed by an inverse Fourier transform:

$$s(t) = \frac{1}{2\pi} \int_{-\infty}^{+\infty} \hat{s}(\omega) e^{i\omega t} d\omega \qquad (2.18)$$

The properties of Fourier transform are well known. Here only the Parseval-Plancherel theorem is recalled, which will help us move back and forth between time and frequency domains. It establishes the following relation for two functions $f(t)$ and $g(t)$:

$$\int_{-\infty}^{+\infty} f(t) \overline{g}(t) dt = \frac{1}{2\pi} \int_{-\infty}^{+\infty} \hat{f}(\omega) \overline{\hat{g}}(\omega) d\omega \qquad (2.19)$$

where $\overline{g}$ is the complex conjugate of g.

Figures 2.10(a) and (b) show an example of one-dimensional Fourier transform. As long as we are satisfied with linear time-invariant operators, the Fourier transform provides simple answers to most questions. It is suitable for a wide range of applications such as signal transmissions or stationary signal processing. However, if we are interested in transient phenomena, Fourier transform becomes a cumbersome tool. The Fourier coefficient is obtained in Eq. (2.17) by correlating $s(t)$ with a sinusoidal wave $e^{i\omega t}$. Since the support of $e^{i\omega t}$ covers the whole real line, $\hat{s}(\omega)$ depends on the values $s(t)$ for all times $t \in R$. This global "mix" of information makes it difficult to analyze the local property of $s(t)$ from $\hat{s}(\omega)$. For this reason different types of representation were created. One of them is the short-time Fourier transform (STFT).

In STFT, a window function $w(t - \tau)$ localized at a time τ is used to isolate a small portion of the signal $s(t)$. The product $s(t)\overline{w}(t - \tau)$ is then Fourier transformed to generate an estimation of the instantaneous spectrum $S(\omega, \tau)$:

$$S(\omega, \tau) = \int_{-\infty}^{+\infty} s(t)\overline{w}(t - \tau)e^{-i\omega t} dt = \frac{1}{2\pi} \int_{-\infty}^{+\infty} \hat{s}(\alpha)\overline{\hat{w}}(\alpha - \omega)e^{i\alpha t} d\alpha \qquad (2.20)$$

The second term is a consequence of Eq. (2.19). It shows that the time localization corresponds to frequency localization. A particular spectrum component $S(\omega, \tau)$ is influenced by the weighted value of $s(t)$ in a region surrounding τ; on the other hand, it is influenced by a set of frequencies α such that $\hat{w}(\alpha - \omega) \neq 0$. The time-frequency uncertainty principle affects the resolution, which leads to trade-off between time and frequency localization. The narrower the time window, the better the temporal resolution can be achieved, at the cost of a poorer resolution in frequency and vice versa. In the case of Fourier transform being applied to the whole signal, $w(t)$ is as large as the signal support. Hence, the corresponding frequency band can be very narrow, which implies that the frequency resolution is high. This trade-off is the consequence of the uncertainty principle which states that the product of the temporal duration Δt and frequency bandwidth $\Delta \omega$ is necessarily larger than a constant factor: $\Delta t \Delta \omega \geq 1/2$. Equality holds if and only if the window function w is Gaussian. Hence, no function can be better localized in both temporal and spectral domains than a Gaussian window. The use of Gaussian window in STFT is called *Gabor transform* (Abbate et al. 2001) which was originally proposed by Gabor in 1946:

$$G(\omega, \tau) = \int_{-\infty}^{+\infty} s(t)\exp\left[-\frac{(t - \tau)^2}{2\sigma^2}\right]e^{-i\omega(t - \tau)} dt \qquad (2.21)$$

The only parameter is the variance σ^2 of the Gaussian window, which permits best time-frequency localization for a certain signal.

When STFT is used, $\Delta t \Delta \omega$ is constant in the whole time-frequency plane once the window function $w(t)$ is selected. This means that STFT at any point (t_0, ω_0) in the time-frequency plane provides information about the signal $s(t)$ with an accuracy given by Δt and $\Delta \omega$ in the time and frequency domain. This localization is uniform in the entire plane, resulting in a uniform tiling of this plane with a rectangular cell of fixed dimension as shown in Fig. 2.13(a).
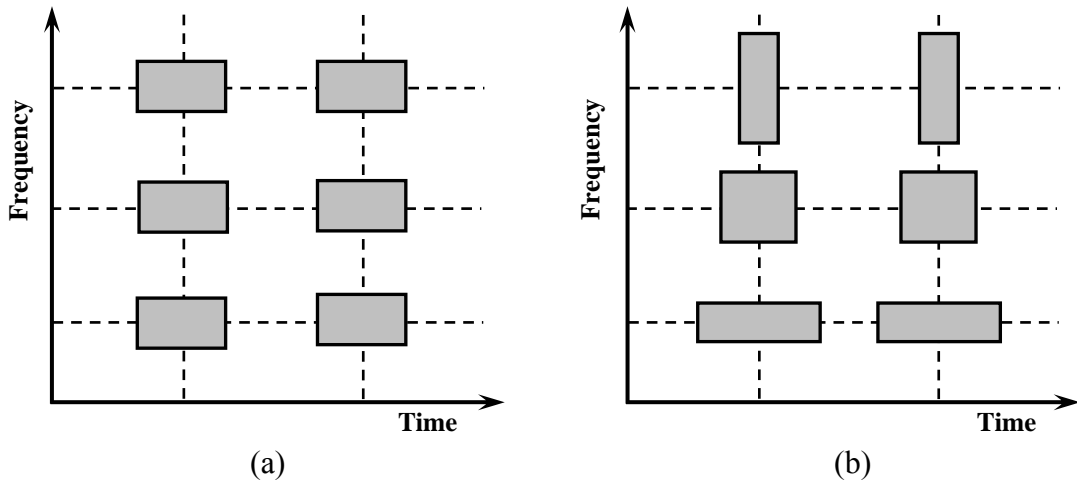
Figure 2.13 Time-frequency analysis cell in the case of : (a) Short-time Fourier transform (b) wavelet transform

If signal $s(t)$ has a transient component with a *support* (duration) smaller than Δt, it is difficult to locate the signal with an accuracy better than Δt. A similar situation is observed for signals with a small support in the frequency domain. If we choose a smaller value of Δt, the time resolution increases while the frequency resolution $\Delta \omega$ decreases. Therefore, if the signal $s(t)$ is composed of a very short transient time with monochromatic (single frequency) sinusoidal waves, it is difficult to find an optimal window $w(t)$. Hence STFT is only suitable for analyzing signals

that have signal components with similar ranges as the temporal and frequency supports.

In dynamic problems, the actual frequency of a signal may range from very low frequencies up to Nyquist frequency. Similar observations led Morlet, working in seismic signals, to devise a different type of analysis ------ wavelet transform, where the width of the analyzing window is automatically adapted to the particular frequency band of interest. In the case of continuous wavelet transform, time-frequency resolution will vary according to the frequency of interest, as shown in Fig. 2.13(b), where at higher frequencies the time resolution is smaller at the cost of a large frequency window. The uncertainty principle ensures that the area of each tile is constant and equivalent to $\Delta t \Delta \omega$ as in STFT case.

Wavelet transform, similar to STFT, maps a signal $s(t)$, into a two-dimensional domain (the time-frequency plane) and is denoted by

$$W_S(a,b) = \frac{1}{\sqrt{a}} \int_{-\infty}^{+\infty} s(t) \overline{\Psi}\left(\frac{t-b}{a}\right) dt = \int_{-\infty}^{+\infty} s(t) \overline{\Psi}_{ab}(t) dt \qquad (2.22)$$

where $\Psi(t)$ is in general called the mother wavelet, and the basis functions of the transform, called daughter wavelets, are given by:

$$\Psi_{ab}(t) = \frac{1}{\sqrt{a}} \Psi\left(\frac{t-b}{a}\right) \qquad (2.23)$$

Ψ_{ab} is a set of basis functions obtained from the mother wavelet $\Psi(t)$ by compression or dilation using scaling parameter a and temporal translation using shift parameter b. $\overline{\Psi}_{ab}$ denotes the complex conjugate of Ψ_{ab}.

The scaling parameter a is positive and varies from 0 to ∞. For $a < 1$, the transform performs compression of the signal, and for $a > 1$, the transform performs dilation of the signal. The signal $s(t)$ can be recovered from the wavelet coefficients $W_S(a,b)$ by inverse wavelet transform

$$s(t) = \frac{1}{c} \int_{-\infty}^{+\infty} \int_{0}^{+\infty} W_S(a,b) \Psi\left(\frac{t-b}{a}\right) \frac{da}{a^2} db \qquad (2.24)$$

provided that constant c is

$$c = \int_{-\infty}^{+\infty} \frac{\left|\hat{\Psi}(\omega)\right|^2}{\omega} d\omega < \infty \qquad (2.25)$$

Equation (2.24) is also referred to as the reconstruction formula, inverse transform, or synthesis, and Eq. (2.25) is generally known as the admissibility condition. In practice, this reconstruction is not very useful for a particular application in optical measurement, but the fact that c must exist leads to some admissibility conditions (Chui, 1992) on the function $\Psi(t)$. First, $\Psi(t)$ must be a square-integrable complex-value function (note $\Psi \in L^2(R)$), that is:

$$\int_{-\infty}^{+\infty} \left|\Psi(t)\right|^2 dt < \infty \qquad (2.26)$$

As $\Psi(t)$ is supposed to be a window function, it should also verify:

$$\int_{-\infty}^{+\infty} \left|\Psi(t)\right| dt < \infty \qquad (2.27)$$

Consequently, $\hat{\Psi}(t)$ is a continuous function. It follows from Eq. (2.25) that $\hat{\Psi}(0)$ must be zero. As explained earlier, wavelet analysis is performed differently for high

and low frequencies. This is illustrated in Fig. 2.13 where the elementary "cells" in the time-frequency domain are compared for wavelet and STFT. Accordingly, wavelet transforms present a better frequency resolution in the low frequencies domain, at the expense of time localization, and a higher temporal resolution at high frequencies, at the expense of spectral resolution.

The following shows an example of the wavelet transform mentioned above. Figure 2.14 shows a signal with two frequencies which occur consecutively along the time axis. The frequencies are $2\pi/10$ and $2\pi/15$, respectively. The modulus of CWT using complex Morlet wavelet is presented in Fig. 2.15. The dashed line shows the maximum modulus of wavelet transform, which indicates the instantaneous frequencies with maximum energy.

The wavelet decomposition presented above is continuous, but a standard approach is to explore a signal at a specific number of locations obtained by "binary dilation" and "dyadic translation", which means wavelet coefficients are calculated for the set of points $a = 2^j$, where j is an integer. In the case of orthogonal wavelets this type of decomposition is efficient and non-redundant. Many algorithms (Wickerhauser, 1994) have been developed for filtering or compression of signals using the so-called multi-resolution feature of wavelet. However, our goal is to extract an accurate phase from instantaneous frequency of a signal. Hence our focus is on continuous wavelet transform (CWT).

CWT expands a one-dimensional temporal intensity variation of certain pixels into a two-dimensional plane of frequency (related to scaling a) and position b as shown in Fig. 2.15. The dashed line is called the 'ridge' of the continuous wavelet transform, which is the trajectory of maximum $|W_S(a,b)|^2$ on the temporal-frequency

plane. The instantaneous frequency of the signal can be obtained by ridge extraction. More details will be given in Chapter three.
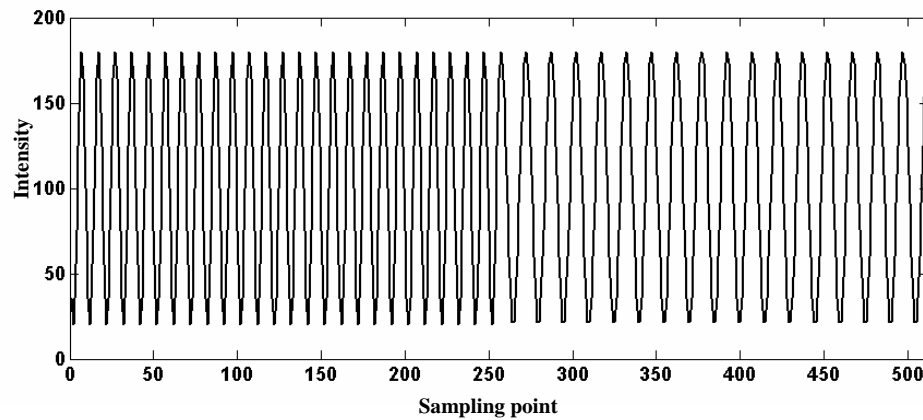
Figure 2.14 A signal with two frequencies occurred consecutively along time axis
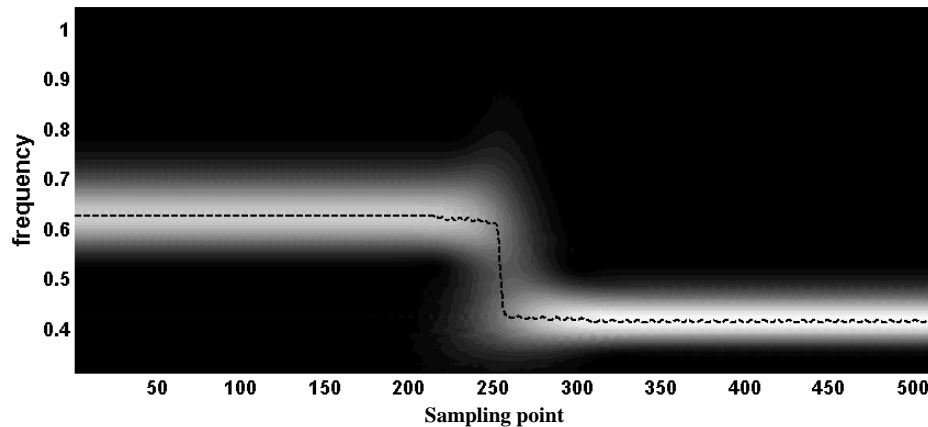
Figure 2.15 Modulus and ridge of CWT obtained by Complex Morlet wavelet ($\omega_0 = 4\pi$)

The main difference between Fourier transform and continuous wavelet transform is in the choice of basis functions or the functions with which convolution of the signal is carried out. Fourier transform uses wave, while wavelet transform use functions which have a compact support --- wavelet. Wavelet transform makes it possible to separate signals from different frequency components and simultaneously study their local structure with a resolution corresponding to the chosen scale. This feature makes it more suitable for temporal analysis.

2.3.2 Wavelet in optical metrology

In optical interferometry, wavelet analysis is mainly applied in (1) phase retrieval; (2) speckle noise reduction and (3) flaw detection and feature analysis.

2.3.2.1 Phase retrieval

As wavelet is able to extract the instantaneous frequency of a signal, this feature is mainly applied to the retrieval of phase from spatial intensity variations. There are two methods to obtain the phase: one is by integration of the instantaneous frequency (Watkins et al., 1999). Using this method, phase unwrapping is not required (Afifi et al. 2002). Similar to Fourier transform, using wavelet analysis one is also unable to determine the sign of phase. This is the problem of phase ambiguity. Watkins et al. (1997) and Tan et. al (1997) used a two-step phase shifting to overcome this problem. The phase step can be chosen arbitrarily between 0 and π. Another way for phase extraction is to compute the phase at a wavelet ridge:

$$\varphi(b) = \tan^{-1}\left(\frac{\text{Im}[W_S(a_{rb},b)]}{\text{Re}[W_S(a_{rb},b)]}\right) \tag{2.28}$$

where Im and Re are respectively the imaginary and real part of a complex wavelet coefficients. a_{rb} is a scaling on the ridge. Obviously, phase unwrapping cannot be avoided. Morimoto et al. (1995; 2002) used the method for phase retrieval in the grid method, while Wei et al. (1999) used it to analyze an interferogram of a temperature field produced by two heaters. It was also applied to analyze the crystal growth (Xiong et al., 2000; Fang et al., 2001a) and speckle-shearing interferometry (Fang et al. 2001b). In speckle-shearing interferometry, differentiation was applied on a phase map obtained by wavelet analysis, and curvature information is extracted. It was mentioned that the wavelet analysis gives a better solution with noise reduction and

without deficiency of filter window choice as in Fourier transform. However, due to phase ambiguity, carrier technique is still applied on an initial interferogram. Qian et al. (2003a) applied a phase-shifting windowed Fourier ridges method to solve this problem and show better results than the normal phase-shifting and digital shearing methods. As wavelet analysis is able to extract the instantaneous frequency of a signal, it gains wide applications in analyzing moiré fringe patterns. In the moiré technique, the strain measured is the first derivative of the phase value, which can be directly obtained from the instantaneous frequency. Wang (2002) and Asundi (2002) applied Gabor filters to extract the strain contour. Qian et al. (2003b) extracted the strain map directly using two-dimensional continuous wavelet and their results are presented in Fig. 2.16. Figure 2.16(a) is a typical moiré interferometric pattern and Fig. 2.16(b) is its Fourier transform, which is very complex; Fig. 2.16(c) shows the strain contour by conventional moiré of moiré method while Fig. 2.16(d) is the whole field strain distribution obtained by wavelet ridge extraction. Similar results in moiré interferometry were reported by Kadooka et al. in 2003. Wavelet analysis has also been used to process the speckle patterns (Federico and Kaufmann, 2001; 2002). However, due to the noise effect of the speckle, only simulated fringe patterns with carrier were evaluated at present. Similar applications (Dursun et al. 2003; Zhang and Weng, 2004) can be found in fringe projection techniques.

The applications mentioned above are in spatial domain. The wavelet analysis shows an alternative method of carrier based Fourier transform, and is able to produce better results. Wavelet transform has also been applied to temporal phase analysis of speckle interferometry. The concept was first introduced by Colonna de Lega in 1996 and some preliminary results were presented (1997). Cherbuliez et al. (1999; 2001) extended the study to phase retrieval from fringe patterns in dynamic problems.
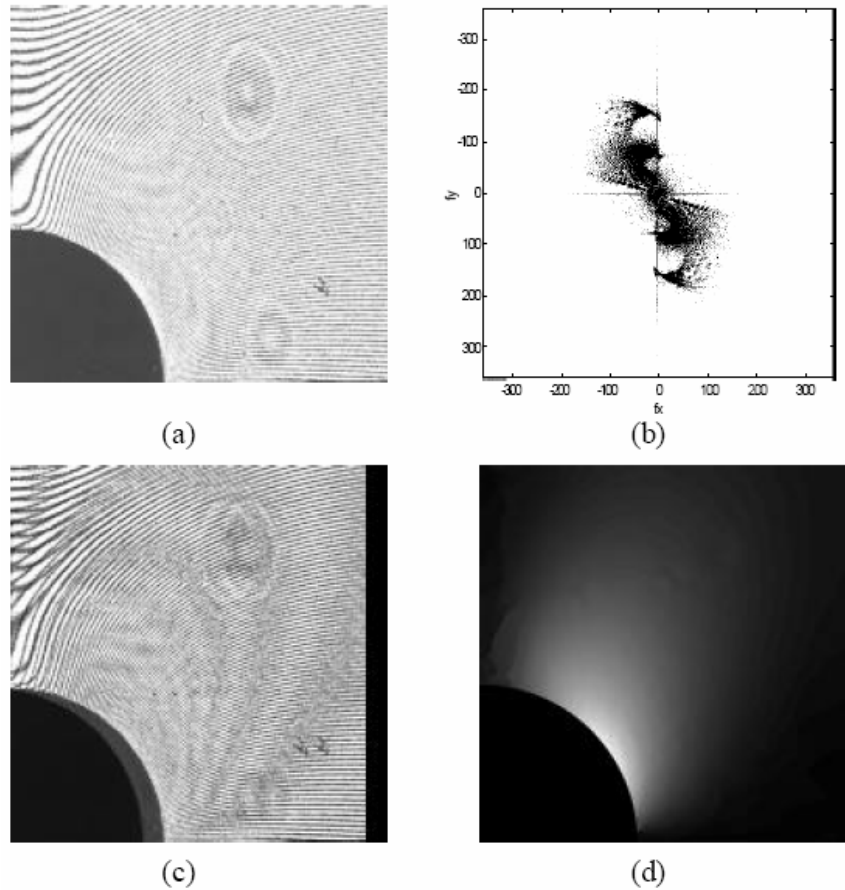
Figure 2.16 (a) Original moiré fringe pattern; (b) Fourier spectrum of (a); (c) strain contour by moiré of moiré; (d) strain map by wavelet analysis (Qian et al. 2003b)

2.3.2.2 Speckle noise reduction

Another main application of wavelet analysis in optical interferometry is speckle noise reduction. The method is also effective for other noises, such as electronic noise. As mentioned above, one is able to extract the instantaneous frequency of a signal using CWT which acts as an adaptive filter, and it reduces the noise effectively. Liu et al. (2004a and 2004b) used CWT to improve a fringe pattern in moiré interferometry and accurate results were obtained. However, it is only effective for fringe patterns with a cosine profile and is comparatively slow in computing. Another method is the use of discrete wavelet transform (DWT). Speckle pattern interferometry by wavelet denoising was realized by Kaufmann et al. (1996) and

Berger et al. (1997). When wavelet denoising was applied to time-averaged digital speckle pattern interferometry fringes, Shakher et al. (2001) found a median filtering before wavelet denoising would improve the results. Some recent developments on this topic were reported by Federico and Kaufmann (2001b), Shakher et al. (2002) and Kumar et al. (2004).

One advantage of wavelet denoising is the preservation of discontinuities with noise removal. Miao et al. (2002) achieved it by recognizing the high-frequency components from wavelet coefficients. It is more complicated than wavelet thresholding. An example of wavelet denoising is given in Fig. 2.17 which is a simulated noisy fringe pattern. Processed results using wavelet and low-pass filtering are shown in Figs. 2.17(b) and (c).

2.3.2.3 Flaw detection and feature analysis

In optical nondestructive testing, detecting a defect on products is a process different from deformation measurement. Usually a defect exists when an unusual frequency appears. The main purpose of flaw detection is to identify whether unusual frequencies exist and where they are located. Since wavelet transform reveals frequency as well as spatial information, it is an ideal tool for this purpose. In order to classify the different types of features (flaws), a suitable wavelet base with certain parameters should be designed. It should be sensitive only to certain features and reject any others. This has been realized not only through simulation but also by opto-electronic image processor with a solution suitable for industrial applications. Recently, several developments on this application have been reported by Kayser et al. (1999), Kruger et al. (2000; 2001) and Kallmeyer et al.(2002). The above-mentioned

work can also be understood as wavelet matched filters (Roberge and Sheng, 1994) for pattern recognition. An application on wineglass inspection was presented by Wang and Asundi (2000) using Gabor filtering. Recknagel et al. (2000) proposed another interesting method for defect detection. Usually a surface can be represented by a polynomial but not the defects. A suitable wavelet with a certain order of vanishing moments is able to suppress the surface. Thus the surface has no contribution to the wavelet coefficients. As wavelet coefficients caused by noise is dense and small while that contributed by defects are sparse and large, they can be separated.
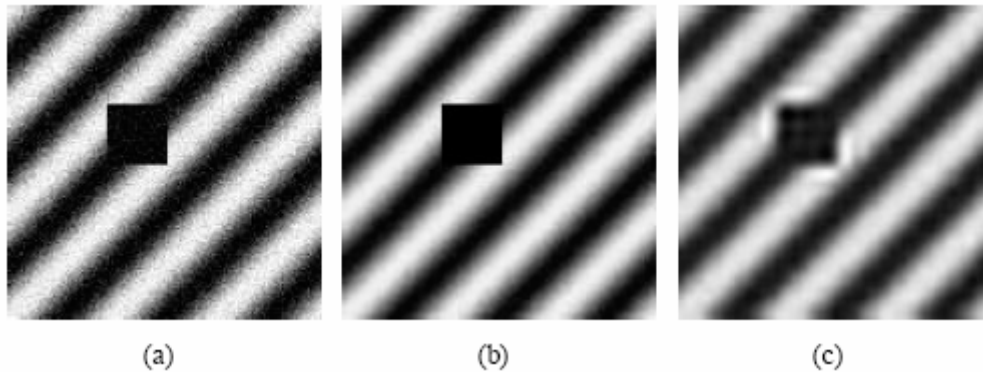
Figure 2.17 A comparison of results from wavelet denoising and low-pass filtering: (a) computer generated fringe pattern; (b) pattern after wavelet denoising; (c) pattern after low-pass filtering

Another application is in 3D profile measurement (Sandoz, 1997) using white light interferometry, where the output irradiance of one point is a cosine function modulated by an envelope. Once the light source is chosen, both the frequency of the cosine function and the envelope are known and the positions of fringe patterns are retrieved. Since the patterns appear like a wavelet atom, a similar wavelet base can be selected to detect the position with good accuracy.

CHAPTER THREE

THEORY OF TEMPORAL PHASE ANALYSIS

When optical interferometry is applied in dynamic measurement, a series of speckle or fringe patterns is captured. The intensity variation of each pixel can be expressed as

$$I(x,y;t) = I_0(x,y;t) + I_M(x,y;t)\cos\left[\varphi_0(x,y) + \varphi(x,y;t)\right] \qquad (3.1)$$

where $\varphi_0(x,y)$ is the initial phase on each pixel, $\varphi(x,y;t)$ is a time-dependent phase function related to the object motion or deformation. $I_0(x,y;t)$ and $I_M(x,y;t)$, which are also functions of time, are both slowly-varying functions. Temporal phase analysis extracts the phase $\varphi(x,y;t)$ from this one-dimensional signal. As shown in the previous chapter, Fourier transform is most commonly used in temporal phase analysis. Phase scanning is another option; however, it has not been used in the analysis of vibrating objects. In this chapter, we will only focus on: (1) wavelet transform and (2) phase scanning method on vibrating objects.

3.1 Temporal wavelet analysis

3.1.1 Transform representation: spectrogram and scalogram

The concept of continuous wavelet transform (CWT) is presented briefly in the last chapter. It maps a signal *s(t)*, into a two-dimensional plane of scaling *a* and shift *b*. Here we recall the Eqs.(2.22) and (2.23) as follows:

$$W_S(a,b) = \frac{1}{\sqrt{a}} \int_{-\infty}^{+\infty} s(t) \overline{\Psi}\left(\frac{t-b}{a}\right) dt = \int_{-\infty}^{+\infty} s(t) \overline{\Psi}_{ab}(t) dt \tag{3.2}$$

where $\Psi(t)$ is in general called the mother wavelet, and the basis functions of the transform, called daughter wavelets, are given by:

$$\Psi_{ab}(t) = \frac{1}{\sqrt{a}} \Psi\left(\frac{t-b}{a}\right) \tag{3.3}$$

Ψ_{ab} is a set of basis functions obtained from the mother wavelet $\Psi(t)$ by compression or dilation using scaling parameter a and temporal translation using shift parameter b. The results of continuous wavelet transform are usually presented in "spectrograms" or "scalograms". The example shown in Fig. 2.15 is the spectrogram of a signal of two frequencies. The vertical scale indicates the frequency.

The second type of representation is the scalogram, Fig. 3.1, where the linear frequency scale is replaced by a linear representation of a scaling factor a. As a general case, the frequency is proportional to the reciprocal of scaling factor a. For example, in a complex Morlet wavelet, the analysis frequency ω and the scaling factor a has a relationship of

$$\omega = \frac{\omega_0}{a} \tag{3.4}$$

where ω_0 is a coefficient of wavelet basis. In Morlet wavelet transform, the physical meaning of a is the number of sampling points in a cycle of ω_0 phase change. The top of Fig. 3.1 corresponds to the lowest frequency, while the bottom of the image corresponds to the highest frequency. The frequency domain is identical in scalogram

(Fig. 3.1) and spectrogram (Fig. 2.15). In this work, a scalogram is adopted as it is the direct result of a CWT and is easily understood by the reader.
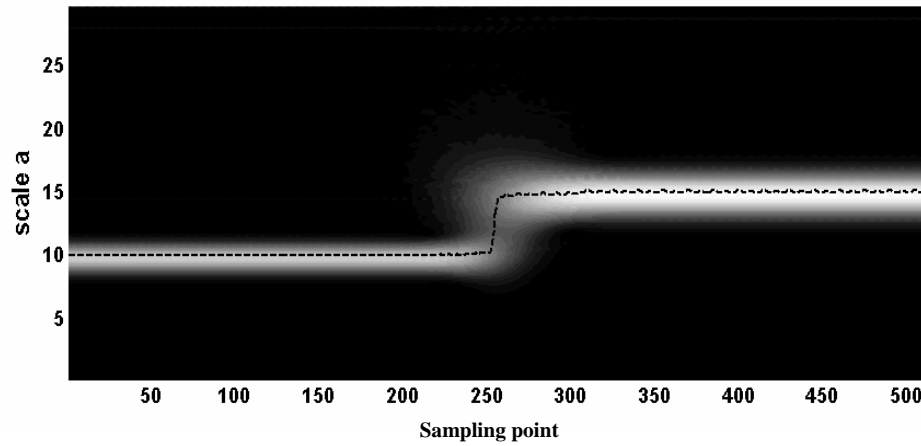
Figure 3.1 Scalogram of Morlet wavelet transform of a signal in Fig. 2.14

3.1.2 Selection of wavelet

The choice of wavelet depends on the nature of a particular application. For space-frequency analysis, a wavelet that is optimally localized in terms of both spatial width and frequency bandwidth is needed. For a smooth signal, a good choice is a wavelet that is smooth itself and therefore has good frequency localization. In contrast, a signal that contains discontinuities is better analyzed using wavelets with good spatial localization to accurately map the rapid changes in signal. This is similar in time-frequency analysis.

Delpart et al. (1992) and Guillemain and Kronland-Martinet (1996) who work in the field of acoustic signal processing showed the use of wavelet analysis to obtain the phase information. Their work deals with complicated signals with many components and mixed harmonics. In the present work, the signals obtained, either spatial or temporal signals, are similar to a simple sinusoidal signal with the presence of noise. Their signals are usually sufficiently over-sampled so that they do not suffer

from any aliasing problem. Furthermore, they are not interested in the phase of the different frequencies, while this is the quantity of prime importance in the present work.

To measure accurately the time evolution of frequency transients or tones, it is more appropriate to utilize a complex function as the mother wavelet, in order to properly separate the phase and amplitude information of the signal. To analyze phase related properties of a real function (e.g. determination of instantaneous frequency), a complex CWT is more suitable than a real CWT or a discrete wavelet transform (DWT). The most commonly-used mother wavelet for such an application is the complex Morlet wavelet which is the product of a real Gaussian window by a complex oscillating exponential function:

$$\Psi(t) = g(t)\exp(i\omega_0 t) \tag{3.5}$$

where $g(t) = \exp\left(-\dfrac{t^2}{2}\right)$ ω_0 is the "mother" frequency or central frequency, the only parameter that has to be selected. Figure 3.2 shows the real part and imaginary part of a complex Morlet wavelet when the central frequency is chosen as $\omega_0 = 2\pi$. The different wavelets used during time-frequency analysis are derived from the mother wavelet by a scaling a and time translation b. Hence, a wavelet derived from the mother wavelet takes the form:

$$\psi_{ab}(t) = \psi\left(\frac{t-b}{a}\right) = \exp\left(-\frac{(t-b)^2}{2a^2}\right)\exp\left(i\frac{\omega_0}{a}(t-b)\right) \tag{3.6}$$

The scale parameter a determines the width of the analysis window. At the same time, it defines the analysis frequency as shown in Eq. (3.4). Unlike the Gabor

transform, the functions used at different frequencies have the same "shape" and a varying width. This is illustrated in Fig. 3.3 where the real part of Morlet wavelet and Gabor windows are plotted for three frequencies, along with their Gaussian envelopes. The extent of the analysis window depends on the analysis frequency ω of the Morlet wavelet. Wavelets are "constant shape" windows in the sense that there is always the same number of oscillations in the window, whatever the scaling factor. This is obviously not the case for Gabor transform.
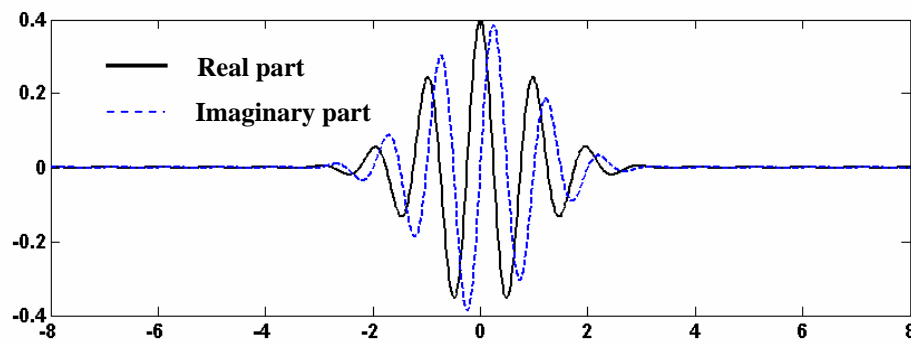
Figure 3.2 Real part and imaginary part of complex Morlet wavelet ($\omega_0 = 2\pi$)

(a)

(b)
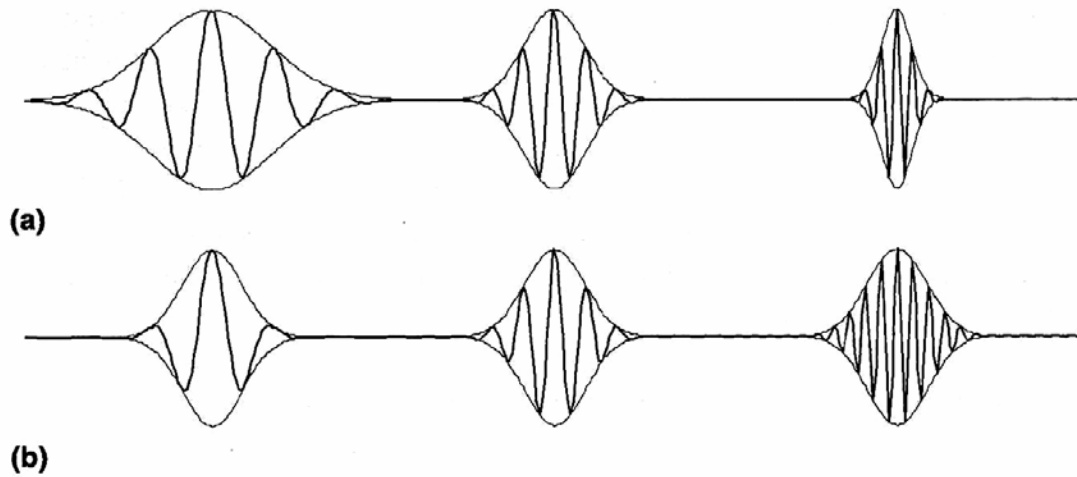
Figure 3.3 (a) Real part of a Morlet wavelet in time domain with three frequencies, from left to right: (1) $\omega_0/2$ ($a = 2$); (2) ω_0 ($a = 1$); (3) $2\omega_0$ ($a = 1/2$). (b) real part of the Gabor windows for the same frequencies.

Substituting Eq. (3.6) into Eq. (3.2), a wavelet coefficient of continuous complex Morlet wavelet transform is obtained:

$$W_S(a,b) = \frac{1}{\sqrt{a}} \int_{-\infty}^{+\infty} s(t) \exp\left(-\frac{(t-b)^2}{2a^2}\right) \exp\left(-i\frac{\omega_0}{a}(t-b)\right) dt \tag{3.7}$$

A normalization factor $\frac{1}{\sqrt{a}}$ is adopted here to ensure all dilated wavelets have the same energy. It is worth noting that we restrict ourselves to the positive frequency domain, since the spectral information of a real signal is completely and equivalently represented in both the positive and negative frequency domains. Using Parseval-Plancherel theorem, Eq. (3.7) can also be written as:

$$W_S(a,b) = \frac{1}{\sqrt{2\pi}} \int_{-\infty}^{+\infty} \hat{s}(\omega) \exp\left[-\frac{a^2}{2}\left(\omega - \frac{\omega_0}{a}\right)^2\right] \exp(i\omega b) d\omega \tag{3.8}$$

where $\hat{s}(\omega)$ denotes the Fourier transform of signal $s(t)$. Equation (3.8) shows that the wavelet coefficient is obtained by a integral on the product of Fourier transform of the signal by a frequency window of $\exp\left[-\frac{a^2}{2}\left(\omega - \frac{\omega_0}{a}\right)^2\right]\exp(i\omega b)$, which is a Gaussian window of variance $1/a^2$, centered at $\omega = \omega_0/a$, multiplied by a phase term. It illustrates the fact that the frequency band used to calculate a particular wavelet coefficient varies according to the central analysis frequency. If $\Delta\omega$ is defined as the width of the frequency window, it can be shown that the wavelet analysis is performed at a constant value of $\Delta\omega/\omega$ whereas Gabor transform performs an analysis at a constant $\Delta\omega$ value. Figure 3.4 shows various Morlet wavelets with

scaling factors of $a = 1, 2, 4$ and 8 in frequency domain. The mother frequency is selected as $\omega_0 = 2\pi$.
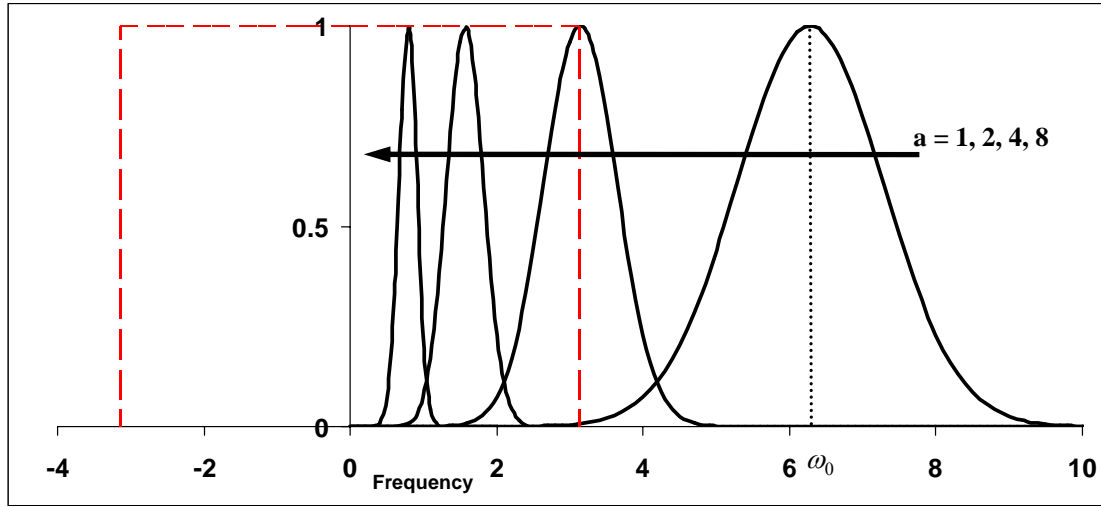
Figure 3.4 Morlet wavelets ($\omega_0 = 2\pi$) in frequency domain ($a = 1, 2, 4$ and 8)

From Fig. 3.4, it can be observed that in a complex Morlet wavelet transform, a high frequency resolution is obtained for low frequency signals, while the corresponding time localization is poor and vice versa. The behavior of a Gabor transform is simpler as the same frequency resolution and time localization are obtained for all frequency components of a signal. The popularity of a complex Morlet wavelet as an analyzing tool is due to the fact that it is described by an analytic function, and so is its Fourier transform. However, it has an infinite support, though this is not a practical problem as its envelope decreases rapidly from $t = 0$. In addition, the Morlet wavelet is not strictly speaking an admissible wavelet, though for $\omega_0 > 5$, the admissibility condition is practically satisfied.

The maximum frequency, ω_{max}, for which a CWT is meaningful is determined by the sampling rate of the signal, and its Nyquist frequency $\omega_{Nyquist}$ (Oppenheim et al., 1999).

$$\omega_{\max} < \omega_{Nyquist} = \frac{\pi}{\Delta t} \tag{3.9}$$

where Δt is the sampling time interval, which implies that the minimum meaningful

scale for wavelet transform is

$$a_{\min} > \frac{\omega_0 \Delta t}{\pi} \tag{3.10}$$

The Nyquist frequency $\omega_{Nyquist}$ is represented by the dashed line in Fig. 3.4. The

minimum meaningful frequency (maximum scale) is determined by the length of the

window such that at least one period $T = 2\pi/\omega$ should be contained within the

window of the wavelet, and ultimately by the length of the signal, i.e. the window

length should always be shorter than the length of the signal.

3.1.3 Selection of wavelet parameters

As mentioned before, ω_0 is the only parameter needed to be properly selected, and in

order to satisfy the admissibility condition, ω_0 must be larger than 5. Proper selection

of the mother frequency ω_0 determines the overall "balance" between time and

frequency resolution. In this section, based on the scalogram of a wavelet transform,

some examples will be given to show how ω_0 affects the results of a continuous

wavelet transform. This would throw some light on the preparation of guidelines for

proper selection of ω_0.

Figure 2.14 shows a signal with a frequency jump, i.e. two frequencies which

occur consecutively along time axis. The frequencies are $2\pi/10$ and $2\pi/15$ (10 and

15 sampling-points /cycle), respectively. Figure 3.5 shows three scalograms of a

continuous complex Morlet wavelet transform with different mother frequencies. O_T is the overlapping length of two frequencies in the time axis. B_F is the width of the coefficient peak in scale (frequency) domain. From Fig. 3.4, it is clear that a higher ω_0 would shift the frequency window to the right, which is the high frequency area; thus at a particular frequency, a narrower window is obtained, resulting a more detailed analysis of the frequency content of a signal. This will increase the resolution in frequency domain, but decrease the resolution in time domain due to the use of large temporal windows as shown in Fig. 2.13. It can be observed that O_T increases with ω_0, which implies that the resolution in time domain decreases with increasing ω_0; It is also seen that B_F decreases with increasing ω_0 which indicates that the resolution in frequency domain increases with ω_0.

Another example given in Fig. 3.6 is a sum of two signals with different but close frequencies: $2\pi/20$ and $2\pi/23$. Figures 3.6(b), (c) and (d) show the scalograms of a complex Morlet wavelet transform with different mother frequencies ω_0. In Fig. 3.6(b), the two components are too near to each other to be correctly resolved in the scalogram. However, if we increase the value of ω_0, as shown in Figs. 3.6(c) and (d), the two frequencies are distinctly resolved.

Figure 3.7 shows the scalograms obtained for a simulated sinusoidal signal of frequency $2\pi/20$ and modulation $I_{SM} = 50$ with added random noise with modulation $I_{NM} = 200$. It is clear that not much of the sinusoidal signal is visible in the signal plot of Fig. 3.7(a). Accordingly, the analysis with a very well temporally localized wavelet, $\omega_0 = 2\pi$, does not give much information about the signal's actual frequency evolution. However, doubling the mother wavelet frequency, as shown in

Fig. 3.7(c), provides a good frequency resolution and the ridge which represents the peak becomes visible. When the wavelet coefficients are calculated near the signal's frequency, only a small frequency band is used, which limits the amount of noise that affected the transform. In other words, the signal-to-noise ratio (SNR) is increased. If ω_0 is increased to 8π, Fig. 3.7(d), most of the noise is filtered out, thus showing the frequency evolution of the signal more clearly. The continuous line shows the location of maximum wavelet coefficients; it is almost a straight line at scale $a = 20$.

The previous examples might lead the reader to conclude that a large ω_0 value is always beneficial. This is true only when the signal frequency does not change significantly. However, in cases where the frequency changes dramatically, the time localization should be preserved in order to keep the analysis tool flexible. Sometimes striking a good time/frequency resolution balance is difficult, particularly if the analysis is supposed to be automatic. More discussion on the effect of ω_0 on the accuracy of phase extraction is given in the following section. In this study, ω_0 is normally selected as 2π to satisfy the admissibility condition and keep the flexibility of the wavelet analysis. This is because in temporal phase analysis, the signals are generally not seriously affected by the noise which is usually more serious in spatial domain.
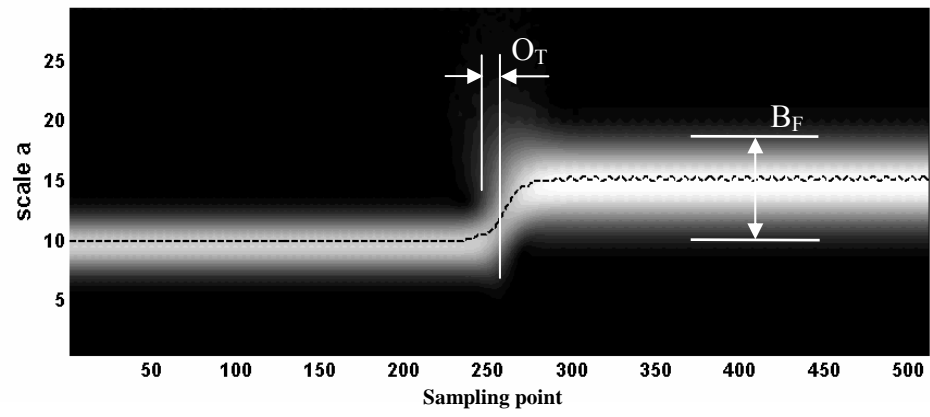
(a)
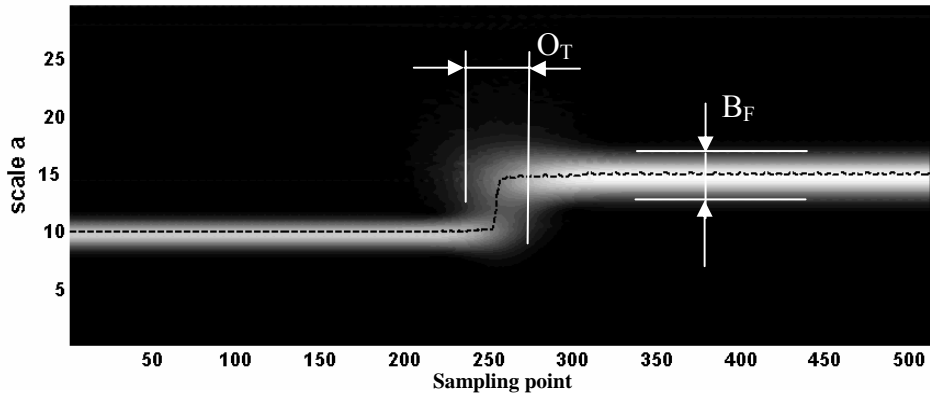
(b)
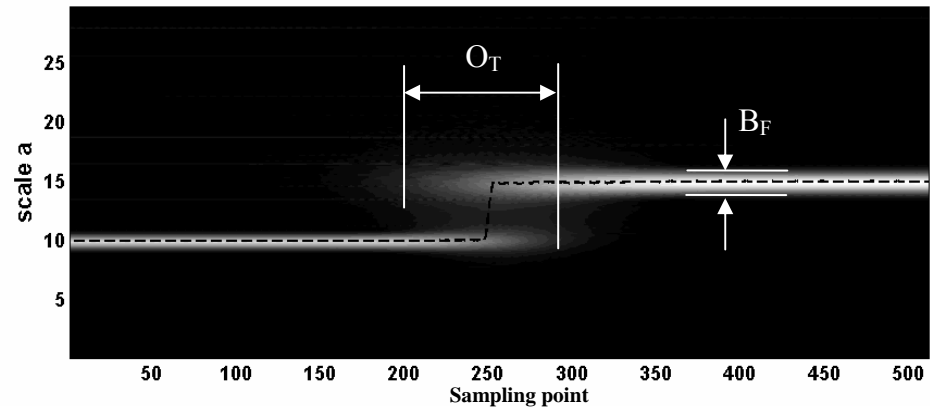
(c)

Figure 3.5 Complex Morlet wavelet transform of a signal with frequency jump: (a) $\omega_0 = 2\pi$; (b) $\omega_0 = 4\pi$; (c) $\omega_0 = 8\pi$

(a)

(b)

(c)

(d)
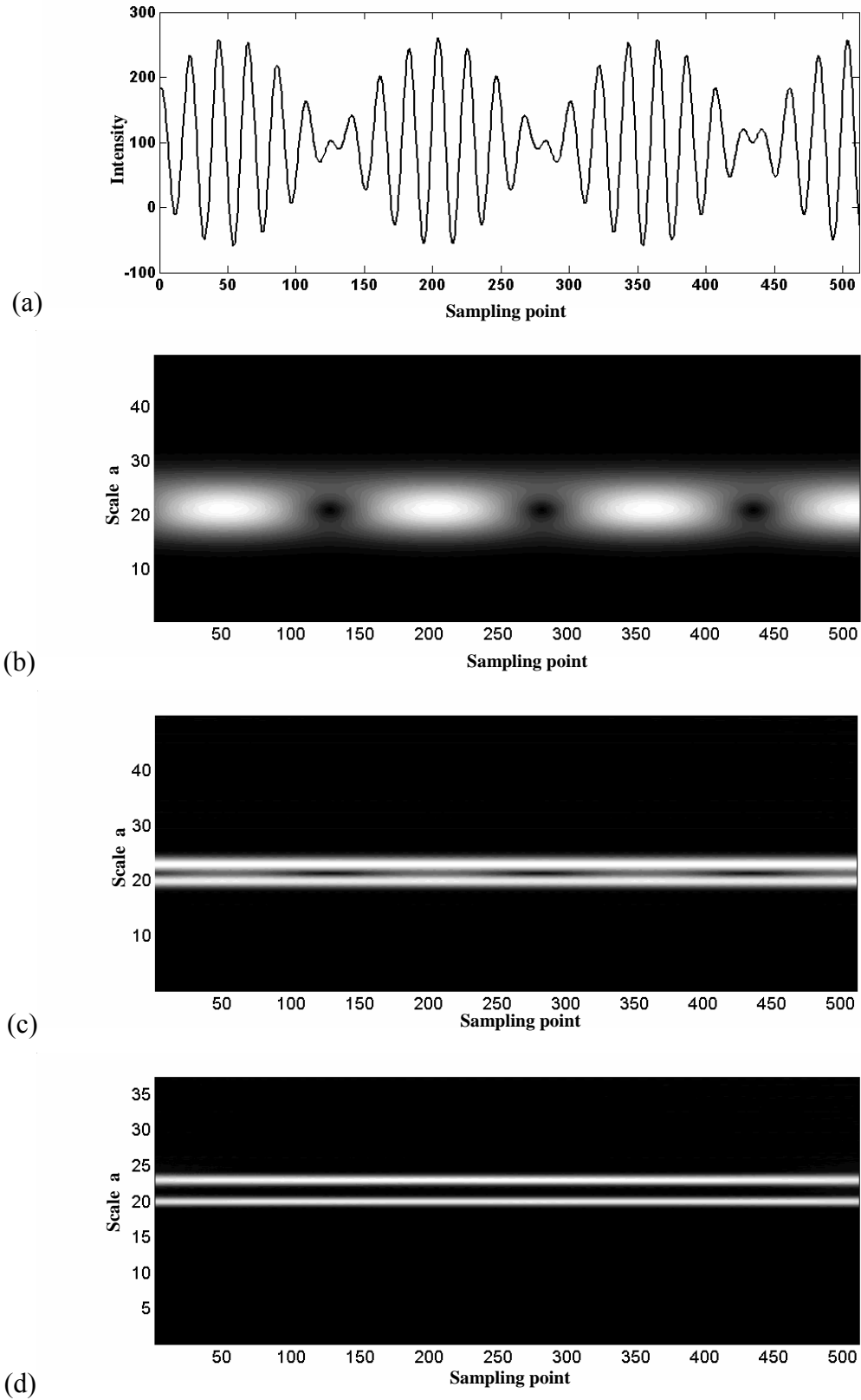
Figure 3.6 (a) A simulated signal with frequencies of $2\pi/20$ and $2\pi/23$ and its Complex Morlet wavelet transform (b) $\omega_0 = 2\pi$; (c) $\omega_0 = 8\pi$; (d) $\omega_0 = 16\pi$.

(a)

(b)

(c)

(d)
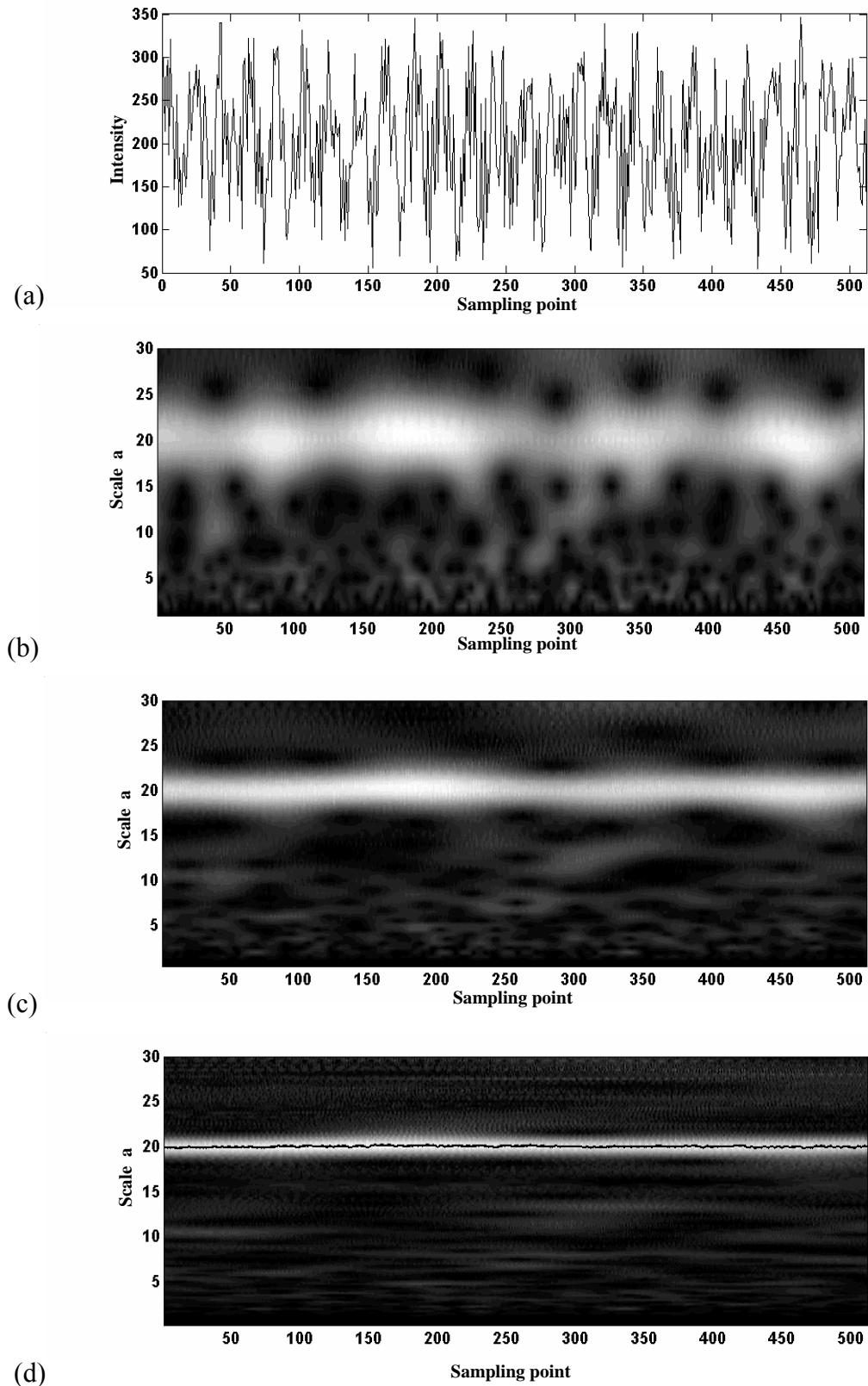
Figure 3.7 (a) A simulated sinusoidal signal with frequency of $2\pi/20$ (20 sampling-points/cycle) and added random noise $[100 + I_{SM}\cos\varphi + I_{NM} \times$ random noise] and its complex Morlet wavelet transform: (b) $\omega_0 = 2\pi$; (c) $\omega_0 = 4\pi$; (d) $\omega_0 = 8\pi$

3.1.4 Phase extraction from a ridge

In this section, the phase extraction techniques from the ridge of a wavelet transform is discussed. The instantaneous frequency $\omega_I(t)$ of a cosine modulation $f(t) = I_M(t)\cos\varphi(t)$ is defined as the positive derivative of the phase:

$$\omega_I(t) = \varphi'(t) \geq 0 \tag{3.11}$$

The derivative can be chosen to be positive by adapting the sign of $\varphi(t)$. As shown in Eq. 3.5, the complex Morlet wavelet is constructed by multiplying a window $g(t)$ with a sinusoidal wave. The Fourier spectrum $\hat{g}(\omega)$ of $g(t)$, is maximum at $\omega = 0$. The coefficient of a complex Morlet wavelet transform can be written as (Mallat, 1998)

$$W(a,b) = \frac{\sqrt{a}}{2} I_M(b)\{\hat{g}[a(\zeta - \varphi'(b))] + \varepsilon(b,\zeta)\} \cdot \exp[i\varphi(b)]$$

$$+ \frac{\sqrt{a}}{2} I_M(b)\{\hat{g}[a(\zeta + \varphi'(b))] + \varepsilon(b,\zeta)\} \cdot \exp[-i\varphi(b)] \tag{3.12}$$

where $\zeta = \dfrac{\omega_0}{a}$, as the term $\exp[-i\varphi(b)]$ and the DC terms are negligibly small with a proper selection of ω_0, only the term $\exp[i\varphi(b)]$ remains in Eq. (3.12). Thus, the wavelet coefficient can be written as

$$W(a,b) = \frac{\sqrt{a}}{2} I_M(b)\{\hat{g}[a(\zeta - \varphi'(b))] + \varepsilon(b,\zeta)\} \cdot \exp[i\varphi(b)] \tag{3.13}$$

where $\varepsilon(b,\zeta)$ is a corrective term which is negligible if the following conditions are satisfied:

$$\frac{\omega_0^2}{\left|\varphi'(b)\right|^2}\frac{\left|I_M''(b)\right|}{\left|I_M(b)\right|} << 1 \tag{3.14}$$

and

$$\omega_0^2\frac{\left|\varphi''(b)\right|}{\left|\varphi'(b)\right|} << 1 \tag{3.15}$$

The presence of φ' in the denominator of Eq. (3.14) and Eq. (3.15) shows that I_M'' and φ' are slow varying if φ' is small but may vary much more quickly for large instantaneous frequencies. Delprat et al. (1992) shows a different proof with similar results using a stationary phase approximation. The complete development of Mallat's method is presented in Appendix A.

The examples presented above show that instantaneous frequency information appears in a scalogram in the form of a "peak" in the modulus. Its vertical variation reflects a signal frequency variation. The width of this peak for a given time b is shown by the width of the Gaussian frequency window shown in Fig. 3.3. The trajectory of maximum value of $\left|W(a,b)\right|^2$ on the a-b plane is called a 'ridge'. Since $\left|\hat{g}(\omega)\right|$ is maximum at $\omega = 0$, and if $\varepsilon(b,\zeta)$ is negligible, $\left|W(a,b)\right|^2$ reaches a maximum when

$$\varphi'(b) = \zeta_{rb} = \frac{\omega_0}{a_{rb}} \tag{3.16}$$

where $\varphi'(b)$ is the instantaneous frequency of the signal, and a_{rb} denotes the value of a at instant b on the ridge. The wavelet transform on the ridge can then be expressed as

$$W(a_{rb},b) \approx \frac{\sqrt{a_{rb}}}{2} I_M(b)\hat{g}(0)\exp[i\varphi(b)] \qquad (3.17)$$

It can be observed that the phase of the wavelet coefficient on the ridge is exactly equal to the phase of the signal. The phase can be retrieved by two methods. One method calculates the arctangent of the ratio of the imaginary and real parts of the wavelet transform on the ridge.

$$\varphi(b) = \tan^{-1}\left(\frac{\text{Im}[W(a_{rb},b)]}{\text{Re}[W(a_{rb},b)]}\right) \qquad (3.18)$$

where Re and Im denote respectively the real and imaginary parts of the wavelet transform. However, $\varphi(b)$ obtained from Eq. (3.18) is within $[-\pi,\pi)$ and phase unwrapping cannot be avoided if a continuous phase value is needed. One of the advantages of this method is that the initial phase value of the first sampling point can be partially obtained. "Partially" means whatever the initial phase value is, the calculated phase value is within the range of $[-\pi,\pi)$. This phase value is not useful if only the displacement is measured in optical interferometry. However, sometimes the instantaneous shape of the object is also needed. In this case, the phase can only be calculated by Eq. (3.18), and temporal and spatial phase unwrapping are required.

In the second method, the phase value $\varphi(b)$ is calculated by integration of the instantaneous frequency shown in Eq. (3.16), and phase unwrapping procedure can be avoided. The main problem involved in this method is that the boundary conditions of

integration can not be determined. This method can only be used to calculate the
phase change between two instants. Figures 3.8 and 3.9 show an example of phase
extraction by the two methods mentioned above.

(a)

(b)

(c)

Figure 3.8 (a) A simulated single-frequency signal; (b) theoretical phase value of the
signal; (c) modulus of complex Morlet wavelet transform and its ridge.

Figure 3.8(a) shows a simulated signal with a signal frequency of $2\pi/25$, its theoretical phase values is given in Fig. 3.8(b). The initial phase of the first sampling point is $2\pi+3$ (rad). Figure 3.8(c) shows the scalogram of complex Morlet wavelet transform, and the dashed line shows its ridge. The ripple is observed on the ridge. Figure 3.9(a) are the phase values obtained by Eq. (3.18) and one-dimensional phase unwrapping. Theoretically, the initial phase of the first sampling point will be retrieved as 3 (rad) instead of $2\pi+3$ (rad). In optical interferometry, this 2π phase difference may be recovered by spatial phase unwrapping. However, the value we obtained by wavelet transform is 2.863 (rad). A 0.137 (rad) phase difference is found between the calculated phase and theoretical phase. The error at the start point will remain in the unwrapping process, but it will not affect the relative phase difference between two sampling points. Figure 3.9(b) is the phase change obtained by the method of integration. The initial phase of the first sampling point cannot be retrieved, and if it is set to zero, the graph represents the phase change of the signal. The theoretical phase change within the first one hundred sampling points is 24.88(rad). The difference between the initial phases obtained by these two methods is circled in Figs. 3.9(a) and (b). Figure 3.10 shows the error in phase change using different phase retrieving methods. The first method shows good results with a maximum fluctuation of 0.0024(rad). However, the second method gives the results of 24.78 (rad), or a 0.41% error. The errors observed in these two methods are mainly due to the discreteness of the signal and the wavelet. The a_{rb} values obtained fluctuate between 25 and 25.5 when the step in scale sweeping used is 0.5. This error could be reduced by increasing the resolution of scale sweeping with the cost of longer computing time. When the frequency of the signal processed is not very high, the error is generally not

large and can be neglected. However, two important observations are made from Fig.

3.10: (1) The process of integration may smoothen the random errors but will

accumulate system errors; (2) The phase values obtained directly from the modulus of

wavelet transform is not sensitive to a_{rb}, and unlike the process of integration, the

unwrapping process will not accumulate system error significantly. Generally, the

phase obtained by the first method mentioned above is more accurate than the results

from the second method.

(a)

(b)
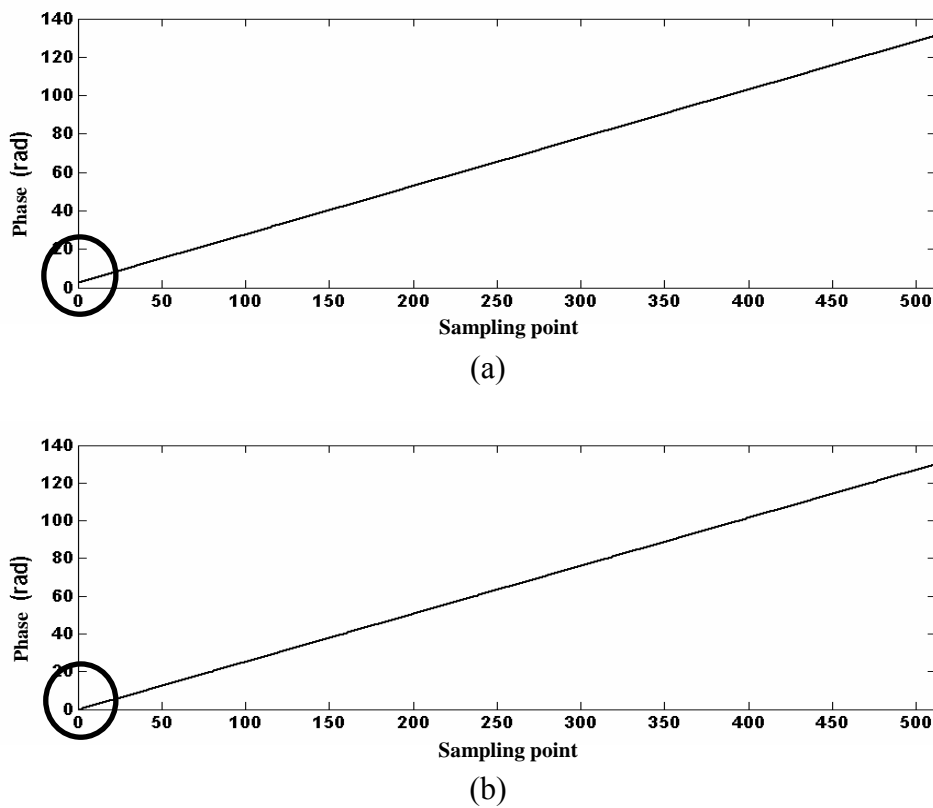
Figure 3.9 (a) Phase change obtained by arctan term and phase unwrapping; (b) phase
change obtained by integration

Figure 3.11 shows another example of wavelet phase extraction. As shown in

Fig. 3.11(a), the frequency of the signal is increasing along the time axis, and the

phase evolution is given in Fig. 3.11(b). Fig. 3.11(c) shows the scalogram and ridge of

wavelet transform between sampling point No. 301 and No. 400.
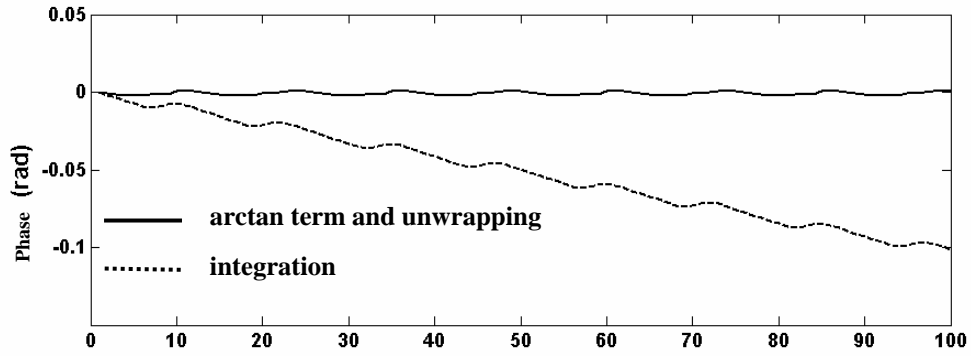
Figure 3.10 Errors in phase change within first 100 sampling point using different phase extraction methods.
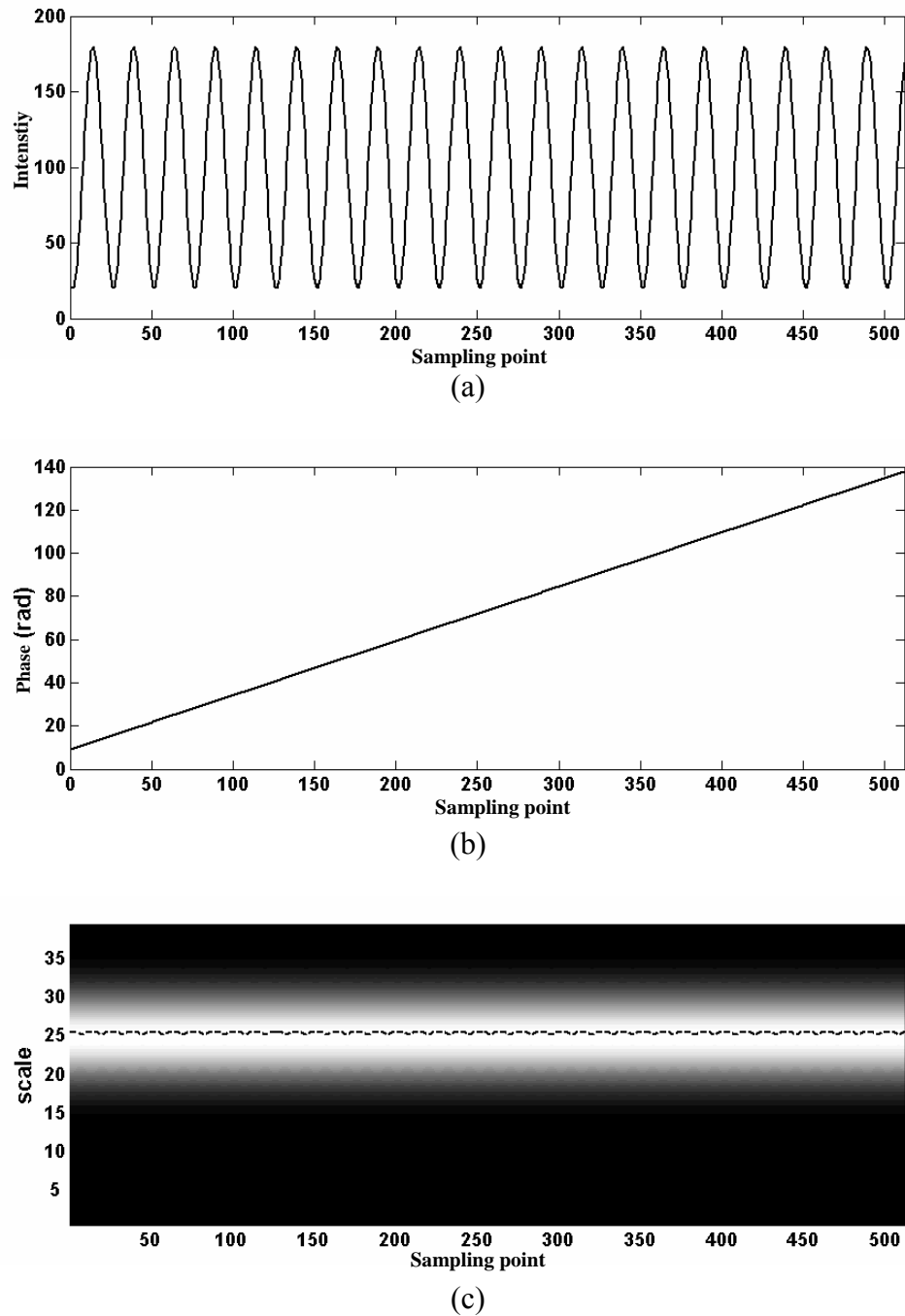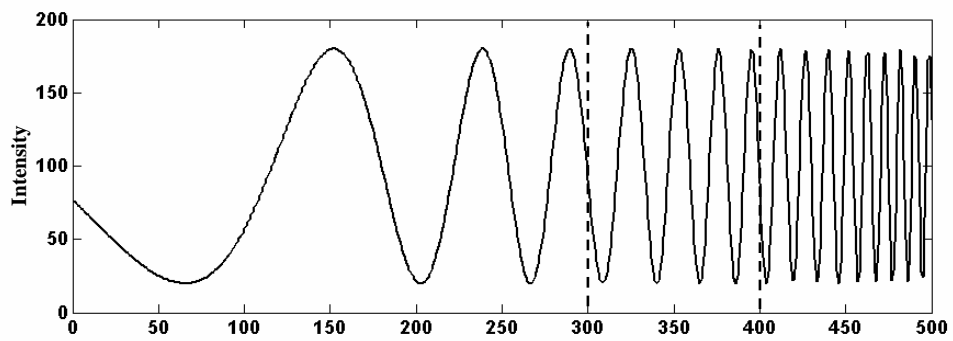

(a)
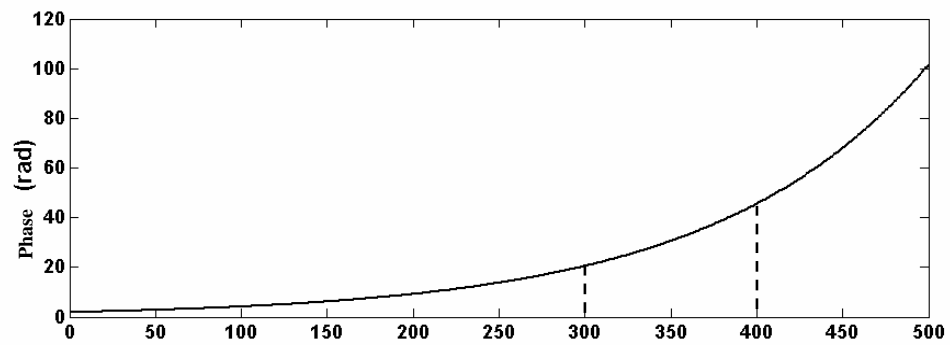
(b)
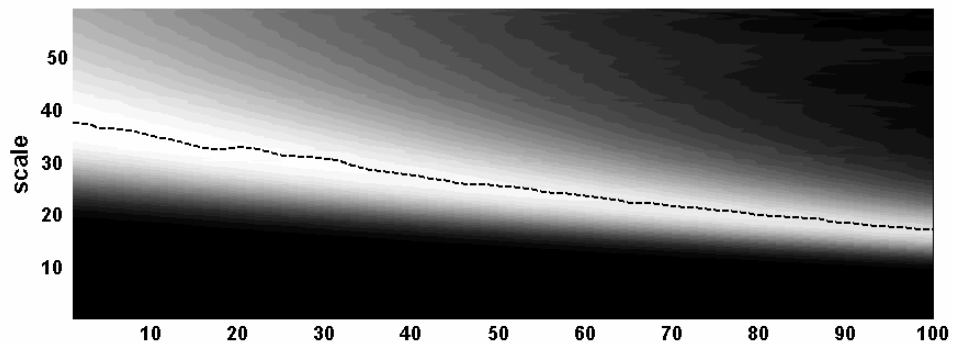
(c)

Figure 3.11 (a) A simulated signal with increased frequency; (b) theoretical phase value of the signal; (c) modulus of complex Morlet wavelet transform and its ridge from sampling point No. 301 to No. 400.

The theoretical phase change between sampling point No. 301 and No. 400 is 25.00 (rad), but the results obtained by Eq. (3.18) and unwrapping is 24.62(rad) or 1.52% in error. The result from integration method is less accurate, 24.41(rad) or 2.36% in error. Compared to the single frequency signal, there is another source of error. When the frequency of the signal is changing along the time axis, $\varphi''(b)$ is no longer zero and a system error due to the corrective term ε in Eq. (3.13) will be introduced. From Eq. (3.15), $\varepsilon(b,\zeta)$ remains small only when the value of $\omega_0^2 \dfrac{|\varphi''(b)|}{|\varphi'(b)|}$ is much smaller than one. $\dfrac{|\varphi''(b)|}{|\varphi'(b)|}$ is the factor which represents how fast the frequency changes at a certain instant. Generally, this value is different at different instants. However, the error in phase change is contributed by each sampling point between two instants. To evaluate the error introduced by a certain value of $\dfrac{|\varphi''(b)|}{|\varphi'(b)|}$ is difficult. In order to analyze the error of a certain ratio, a signal with following special phase function is simulated.

$$\varphi(t) = m \cdot e^{St} \tag{3.17}$$

where S and m are variable coefficients. With this phase function, the signal $a = I_0 + I_M \cos\varphi(t)$ will have an identical value of $\dfrac{|\varphi''(t)|}{|\varphi'(t)|} = S$ along the time axis. With a certain value of ω_0, each sampling point will have the similar contributions to the phase error. Figure 3.12 shows the phase evolution when S is varied from 0.001 to 0.015. Figure 3.13 shows two examples of simulated signal for $S = 0.001$ and $S = 0.010$. The value of m here is adjustable so that the signal simulated is suitable

for analysis. Here, it is selected such that theoretical phase change which occurs within point Nos. 301 and 400 equals to 25 (rad) at different values of S. Figure 3.14 shows the scalograms and the ridges of wavelet transform of these two signals.

Figure 3.15 shows the percentage errors for different values of S using two different phase extraction methods. Although some fluctuations are found on each curve, generally the error increases with the value of S. The error in the integration method is generally larger than that by arctangent method. However, when the mother frequency is selected as $\omega_0 = 2\pi$, the errors are small and will not affect the results too much. Figure 3.16 shows the percentage error of the integration method using wavelet with different mother frequencies ω_0. The error remains small in both cases when there is no drastic phase change. However, when $S > 0.008$, it is found that the error increases drastically using a wavelet of $\omega_0 = 4\pi$. For wavelet with $\omega_0 = 4\pi$, time localization is poorer than that with $\omega_0 = 2\pi$. When a signal with a large frequency variation is processed, it will generate larger errors in phase extraction. This is another point that should be considered when selecting ω_0. ω_0 should not be too large so that the time localization is preserved and system error is limited.
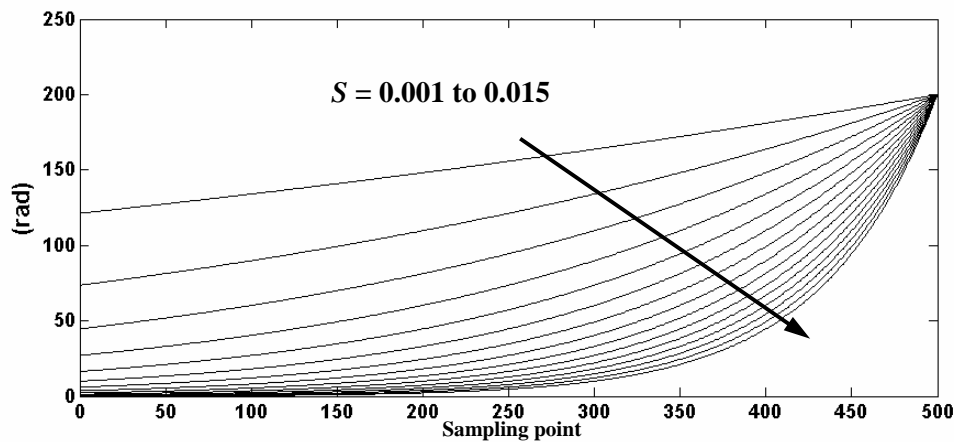
Figure 3.12 Phase evolution of signal with different values of S

(a)

(b)
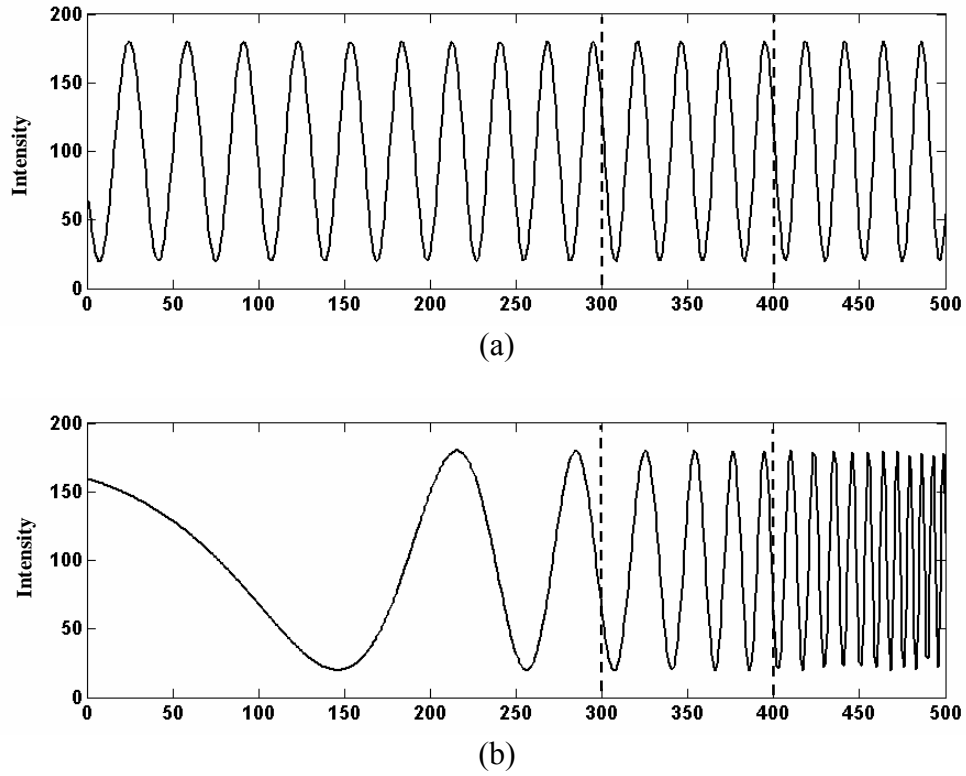
Figure 3.13 Examples of signal with different S: (a) $S = 0.001$; (b) $S = 0.010$.

(a)

(b)
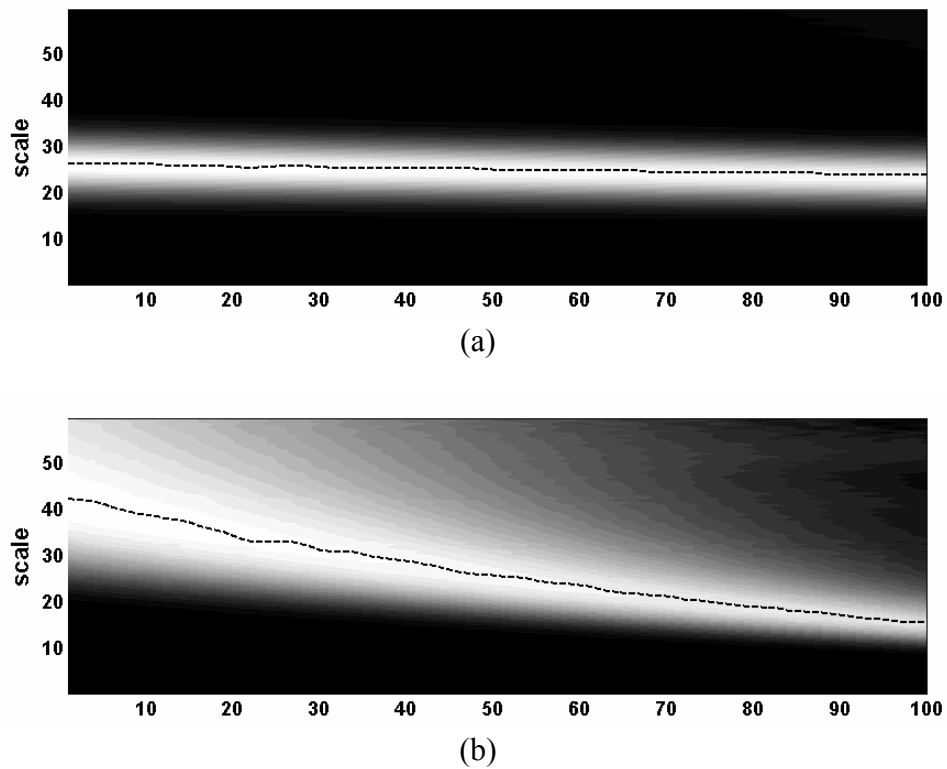
Figure 3.14 Scalograms of signals and their ridges with (a) $S = 0.001$; (b) $S = 0.010$ in the range from sampling point No. 301 to sampling point No. 400 ($\omega_0 = 2\pi$)
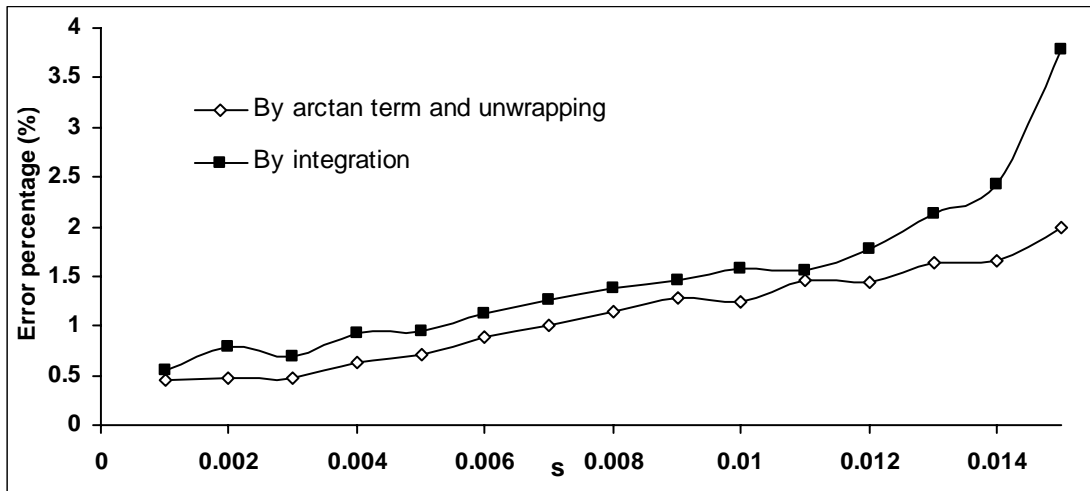
Figure 3.15 Percentage error with different values of S using two phase extraction methods ($\omega_0 = 2\pi$)
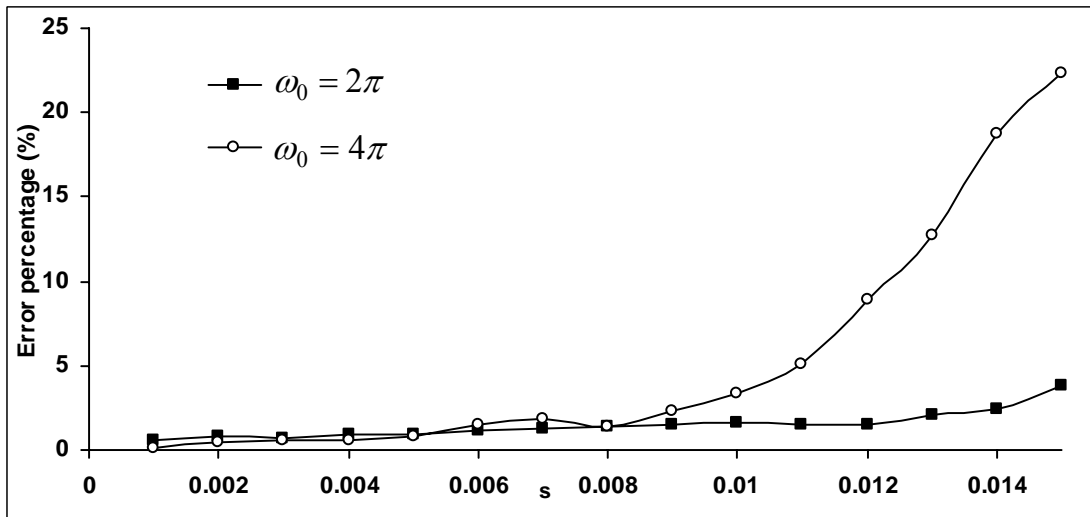
Figure 3.16 Percentage error with different mother frequencies ω_0 using integration method

In the above analysis, wavelet transform has been used to extract phase from simulated signals without noise. If a signal is contaminated with noise, its wavelet transform (modulus and phase) will also be contaminated. The signal-to-noise ratio (SNR) however will be the largest near the ridge, because most of the energy of the signal is concentrated near the ridge (unless the noise is also of narrow-band and with frequencies near that of the signal). Hence using the transform to estimate the

instantaneous frequency is better than using the signal directly like phase scanning method.

3.1.5 Other problems in wavelet phase extraction

1. Border effects

As shown in Eq. (3.2), wavelet transform is a process of calculating the correlation coefficient between a wavelet function and the signal. Obviously this process will generate large errors at the beginning and end of the signal. This is known as the border effect of the wavelet transform. Figure 3.17 shows a scalogram of the simulated signal with a frequency of $2\pi/25$ as shown in Fig. 3.8(a). Large errors are observed at the beginning and end of the signal.
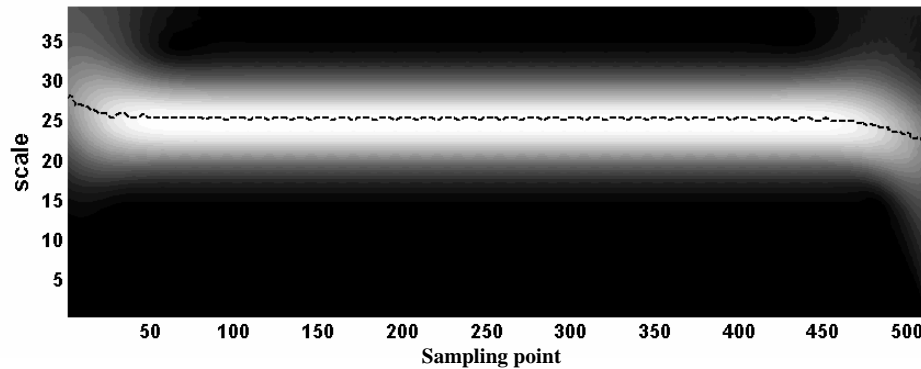
Figure 3.17 Scalogram of a wavelet transform on the signal shown in Fig. 3.8(a)

The easiest way to remove the border effect is to truncate the result of wavelet transform and discard the results near the left- and right-hand edges of the signal. This will result in a loss of information. A more proper method is to first extend the signal without changing the properties at the edges, process the wavelet transform and then truncate the results accordingly. There are several techniques to extend the signal. Symmetrical or zero padding extension techniques are commonly used. However, in

this study, a linear predictive extrapolation method introduced by Press et al. (1992) is used. According to their algorithm, the phase and frequency of the signal are maintained after the extension. The wavelet transforms and scalograms shown above are applied on the extended data, and the results are truncated appropriately.

2. Ridge extraction algorithm

The most straightforward method for determining the ridge of the CWT (hence the instantaneous frequency) of a signal from its modulus is to determine, for each time b, the scale a for which the modulus of the transform is maximum. The drawback of this method is that it would take a lot of time to explore the whole frequency domain. Furthermore, this method would be vulnerable to noise, which occurs frequently in speckle interferometry. However, it is easy to incorporate a priori information on the ridge as a constraint, for example, the ridge is smooth. So the value of a_{rb} at a certain instant can be predicted using the value of neighboring points. In this study, the value $a_{rb}(i)$ on a point i is predicted as $a_{predict}(i) = 2a_{rb}(i-1) - a_{rb}(i-2)$, and the modulus in the range of $a_{predict}(i) \pm 5$ is calculated to determine the maximum value. This algorithm also assumes that the change of scale a between two adjacent sampling points is not dramatic.

3. Phase ambiguity

Similar to temporal Fourier transform, the wavelet transform is unable to determine the sign of a phase. It is also not possible to analyze a part of the object that is not moving. Adding a temporal carrier to the image acquisition process would overcome the problem. However, temporal wavelet transform is also limited by the Nyquist

sampling theorem. Analyzing signals with a frequency higher than half of the acquisition rate is impossible. The selected temporal carrier frequency should be high enough so that the phase change of each point on the object is in one direction. However, it cannot be too high due to the limitation of Nyquist sampling theorem mentioned above. Sometimes a compromise is not easily reached if the capturing rate of the camera is not high enough.

3.2 Phase scanning method

Phase scanning method is a simple phase extraction algorithm which calculates the phase directly from a signal. As mentioned before, if the signal is contaminated seriously with noise, this method is weak in eliminating errors. Generally, this method is not suitable to process speckle patterns of ESPI or DSSI. It is more suitable for processing fringe patterns obtained from fringe projection or shadow moiré in which the SNR is much higher. Furthermore, it is also more suitable for measurement on vibrating objects. In this study, phase scanning is used to measure instantaneous shape and displacement of a low frequency vibrating object using fringe projection and shadow moiré.

As mentioned at the beginning of this chapter, in dynamic measurement, the intensity variation of each pixel can be expressed by Eq. (3.1) regardless of the method applied. The phase scanning method is based on two assumptions: (1) $I_0(x, y; t)$ and $I_M(x, y; t)$ are both slowly-varying functions, and can be regarded as constants within one period of intensity change; (2) phase change $\varphi(x, y; t)$ is more than 2π. With these assumptions, the detectable maximum and minimum intensities

within one period of intensity change at a certain point $P\ (x,y)$ on a test surface can be written as

$$I_{\max}(x,y) = I_0(x,y) + I_M(x,y) \qquad\qquad (3.18)$$

$$I_{\min}(x,y) = I_0(x,y) - I_M(x,y) \qquad\qquad (3.19)$$

Subsequently, Eq. (3.1) is rewritten as

$$I(x,y;t) = \frac{1}{2}\left[I_{\max}(x,y) + I_{\min}(x,y)\right] + \frac{1}{2}\left[I_{\max}(x,y) - I_{\min}(x,y)\right]\cos\phi(x,y;t) \qquad (3.20)$$

where $\phi(x,y;t) = \varphi_0(x,y) + \varphi(x,y;t)$. Hence the phase value can be expressed as

$$\phi(x,y;t) = \arccos\left[\frac{2I(x,y;t) - I_{\max}(x,y) - I_{\min}(x,y)}{I_{\max}(x,y) - I_{\min}(x,y)}\right] \qquad (3.21)$$

As the first phase term in Eq.(3.1) is constant on the time-axis, the relative phase variation due to vibration or deformation at point P can be obtained as

$$\varphi(x,y;\varDelta t) = \phi(x,y;t_2) - \phi(x,y;t_1) \qquad\qquad (3.22)$$

At a certain time T, the instantaneous phase map, which represents the contour of a specimen can be expressed as

$$\phi(x,y;T) = \varphi_0(x,y) + \varphi(x,y;T) \qquad\qquad (3.23)$$

where $\varphi(x,y;T)$ denotes the phase which is related to the vibration amplitude or deformation at instant T. Both phase values $\varphi(x,y;\varDelta t)$ and $\phi(x,y;T)$ are wrapped

phase, as $\phi(x, y; t)$ given by Eq. (3.21) is between 0 to π. These values have to be converted from $[0, \pi)$ to $[0, 2\pi)$ for unwrapping. Table 3.1 shows the details of the conversion. The phase values after conversion are determined by two factors, namely direction of vibration or deformation and the slope of intensity $\dfrac{\partial I}{\partial t}$ along the time axis. Unwrapping the phase values $\varphi(x, y; \Delta t)$ given by Eq.(3.22) along the time-axis is a one dimensional problem; retrieving the continuous phase values from $\phi(x, y; T)$ in Eq.(3.23) is a two-dimensional unwrapping problem and numerous unwrapping algorithms are applicable.

Table 3.1 Conversion of phase values from $[0, \pi)$ to $[0, 2\pi)$

Phase value between $[0, \pi)$	Direction of vibration or deformation	Slope of intensity along Time Axis $\dfrac{\partial I}{\partial t}$	Phase value between $[0, 2\pi)$ after conversion
ϕ	Outward	≥ 0	$2\pi - \phi$
		< 0	ϕ
	Inward	≥ 0	ϕ
		< 0	$2\pi - \phi$

Another problem involved in the measurement of a vibrating object is to identify the extreme positions of vibration. Theoretically, it is impossible to identify them from a one-dimensional signal on a pixel. However, in most of the low frequency vibration applications, all points on an object have the same direction of movement. They reach an extreme position at the same instant. In this case, these instants are readily identified since the first derivative of intensity ($\dfrac{\partial I}{\partial t}$) of most pixels changes sign (either from negative to positive or vice versa). Figure 3.18 shows an example of the phase scanning method in extracting temporal phase from the gray value intensity of a pixel. Figure 3.18(a) is the intensity variation of that pixel. Four

extreme positions of vibration [as indicated in Fig. 3.18(a)] are identified in ninety

sampling points. The wrapped phase values are shown in Fig. 3.18(b). After

unwrapping along the time-axis, the continuous phase profile, as shown in Fig.

3.18(c), can be obtained.
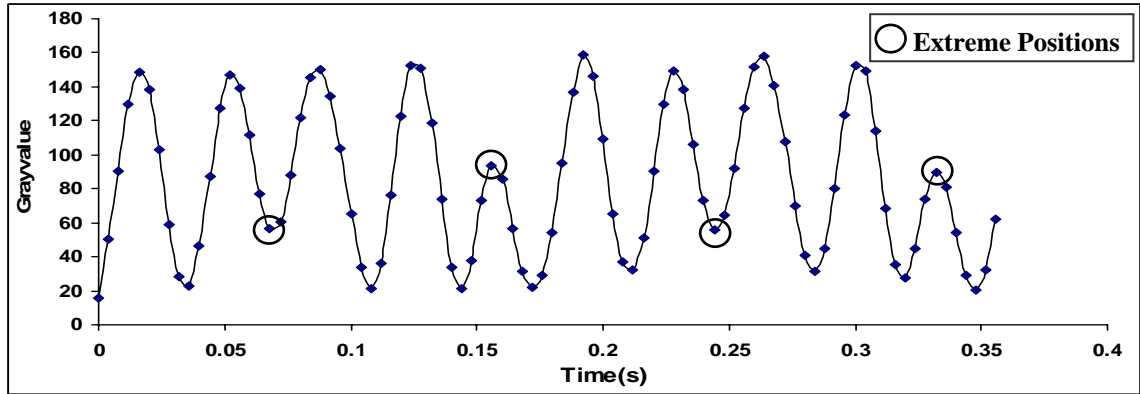
(a)
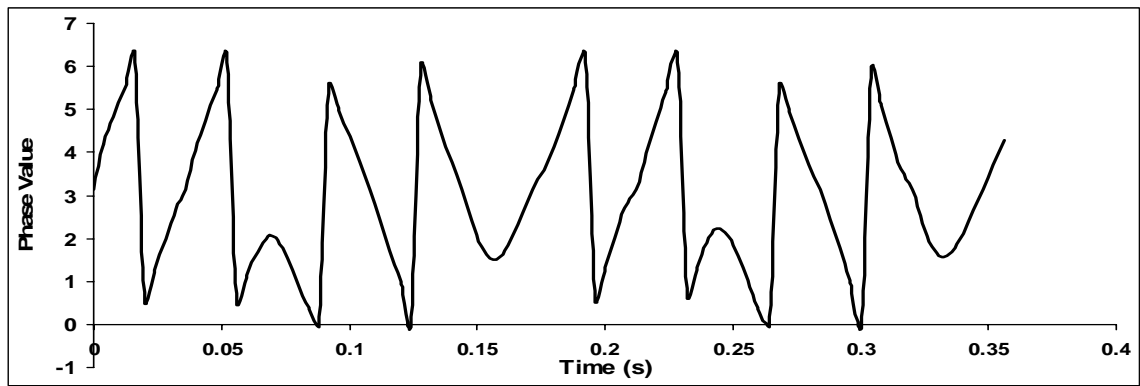
(b)
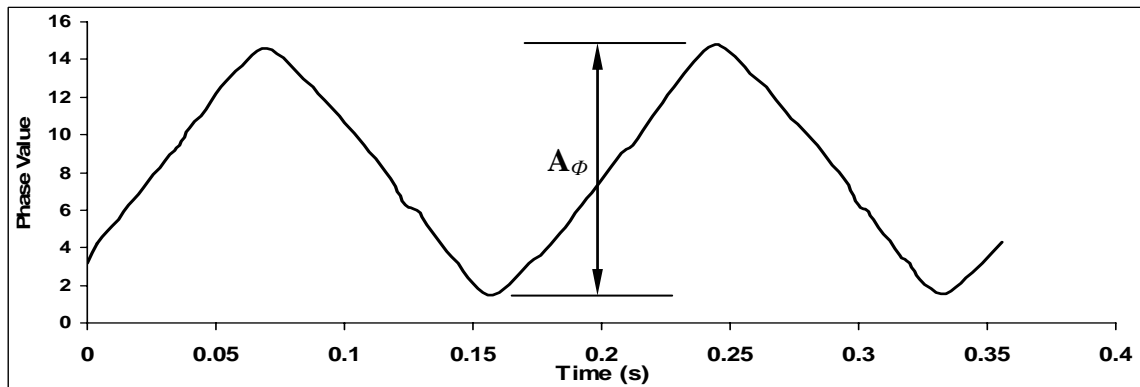
(c)

Figure 3.18 (a) Intensity variation of a pixel; (b) wrapped phase values; (c) continuous
phase profile after unwrapping

From Fig. 3.18, it can be observed that the phase change A_Φ representing the amplitude of vibration is around 13 (rad). 22 sampling points are found within the phase change of A_Φ. Theoretically, this signal can be separated into 5 sections in which the phase change is in one direction, and temporal Fourier transform and temporal wavelet transform can also be applied on these sections. Obviously these two methods are not suitable for such short signals due to the border effect mentioned above. Although the signal can be extended to avoid the errors at the border, this will increase the processing time drastically as the extended signal may be several times larger than the original signal.

Another problem that should be emphasized in the measurement of vibrating objects is the method to identify the extreme positions of the vibration. These positions are identified according to the behavior of the pixels in the images. It is impossible to identify them from a one-dimensional signal on an individual pixel. If the points on the object have different directions of movement and reach extreme positions at different instants, it would be impossible to process the signal as mentioned above. In this case, the temporal carrier technique is the only solution to the problem.

CHAPTER FOUR

DEVELOPMENT OF EXPERIMENTATION

To demonstrate the application of temporal phase analysis method mentioned in the previous chapter, four optical techniques with different measurement sensitivities are chosen. They are electronic speckle pattern interferometry (ESPI), shadow moiré, fringe projection technique and shearography. In the first section of this chapter, some equipment used in dynamic measurement are introduced. In the subsequent sections, experimental techniques used in these methods are described in detail.

4.1 Equipments used for dynamic measurement

4.1.1 High speed camera

The recording rate of a normal CCD camera is about 30 frames per second (fps). However, even in low frequency vibration measurement, this is not sufficient for minimum requirement of phase measurement ------ Nyquist sampling rate. A high-speed camera is thus indispensable. In this investigation, a high-speed camera, Kodak Motion Carder Analyzer, Monochrome Model SR-Ultra is used (shown in Fig. 4.1). It is a compact monochrome high-speed motion analyzing system designed for high-speed applications. It includes a full range of standard features, and optional accessories to record, view, measure and store the information required for high-speed manufacturing.

Figure 4.1 Kodak Motion Corder Analyzer, Monochrome Model SR-Ultra

The sensor of the high-speed camera is a CCD with a pixel size of 7.4 μm ×
7.4 μm, and an array of 658 pixels × 496 pixels. It has recording rates ranging from 30,
to 10,000 fps. The size of an output image varies with the recording rate. At a
recording rate of 250 fps, it has 512 pixels × 480 pixels, and 546 images can be
recorded within a 2.2 second period. At the highest recording rate of 10,000 fps, the
image size is reduced to 128 pixels × 34 pixels and 30,832 images can be recorded
within 3.0 seconds. The camera has a standard 8-bit monochrome BMP or TIFF
output with 256 gray levels. It is also compatible with all C-mount camera lenses.

4.1.2 Telecentric gauging lens

Temporal phase analysis technique traces the intensity of a pixel on a series of images.
Hence, it is necessary that a particular pixel on the series of images represents the
same point on an object. Generally, the method is only suitable for analyzing out-of-
plane displacement or very small in-plane displacement. However, when out-of-plane
displacement is measured using shadow moiré or fringe projection technique, the
displacement is already in the range of at least several millimeters. In-plane shifting of

the object on the images can be eliminated by capturing the object at right angles. However, when a conventional camera is used, the magnification varies with the working distance. To avoid error due to variation of magnification, a telecentric gauging lens is used. The magnification of a telecentric lens, unlike conventional lenses, is independent of working distance. It remains constant regardless of the distance of the camera from an object. This reduces magnification errors and greatly extends the gauging depth of field. Figure 4.2 illustrates the difference between a telecentric and a conventional lens. With this special lens, the location of a non-stationary object remains the same within an image and only the fringe pattern in an image is shifted periodically. The model of telecentric lens used in this investigation is a Melles Groit 59LGH416 lens.

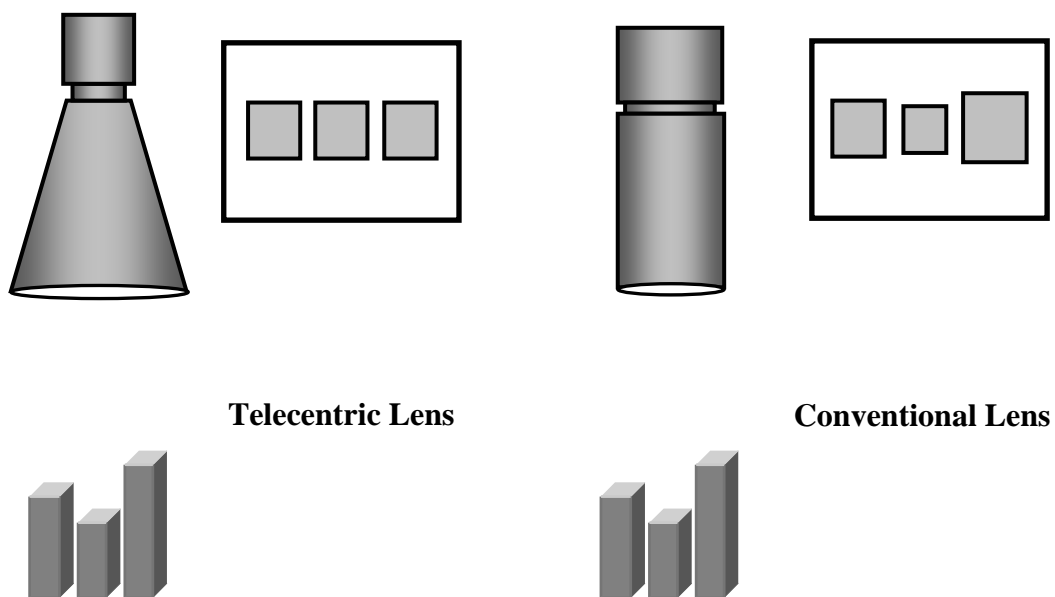**Telecentric Lens**   **Conventional Lens**

Figure 4.2 Difference between telecentric gauging and conventional lens imaging

4.1.3 PZT translation stage

A piezoelectric translation stage with a computer control system is one of the key equipment to ensure precise dynamic measurement in ESPI. It is mainly used for: (1)

generating a temporal carrier by shifting a reference object at constant speed; (2) prescribing a linear or nonlinear displacement. The translation stage used is a Piezosystem Jena, PX 300 CAP PZT stage. It can generate a maximum horizontal displacement of 300 μm. It contains a closed loop capacitive control system with a position accuracy of 0.05% at a full motion of 300 μm. It has a resolution of 1 nm and works well for high-precise positioning. It has a maximum load of 10N.
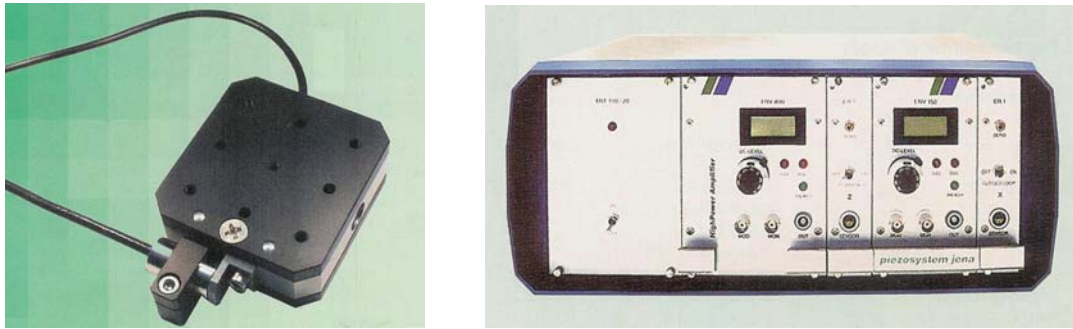
Figure 4.3 PZT translation stage (Piezosystem Jena, PX 300 CAP) and its controller

4.2 Experimental setup

In this section, the experimental setups are described in detail according to the different optical techniques: fringe projection, shadow moiré, ESPI and digital shearography. In these techniques, the basic setups are similar. However, the test samples and loading methods are varied.

4.2.1 Fringe projection

The fringe projection experiment is employed to study a vibrating object by phase scanning. The experimental setup is shown in Fig. 4.4. A coin of 21 mm diameter and having a diffused surface is subjected to vibration at different amplitudes with a vibrator. The frequency of vibration is controlled by a function generator and a

vertical sinusoidal fringe pattern is projected onto the object at the same time by a programmable LCD projector. The fringe patterns are captured at right angles by a Kodak high-speed CCD camera with telecentric gauging lens.
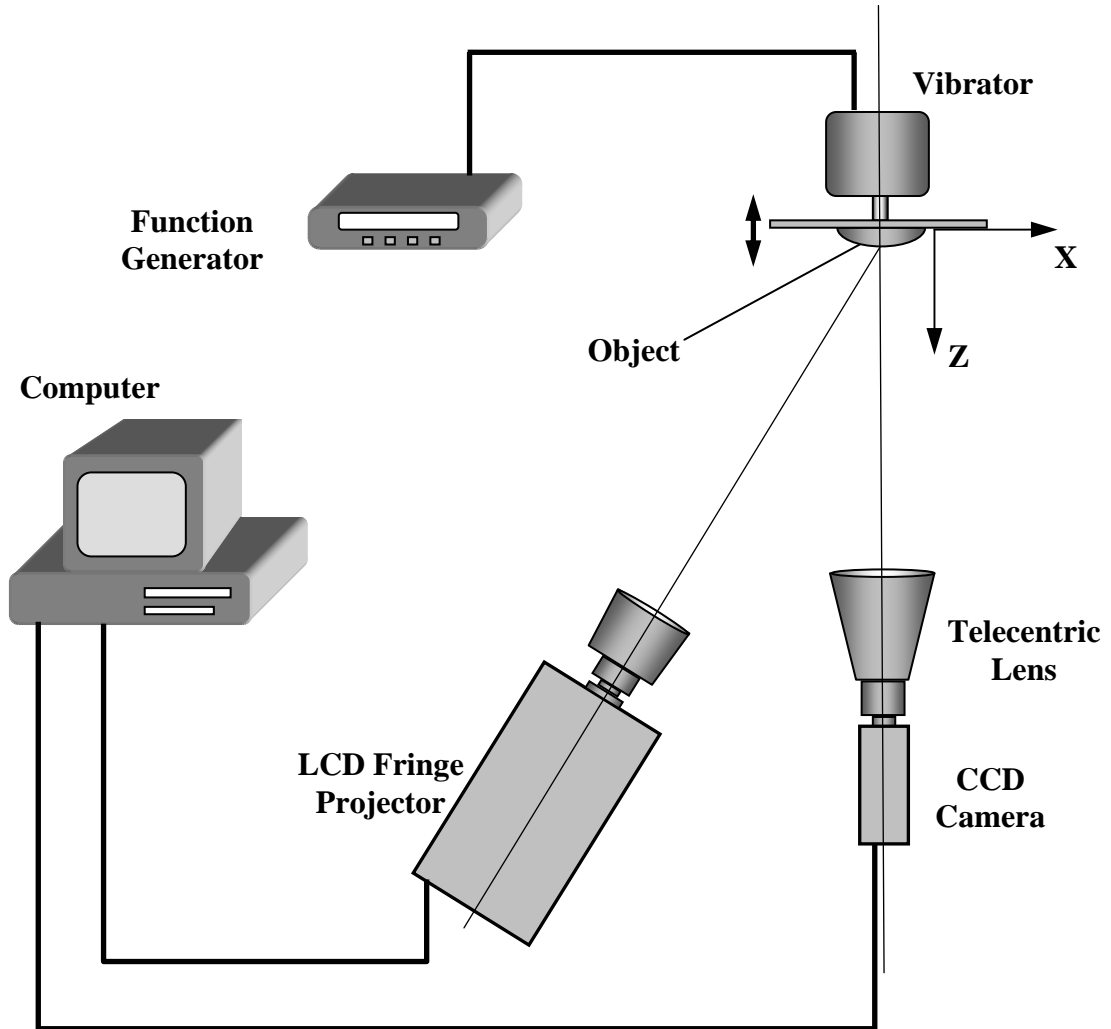
Figure 4.4 Experimental setup of fringe projection method for phase scanning

The pitch of the fringe pattern and angle of projection are selected according to the amplitude of vibration such that the phase variation in one cycle of vibration is more than 2π. Coefficient k_F in Eq. (2.1) is calibrated by shifting an object through a known distance in the z-axis and the corresponding phase difference on the object is determined by conventional 4-step phase shifting method.

4.2.2 Shadow moiré

Shadow moiré method is also employed in this investigation to illustrate the algorithms for temporal phase analysis. Figure 4.5 shows the experimental setup for measurement on a continuously-deforming or vibrating object. A vertical sinusoidal grating with a certain frequency is positioned close to an object with diffused surface. The pitch of the grating is selected according to the displacement or contour of the object to be measured. A coarse grating will reduce the sensitivity; however, the fringes will produce good contrast. Due to diffraction, the grating frequency used in shadow moiré technique should be less than 6 lines/mm. A 150W DC white-light source with an optical fiber illuminates a test object at a certain angle. The moiré fringe patterns are captured at right angles by a high-speed CCD camera with a telecentric gauging lens. As the imaging area is smaller than the telecentric lens, each point on the object would be imaged at right angles. In this case, the camera and the light source do not have to be placed at the same distance from the object as required in Fig. 2.3. This will reduce errors caused by mis-alignment.

To determine whether the fringes represent a convex or concave surface, carrier fringes are introduced by a rotating grating inclined at a small angle in x-z plane. This changes the relative distance between the grating and the object, but will not introduce any error in contouring. However, due to diffraction effect, the fringe contrast would reduce with an increase in distance. As the angle of rotation is small, it will not significantly affect the results. The variation of the grating pitch due to the rotation is also not considered for the same reason.

Different test samples and loading methods are used in this study. Figure 4.5 shows a simply-supported Perspex beam (8 mm in width and 60 mm in length) which is subjected to a continuous deformation in the z-direction. A test coin subjected to a

rigid body motion in the z-direction is also used.   These experiments employ the

temporal phase analysis algorithm for continuous deformation. For measurements on

a vibrating object, the specimen (within dotted circle) in Fig. 4.5 is replaced by an

object subjected to low frequency vibration using a shaker (as shown in Fig. 4.6). The

frequency of vibration is controlled by a function generator. Two vibrating specimens

are tested, a spherical cap and a coin.

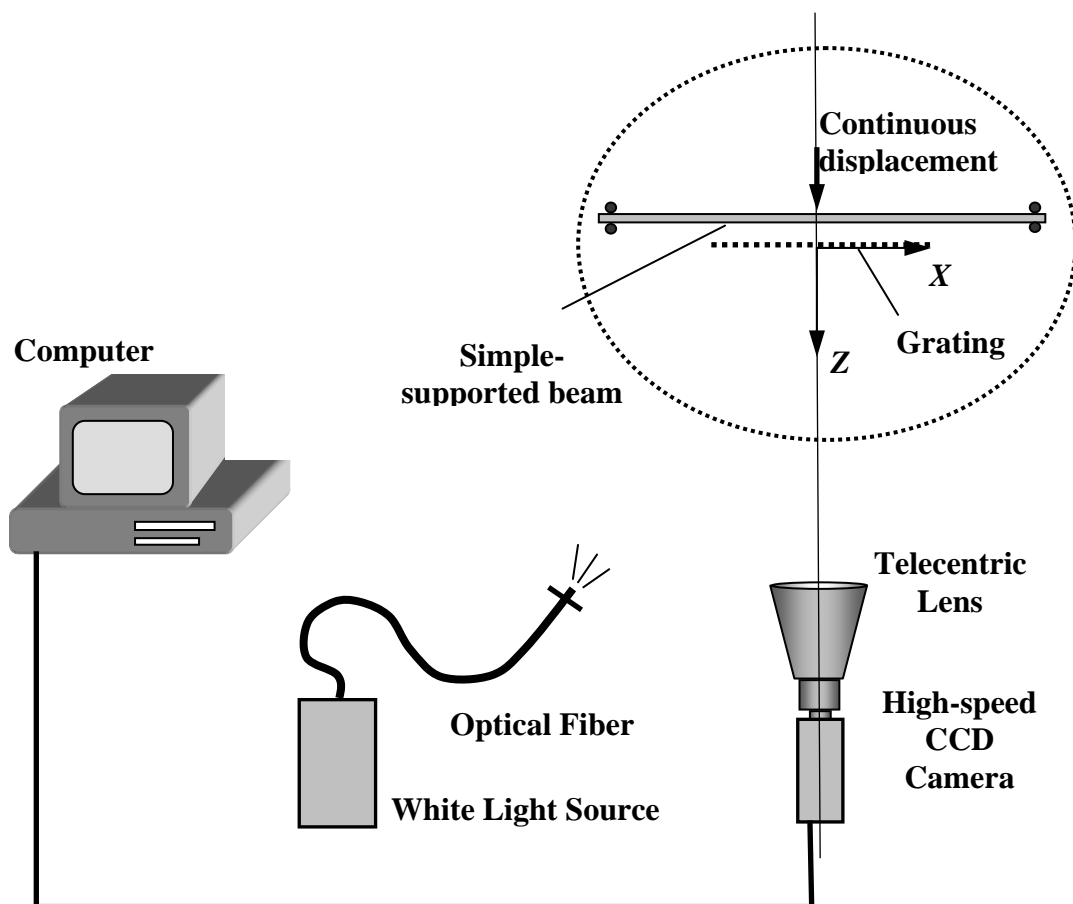Figure 4.5 Typical shadow moiré setup for continuous deformation measurement

Shadow moiré technique is also applied on profile measurement of an object

with step change. In this application, the specimen tested is stationary, however the

frequency of a grating is varied by rotating the grating, and a series of fringe patterns

is captured during the rotation. Figure 4.7 shows the experimental setup. A linear

sinusoidal grating, placed close to the specimen, is mounted on a rotary indexing stage that has an accuracy of 0.0167^{0}. A 150W DC white-light source with an optical fiber illuminates the object at a certain angle. Moiré fringe patterns are recorded using a CCD camera whose optical axis is normal to the plane of the grating. The grating is rotated from $\alpha = 0°$ to $\alpha = 90°$ at increments of $\Delta\alpha = 0.5°$ which is achieved with a computer-controlled motorized rotating stage. A total of 181 images are recorded for processing. Two specimens are measured in this study, an object with a stepped profile and a coin with small variation in surface profile.
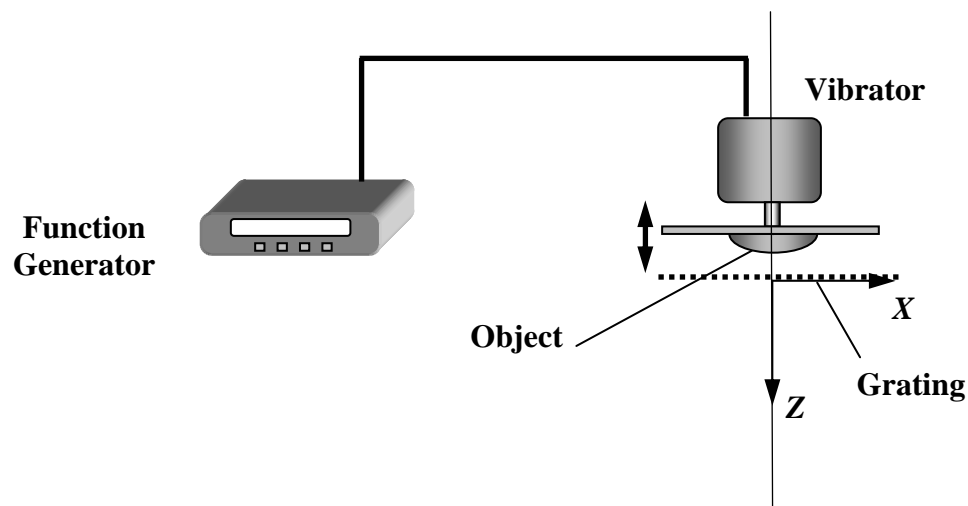
Figure 4.6 The vibrating object and loading device

4.2.3 ESPI

Figure 4.8 shows a typical setup of ESPI. A beam of He-Ne laser (30 mW, λ = 632.8 nm) illuminates a specimen with diffuse surface and a reference plate at right angles through a beam splitter. The object and reference beams are recorded on a CCD sensor. During deformation of the object, a series of speckle patterns is captured by a high speed CCD camera with a telecentric gauging lens. For continuous deformation measurement, several specimens are used. The first specimen is a fully-clamped

square plate with several artificial defects (circular blind holes with different depths).

The width and thickness of the plate are 80 mm and 5 mm, respectively. The plate is

loaded by a uniformly-distributed pressure applied with compressed air, and

continuously deformed by increments of pressure in the chamber (shown in Fig. 4.8).
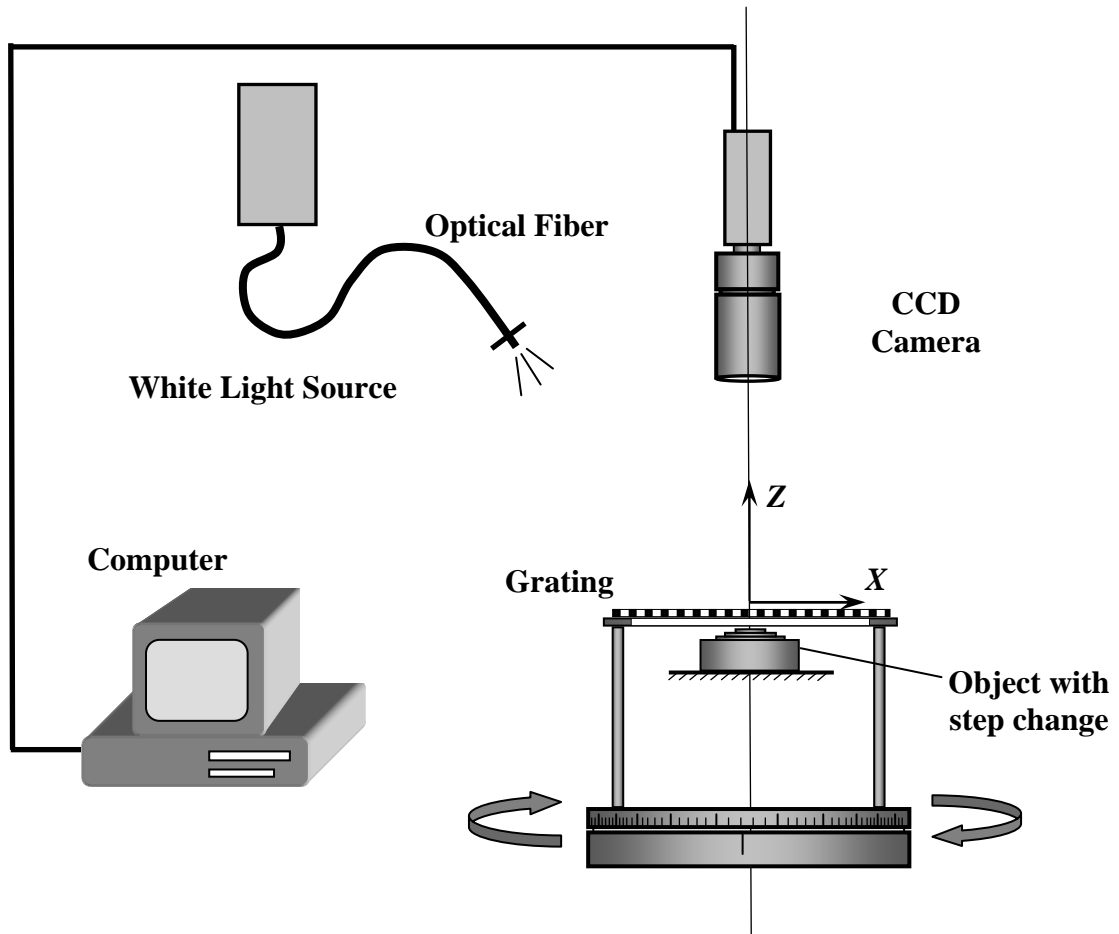
Figure 4.7 Shadow moiré setup for profile measurement on objects with step change

The second specimen is a cantilever beam which is loaded with a non-linear

motion at the free end using a computer-controlled piezoelectric translation stage

(shown in Fig. 4.3). The setup is similar to that shown in Fig. 4.8. Only a portion of

the beam is inspected. Figure 4.9 shows the cantilever beam with the loading device

and the area of interest. This experiment is to study the effect of varying frequency on

phase evaluation. Figure 4.10 shows another specimen which is a micro-beam tested by ESPI. The length, width and thickness of the beam are 2.5 mm, 0.25 mm and 0.25 mm, respectively. The setup is similar to that shown in Fig. 4.8, however the telecentric lens is replaced by a long working distance microscopic lens (OPTEM Zoom 100). The beam is subjected a prescribed displacement by a PZT translation stage at the free end.

Figure 4.8 Typical ESPI setup for continuous deformation measurement.
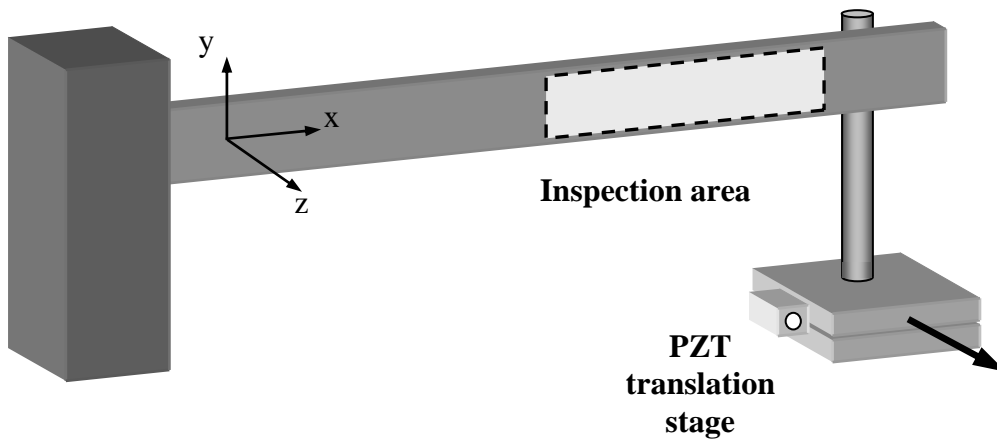
Figure 4.9 A cantilever beam with non-linear motion
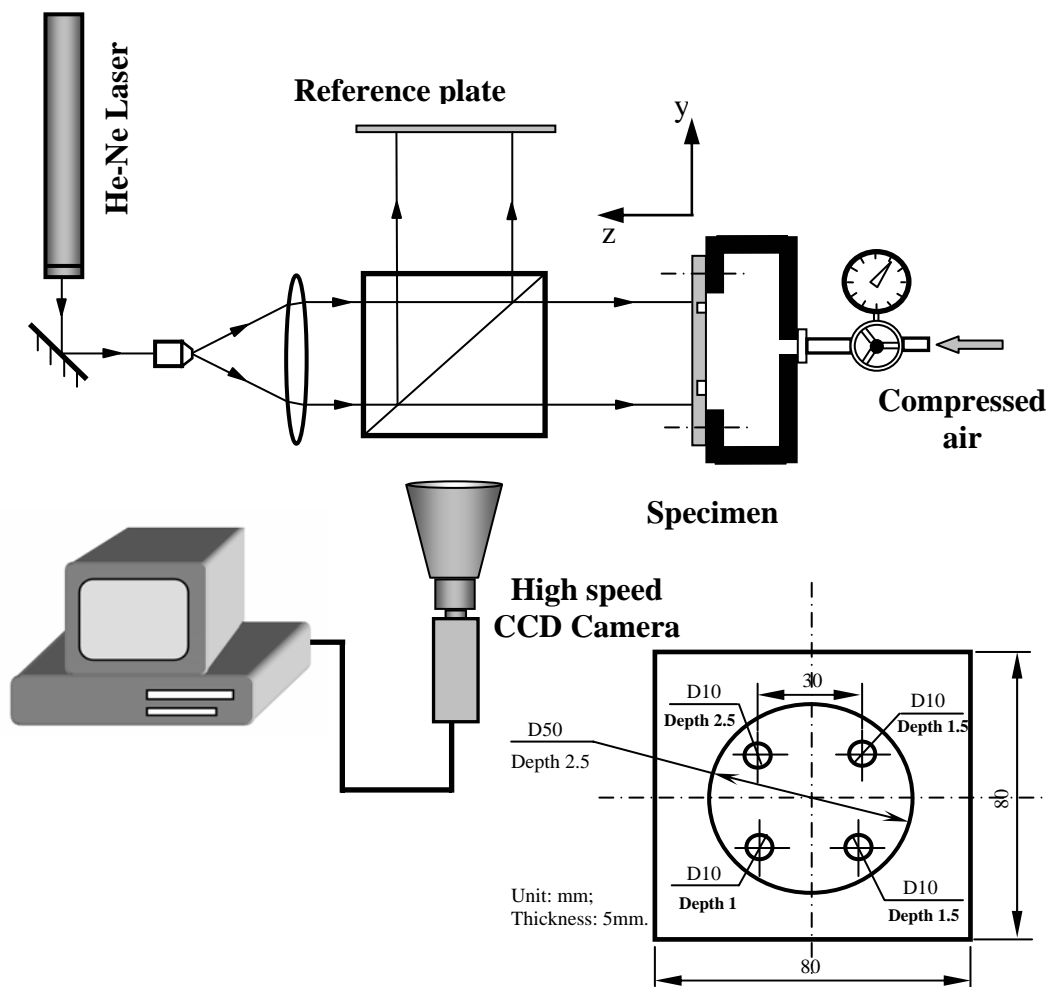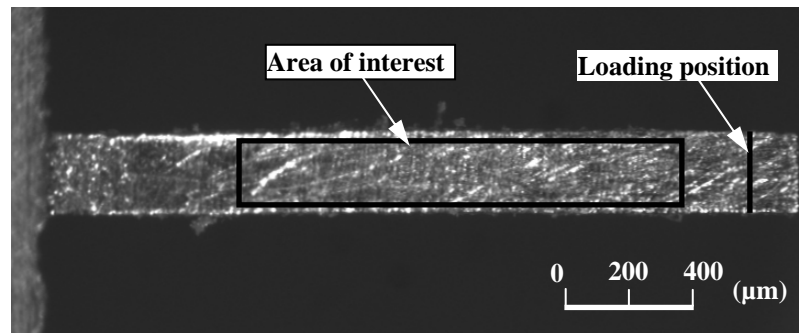

Figure 4.10 A micro-beam tested by ESPI

Figure 4.11 shows another ESPI setup for measurement of a vibrating object with a temporal carrier. The test specimen (shown in Fig. 4.12) is a Perspex cantilever beam with a diffuse surface. The length, width and thickness of the beam is 400 mm, 20 mm and 4 mm, respectively. It is subjected to a sinusoidal vibration at the free end using a vibrator. The frequency of vibration is controlled by a function generator and the area near the clamped end is measured. To generate a temporal carrier, the reference plate is mounted on a computer-controlled piezoelectrical transducer. During vibration, the reference plate is given a linear rigid body motion with a certain velocity. In order to retrieve the phase change of temporal carrier, a stationary reference block with a diffuse surface is mounted above the vibrating beam and it is captured together with the beam.
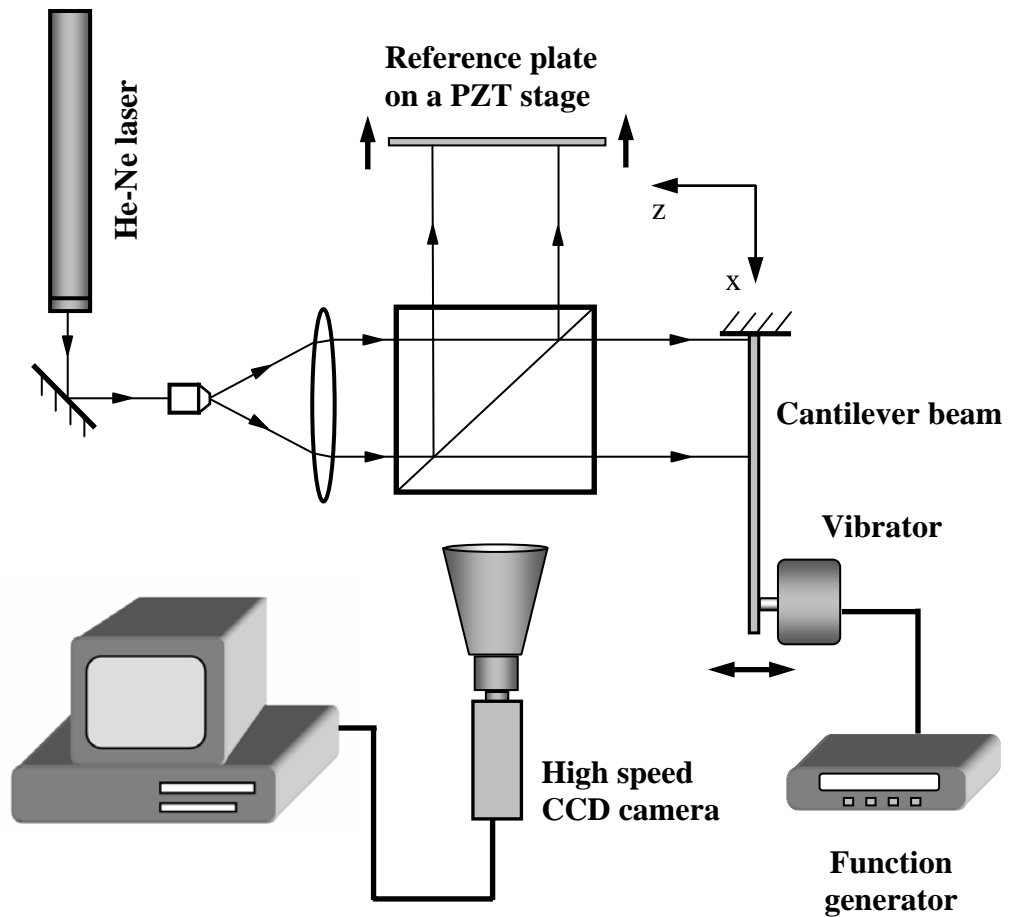
Figure 4.11 ESPI setup with temporal carrier
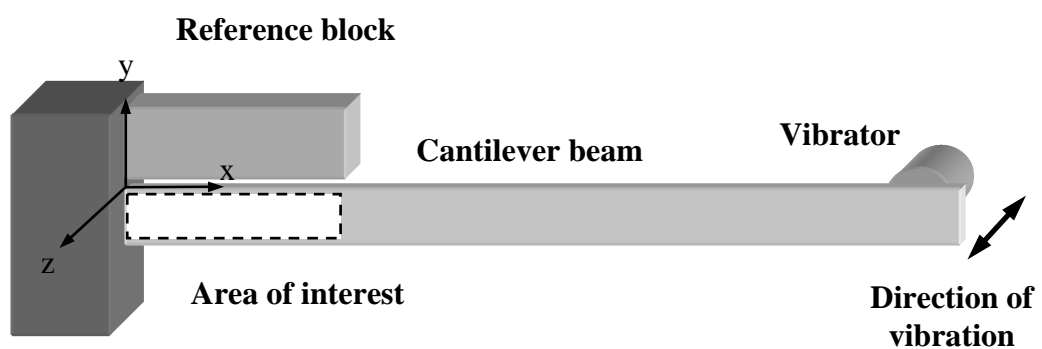
Figure 4.12 Reference block, cantilever beam and loading device for experimental
setup shown in Fig. 4.11
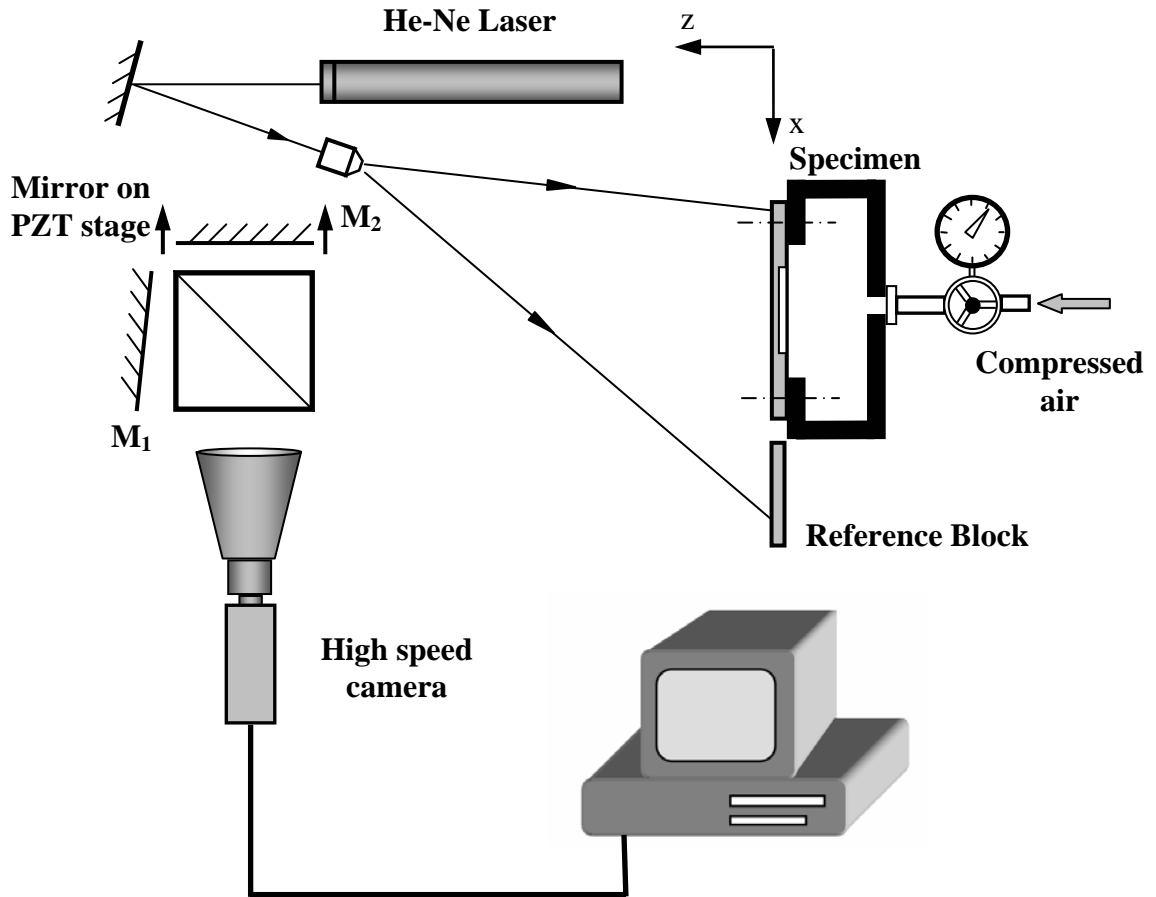
Figure 4.13 Digital shearography setup with temporal carrier

4.2.4 Digital Shearography

Figure 4.13 shows a typical setup of digital shearography. The test specimen in this study is a square plate with a circular blind hole (50 mm in diameter), clamped at the edges by rows of screws. The width and thickness of the plate are 80 mm and 5 mm, respectively. The plate is loaded by a uniformly distributed pressure applied with compressed air, and continuously deformed by increments of pressure in the chamber. The plate is with near normal illumination using a He-Ne laser (30 mW, λ = 632.8 nm). A modified Michelson shearing interferometer is adopted as the shearing device. The image shearing $\delta x = 3mm$ is generated by rotating mirror M1 with a small angle.

To generate a temporal carrier, mirror M2 is mounted on a computer-controlled PZT stage. During the deformation of the plate, it is applied with a linear rigid body motion at certain velocity. To retrieve the phase change of the temporal carrier, a stationary reference block with a diffuse surface is mounted besides the object and its image is captured along with the plate. During deformation of the object, a series of speckle patterns is captured by a high speed CCD camera (KODAK Motion Corder Analyzer, SR-Ultra) with a recording rate of 60 frame/s (fps).

CHAPTER FIVE

RESULTS AND DISCUSSION

In this chapter, the results of temporal phase analysis are presented in detail according to different applications. They are profiling object surface with step change; instantaneous velocity, displacement and contour measurement on continuously deforming objects, displacement and contour measurement on vibrating objects and displacement derivatives measurement on continuously deforming objects. Each application may include more than one optical technique. The results from temporal wavelet analysis are described in detail, temporal Fourier analysis is normally used to generate the results for comparison. Phase scanning method is only used on vibrating objects. Temporal wavelet and Fourier analyses are executed on Matlab platform; and phase scanning is executed using Visual C++.

5.1 Surface profiling on an object with step change

As mentioned in Chapters 2 and 3, the intensity distribution captured by the CCD camera in Fig. 4.7 is governed by Eqs. (2.3) and (3.1). When the grating is rotated at an angle β (see Fig. 5.1), Eq. 2.3 can be rearranged as

$$I(x,y) = I_0(x,y) + I_M(x,y)\cos\left[\frac{2\pi\cos\beta}{p_0}\cdot H(x,y)\right] \tag{5.1}$$

where p_0 is the physical pitch of the grating, $H(x,y) = \dfrac{d_S \cdot h_S(x,y)}{l_S + h_S(x,y)}$ is a parameter related to the profile.
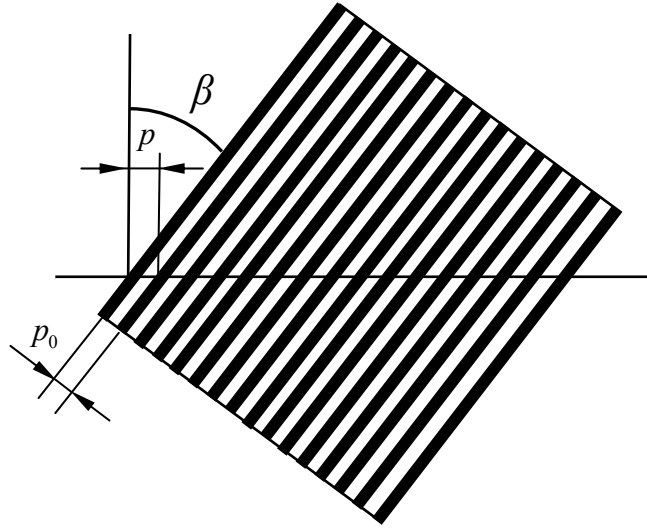
Figure 5.1 The rotation of a grating

The first specimen tested in this application is an object with a step-change profile. Figure 5.2(a) shows the dimensions of the object. The heights of the steps are respectively 1.62 ± 0.01 mm and 3.31 ± 0.01 mm when measured from the topmost surface using a dial gauge. Figure 5.2(b) shows the area of interest on a test object without the grating. The frequency of the grating used is 4 lines/mm. The distance d_S and l_S (shown in Fig. 2.3) are 175 mm and 355 mm respectively. The fringe patterns are captured at right angles by a CCD camera when the grating is rotated from $\beta = 0°$ at increments of $\Delta\beta = 0.5°$. One hundred and eighty one images are captured for processing. A 5×5 mean mask is applied to remove high-frequency grating lines on the images. At each pixel, 181 sampling points along the time axis are obtained. Figures 5.3(a) and 5.3(b) show respectively the gray value variation of points A_1 and B_1 [see Fig. 5.2(b)]. Lower frequency of gray value variation is observed at point A_1 than point B_1, which implies that $h_S(x, y)$ at point A_1 is smaller than that at point B_1. Due to diffraction effect, fringe contrast is low when the distance between the object and grating is large. Figure 5.3 shows that point A_1 has a much better contrast than

point B_1. However, different contrast at individual pixels will not affect the results of

pointwise phase extraction.
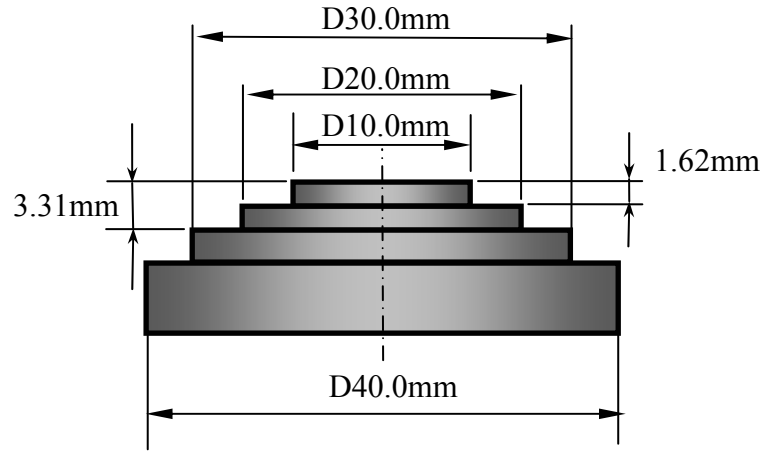
(a)
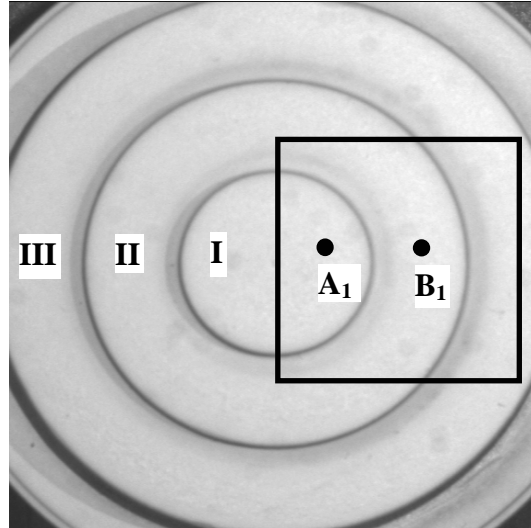
(b)

Figure 5.2 (a) Dimension of a step-change object; (b) area of interest on a specimen
with step-change.

Continuous wavelet transform is used to extract the phase from the intensity

variation of each pixel. At a point *P(x, y)*, the phase value $\varphi_{xy}(b)$ of wavelet

transform $W_{xy}(a,b)$ on the ridge is related to distance $h_S(x,y)$. Figure 5.4 shows a

scalogram of wavelet transform and the ridge at points A_1 and B_1. To determine the

phase variation $\Delta\varphi$ between two rotating angles β_1 and β_2, an integration on the instantaneous frequency $\varphi'_{xy}(b)$ is performed, and phase unwrapping procedure is avoided in both temporal and spatial domain. $H(x,y)$ in Eq. (5.1) can then be determined by

$$H(x,y) = \frac{\Delta\varphi \cdot p_0}{2\pi(\cos\beta_1 - \cos\beta_2)} \tag{5.2}$$
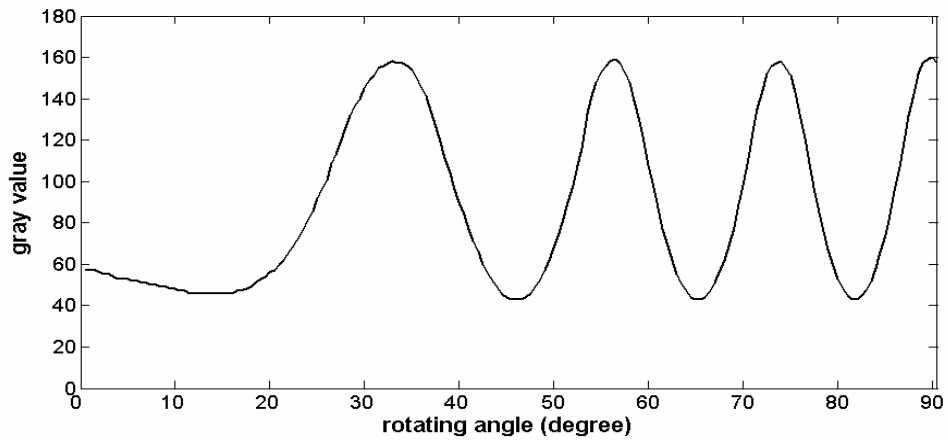
(a)
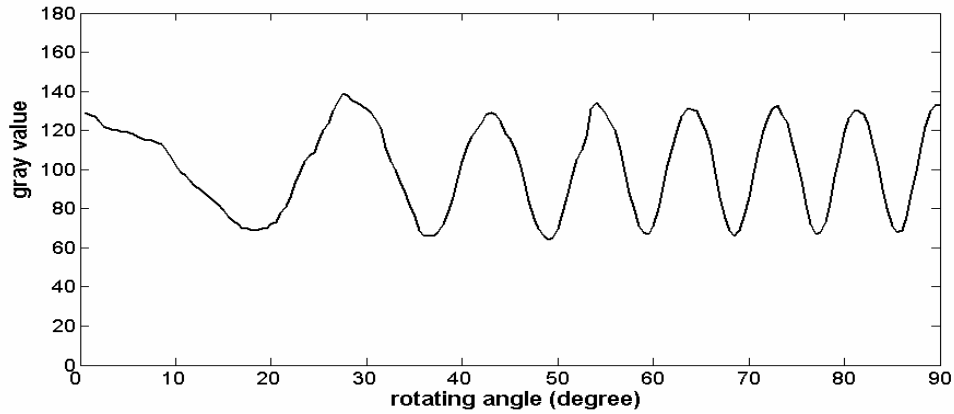
(b)

Figure 5.3 (a) Gray value variation of point A_1; (b) Gray value variation of point B_1.

Theoretically, a phase change $\Delta\varphi$ between two known rotating angles β_1 and β_2 is sufficient to obtain the value of $H(x,y)$. However, with a selected β_1 value, a

series of $\Delta\varphi$ can be obtained for different angles of β_2. Hence, it is more reasonable

to calculate $H(x,y)$ by a series of $\Delta\varphi$ instead of just one. In this study, $H(x,y)$ is

determined using least square fitting in Eq. (5.2); subsequently $h_S(x,y)$ is obtained

by

$$h_S(x,y) = \frac{H(x,y) \cdot l_S}{d_S - H(x,y)}$$

(5.3)
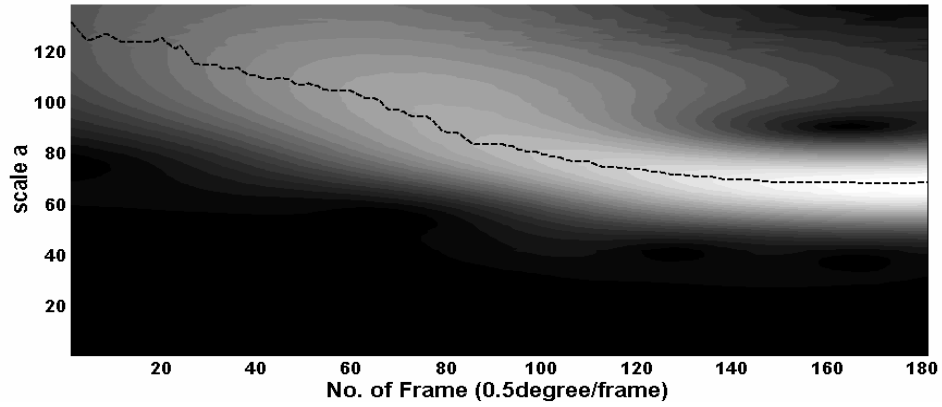
(a)
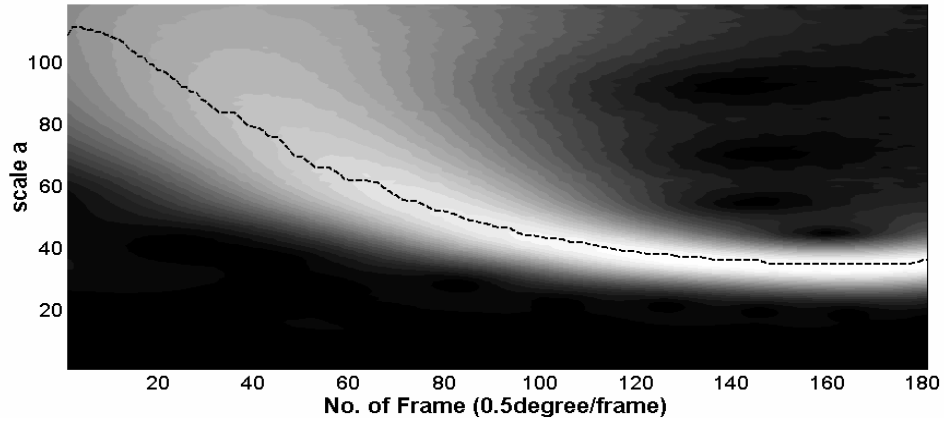
(b)

Figure 5.4 Scalograms of a wavelet transform on intensity variation and the ridges at (a) point A$_1$ and (b) point B$_1$.

In this study, β_1 is selected as 30° and β_2 varies from 30.5° to 70°. $H(x,y)$ on

each point is obtained by least-square fitting; subsequently, the heights $h_S(x,y)$ at

step I, II, and III (see Fig. 3b) are obtained as 1.97±0.01 mm, 3.59±0.02 mm and

5.27±0.03 mm respectively. Figure 5.5(a) shows a gray scale map of height difference.

The absolute height of each step measured from the top surface are 1.62±0.03 mm and

3.30±0.04 mm respectively. The average discrepancy, when compared with results

from dial gauge measurement, is 0.3%. Figure 5.5(b) shows a 3D reconstruction of

the area of interest on the object. A relatively high unevenness is observed at step III,

this is due to the lower contrast of the intensity variation and noise.
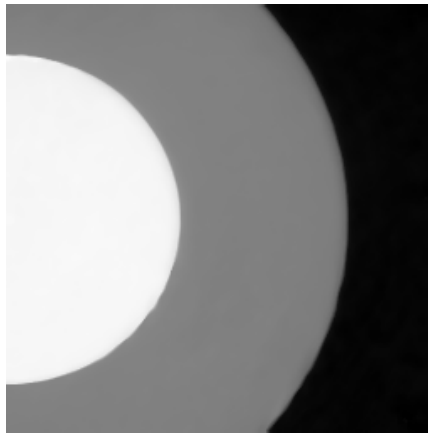
(a)
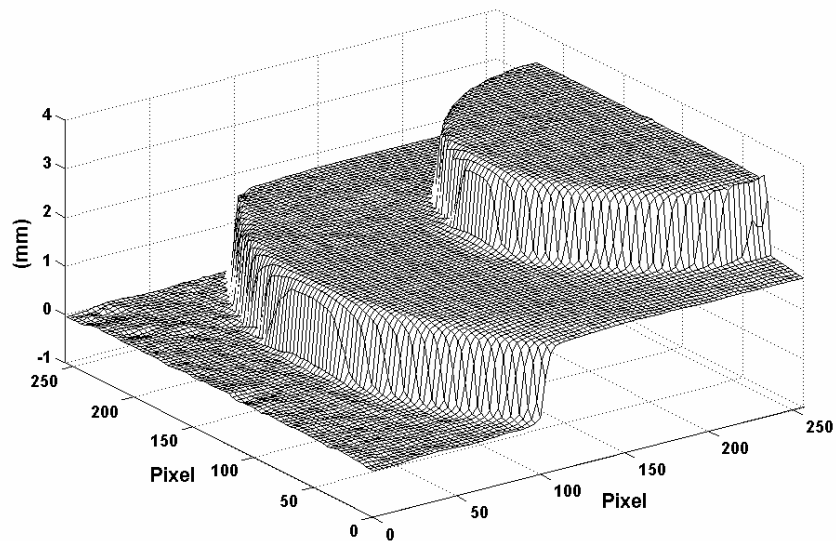
(b)

Figure 5.5 (a) gray scale map on area of interest; (b) 3D plot of area of interest

The temporal wavelet analysis is also applied on a coin of 24.5 mm diameter [shown in Fig. 5.6(a)]. A small area of interest containing 300×300 pixels [also indicated in Fig. 5.6(a)] is cropped. A grating with frequency of 6 lines/mm is selected. The distance d_S and l_S are respectively 310 mm and 160 mm. The fringe patterns are also captured at right angles by a CCD camera when the grating is rotated at increments of $\Delta\beta = 0.5°$. Similarly 181 images are captured for processing. A 3×3 mean mask is also applied to remove the high-frequency grating lines on each image. At each pixel, 181 sampling points along the time axis are obtained. The processes are similar with the object mentioned above. Figures 5.6(b) and 5.6(c) show typical moiré fringe patterns at $\beta = 30°$ and $\beta = 40°$. The gray scale map representing the contour of the coin is given in Fig. 5.7(a). Figure 5.7(b) shows a 3D plot of the area of interest. To verify the accuracy of the proposed method, a comparison with the mechanical stylus method is carried out. Figure 5.8 shows a comparison of the profile on cross section C_1-C_1 [see Fig. 5.6(a)]. The results compared well with the mechanical stylus method and the accuracy of proposed method is in the order of 10 μm. However, a slightly larger error is observed in the circled area. This is due to the presence of the shadow on that part of the object.

It is worth noting that only sampling points between 30º and 70º are used in the calculation as it is not necessary to capture fringe patterns from of 0º to 90º. As shown above, accurate results can be obtained by using signals between 30º and 70º and extending the signals using linear prediction algorithm as mentioned in Chapter 3. Comparing the results with that of Jin et al. (2001), temporal wavelet analysis gives much better results. Jin et al. show an uncertainty value of ±0.57 mm using temporal Fourier transform, this value is at least ten times that of temporal wavelet transform.

Furthermore, since the grating frequency variation is not linear during rotation, non-consistent angle steps were used in their application to obtain a single frequency of intensity variation. This increases the difficulty of automatic measurement as the grating rotating speed and the recording rate of a CCD camera are normally consistent. This shortcoming of the Fourier analysis can thus be overcome by the use of temporal wavelet analysis.

(a)

(b)   (c)
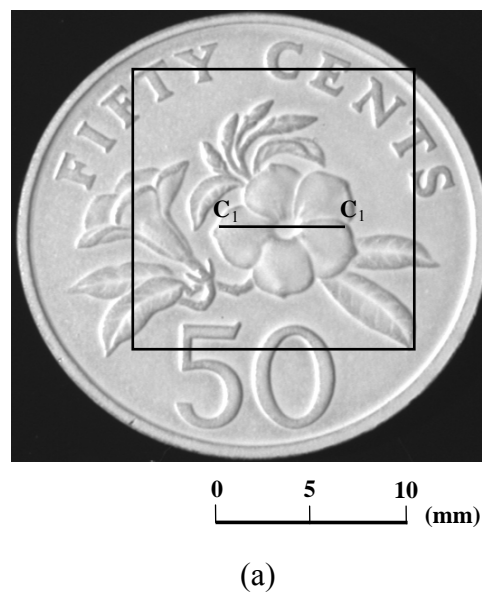
Figure 5.6 (a) Area of interest on a 50-cent coin and typical moiré fringe patterns at (b) $\beta = 30°$; (c) $\beta = 40°$.

(a)
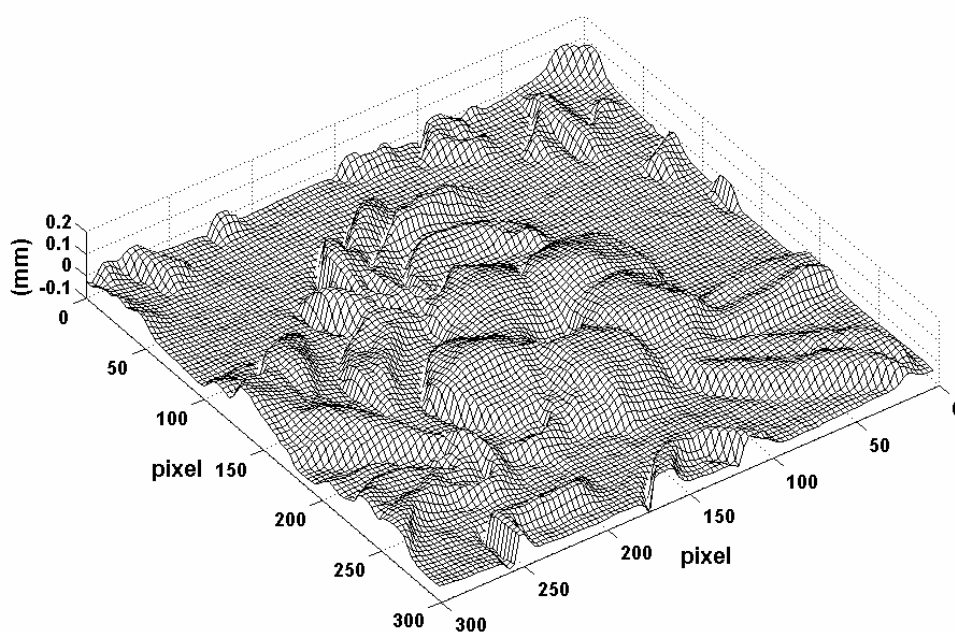
(b)

Figure 5.7 (a) gray scale map of area of interest of a 50-cent coin;
(b) 3D plot of area of interest.
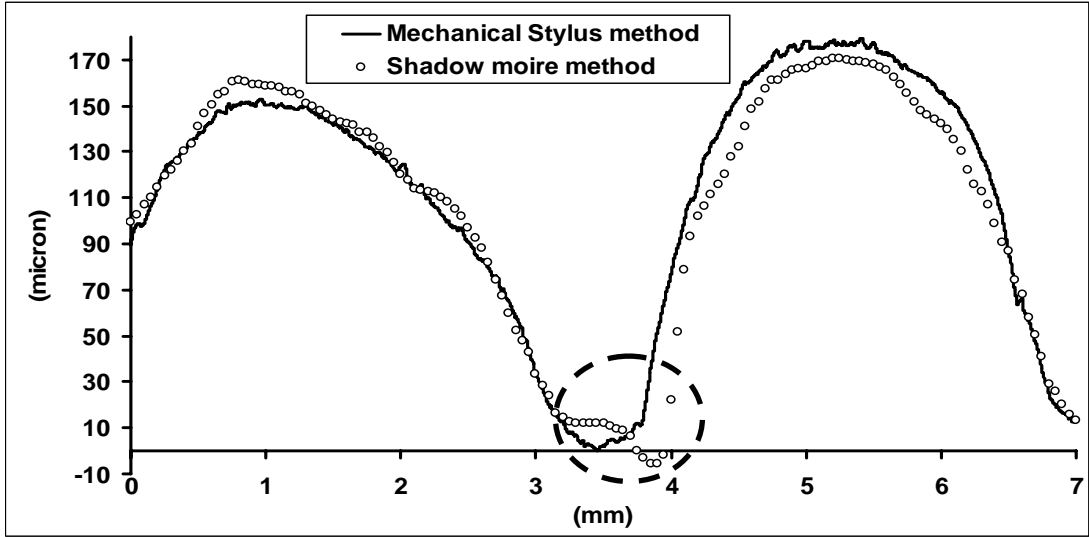
Figure 5.8 A comparison of surface profile of a 50-cent coin at cross-section C_1-C_1 between shadow moiré and mechanical stylus methods.

5.2 Measurements on continuously-deforming objects

In this section, temporal wavelet transform is used to process fringe patterns captured during continuous deformation of an object. Two methods, shadow moiré and ESPI, are used in the measurements for different ranges. Results showing instantaneous velocity, displacement and contour of various objects are presented.

5.2.1 Results of shadow moiré method

According to Eq. (2.4), when a continuously-deforming object is measured by the shadow moiré technique, the instantaneous phase $\varphi_{xy}(t)$ at a point $P(x,y)$ is given by

$$\varphi_{xy}(t) = \varphi_{0xy} + \Delta\varphi_{xy}(t) = k_S h_S(x,y;t) = k_S\left(h_{S_0}(x,y) + \Delta h_S(x,y;t)\right) \tag{5.4}$$

where $k_S = \dfrac{2\pi d_S}{p l_S}$ is a constant related to the optical setup. $h_{S_0}(x,y)$ is a dimension representing the initial shape of the object. $h_S(x,y;t)$ represents an instantaneous

shape, and $\Delta h_S(x,y;t)$ represents the displacement of point P. The instantaneous

shape and displacement can be obtained by retrieving the phase $\varphi_{xy}(t)$ from intensity

variation of each point using temporal wavelet transform. Furthermore, as the

instantaneous frequency $\varphi'_{xy}(t)$ can be extracted, the velocity of deformation can also

be obtained.

The first test specimen is a simply-supported Perspex beam subjected to

continuous deformation in the z-direction using a motorized stage and the

experimental setup is shown in Fig. 4.5. Figure 5.9 shows three typical fringe patterns

captured on a part of the simply-supported beam at intervals of 0.008s with an

imaging rate of 125 fps. The distance d_S and l_S (see Fig. 2.3) are respectively 360

mm and 465 mm, and as the grating is placed close to the object, the assumption of

$l_S \gg h_S(x,y)$ is satisfied. Five hundred fringe patterns are captured during a four-

second period and the first 128 consecutive images are processed. At each pixel, 128

sampling points along the time axis are obtained. Figure 5.10(a) shows the gray value

variation of points A_2 and B_2 [see Fig. 5.9(a)]. Due to diffraction effect, fringe

contrast is low when the distance between the object and grating is large. A slight

increase in contrast is observed at both points A_2 and B_2, which implies that distance

$h_S(x,y;t)$ is decreasing. The errors on phase extraction due to amplitude variation

can be omitted as it is slow-varying and Eq. (3.14) is satisfied. A slight difference in

amplitude between points A_2 and B_2 is also observed due to non-uniform illumination

and surface reflectivity. This will not affect the results as each pixel in the image is

processed independently of each other. Only temporal frequencies are considered as

they contain information on velocity and displacement. Compared to point B_2, a

higher temporal frequency is observed at point A_2. This implies that point A_2 deforms

faster than point B_2. The modulus of the Morlet wavelet transform of intensity variation of points A_2 and B_2 are shown respectively in Figs. 5.10(b) and 5.10(c). The dashed line shows the ridge of the wavelet transformation where the maximum modulus are found. Only a slight variation of a_{rb} is observed on the ridge, which implies that the velocities do not vary significantly along the time axis.

(a)

(b)

(c)
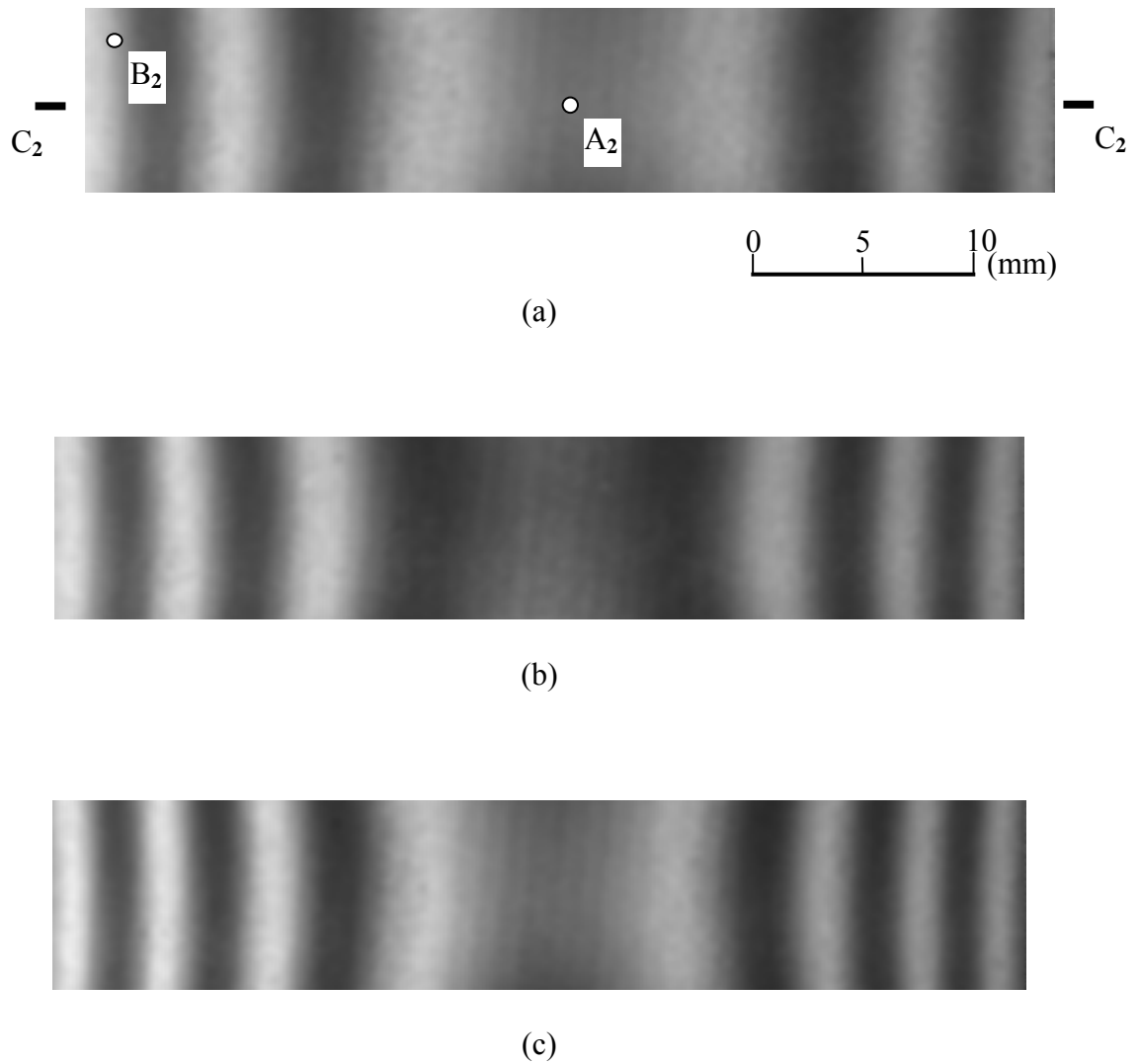
Figure 5.9 Typical moiré fringe patterns of a simply-supported beam at: (a) 0.4s; (b) 0.64s; (c) 0.88s.
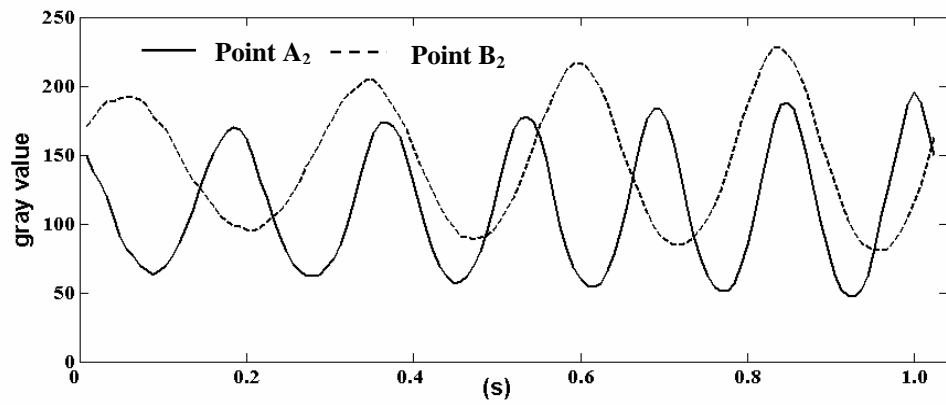
(a)
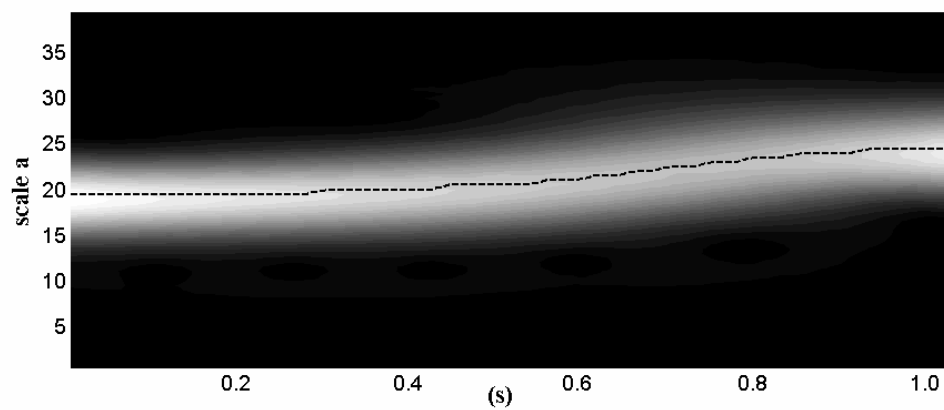
(b)
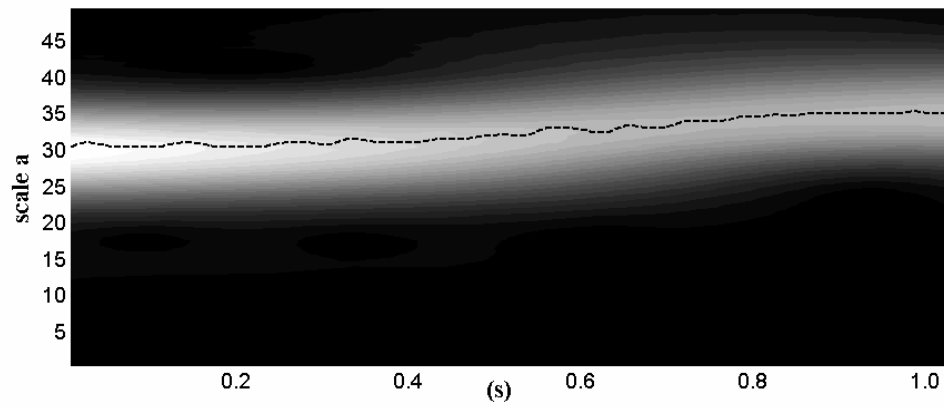
(c)

Figure 5.10 (a) Gray values of points A_2 and B_2. (b) modulus of Morlet wavelet transform at point A_2; (c) modulus of Morlet wavelet transform at point B_2.

The transient velocities of points A_2 and B_2, obtained directly from the instantaneous frequency, are given in Fig. 5.11(a). In this application, integration method mentioned in Chapter 3 is applied on continuous deformation measurement as the frequencies of the signal are quite uniform. Integration of $\dfrac{2\pi}{a_{rb}}$ is carried out on each pixel to obtain a continuous temporal displacement curve at each pixel [see Fig. 5.11(b)]. Displacement between any two instants T_1 and T_2 can be obtained from $(\varphi_{T_2} - \varphi_{T_1})$. Figure 5.12 shows a spatial displacement distribution within two instants $T_1 = 0.4s$ and $T_2 = 0.8s$.

(a)

(b)
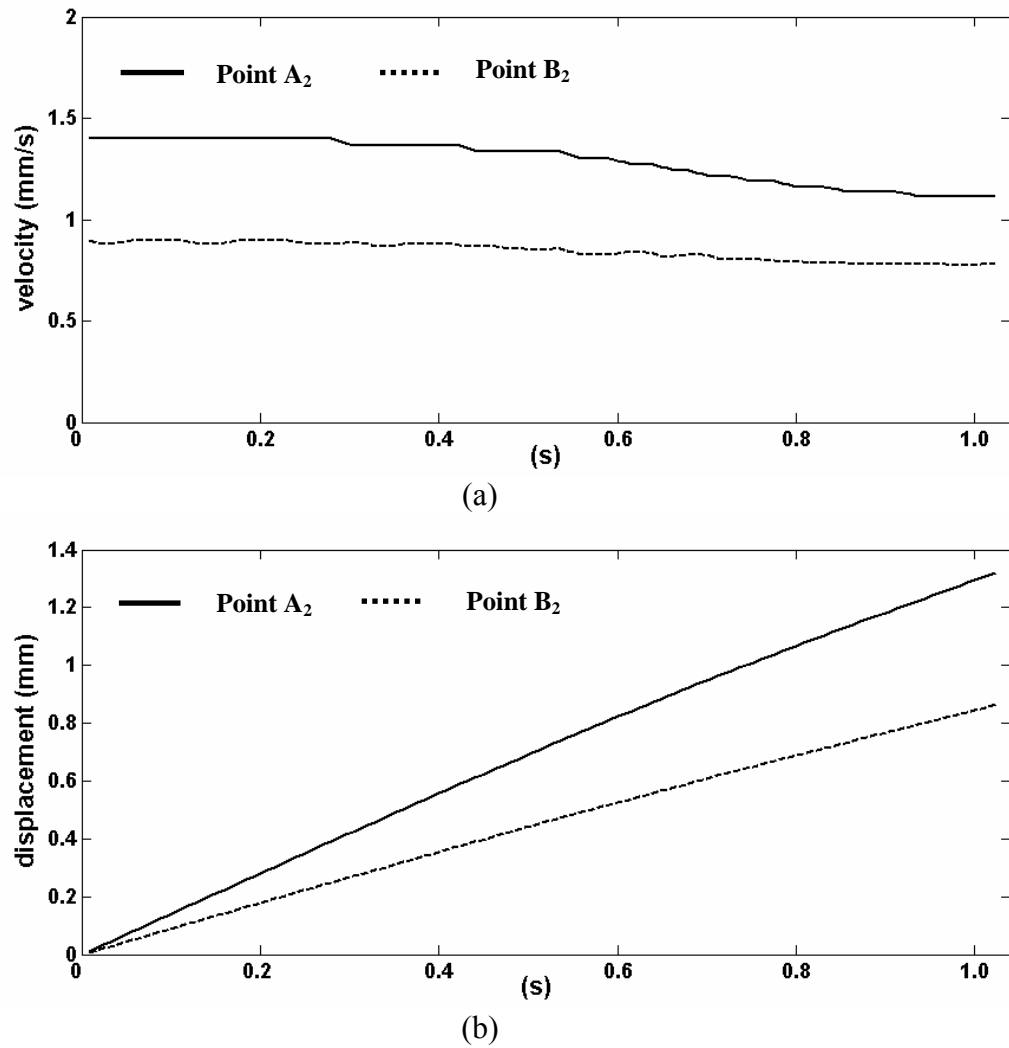
Figure 5.11 (a) Instantaneous velocity and (b) displacement of points A_2 and B_2.

For comparison of the results on continuous displacement measurement, temporal Fourier analysis is also applied on the same fringe patterns. As the displacements of each pixel are different, different frequency spectrums are expected. To cover all frequencies, a relatively wider bandpass filter is selected. The filtered spectrum is inverse-transformed to obtain a wrapped phase. One-dimensional phase unwrapping is then applied on each pixel along the time axis. Figure 5.13 shows a 3D displacement plot obtained by temporal Fourier transform. Figure 5.14 shows a comparison of displacement on cross section C_2-C_2 [see Fig. 5.9(a)]. It is observed that results from these two methods agree well. However, wavelet method provides a much smoother displacement map. The fluctuation in Fourier transform is about 0.02 mm. However, the fluctuation is less than 0.01 mm in the wavelet method. From the comparison, it is seen that more accurate displacements are obtained using the wavelet method.
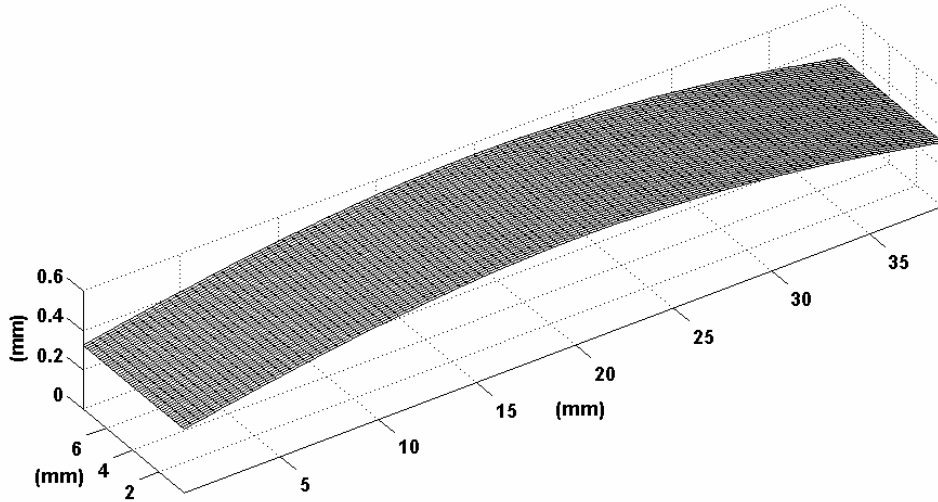
Figure 5.12 Displacement of a beam between $T_1 = 0.4s$ and $T_2 = 0.8s$ using temporal wavelet analysis
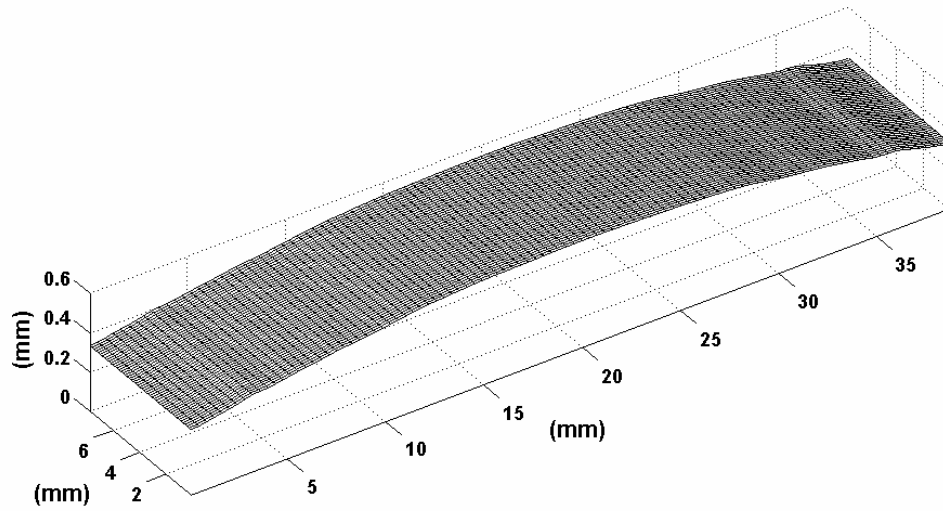
Figure 5.13 Displacement of a beam between $T_1 = 0.4s$ and $T_2 = 0.8s$ using temporal Fourier analysis
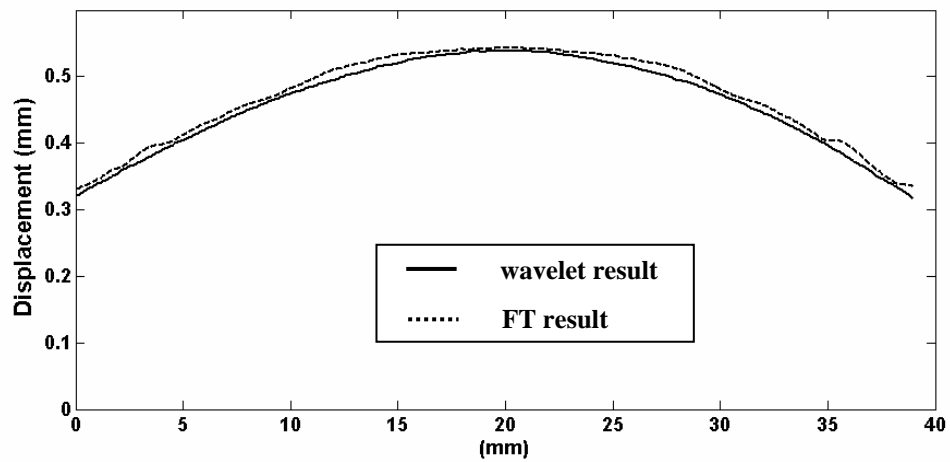
Figure 5.14 Comparison of displacement at cross section C_2-C_2 between temporal wavelet and Fourier analysis.

To retrieve an instantaneous contour of the specimen, Eq. (3.18) plus unwrapping process is the only method to obtain a wrapped phase map [see Fig. 5.15(a)], as the integration method can only retrieve the phase change $\Delta\varphi_{xy}(t)$ in Eq.

(5.4). Obviously, the unwrapping process cannot be avoided. Figures 5.15 (b) and

5.15 (c) show respectively an unwrapped phase map in spatial domain and a 3-D

contour at instant $T_2 = 0.8s$.

(a)
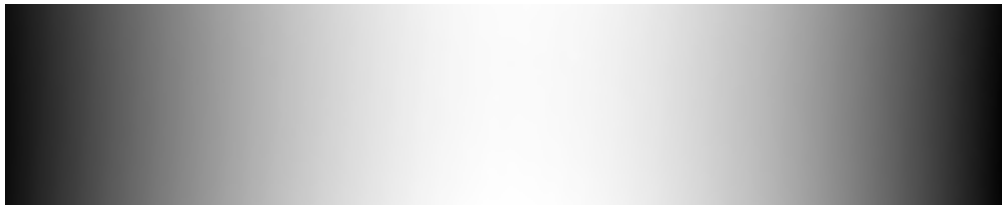
(b)
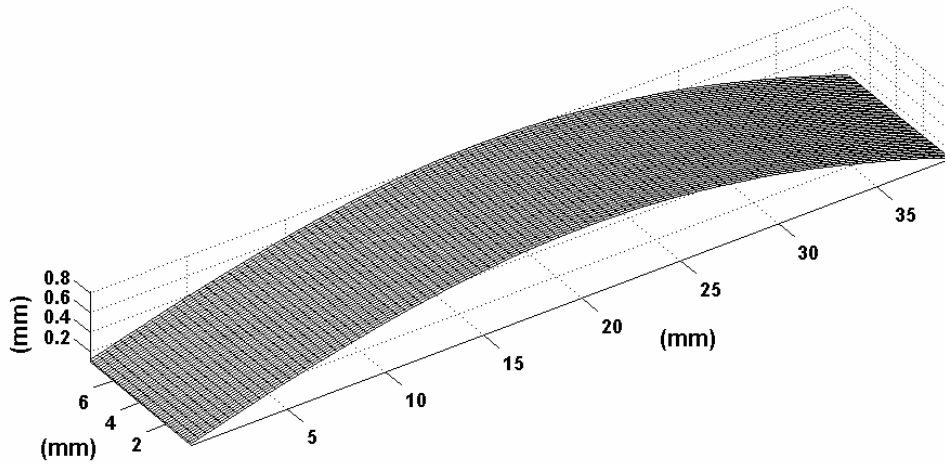
(c)

Figure 5.15 (a) Wrapped phase map; (b) phase map after unwrapping; and (c) 3-D
          plot of instantaneous surface profile at $T_2 = 0.8s$.

To verify the accuracy of the contour measurement, a test coin of 22.4 mm diameter with a diffuse surface is subjected to a rigid body motion in the z-axis [see Fig.5.16(a)]. The distance d_S and l_S (see Fig. 2.3) are 300 mm and 450 mm respectively and the frequency of the grating is 6 lines/mm. The camera recording rate remains at 125fps. Figures 5.16(b) and 5.16(c) show typical fringe patterns recorded at different instants. Carrier fringes are introduced by slightly rotating the grating in x-z plane. One hundred and twenty eight consecutive images are selected for processing from a total of 500 frames. Figure 5.17(a) shows the gray value variation of points D_2 and E_2. Although the initial phases of these two points are different, the frequencies of gray value variation along time-axis are the same, which implies that these two points have similar velocities and displacements. The moduli of the Morlet wavelet transform of these two points are also the same and one of them is shown in Fig. 5.17(b). Figures 5.18(a) and 5.18(b) show respectively a wrapped and unwrapped phase map at instant $T = 0.8s$. In Fig. 5.18(b), the unwrapped phase has been subtracted from a base plane value to remove the carrier effect. Figure 5.19 shows a 3D reconstruction of the area of interest on the coin. Figure 5.20 shows a comparison of the profile on cross section F_2-F_2 (see Fig.9a) using the proposed wavelet and mechanical stylus methods. The results generally agree well and the maximum discrepancy is about 15 μm. This is of the same order of error as that of the phase shifting method. It should be noted however, that in phase shifting method, at least three images are required.
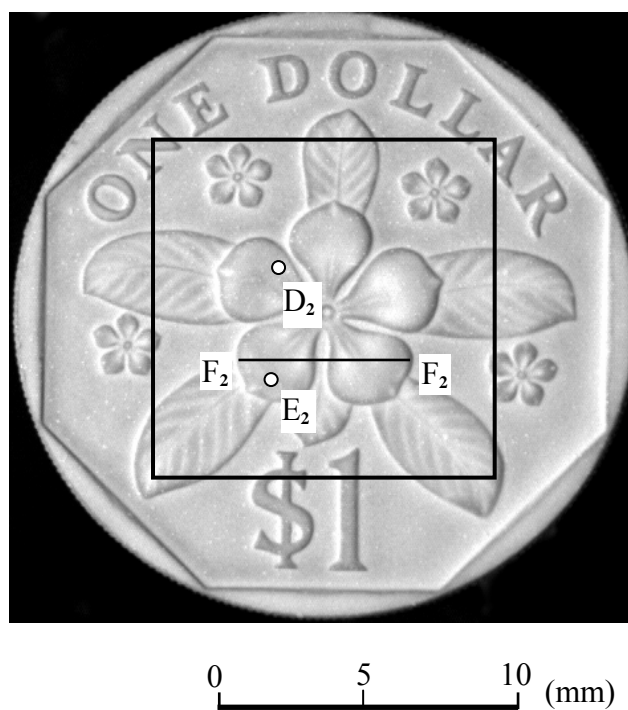
(a)
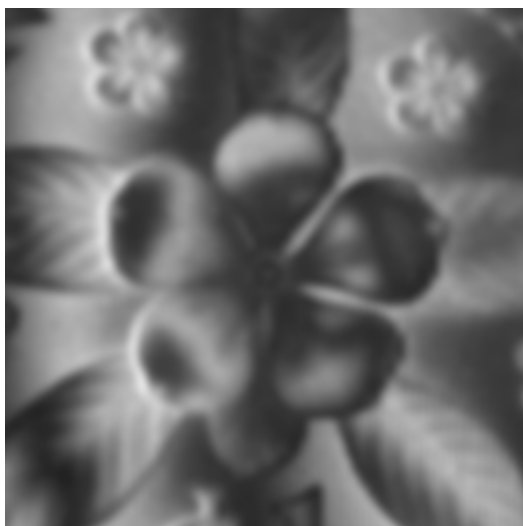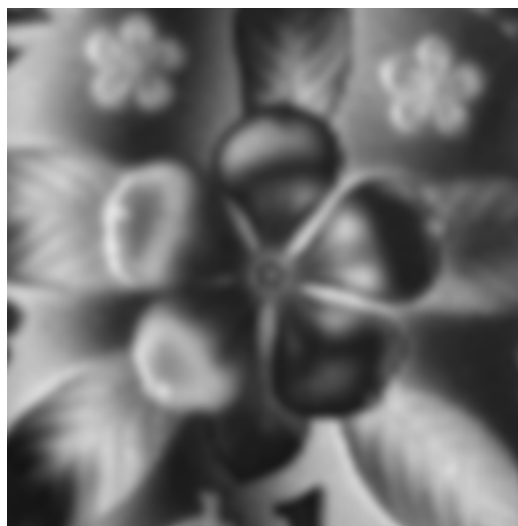
(b)   (c)

Figure 5.16 (a) Area of interest on a coin and typical moiré fringe patterns at (b) 0.4s; (c) 0.8s.

(a)

(b)
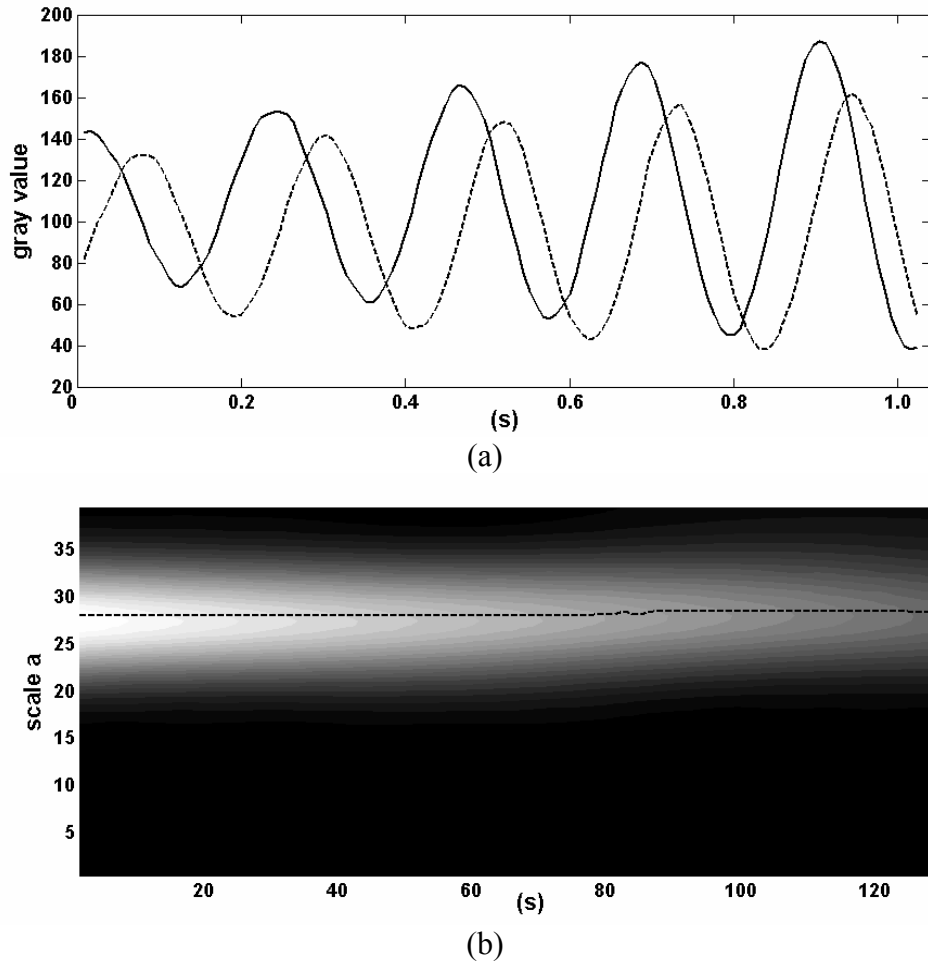
Figure 5.17 (a) Gray values of points D_2 and E_2; (b) modulus of Morlet wavelet transform at point D_2 and E_2.

(a)   (b)
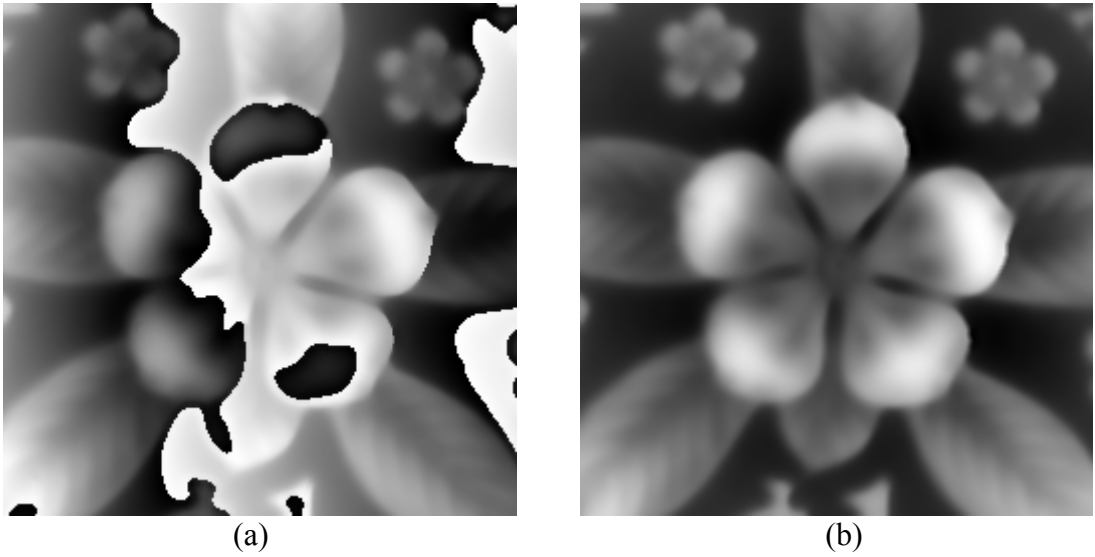
Figure 5.18 (a) wrapped phase map; (b) phase map after unwrapping at $T_2 = 0.8s$.
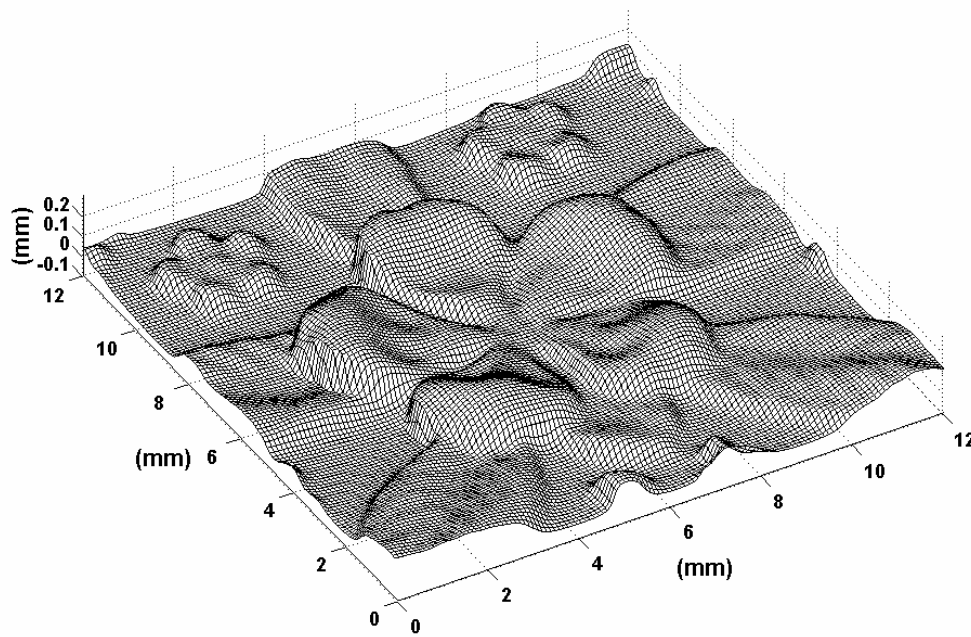
Figure 5.19 Reconstructed 3-D plot of instantaneous surface profile of a test coin at
$T_2 = 0.8s$.
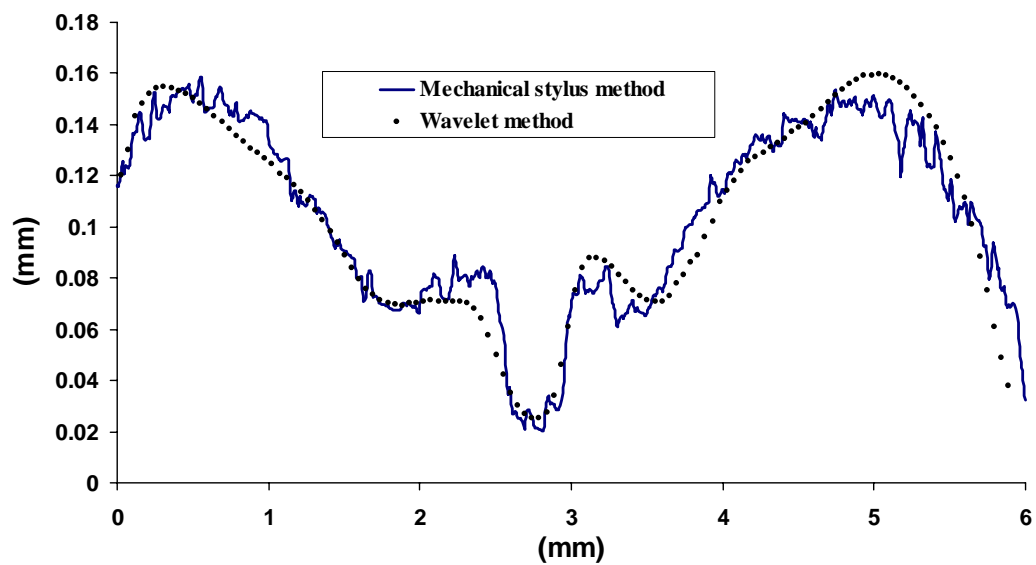
Figure 5.20 A comparison of surface profile of a test coin at cross-section F_2-F_2
between wavelet and mechanical stylus

5.2.2 Results of ESPI and Micro-ESPI

From the results presented in the previous section, it may not be obvious that temporal wavelet analysis shows better results than temporal Fourier transform, as the noise effect is not very serious in shadow moiré fringe patterns. In this section, temporal wavelet analysis is applied on ESPI fringe patterns where noise effect is more obvious.

According to Eq. (2.5), when a continuously-deforming object is measured by ESPI, the intensity variation on each pixel can be expressed as

$$
\begin{aligned}
I(x,y;t) &= I_0(x,y;t) + I_M(x,y;t)\cos[\varphi_{xy}(t)] \\
&= I_0(x,y;t) + I_M(x,y;t)\cos[\varphi_{0_{xy}} + \varDelta\varphi_{xy}(t)] \\
&= I_0(x,y;t)\left\{1 + V\cos\left[\varphi_{0_{xy}} + \frac{4\pi z(x,y;t)}{\lambda}\right]\right\}
\end{aligned}
\tag{5.5}
$$

where $I_0(x,y;t)$ is the intensity bias of the speckle pattern, V is the visibility, and $z(x,y;t)$ is the out-of-plane deformation of the object. As $\varphi_{0_{xy}}$ is a random phase, it is impossible to retrieve shape information from phase value $\varphi_{xy}(t)$. Instantaneous velocity and deformation can only be retrieved from phase change $\varDelta\varphi_{xy}(t)$.

As mentioned in Chapter 4, the first test specimen is a fully-clamped square plate with several artificial defects. Figure 5.21(a) shows a typical speckle pattern captured from a part of a fully-clamped plate at intervals of 0.004 s with an imaging rate of 250 fps. A small area of interest containing 300 ×300 pixels is also shown. Five hundred speckle patterns are captured during a two-second period, and the first 128 consecutive images are processed. Figure 5.21(b) shows an ESPI fringe pattern at an instant $T = 0.2s$, which is obtained by subtraction of two speckle patterns. For

each pixel, 128 sampling points along the time axis are obtained. Figure 5.22 shows the gray value variation of points A_3 and B_3 [indicated in Fig. 5.21(a)]. A difference in amplitude is observed due to non-uniform illumination. However, only temporal frequencies are considered as they contain information on velocity and displacement. The temporal frequency of point A_3 is much higher than that of point B_3. This implies that point A_3 deforms faster than point B_3. The modulus of the Morlet wavelet transform of intensity variation of points A_3 and B_3 are shown respectively in Figs. 5.23(a) and 5.23(b). The dashed line shows the ridge of the wavelet transformation where the maximum modulus are found. Little variation of a_{rb} is observed on the ridge, which implies the velocities are almost constant along the time axis. Figure 5.24(a) shows the velocities on points A_3 and B_3 where the transient velocities at each pixel can be retrieved. Integration of $\dfrac{2\pi}{a_{rb}}$ is carried out on each pixel to generate a continuous temporal phase change $\Delta\varphi_{xy}(t)$. The phase change due to the displacement between instant T and T_0 can be obtained from $\Delta\varphi_{xy}(T) - \Delta\varphi_{xy}(T_0)$, where $\Delta\varphi_{xy}(T_0)$ is the phase change at instant $T_0 = 0$. In an ESPI setup as shown in Fig. 4.8, a 2π phase change represents a displacement of $\lambda/2$ (= 316.4 nm) in the z direction. The transient displacements of points A_3 and B_3 are shown in Fig. 5.24(b). Figure 5.25(a) shows a 3-D plot of the out-of-plane displacement at instant $T = 0.2s$. A 3×3 median filter has been used on the phase map to remove several ill-behaved pixels. The corresponding fringe pattern is shown in Fig. 5.21(b). Figure 5.25(b) shows the out-of-plane displacements on cross section C_3-C_3 [indicated in Fig.5.21(a)] at different instants. A smooth spatial distribution of displacement is observed.
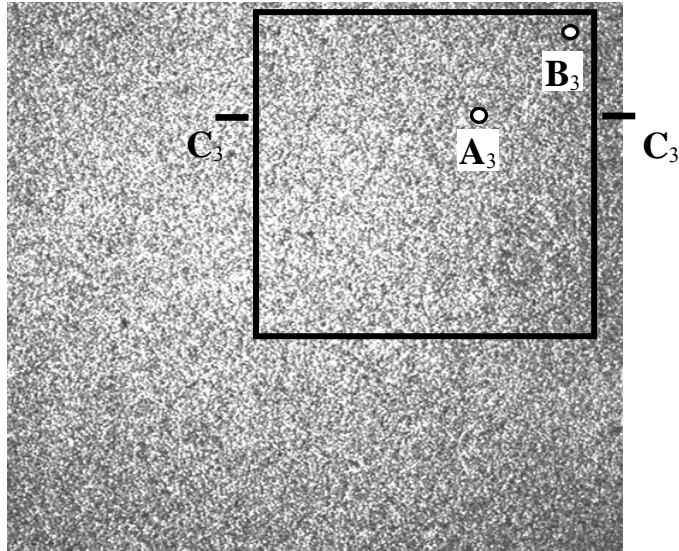
(a)
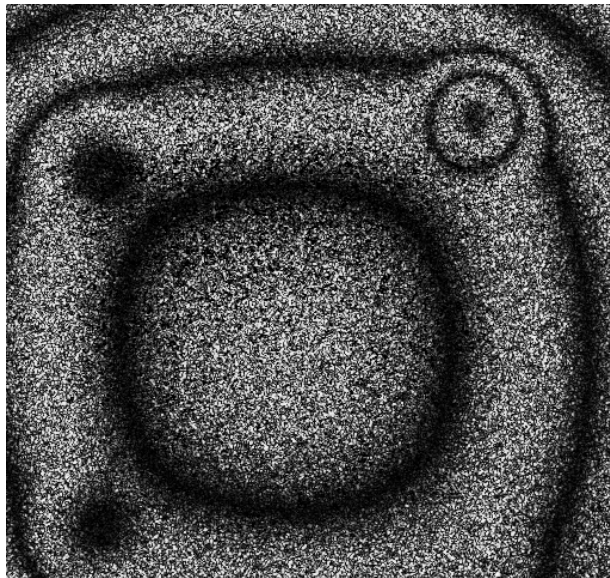
(b)

(c)

Figure 5.21 (a) Area of interest on a typical speckle pattern captured by a high-speed CCD camera on a plate specimen; (b) ESPI fringes at instant $T = 0.2s$ on a test plate; (c) typical speckle pattern captured on a beam specimen.
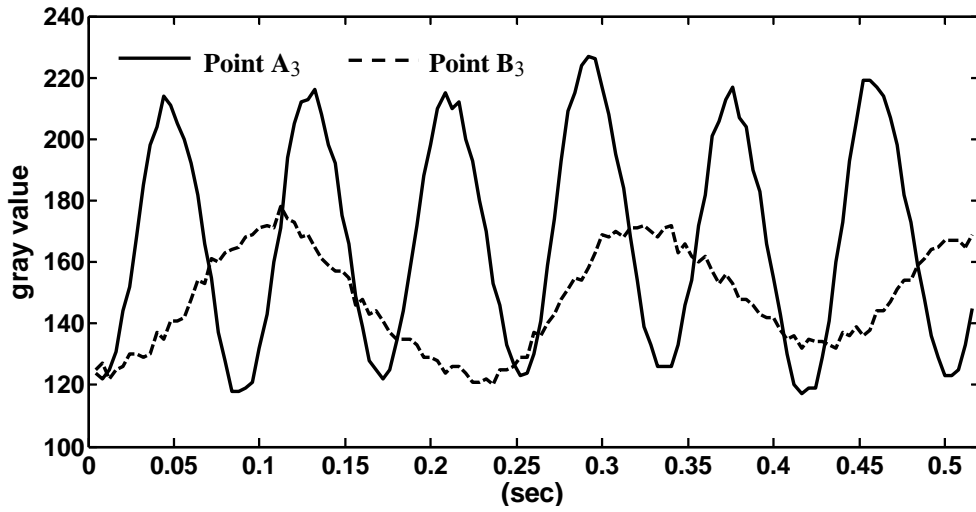
Figure 5.22   Gray values of points A_3 and B_3

(a)

(b)
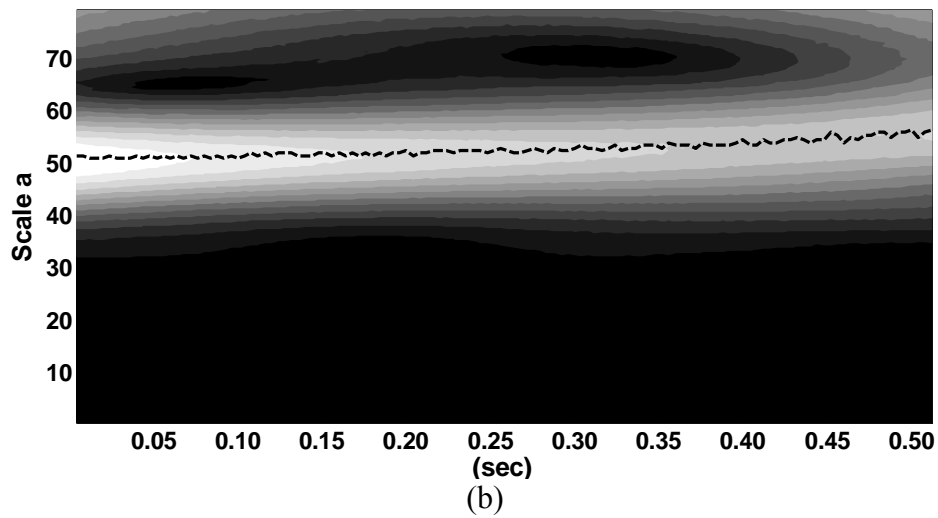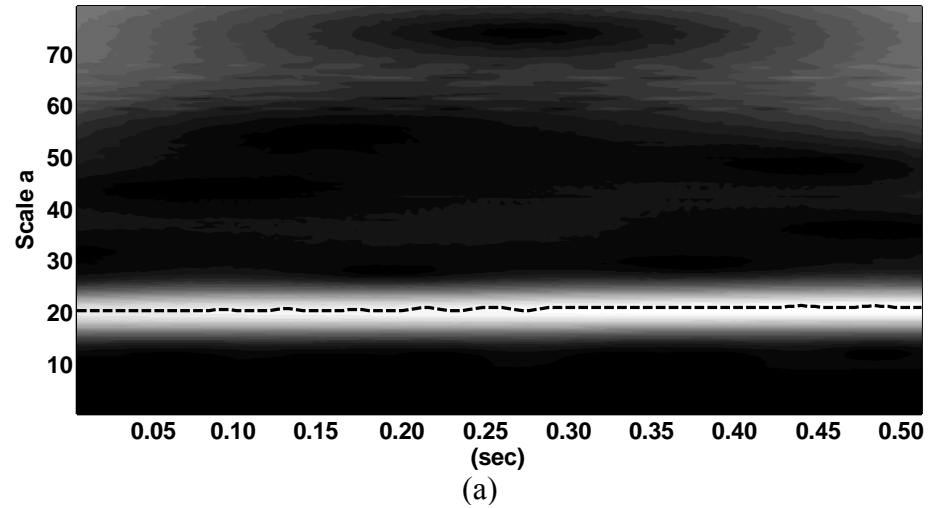
Figure 5.23 (a) Modulus of Morlet wavelet transform at point A_3; (b) modulus of Morlet wavelet transform at point B_3.
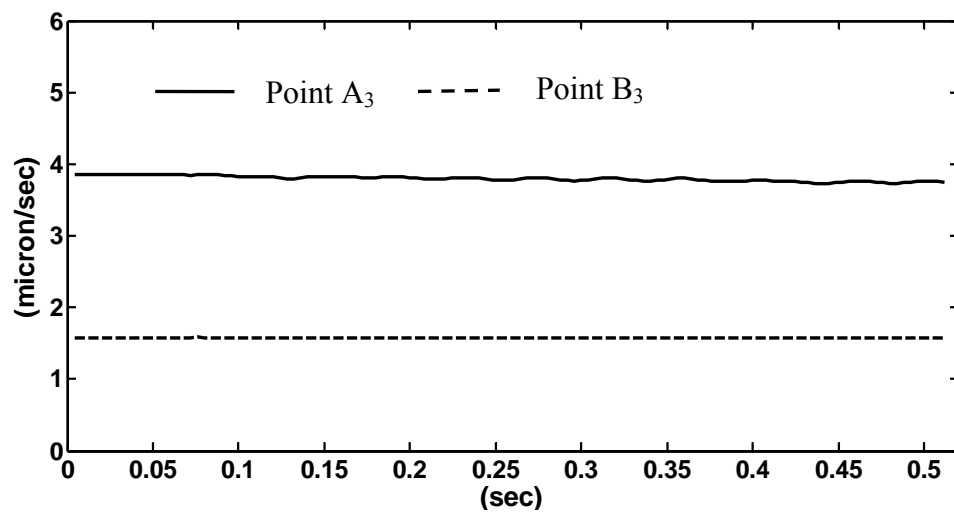
(a)
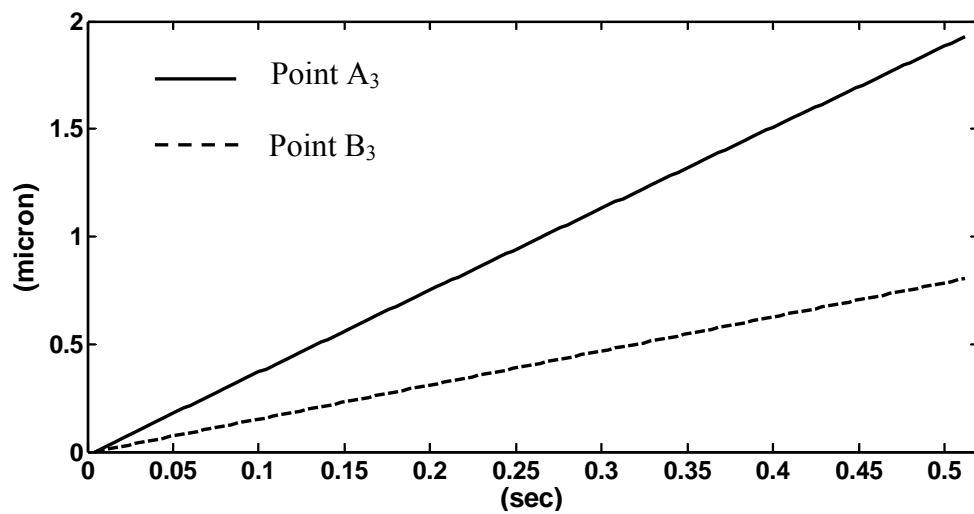
(b)

Figure 5.24 (a) Transient velocities of points A_3 and B_3;
(b) transient displacements of points A_3 and B_3.
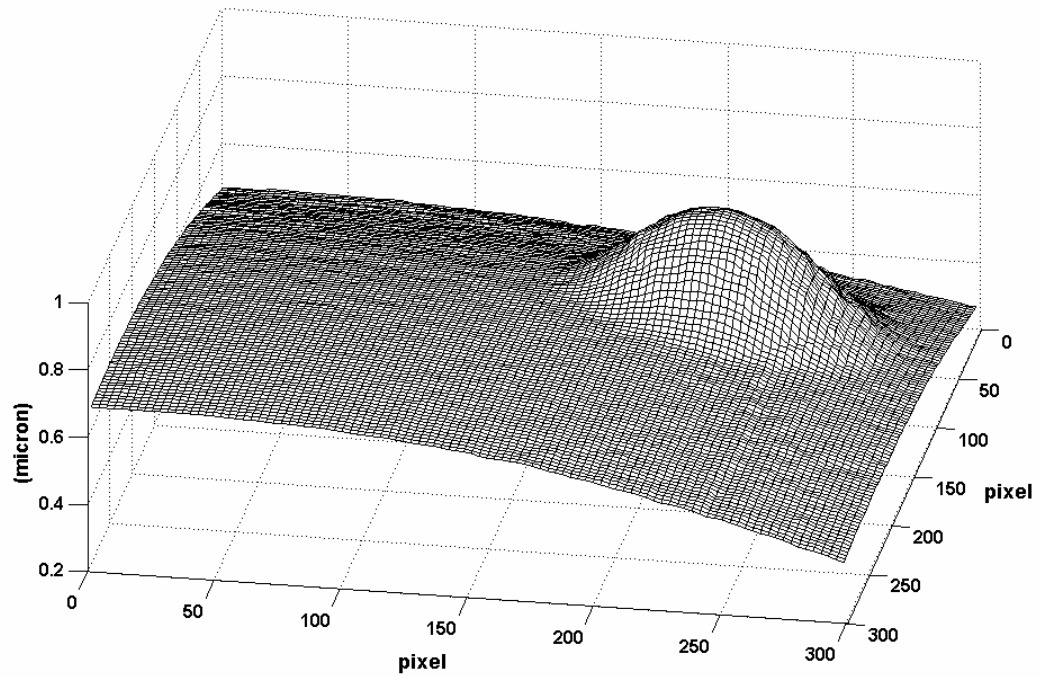
(a)
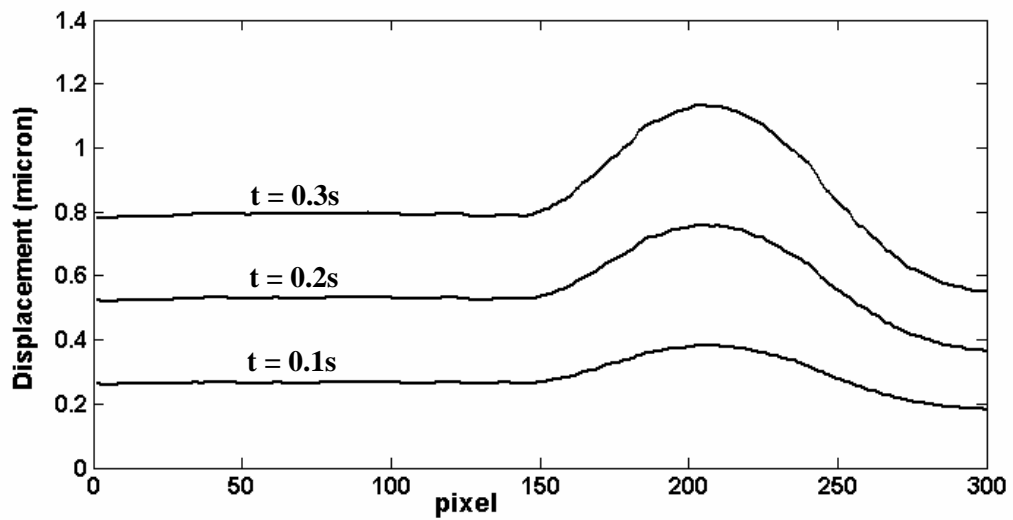
(b)

Figure 5.25 (a) 3D plot of out-of-plane displacement generated by wavelet transform; (b) transient displacements on cross-section C_3-C_3 obtained by wavelet transform.

For comparison, temporal Fourier analysis is also applied on the same speckle patterns. Bandpass filters of different widths are applied. As the temporal frequencies of each pixel are different, a relatively wide filter provides the best results as it includes all frequencies. A one-dimensional phase unwrapping is then applied along the time axis, as all phase values obtained by inverse Fourier transformation are within $[0, 2\pi)$. Figures 5.26(a) shows a 3-D displacement plot from temporal Fourier analysis and Fig. 5.26(b) shows the out-of-plane displacements at cross-section C_3-C_3. As in wavelet transform, a 3×3 median filter is also applied on the phase map. However, the fluctuation due to noise is still obvious. In Figs. 5.25 and 5.26, it is observed that the maximum displacement fluctuation due to noise is around 0.08 μm in Fourier transform, but only 0.02 μm in wavelet analysis.

In the second experiment, a slightly non-linear loading is applied to a cantilever beam using a piezoelectrical transducer. Figure 5.21(c) shows a typical speckle pattern captured from the beam. Figure 5.27(a) shows modulus of the wavelet transform of intensity variation on point D_3 [indicated in Fig. 5.21(c)] which is arbitrarily selected to illustrate the process. Different values of a_{rb} on the ridge are observed which imply the nonlinearity of the velocities. Figure 5.27(b) shows the velocity of point D_3 which is directly derived from instantaneous frequency in Fig. 5.27(a). A smooth transient displacement curve of point D_3 is obtained through integration of velocity (shown in Fig. 5.28). Figure 5.29 shows the velocity distribution on cross-section E_3-E_3 [indicated in Fig. 5.21(c)] at different instants. From a comparison of the displacements using wavelet and Fourier analysis (shown in Fig. 5.30), it is observed that CWT on each pixel generates a smoother spatial displacement distribution at different instants compared to Fourier transform. The maximum displacement fluctuation due to noise is around 0.04 μm in Fourier

transform, but only 0.02 μm in wavelet analysis. Similar results on a tiny beam using

micro-ESPI are presented in Appendix B.
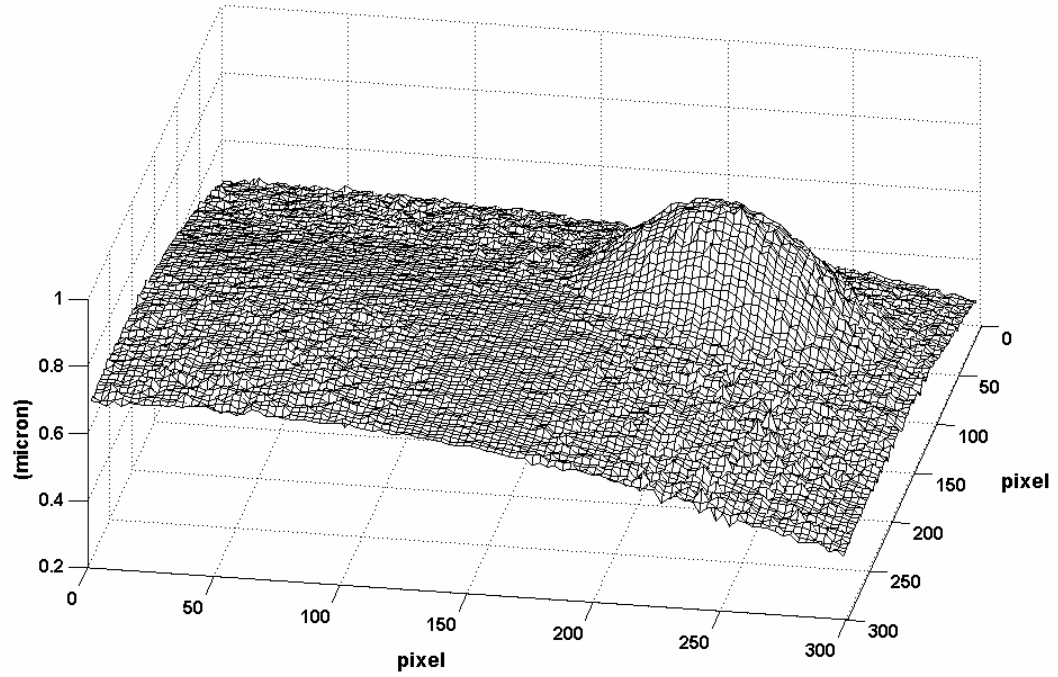
(a)
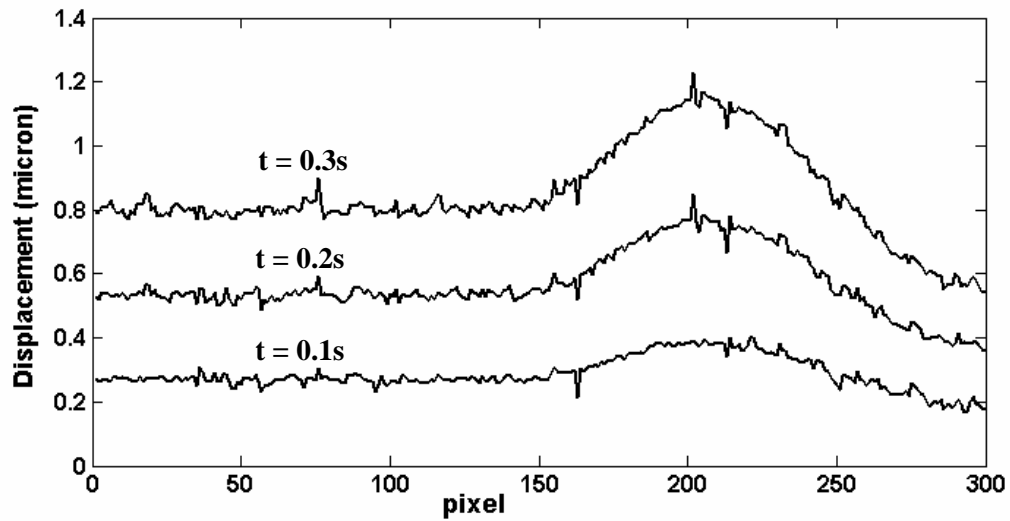
(b)

Figure 5.26 (a) 3D plot of out-of-plane displacement generated by Fourier transform;
(b) Transient displacements on cross-section C_3-C_3 obtained by Fourier transform.
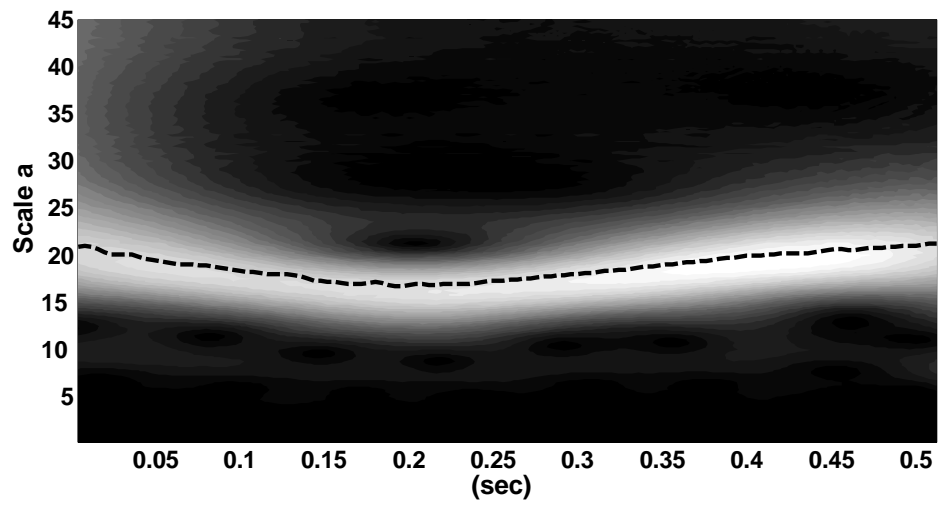
(a)
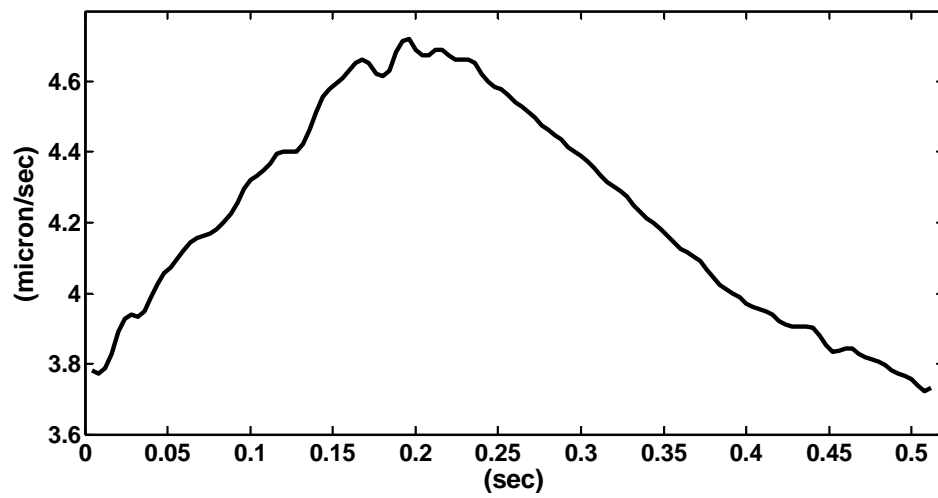
(b)

Figure 5.27 (a) Modulus of Morlet wavelet transform at point D_3;
(b) Transient velocity of point D_3.
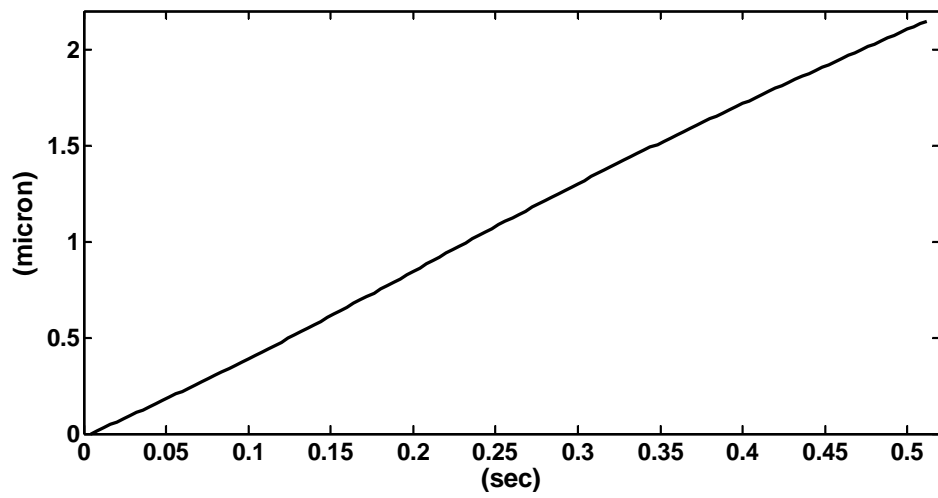
Figure 5.28 Transient displacement of point D_3.
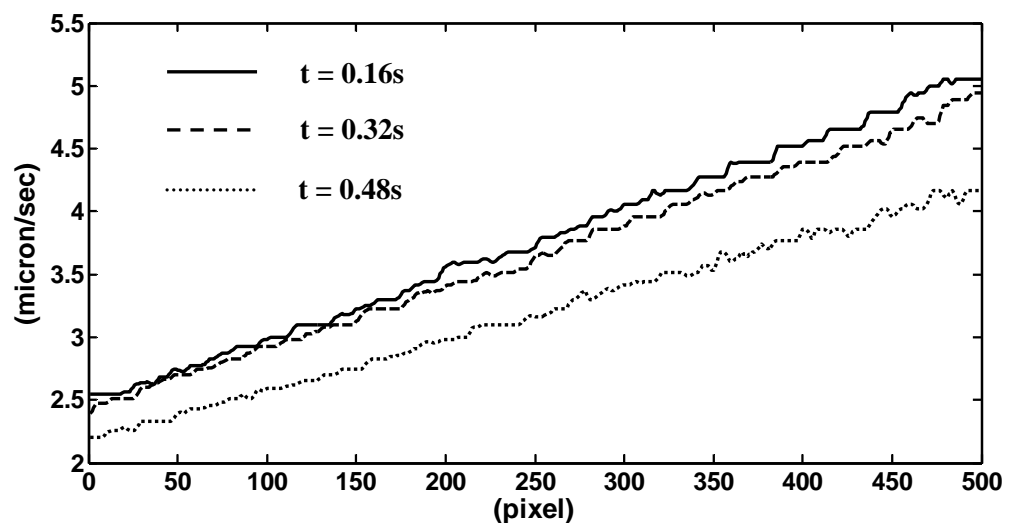
Figure 5.29 Velocity distribution at cross-section E_3-E_3 at different instants
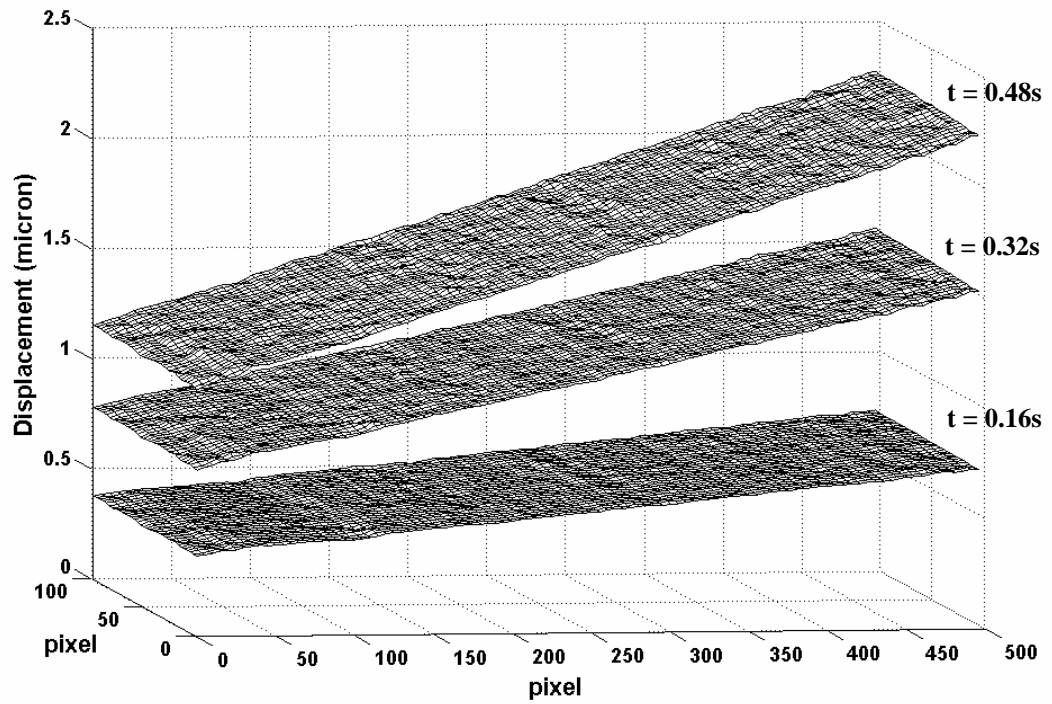
(a)
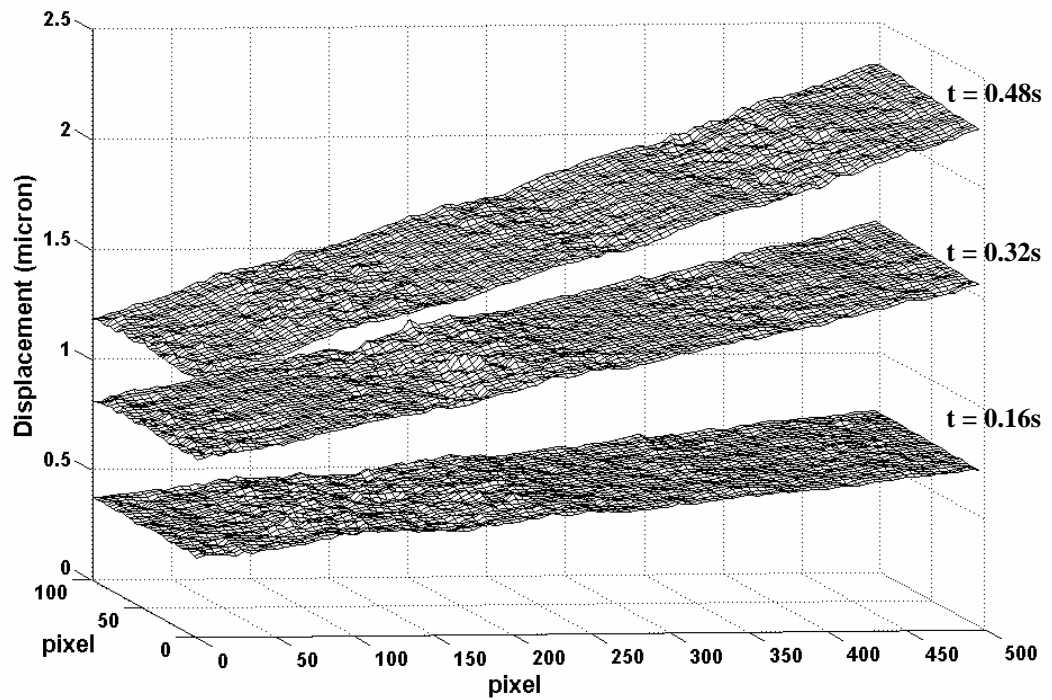
(b)

Figure 5.30   (a) Displacement of a cantilever beam at different instants obtained by
                wavelet transform;
                (b) displacement of a cantilever beam at different instants obtained by
                Fourier transform.

From the above comparison between the results of wavelet and Fourier analysis, it can be observed that wavelet analysis shows better results in continuous displacement measurement. As wavelet analysis calculates the optimized frequency at each instant, it performs an adaptive band-pass filtering of the measured signals, thus limiting the influence of various noise sources and increasing the resolution of measurement significantly. In contrast, Fourier transform uses a broader filter which is less efficient in eliminating noise effect. The maximum displacement fluctuation due to noise depends on width of the band-pass filter and quality of the speckle patterns.

When loading is linearly increased, the values of $I_M(b)$ and $\varphi'_{xy}(b)$ remain constant and the corrective term ε in Eq. (3.13) is negligible. For loading which is nonlinear, a slight nonlinearity of $\varphi'_{xy}(b)$ is observed and the corrective term ε affects the results of the instantaneous frequency extraction slightly. If conditions in Eq. (3.14) and Eq. (3.15) are satisfied, the errors on frequency $\varphi'_{xy}(b)$ are limited. However, when the displacement is extracted by integration, an accumulated error can still be observed. Compared to Fourier transform, a slight offset can be observed in the wavelet results when the displacement is large. Comparing the averaged displacement at the right end (F$_3$-F$_3$) of the beam [shown in Fig. 5.21(b)], a difference of 0.04 μm is observed when the displacement is around 2.3 μm, which indicates that the system error due to ε is around 1.7% for velocity which varies between 3.7 μm/sec and 4.7 μm/sec (see Fig. 5.27).

Continuous wavelet transform maps a one-dimensional intensity variation signal to a two-dimensional plane of position and frequency, and extracts the optimized frequencies. Although some fast-converging iterative algorithms have been

introduced and it is not necessary to explore the whole time-frequency plane, CWT is still a time-consuming process and requires high computing speed and memory. The computation time is about 10 times larger than that of temporal Fourier transform. This is the main drawback of CWT in temporal phase analysis. Similar to other temporal phase analysis methods, wavelet transform is also limited by Nyquist sampling theorem. It is impossible to analyze signals with a frequency higher than half of the acquisition rate. However, these two disadvantages become inconspicuous due to the rapid improvements in capacity of computers and high-speed CCD cameras.

Temporal phase analysis technique has the advantage of eliminating speckle noise, as it evaluates the phase pixel by pixel along the time axis. There are still some ill-behaved pixels; however, compared to the speckle noise in spatial domain, these pixels can be easily identified and removed. Temporal wavelet analysis and Fourier analysis do have their disadvantages and determination of the absolute sign of the computed phase is impossible by both methods. This limits the techniques to the measurement of deformation in one direction. Furthermore, they cannot analyze the part of an object that is stationary. Adding a carrier frequency to the image acquisition process is a method to overcome these problems.

5.3 Measurements on vibrating objects

Measurement of instantaneous displacement using temporal phase analysis technique is more difficult than continuous deformation measurement due to the ambiguity of phase change. Two methods are used to solve this problem. Introducing a temporal carrier in the capturing process is one of the methods. The carrier frequency should be high enough so that the phase change at each point is in one direction. The second method is to separate the signal into several sections with phase change in one

direction. It is applicable only when extreme positions of the vibration can be identified. In this section, applications of these two methods are presented.

5.3.1 Temporal carrier technique

The schematic layout of ESPI setup for out-of-plane measurement with temporal carrier is shown in Fig. 4.11. The temporal carrier is generated by shifting the reference plate constantly with a piezoelectrical transducer stage. A series of speckle patterns are captured by a high-speed CCD camera with a telecentric lens during deformation. The intensity of each pixel can be expressed as

$$I(x,y;t) = I_0(x,y;t) + I_M(x,y;t)\cos[\varphi_{xy}(t)]$$

$$= I_0(x,y;t) + I_M(x,y;t)\cos[\phi_C(t) + \phi_{xy}(t)]$$

$$= I_0(x,y;t)\left\{1 + V\cos\left[2\pi f_C t + \varphi_0(x,y) + \frac{4\pi z(x,y;t)}{\lambda}\right]\right\} \qquad (5.6)$$

where $I_0(x,y;t)$ is the intensity bias of the speckle pattern, V is the visibility, $\varphi_0(x,y)$ is the random phase, f_C is the temporal carrier frequency, $\phi_C(t) = 2\pi f_C t$ is the phase change due to temporal carrier, and $z(x,y;t)$ is the out-of-plane deformation of the object.

The cantilever beam (shown in Fig 4.12) is subjected to a sinusoidal vibration at the free end using a vibrator. A beam of He-Ne laser (30 mW, λ = 632.8 nm) is collimated and illuminates the specimen and a reference plate at right angles through a beam splitter. The object and reference beams are recorded on a CCD sensor. To generate the temporal carrier, the reference plate is applied with a linear rigid body motion at a certain velocity by a computer-controlled PZT translation stage during

vibration of cantilever beam. As shown in Fig. 4.12, a still reference block is captured

together with the beam. A series of speckle patterns is captured by a high-speed CCD

camera with a telecentric gauging lens.

Figure 5.31 shows a typical speckle pattern captured from a part of the

cantilever beam, together with a still reference block above the beam at intervals of

0.004 s and an imaging rate of 250 frames/s. The area of interest on the cantilever

beam contains 400 pixels × 100 pixels with actual length and width of 60.8 mm and

15.2 mm, respectively. Five hundred speckle patterns were captured over a two-

second period, and the first 400 consecutive images were processed. For each pixel,

400 sampling points along the time axis were obtained. Figure 5.32(a) shows the

intensity variation of point R (indicated in Fig. 5.31) on a reference block. The

modulus of the Morlet wavelet transform of intensity variation of point R is shown in

Fig. 5.32(b). The dashed line shows the ridge of the wavelet transform where the

maximum modulus are found. Although the a_{rb} on the ridge is fairly constant, some

variation of a_{rb} due to noise on the pixel and discreteness of the signal are still

observed. To eliminate the noise effect, an average value of a_{rb} was calculated in an

area of 50 pixels × 50 pixels on the reference block (also indicated in Fig. 5.31).

Figure 5.32(c) shows the averaged scaling a_{rb} on the ridge. As the reference block is

stationary, the ridge value represents the effect of temporal carrier, which was applied

on the reference plate by a PZT transducer. Little variations of averaged a_{rb} are

observed, which implies that the temporal carrier is constant along the time axis.

Integration of $\dfrac{2\pi}{a_{rb}}$ was carried out along the time axis to generate a continuous phase

change $\phi_C(t)$ due to temporal carrier.
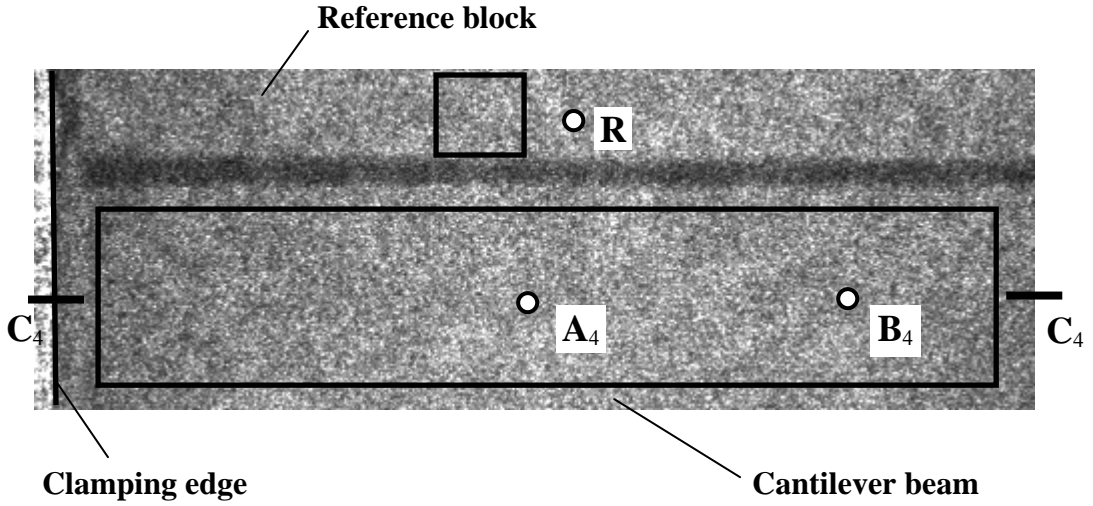
Figure 5.31 Typical speckle pattern on a reference block and a cantilever beam with area of interest.

The phase value $\varphi_{xy}(t)$ equals to the phase of wavelet transform $W_{xy}(a,b)$ on the ridge. Equation (3.18) and one-dimensional phase unwrapping are used to calculate the $\varphi_{xy}(t)$ on each pixel. The phase change between two instants T_1 and T_2 at point $P(x,y)$ can be expressed by

$$\Delta\varphi_{xy} = \varphi_{xy}(T_2) - \varphi_{xy}(T_1) = 2\pi f_C(T_2 - T_1) + \frac{4\pi z(x,y;(T_2-T_1))}{\lambda}, \qquad (5.7)$$

where $z(x,y;(T_2-T_1))$ is the out-of-plane displacement of point P between two instants T_1 and T_2. As the phase change due to temporal carrier $2\pi f_C(T_2-T_1)$ is measured as mentioned above, it can be easily removed from above equation.
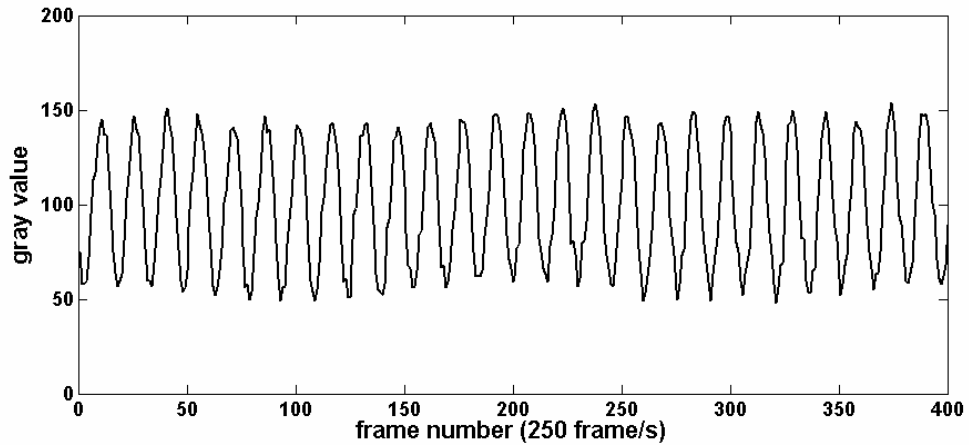
(a)
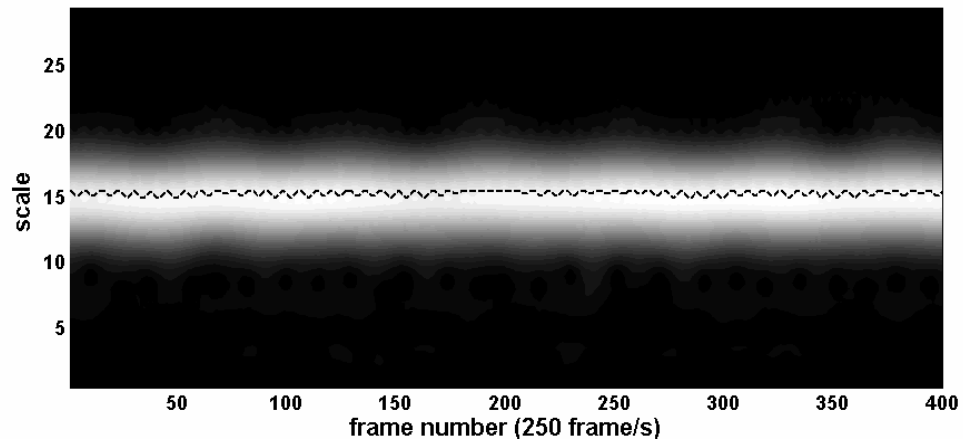
(b)
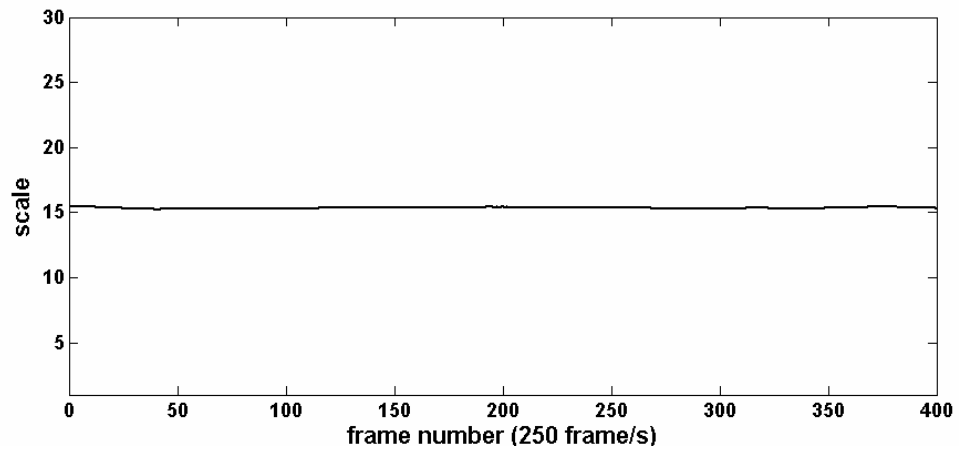
(c)

Figure 5.32 (a) Temporal intensity variation of point R on a reference block. (b) plot of modulus of Morlet wavelet transform at point R; (c) averaged ridge detected on a reference block.

Figures 5.33 and 5.34 show the intensity variations and the modulus of the Morlet wavelet transform on points A_4 and B_4 (indicated in Fig. 5.31). It can be observed that the frequency variation of point A_4 is less than that of point B_4, implying that the vibration amplitude on point A_4 is less than that of point B_4, as these two points have the same vibration frequency in this case. It is reasonable as point A_4 is closer to the clamping end than point B_4. Using Eq. (3.18) and one-dimensional phase unwrapping, the phase value $\varphi_{xy}(t)$ can be retrieved. Subsequently, the continuous temporal phase change $\Delta\varphi_{xy}$ can be obtained. Figure 5.35(a) shows the temporal phase change obtained on point B_4 and on the reference block. The difference between these two lines gives the absolute phase change of point B_4 due to vibration. As 2π phase change represents a displacement of $\lambda/2$ (=316.4nm) in the z direction, the displacement on point B_4 can be obtained [shown in Figure 5.35(b)]. Four instants, T_0, T_1, T_2 and T_3, are selected as indicated in Fig. 5.35(b). Figure 5.36(a) shows the out-of-plane displacement along cross section C_4-C_4 (shown in Fig. 5.31) at different time intervals $(T_1 - T_0)$, $(T_2 - T_0)$ and $(T_3 - T_0)$.

For comparison, temporal Fourier analysis was also applied on the same speckle patterns. A narrow bandpass filter was applied on the reference block as the spectrum of the signal was concentrated. A relatively wider filter was applied on the cantilever beam as it would include all frequencies. A one-dimensional phase unwrapping was then applied along the time axis, as all phase values retrieved by inverse Fourier transform fall within a $[0, 2\pi)$ range. Figure 5.36(b) shows the temporal displacements on cross-section C_4-C_4 obtained by temporal Fourier transform. Figure 5.37 shows 3-D displacement plots obtained by temporal wavelet analysis and Fourier transform. A 3×3 median filter was applied on both phase maps

to remove some ill-behaved pixels. It was observed that CWT on each pixel generates

a smoother spatial displacement distribution at different instants compared to a

Fourier transform. The maximum displacement fluctuation due to noise is around 0.04

μm in Fourier transform, but only 0.02 μm in wavelet analysis.
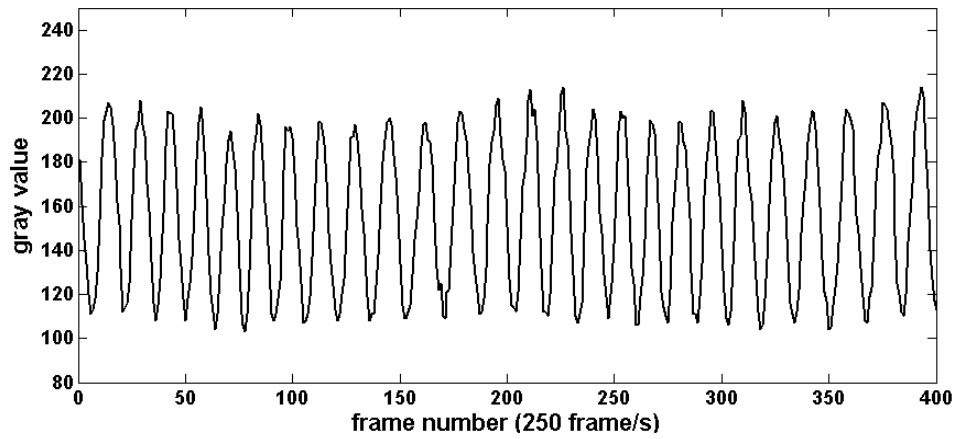
(a)
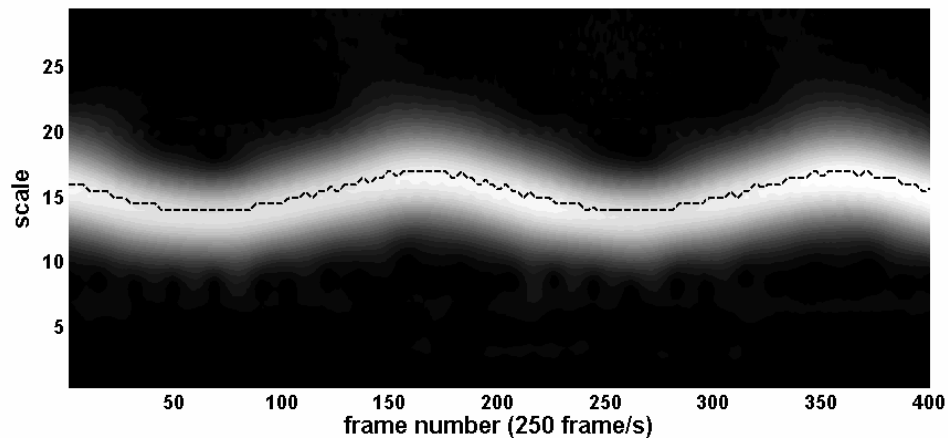
(b)

Figure 5.33 (a) Temporal intensity variation of point A_4 on a cantilever beam;
(b) modulus of Morlet wavelet transform at point A_4.
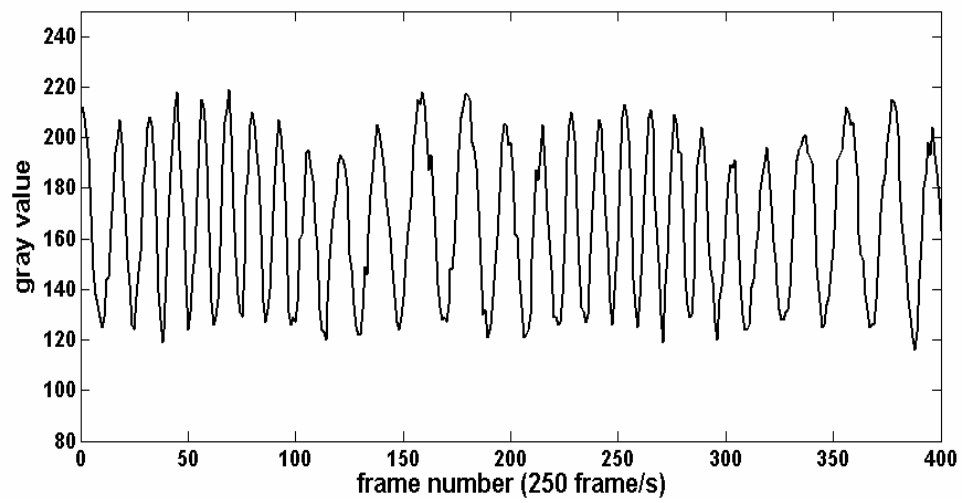
(a)
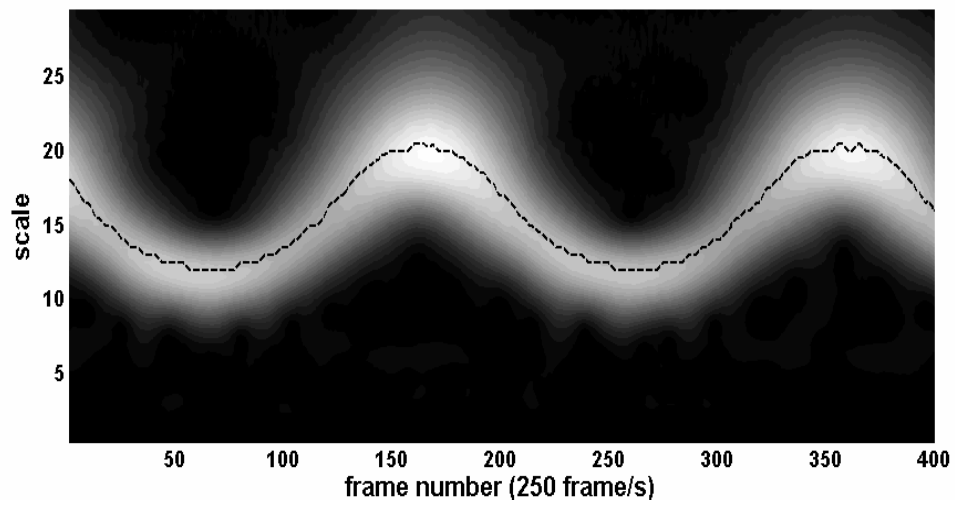
(b)

Figure 5.34 (a) Temporal intensity variation of point B_4 on a cantilever beam; (b) modulus of Morlet wavelet transform at point B_4.
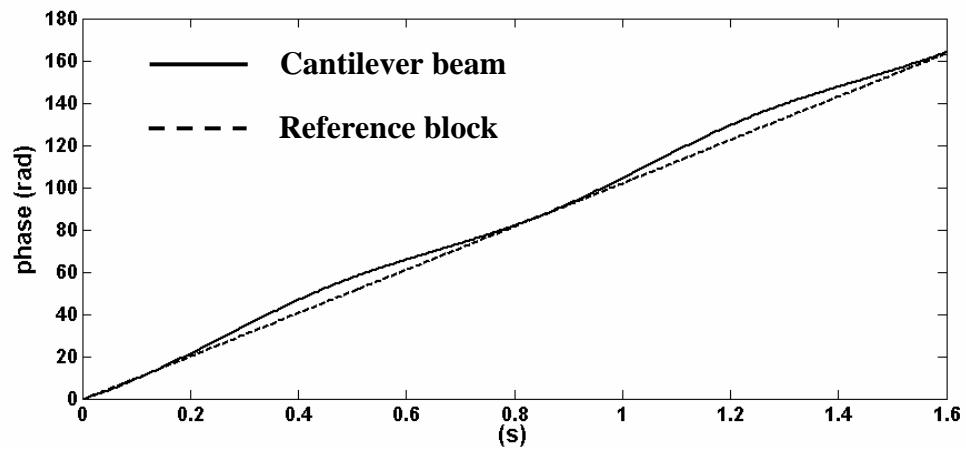
(a)
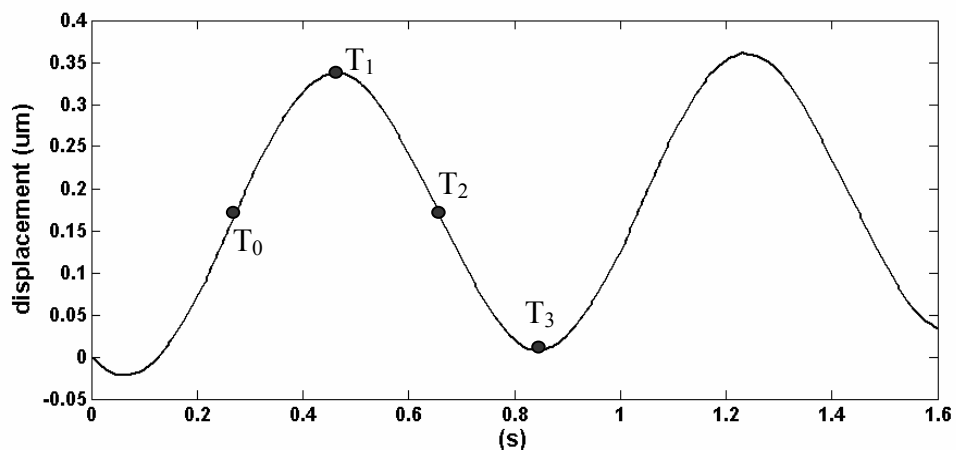
(b)

Figure 5.35 (a) Phase variation on a reference block and point B_4;
(b) out-of-plane displacement of point B_4.
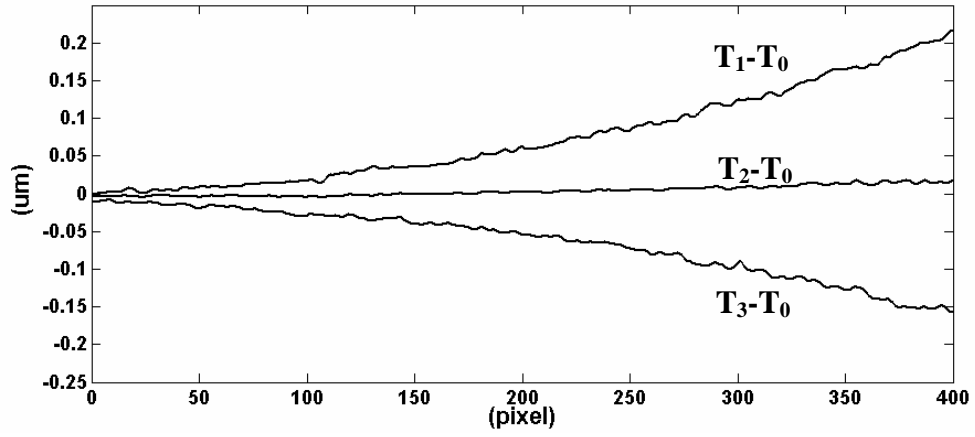
(a)
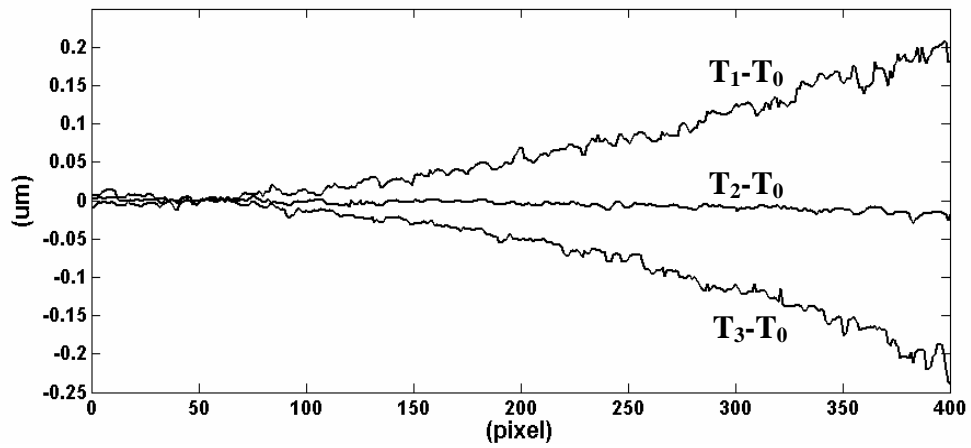
(b)

Figure 5.36 Displacement distribution along cross-section C_4-C_4 at different time intervals obtained by (a) temporal wavelet transform and (b) temporal Fourier transform.
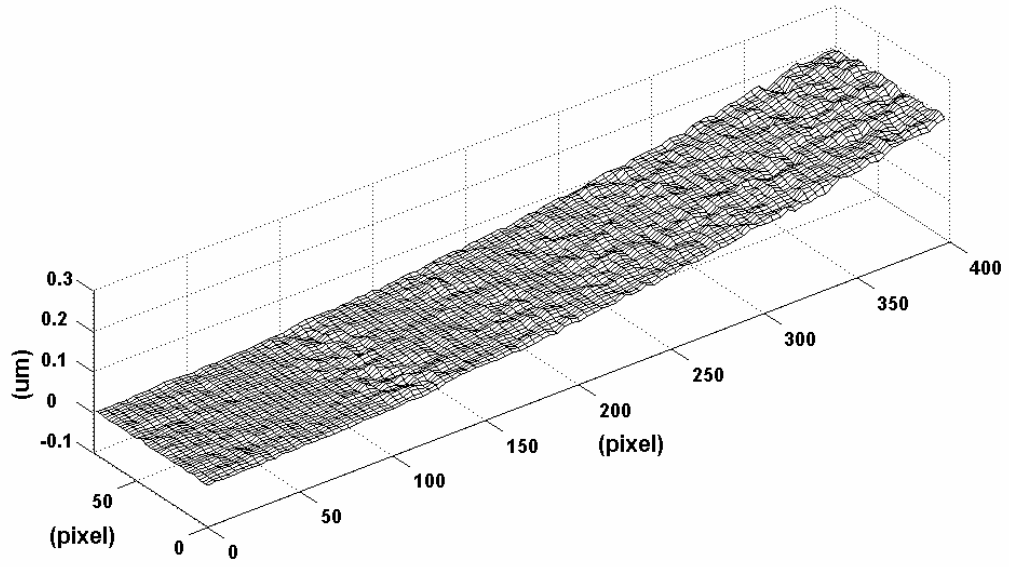
(a)
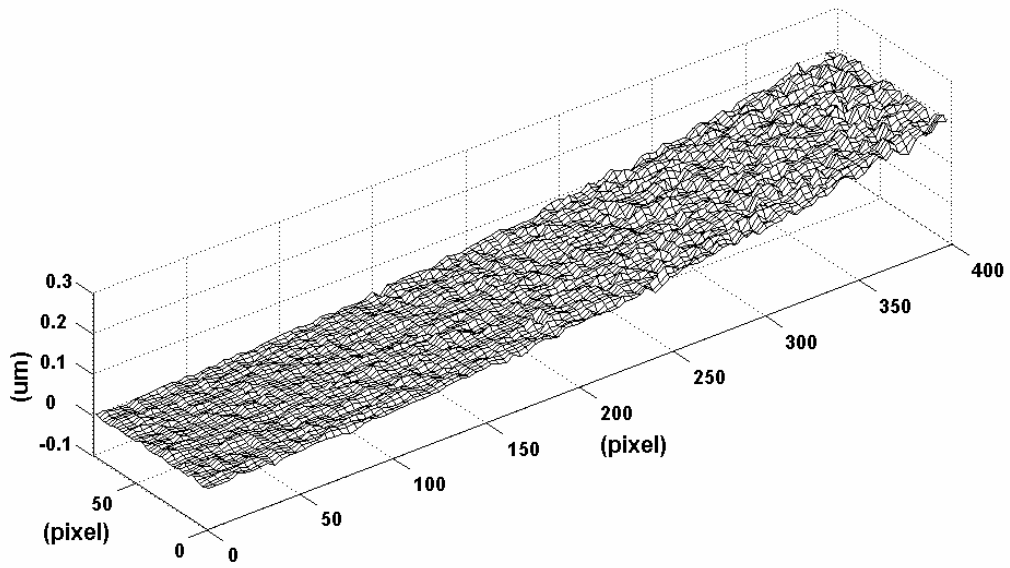
(b)

Figure 5.37 Displacement distribution $(T_1 - T_0)$ on a cantilever beam obtained by (a) temporal wavelet transform and (b) temporal Fourier transform.

In the measurement of vibrating objects, there are two limitations in both temporal wavelet and Fourier analysis when the frequency of temporal carrier is selected. First, the phase change of each point on the object should be in one direction; secondly, both methods are limited by the Nyquist sampling theorem. Analyzing signals with a frequency higher than half of the acquisition rate is impossible. Because of this, selecting a suitable temporal carrier frequency to the image acquisition process, as mentioned above, is not easy. The temporal frequency due to deformation depends on two parameters: frequency and amplitude of the vibration. The temporal carrier frequency should be high enough so that the phase change of each point on the object is in one direction. However, it cannot be too high due to the limitation of Nyquist sampling theorem. This is because the phase change at certain points equals the sum of the temporal carrier and displacement. This is sometimes not easy to compromise when the capturing rate of the camera is not high enough.

5.3.2 Phase scanning method

Although phase scanning method has limitation on eliminating the noise effect, its simple algorithm still gains applications in vibration measurement when the fringe patterns are of good quality. In this section, it is applied with two optical techniques: fringe projection and shadow moiré.

5.3.2.1 Results of fringe projection technique

Figure 4.4 shows the experimental setup of the fringe projection technique. The test specimen is a coin loaded by a shaker. Figure 5.38(a) shows an initial image of the test object before fringe projection. A small area of interest containing 256×256

pixels is shown in Fig. 5.38(b). The coefficient k_F in Eq. (2.1) is calibrated as 0.8692

mm/rad. The test object is subjected to a triangular wave with a frequency of

approximately 6 Hz.   Fringe patterns are recorded at intervals of 0.004 s with a

camera recording rate of 250 fps. Figure 5.38(c) shows typical fringe patterns

captured by the high-speed CCD camera at different instants. Five hundred images

can be captured during a two-second period and the first 90 consecutive images are

processed. Within these 90 images, 4 images representing extreme positions of

vibration are identified; subsequently, the direction of vibration are determined. The

extreme positions are readily identified since the first derivative of intensity ($\dfrac{\partial I}{\partial t}$)

changes sign (either from negative to positive or vice versa).

For each pixel, 90 data points along the time axis are obtained. Figure 3.18(a)

shows the gray value variation of point A_5 [indicated in Fig. 5.38(b)]. The extreme

positions of vibration are indicated as shown in Fig. 3.18(a). The wrapped phase

values are presented in Fig. 3.18(b). After unwrapping along the time-axis, the

continuous phase profile, as shown in Fig. 3.18(c), can be obtained. The frequency of

vibration is evaluated as 5.68 Hz, and the amplitude of phase change A_ϕ is 13.12 rad

and the corresponding amplitude of the vibration is calculated as 11.40 mm. Figure

5.39 shows the gray value variation, wrapped phase map and continuous phase profile

of point B_5 [indicated in Fig. 5.38(b)], when the specimen is vibrated sinusoidally

with a frequency of 4.55 Hz and an amplitude of 13.02 mm.

From Figs. 3.18(a) and 5.39(a), it can be observed that the maximum and

minimum values of each cycle of phase variation (2π change) are slightly different.

This is due to the fluctuation of the LCD panel and intensity of the projector light

source. Relatively large errors in the phase profile also occur when the gray value

approaches the extreme values. The errors are introduced by: (1) the maximum or minimum values detected by the camera are slightly different from the actual extreme gray scale values; (2) for a sine-wave configuration, a slight change in gray level near the extreme values causes a large change in the phase value. The errors can be minimized by proper selection of the recording rate and frequency of the carrier fringe so that the number of sampling points is optimized within one cycle of gray level change. In this study, it is found that 10 to 16 frames per cycle produce the best results.

At a certain instant, a combination of phase values on each pixel produces a spatial wrapped phase map as shown in Fig. 5.40(a). After unwrapping, a continuous phase map, which represents the surface profile, can be obtained. Figure 5.40(b) shows a continuous phase map of the object. Using the calibrated coefficient k_F, the phase map can be converted into a 3-D surface profile as shown in Fig. 5.40(c). Some vertical stripes are observed on the phase map; these are due to the errors introduced by the extreme values of gray level mentioned above. In spatial coordinates, these errors can be reduced by applying a filtering mask on the phase map. In this application, a 3×3 median mask is used.

To verify the accuracy of the proposed method, a comparison is made with the carrier-based fast Fourier transform (FFT) and conventional four-step phase shifting methods. Four fringe patterns with a phase increment of $\pi/2$ are projected onto a stationary test coin using the same experimental setup. For each fringe pattern, an averaged image is obtained from 500 images. Four of such images are subsequently used in the 4-step phase shifting algorithm, while one of the images is used for the FFT method. Figures 5.41(a)-(c) show respectively the phase maps obtained by the phase scanning, FFT and phase shifting methods. As the phase evaluation is carried

out point-by-point along the time-axis, the phase scanning method is best suited to determination of a surface with a complicated profile. As can be seen, the result from the phase scanning method [Fig. 5.41(a)] shows a better image quality than the FFT method [Fig. 5.41(b)], especially at the top half of the image. The results from the phase shifting method [Fig. 5.41(c)] show similar image quality with the phase scanning method. However, as mentioned above, images for the phase shifting method are obtained on a stationary object. Figure 5.42 shows a comparison of the phase profile on cross-section C_5-C_5 [indicated in Fig. 5.38(b)] between the phase scanning and phase shifting methods. It is seen that the phase profiles obtained by the two methods agree well. The maximum discrepancy between the two methods is 0.012 rad, which denotes a height difference of 0.01 mm.

5.3.2.2 Results of shadow moiré technique

Similar results are obtained using shadow moiré technique. The basic setup of shadow moiré is shown in Fig. 4.5, while the specimen and loading device are presented in Fig. 4.6. Figure 5.43(a) shows the initial test object without grating in front. The radius r_{sp}, height h_{sp} and base radius r_b of the spherical cap are respectively 14.5 mm, 4 mm and 10 mm as shown in Fig. 5.43(b). The frequency of the grating is 2 lines/mm. The distance d_S and l_S (shown in Fig. 2.3) are measured as 195 mm and 335 mm, respectively. As the grating is placed very close to the object, the assumption of $l_S >> h_S(x, y)$ is valid. The test object is subjected to a sinusoidal vibration with a frequency of approximately 6 Hz. Fringe patterns are captured at intervals of 0.004s with a camera recording rate of 250 fps. Figures 5.44(a) and 5.44(b) show two typical fringe patterns recorded by a high-speed CCD camera at different

instants. In order to identify whether the surface is convex or concave, a carrier fringe is introduced by rotating the grating with a small angle in the x-z plane. The first one hundred consecutive images are processed. A 5×5 mean mask is used to remove the high-frequency grating lines and random noise on the images. Figures 5.44(c) and 5.44(d) show typical fringe patterns after filtering. The images representing the extreme positions of vibration are identified using a similar procedure as the fringe projection method.

For each pixel, 100 data points along the time axis are obtained. Figure 5.45(a) shows the gray value variation of point A_6 [indicated in Fig. 5.43(a)]. The wrapped phase values are shown in Fig. 5.45(b). After unwrapping along the time-axis, a continuous phase profile, as shown in Fig. 5.45(c), can be obtained. The displacement of point A_6 along the z-axis can be retrieved using Eq. (5.4). In this experiment, the displacements of other points on the object are the same as Point A_6 as no other loads are applied on the object. From Fig. 5.45(c), the frequency of vibration is evaluated as 5.95 Hz, and the amplitude of phase change is 11.52 rad. The corresponding amplitude is calculated as 1.60 mm. At a certain instant, the combination of phase values on each pixel produces a spatial wrapped phase map as shown in Fig. 5.46(a). After unwrapping a continuous phase map, which is proportional to the surface profile, can be obtained. Figure 5.46(b) shows a continuous phase map of the object surface, and the corresponding 3-D surface profile as shown in Fig. 5.46(c).

To verify the accuracy of the proposed method, a comparison is carried out with the mechanical stylus method. Figure 5.47 shows a comparison of the profile on cross section B_6-B_6 [indicated in Fig. 5.43(a)]. The average discrepancy is 3.1%. It is to be noted that errors are introduced when smooth filtering is applied to remove high

frequency grating lines. Similar to the fringe projection method mentioned above, relatively large errors in the profile measurement also occur when the gray levels are in the vicinity of the extreme values.

A further application of the phase scanning method on a vibrating coin using the shadow moiré method is also included in appendix B. In the experiments of shadow moiré and fringe projection, a coin with continuous movement was selected as a test object several times in the project to verify the accuracy of transient profile retrieval in different temporal phase analysis methods. The main reasons of the selection are as follows: (1) during the vibration or continuous movement, the profile of coin at any instant keeps the same. So the accuracy of transient profile obtained by temporal optical methods can be verified by other independent methods, such as mechanical stylus method; (2) the maximum unevenness of the coin is around 100 μm. Generally, the profile at this range can only be precisely retrieved by using phase shifting algorithm in shadow moiré and fringe projection techniques, when an area of 10 mm $\times$ 10 mm is measured in one image (256 pixel $\times$ 256 pixel). From the comparison in Fig. 5.41, it can be observed that the result from two-dimensional FFT is not good enough. As we know, phase shifting technique needs several fringe patterns at one status, and it is very difficult to apply it in the dynamic behavior study. However, using proposed temporal phase analysis algorithm, a precise contour of a vibrating or continuously-moving coin can be retrieved. The contour map obtained has a similar quality as the phase shifting method, which demonstrates the superiority of the proposed methods.

It is worth noting that in all experiments presented in this thesis, the loading was not synchronized with image capturing. Any instant can be selected as a reference

as only the relative displacement is concerned. Regarding to the transient surface

contouring, it is a unique value that is not related to the reference.
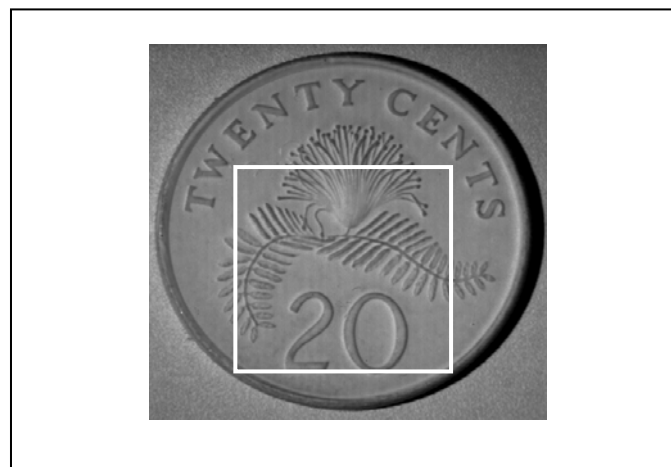
(a)
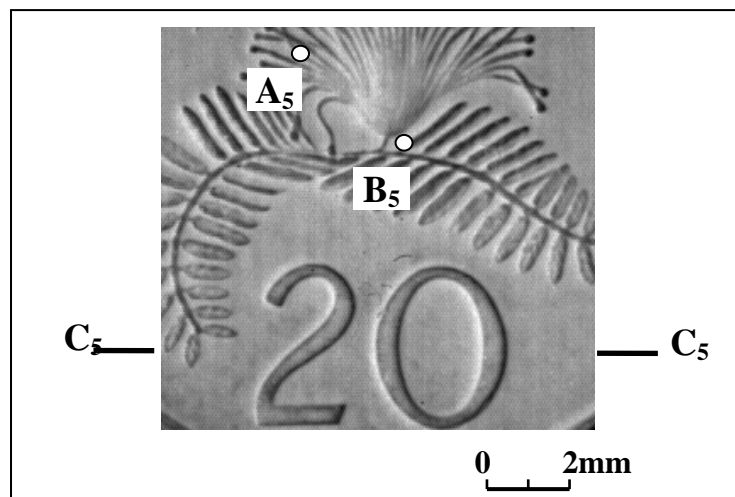
(b)
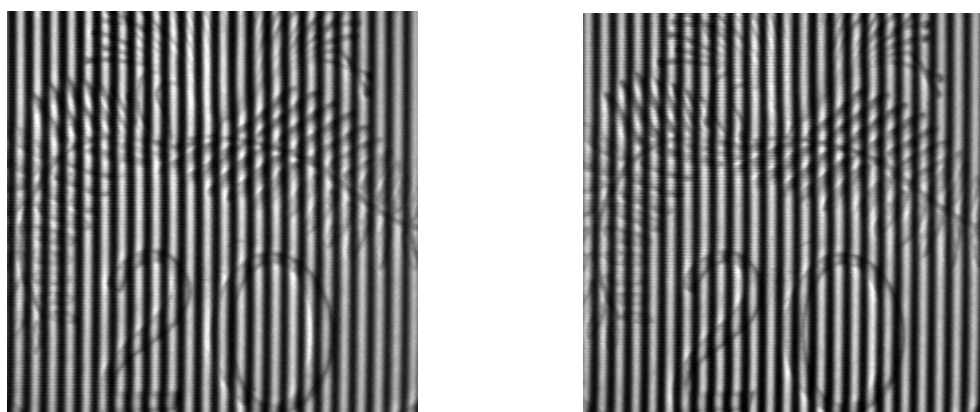
(c)

Figure 5.38 (a) a 20-cent coin specimen; (b) area of interest (c) typical sinusoidal
fringe patterns captured at two different instants: 0s and 0.02s.
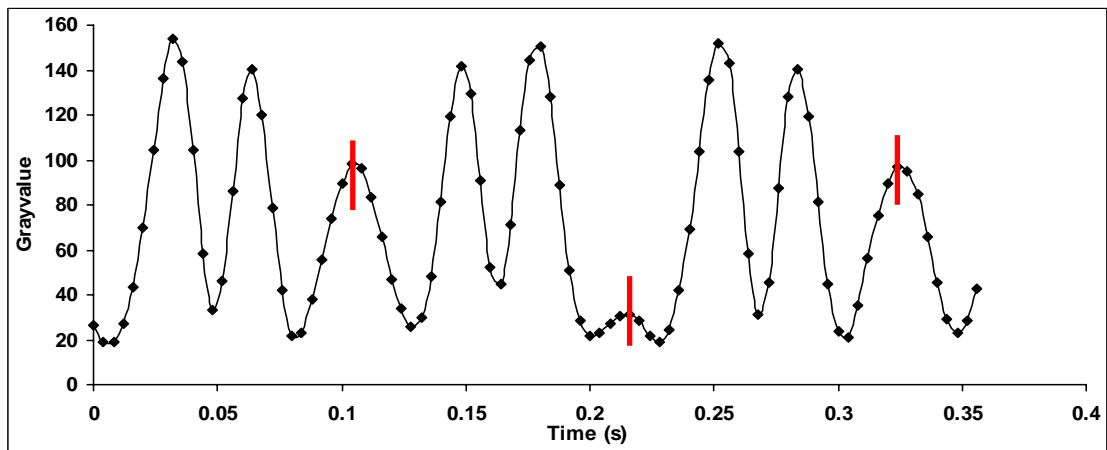
(a)
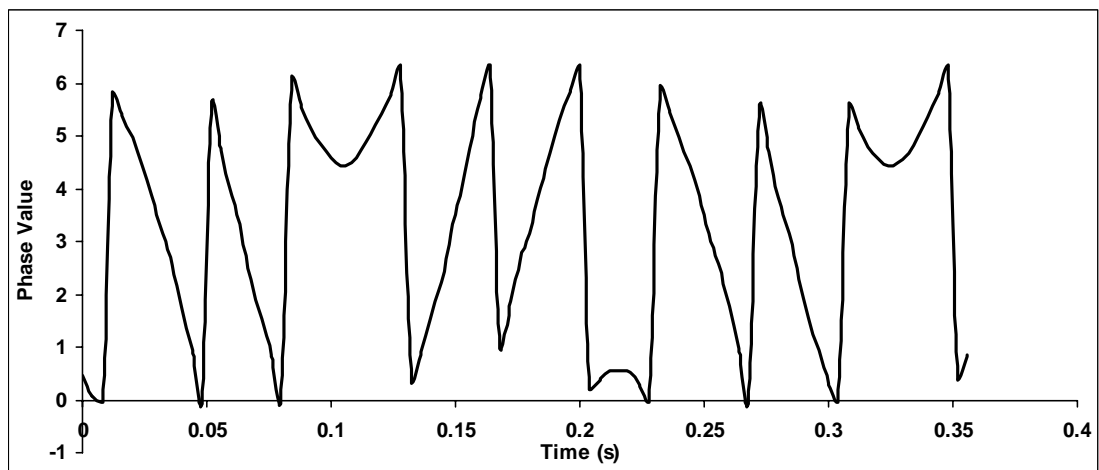
(b)
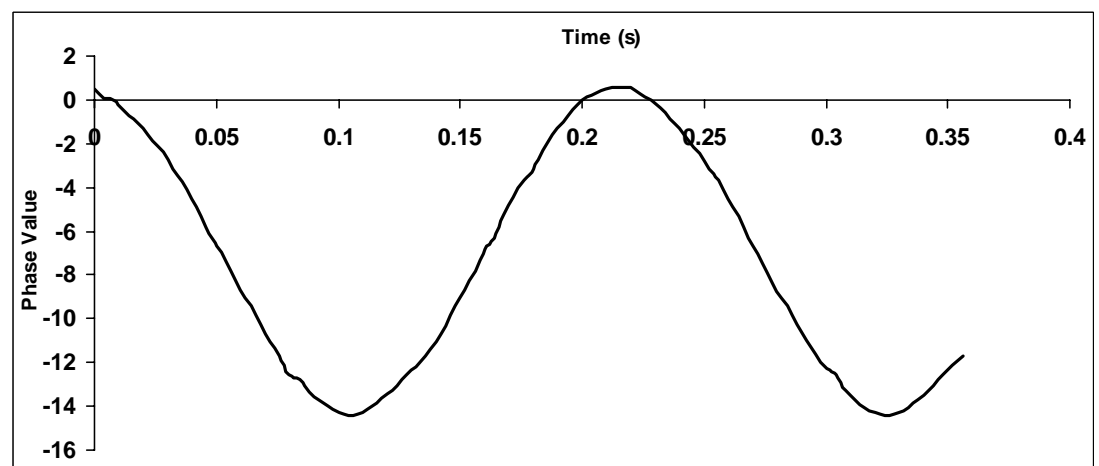
(c)

Figure 5.39   (a) Gray value variation of point B_5; (b) wrapped phase value of point B_5 and (c) continuous phase profile after unwrapping (point B_5).

(a)

(b)

(c)
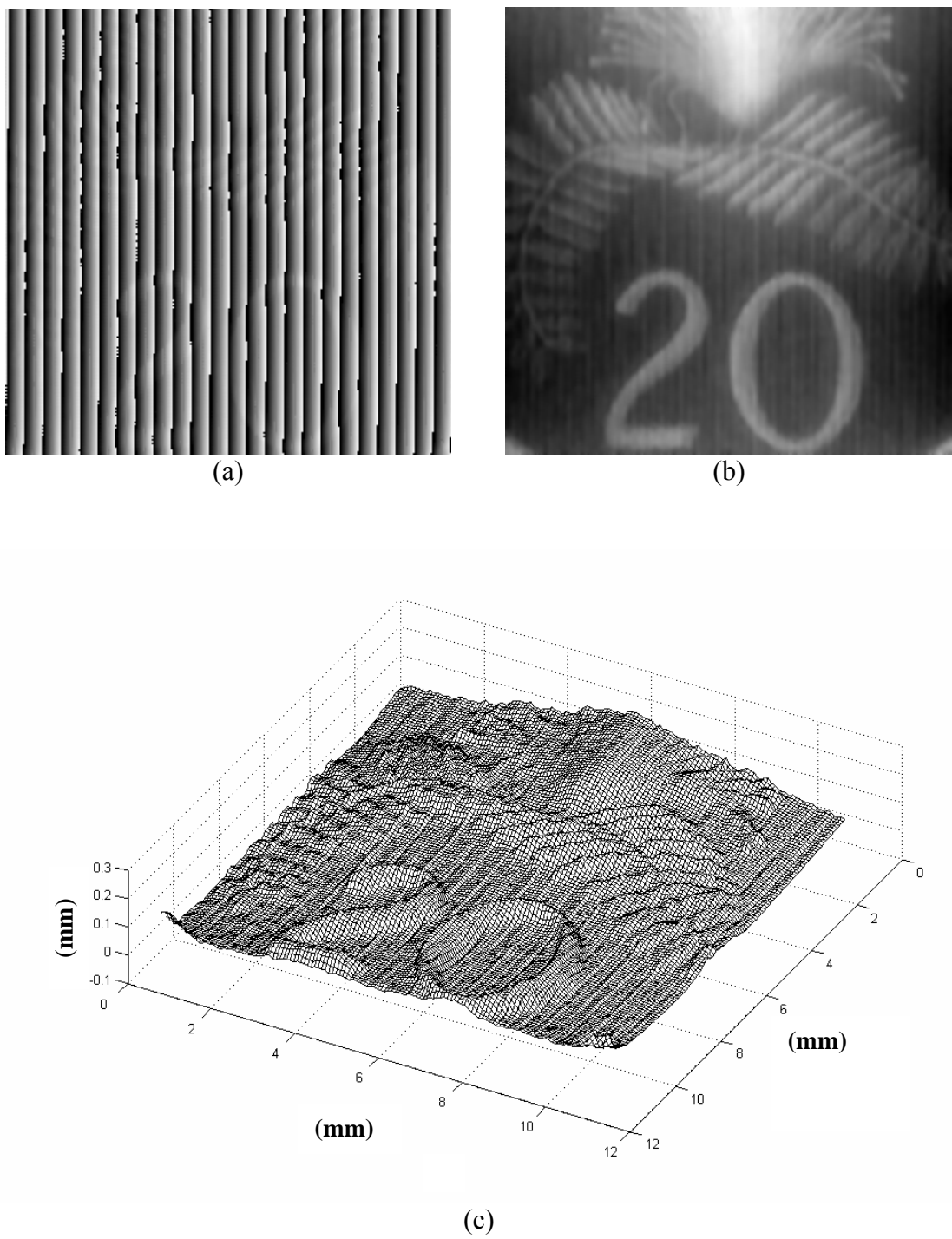
Figure 5.40 (a) Wrapped phase in spatial coordinate at 0.12s
(b) continuous phase map obtained by phase scanning method
(c) corresponding 3-D plot of surface profile

(a)

(b)

(c)

Figure 5.41 A comparison of phase maps obtained by (a) phase scanning method (b) fast Fourier transform with carrier fringe method (c) 4-step phase shifting method.
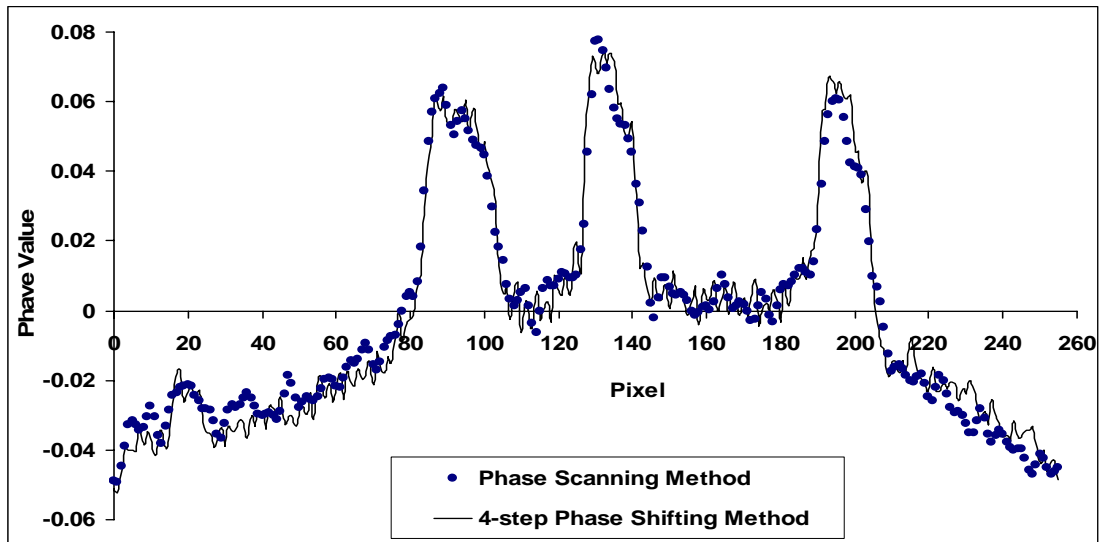
Figure 5.42 A comparison of phase profile between phase scanning and 4-step phase shifting methods on cross-section C_5-C_5

(a)

(b)
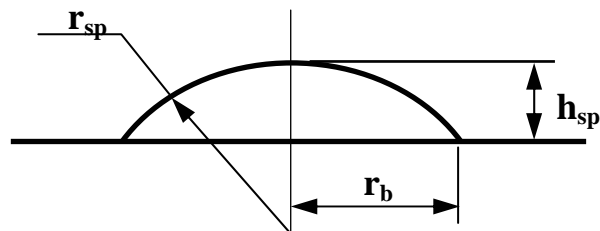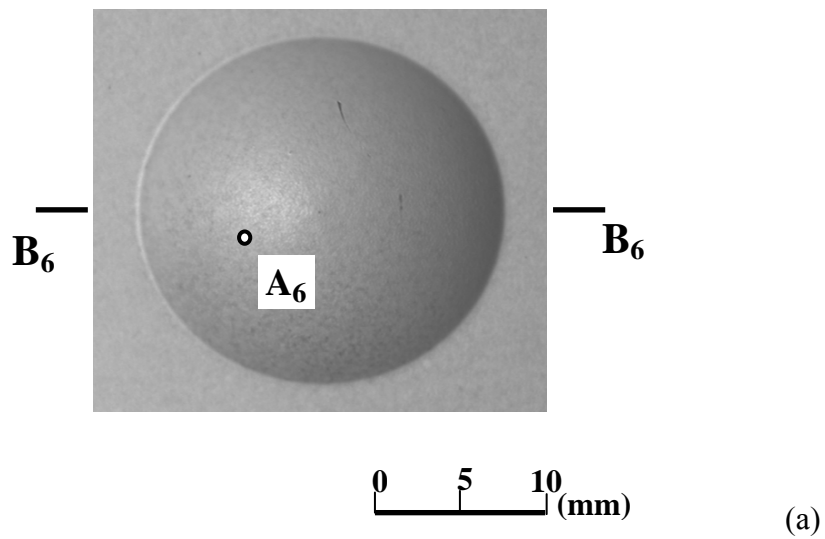
Figure 5.43   Specimen: (a) a spherical cap and (b) its dimensions.

(a)   (b)

(c)   (d)
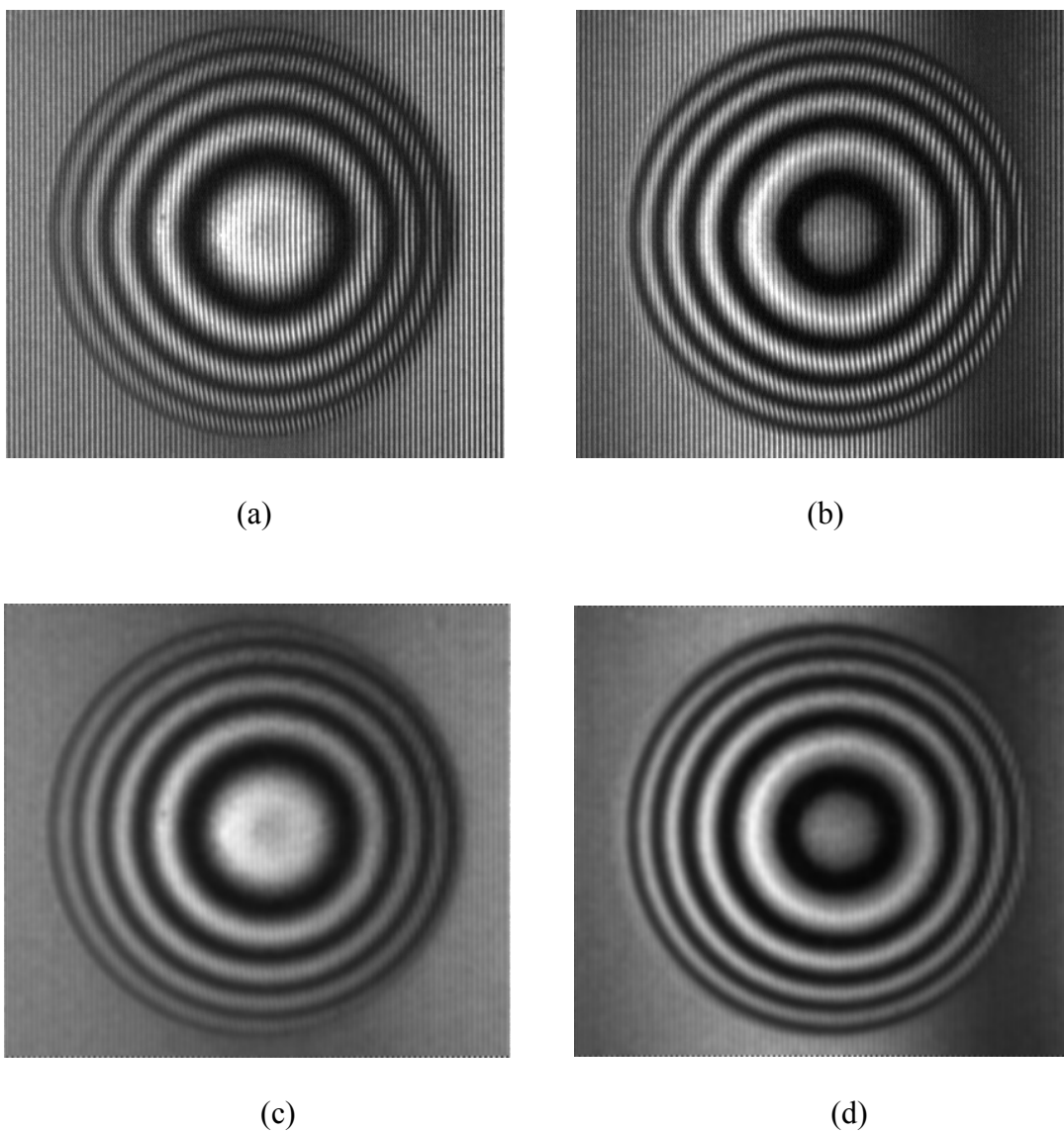
Figure 5.44 Typical moiré fringe patterns of spherical cap captured at different instants (a) 0s (before filtering); (b) 0.092s (before filtering); (c) 0s (after filtering); (d) 0.092s (after filtering).
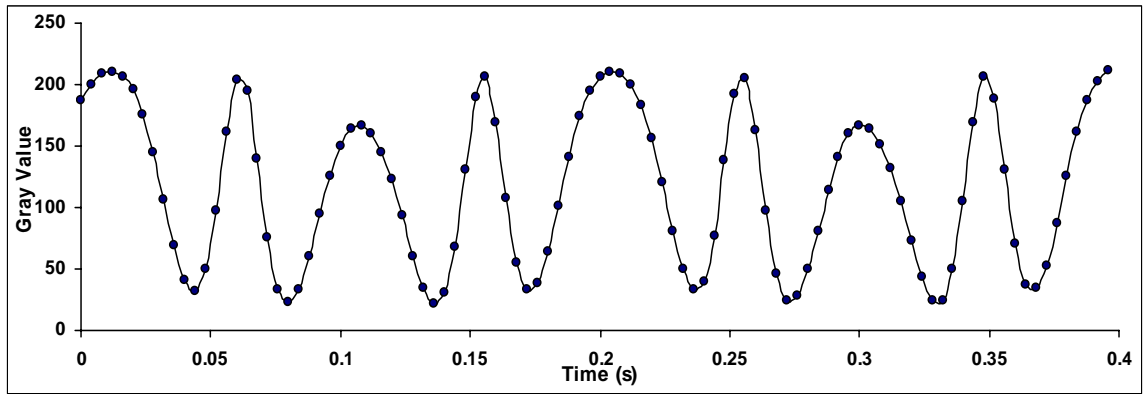
(a)
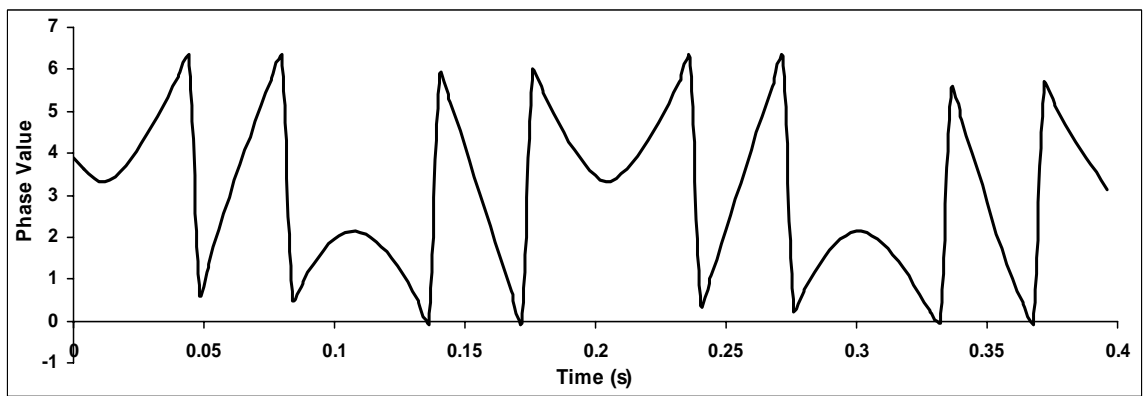
(b)
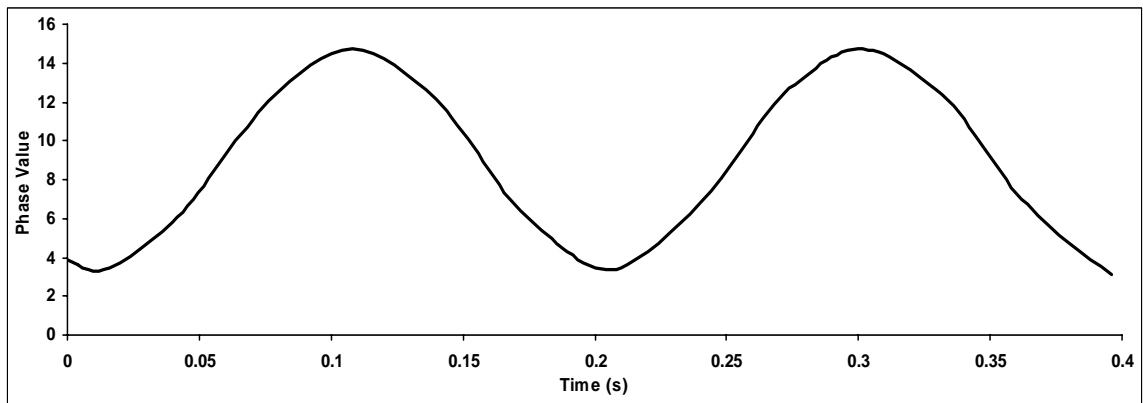
(c)

Figure 5.45 (a) Gray value variation of point A_6; (b) wrapped phase value of point A_6; (c) continuous phase profile after unwrapping (point A_6).

(a)   (b)

(c)
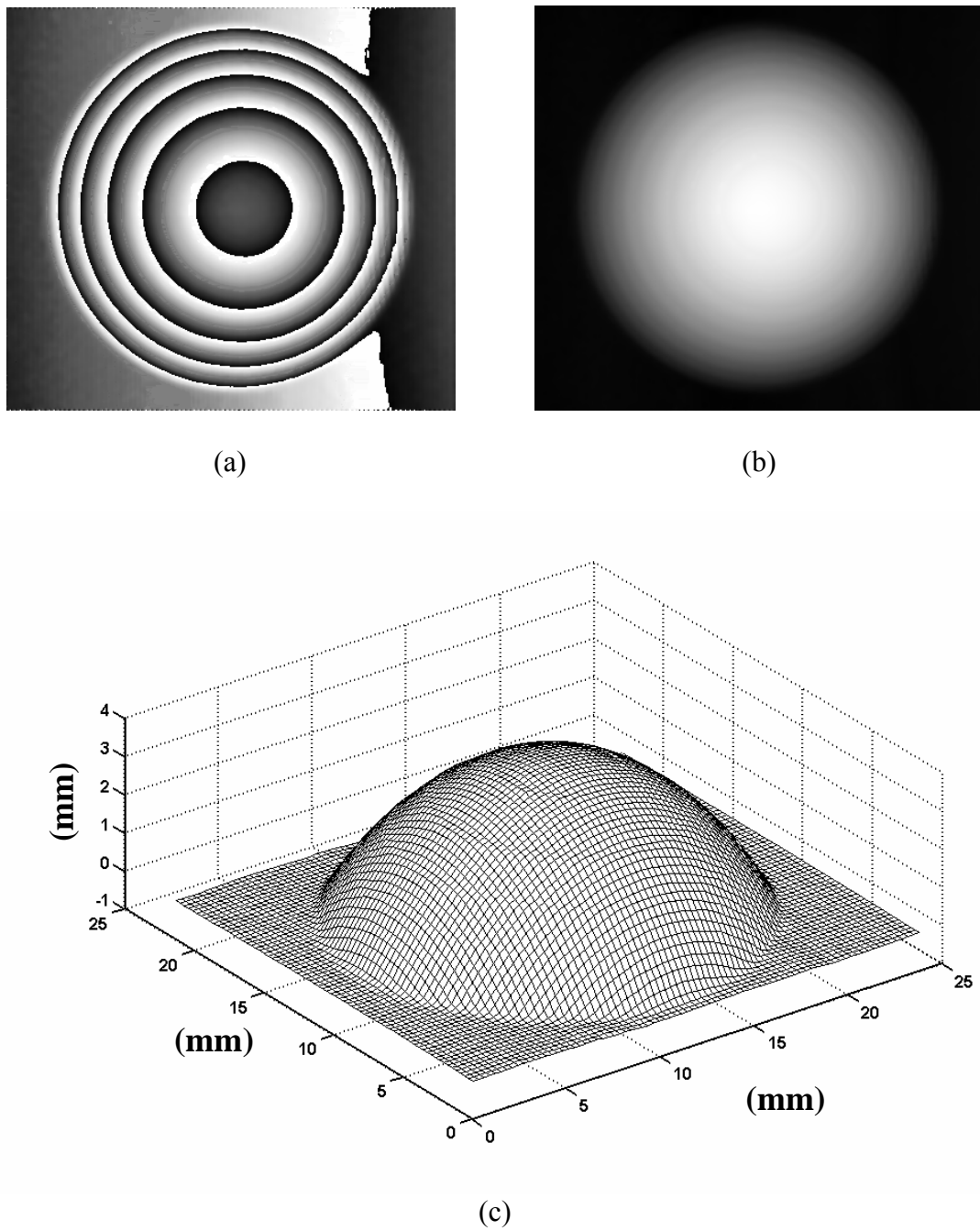
Figure 5.46 (a) Wrapped phase in spatial coordinate at 0.092s; (b) continuous phase map obtained by phase scanning method; (c) corresponding reconstructed 3-D plot of surface profile.
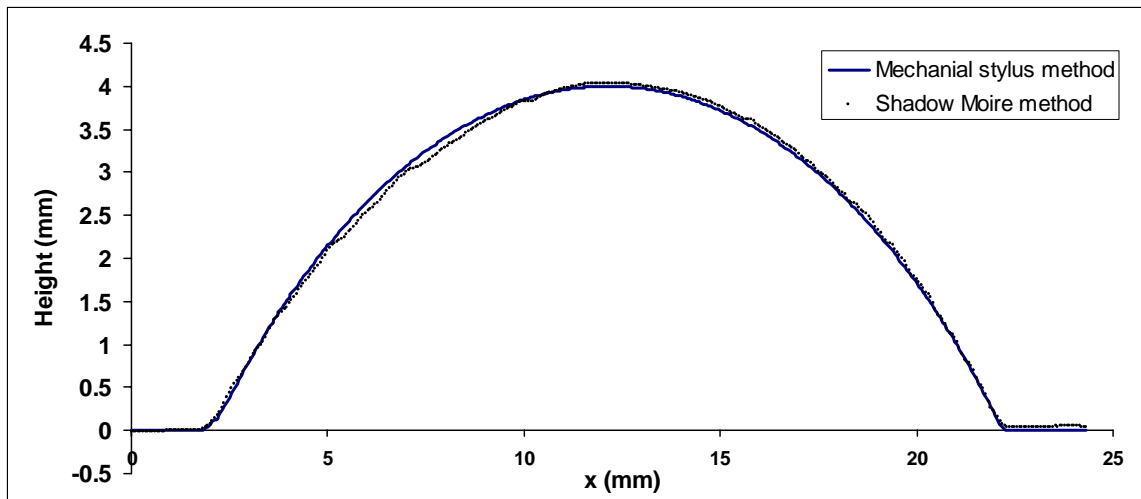
Figure 5.47 A comparison of surface profile on cross-section B_6-B_6 between phase scanning and mechanical stylus methods

5.4 Displacement derivatives measurement

There is another type of phase ambiguity problem when digital shearography is applied to measure the first derivative of the continuous displacement on a plate. Although the plate is deformed in one direction, the phase change at different areas of the plate is in opposite directions. In addition, there are zero-phase-change areas on the plate. In this case, introducing temporal carrier is the only method to solve this problem. The carrier frequency should be high enough so that the phase changes at all points are in one direction.

The schematic layout of digital shearography for displacement derivative measurement with temporal carrier is shown in Fig. 4.13. The temporal carrier is generated by shifting Mirror M2 in modified Michelson interferometer with a PZT stage. A series of speckle patterns are captured by a high-speed CCD camera with a telecentric lens during the deformation. The intensity of each pixel can be expressed as

$$I_{xy}(t) = I_{0xy}(t) + A_{xy}(t)\cos[\varphi_{xy}(t)] = I_{0xy}(t) + A_{xy}(t)\cos[\phi_C(t) + \phi_{xy}(t)]$$

$$= I_{0xy}(t)\left\{1 + V\cos\left[\phi_{0_{xy}} + 2\pi f_C t + \frac{4\pi \dfrac{\partial w_{xy}(t)}{\partial x}\delta x}{\lambda}\right]\right\}, \tag{5.8}$$

where $I_{0xy}(t)$ is the intensity bias of the speckle pattern, V is the visibility, ϕ_{0xy} is the initial random phase, f_C is the temporal carrier frequency, $\phi_C(t) = 2\pi f_C t$ is the phase change due to temporal carrier, $\delta x = 3mm$ is the amount of image shearing in the x-direction, and $w_{xy}(t)$ is the out-of-plane deformation of the object. Figure 5.48 shows the typical shearography fringes of the test specimen with the reference block at an instant $T = 1.5s$, which is obtained by subtraction of two speckle patterns.
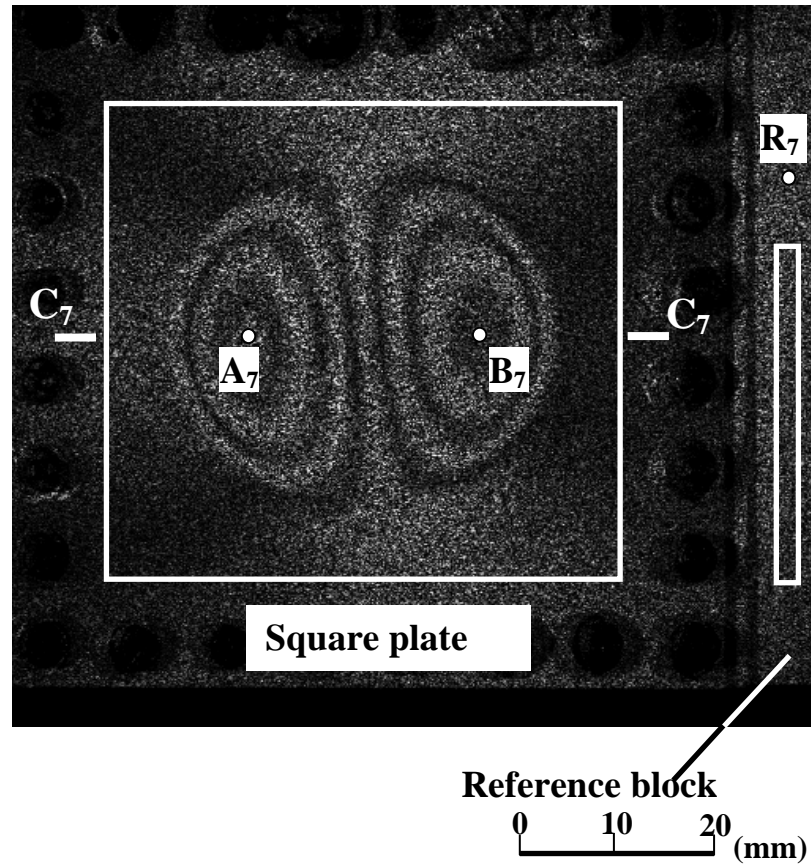
Figure 5.48 Typical shearography fringe pattern on a reference block and a plate with area of interest

Five hundred and forty images are recorded within 9 seconds, and first three hundred speckle patterns are processed pixel-by-pixel along the time axis. The interested area on the plate (shown in Fig. 5.48) contains 330×330 pixels with the actual dimension of 56.3mm $\times$ 56.3mm. For each pixel, 300 sampling points along the time axis were obtained. Figure 5.49(a) shows the intensity variation of point R_7 (indicated in Fig. 5.48) on the reference block. The modulus of the Morlet wavelet transform of intensity variation of points R_7 is shown in Fig. 5.49(b). The dashed line shows the ridge of the wavelet transform where the maximum modulus are found. Although the a_{rb} on the ridge is fairly constant, some variation of a_{rb} due to noise on certain pixel are still observed. To eliminate the noise effect, an average value of a_{rb} was calculated in an area of 20×200 pixels (shown in Fig. 5.48) on reference block. Figure 5.49(c) shows the averaged scaling a_{rb} on the ridge. As the reference block is not moving, the ridge value represents the effect of temporal carrier, which was applied on mirror M2 by a PZT stage. Little variation of averaged a_{rb} is observed, which implies the temporal carrier is constant along time axis. Integration of $\dfrac{2\pi}{a_{rb}}$ was carried out along the time axis to generate a continuous phase change $\Delta\phi_C(t)$ due to temporal carrier.

Figures 5.50 show the intensity variations and the modulus of the Morlet wavelet transform on points A_7 and B_7 (indicated in Fig. 5.48). It can be observed that the frequency of intensity variation of point R_7 is higher than that of point B_7, but lower than that of point A_7, which implies that the phase changes at these two points are of opposite sign. Similar to point R_7, integration was carried out on each pixel to generate a temporal phase change $\Delta\varphi_{xy}(t) = \Delta\phi_C(t) + \Delta\phi_{xy}(t)$. Figure 5.51(a) shows

the temporal phase change obtained on points A_7 and B_7 and the averaged phase change on reference block. Subtracting the phase change $\Delta\phi_C(t)$ due to temporal carrier, the absolute phase change $\Delta\phi_{xy}(t)$ can be obtained on each pixel. Figure 5.51(b) shows the absolute phase change on points A_7 and B_7. Combining the phase change of each point at certain instant, a high-quality spatial distribution of phase change is obtained. Figure 5.52(a) shows the 3-D plot of phase variation obtained by temporal wavelet analysis at $T = 3s$. Figure 5.53(a) shows the phase variation on cross-section C-C (shown in Fig.5.48).

For comparison, temporal Fourier analysis was also applied on the same speckle patterns. On a reference block part, a narrow bandpass filter was applied as the spectrum of the signal was concentrated. On the plate, a relatively wider filter was applied as it should include all frequencies at different pixels. A one-dimensional phase unwrapping was then applied along the time axis, as all phase value retrieved by inverse Fourier transform fall within a $[0, 2\pi)$ range. Figure 5.52(b) shows the 3-D plot of phase variation obtained by temporal Fourier analysis at $T = 3s$. Figure 5.53(b) shows the phase variation on cross-section C_7-C_7 obtained by Fourier analysis. Similar as temporal wavelet analysis, a 3×3 median filter was also applied on phase maps. However, large errors are still found at some pixels, especially in the area where the phase changes are of high positive values. In these areas, the phase change measured is the sum of temporal carrier and object. The frequency of signal is high so that it overlaps with some noise frequencies. Fourier transform shows lack of flexibility when the signal frequency is extracted from noise. From Fig. 5.53 it can be observed that CWT generates a much smoother spatial phase distribution at different instants compared to a Fourier transform.
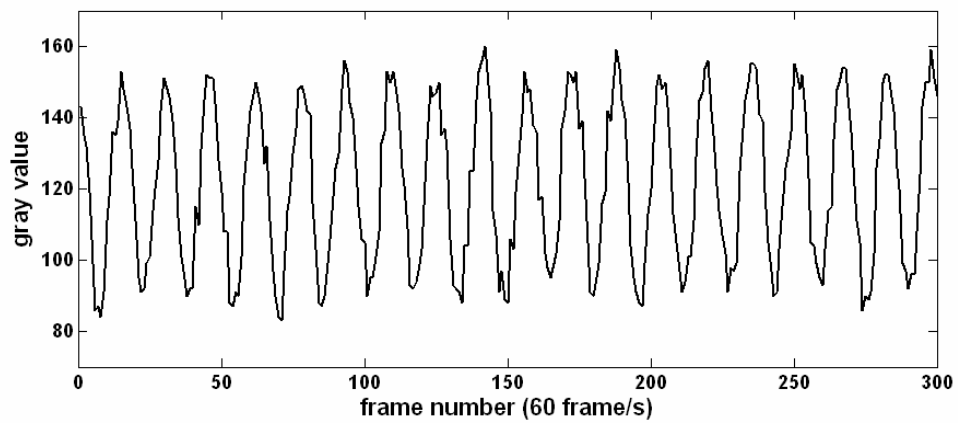
(a)
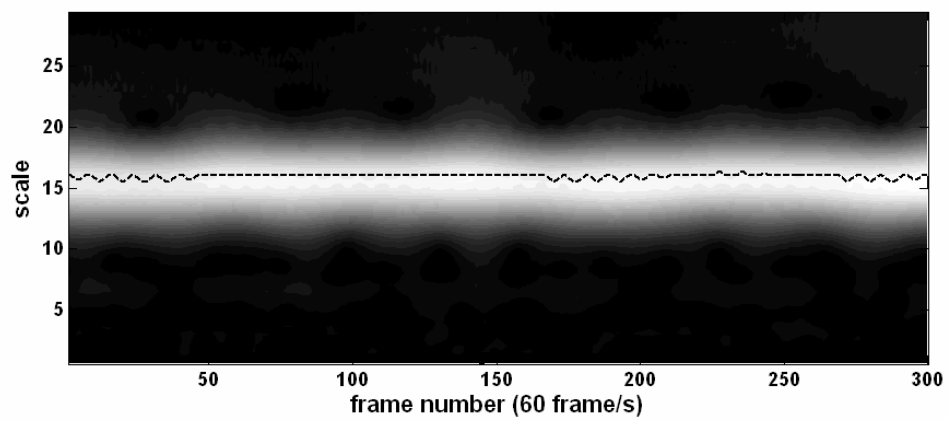
(b)
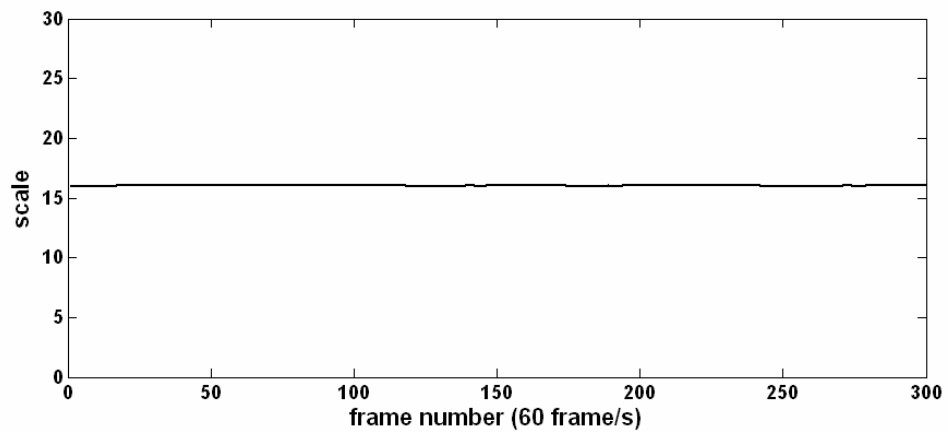
(c)

Figure 5.49 (a) Temporal intensity variation of point R_7 on a reference block. (b) plot of modulus of Morlet wavelet transform at point R_7; (c) averaged ridge detected on a reference block.

(a)

(b)

(c)

(d)
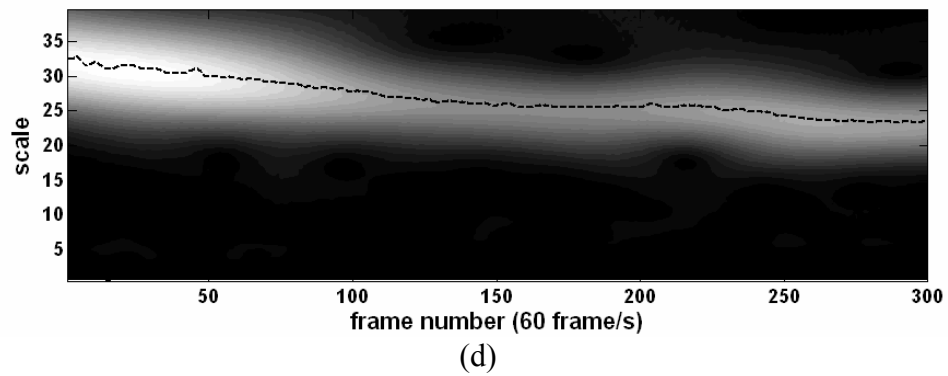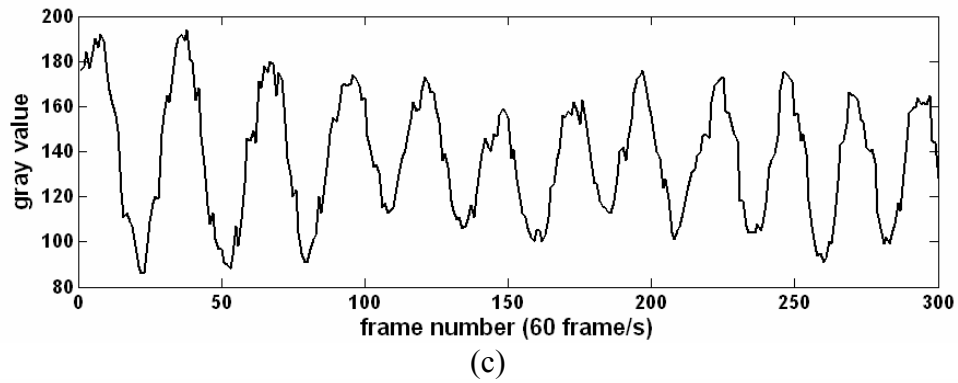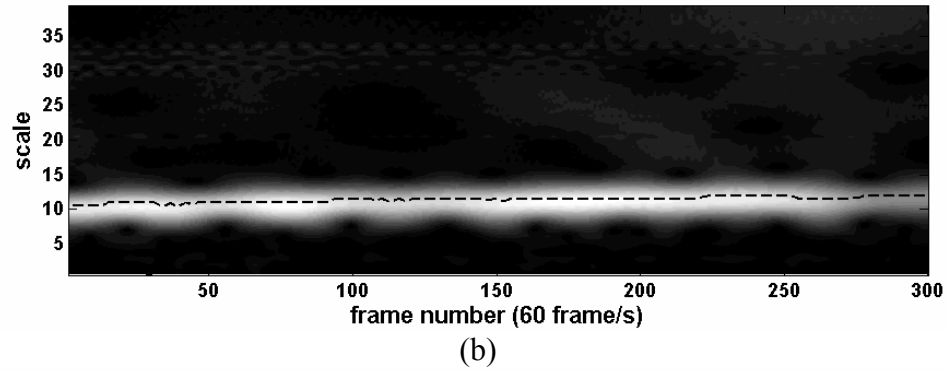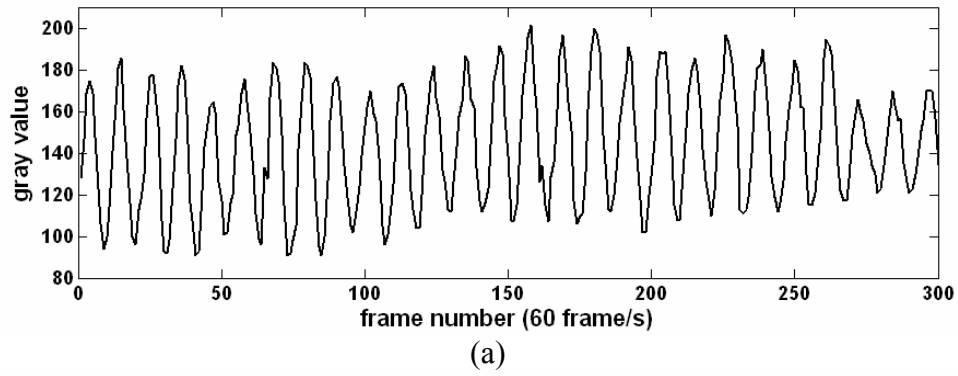
Figure 5.50 (a) Temporal intensity variation of point A_7 on the plate;
(b) modulus of Morlet wavelet transform at point A_7;
(c) Temporal intensity variation of point B_7 on the plate;
(d) modulus of Morlet wavelet transform at point B_7.
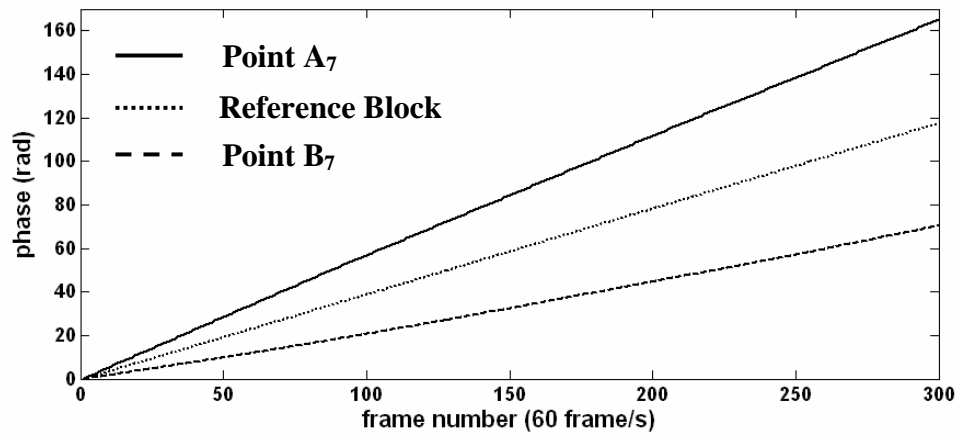
(a)
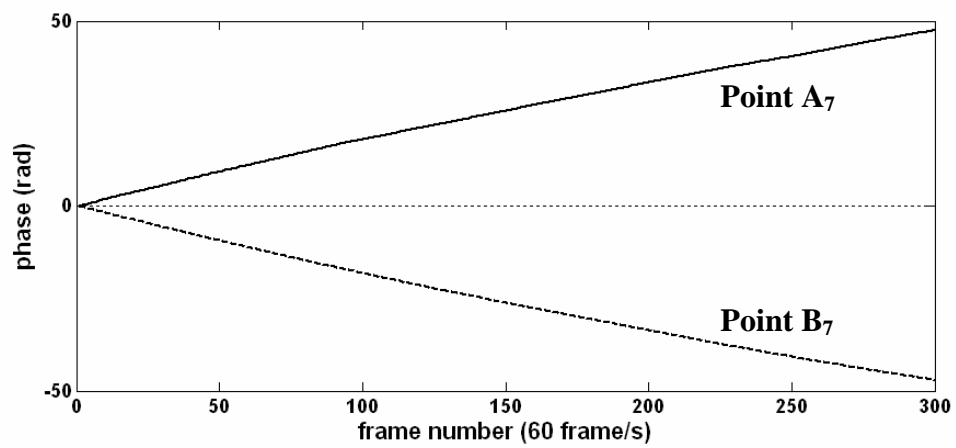
(b)

Figure 5.51 (a) Phase variation on a reference block and point A_7 and B_7;
(b) Absolute phase variation on point A_7 and B_7 after carrier removal.
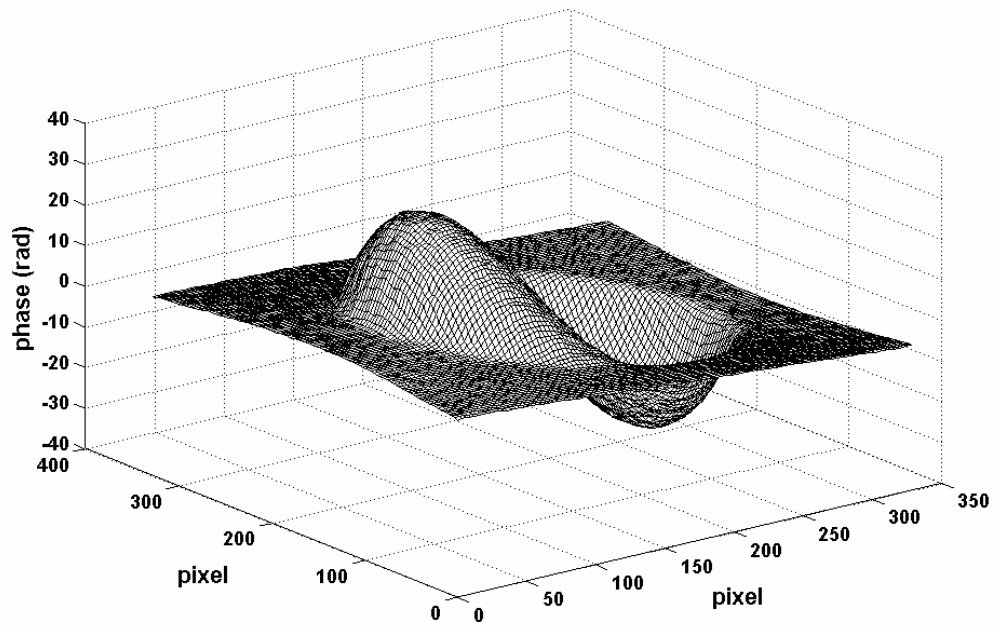
(a)
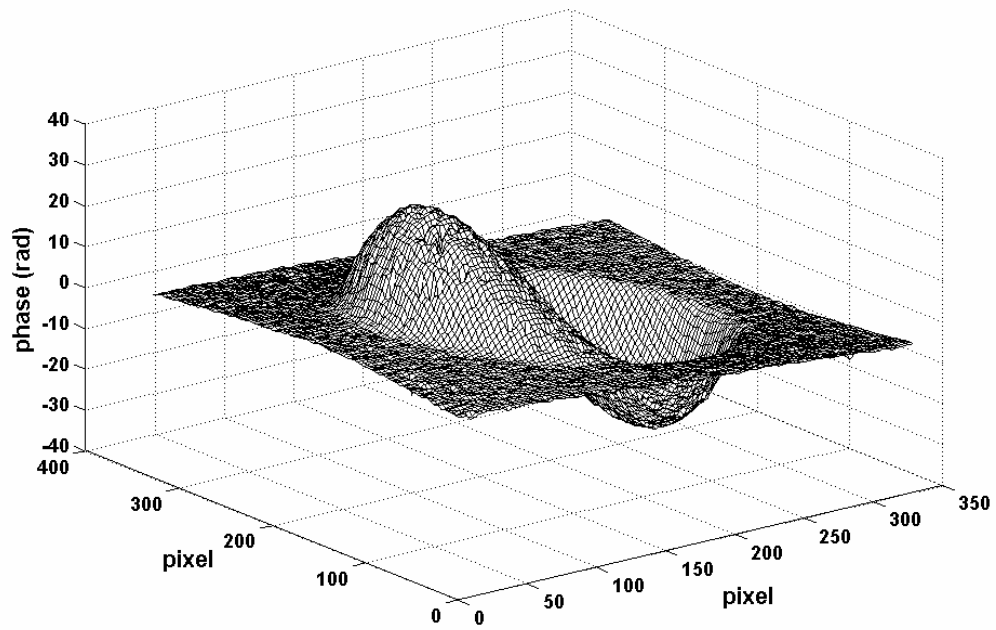
(b)

Figure 5.52 3D plot of spatial phase variation at $T = 3s$ obtained by (a) wavelet
transform and (b) Fourier transform.
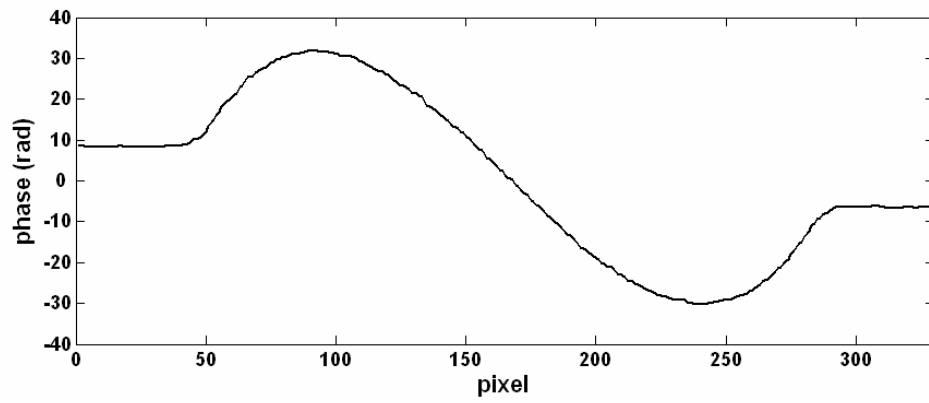
(a)
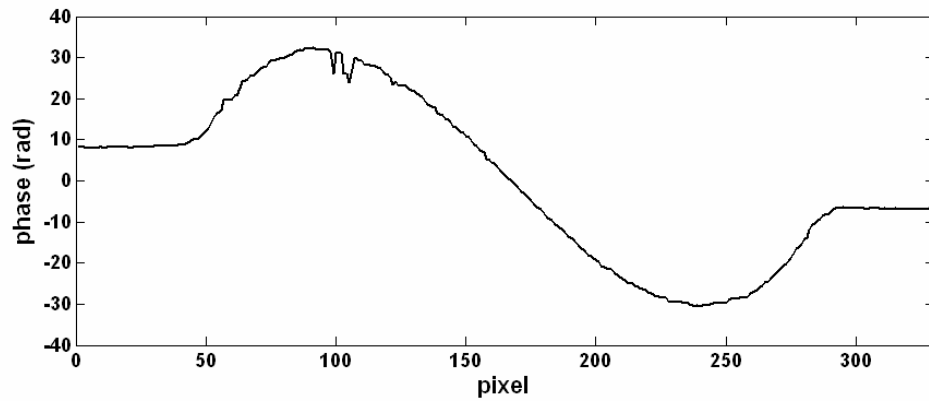
(b)

Figure 5.53 Phase variation on cross section C_7-C_7 at $T = 3s$ obtained by (a) wavelet transform and (b) Fourier transform.

Similar experiment was executed when the image shearing is in y- direction. Figure 5.54(a) shows a phase map representing instantaneous value of $\dfrac{\partial w}{\partial y}$ obtained by continuous Morlet wavelet transform. In the field of engineering, the curvature and twist measurements of plates are more important, because the stresses experienced by the plates are related the to second-order derivatives of displacement (Chau and Zhou, 2003).

Due to the high quality of the transient phase map obtained by temporal wavelet analysis, it is possible to perform a numerical differentiation process spatially. However, numerical differentiation process between two adjacent sampling points is very vulnerable to errors which are magnified during the process and results with acceptable accuracy are rarely obtained.

In this project, another CWT, Haar wavelet transform, is applied spatially as a differentiation operator to obtain the transient curvature and twist. The Haar function is the simplest wavelet, and a flexible differentiation operator

$$\psi(t) = \begin{cases} 1, & if\ 0 \le t < 1/2 \\ -1 & if\ 1/2 \le t < 1 \\ 0 & otherwise \end{cases} \tag{5.9}$$

The wavelet coefficient obtained is the negative value of derivative of the signal. Different scaling factors a can be selected according to the extent of the noise. The discussion on Haar wavelet as a differentiation operator is given in Appendix C. Some preliminary results are presented here. In this application, scaling factor a is selected as twenty and the continuous Haar wavelet transform is applied line by line in the y- and x- direction on the phase map. The wavelet coefficients obtained represent the curvature $\dfrac{\partial^2 w}{\partial y^2}$ and the twist $\dfrac{\partial^2 w}{\partial x \partial y}$. Figure 5.54(b) and (c) show the phase distribution representing the transient curvature and twist obtained.
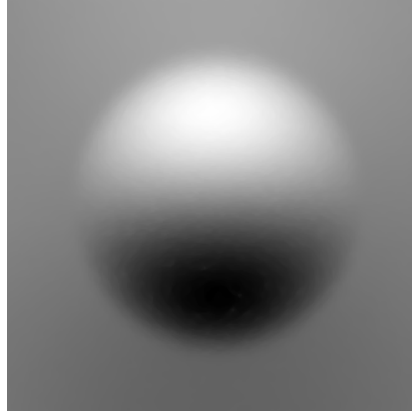
(a)
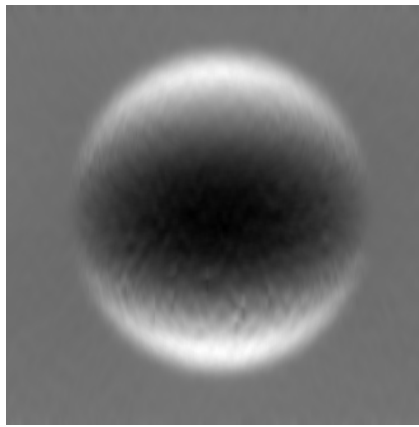
(b)
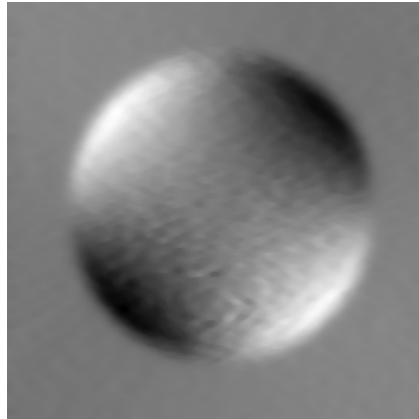
(c)

Fig. 5.54(a) Spatial phase distribution representing $\dfrac{\partial w}{\partial y}$ obtained by continuous Morlet wavelet transform and the phase distribution representing (b) $\dfrac{\partial^2 w}{\partial y^2}$ and (c) $\dfrac{\partial^2 w}{\partial x \partial y}$ after continuous Haar wavelet transform.

CHAPTER SIX

CONCLUSIONS AND FUTURE WORK

6.1 Conclusions

As mentioned in Chapter one, there are four main objectives to be achieved in this project. Two existing temporal phase analysis techniques are first studied. Fourier analysis with the temporal phase unwrapping is the most popular method and is widely used with different optical techniques in various static and dynamic applications. It is a fast algorithm and has filtering process in frequency spectrum so that the noise effects can be eliminated. However, if the phase change on each pixel is nonlinear and the spectrums of pixels are different, automatically selecting a proper bandpass filtering window becomes difficult. In this thesis, the temporal Fourier analysis is generally applied in different applications to generate results for comparison. Another algorithm is the phase scanning method, which retrieves phase values directly from intensity variation. This method has its limitations on noise elimination, as there is no filtering process in the frequency domain. However, its simple algorithm is suitable for less noisy fringe patterns obtained by methods such as the fringe projection and moiré. Furthermore, it is more suitable for measurement on a vibrating object when the extreme positions of the vibration can be identified. The method is applied to fringe projection and shadow moiré to extract the transient surface profile from a vibrating object and it was observed that the results are better than that of the carrier-based spatial Fourier transform.

To overcome the problems encountered in temporal phase analysis mentioned above, a new technique based on continuous wavelet transform has been proposed. One of the important characteristics of wavelet transform is that the instantaneous frequency of a processed signal can be extracted through the ridge of a wavelet coefficient. This characteristic is very useful in eliminating noise effect as it is able to separate the signal and noise frequencies at any instant. An analytic wavelet is normally used for the analysis of phase-related properties of a real function. A complex Morlet wavelet is selected as the mother wavelet as it provides the smallest Heisenberg box. The selection of a central frequency ω_0 is emphasized. It should be large enough to satisfy the admissibility condition of a wavelet transform. Larger values of ω_0 provide better resolution in the frequency domain and are more powerful in extracting the phase from a noisy signal. However, larger ω_0 values also result in lower resolution in the time domain. When the frequency of a signal varies, large errors are generated when a higher central frequency is selected. In this project, as the dynamic behavior of the objects is of more concern, the central frequency is selected as $\omega_0 = 2\pi$. Then the phase change of the intensity variation on each pixel can be retrieved by extracting the 'ridge' of the wavelet coefficient.

Another problem involved in temporal phase analysis techniques is the phase ambiguity. Due to this limitation, the temporal phase analysis can only be applied on objects that deform in one direction. In this project, this problem is avoided by introducing a temporal carrier during the capturing process when a vibrating object is measured. The phase value extracted on each pixel is the combination of the effects from the deformation and the temporal carrier. Subsequently, the temporal carrier is removed and the absolute displacement of a vibrating object is obtained. However, it

is noteworthy that the proper selection of the temporal carrier frequency depends on the evaluation of the frequency range due to displacement, and the limitation of Nyquist sampling theorem has to be considered as well.

Several applications are emphasized using the proposed temporal wavelet transform together with two existing algorithms. They are profiling of a surface with a step change using shadow moiré; instantaneous velocity and deformation measurement on a continuously deforming object using shadow moiré and ESPI; vibration measurement using temporal carrier with ESPI, and displacement derivatives measurement using temporal carrier digital shearography. The phase scanning method is also applied on the measurement of a vibrating object when the extreme position of the vibration can be identified. From a comparison between wavelet transform and Fourier transform, it is observed that wavelet transform provides better results, especially in the processing of speckle patterns. In ESPI, the maximum displacement fluctuation due to noise is limited to 0.02 µm using wavelet transform, while the fluctuation is normally large than 0.06 µm using temporal Fourier transform. The more accurate results obtained using wavelet transform require longer processing time. The computation time is about 10 times larger than that of temporal Fourier transform. However, this limitation becomes insignificant with rapid development in computing speed.

The results obtained also indicate that the accuracy of temporal Fourier transform relies on a proper selection of a filtering window, while the temporal wavelet transform can be 'standardized' and is more suitable for an automatic process without human intervention. In addition, temporal wavelet analysis is more powerful in eliminating the noise effect and produces more accurate results. With the rapid

development in computer capacity, wavelet transform will thus gain more acceptances in optical measurements.

The contributions of this project are highlighted as follows:

Wavelet is still a new algorithm for phase extraction from interferograms. Although it has been applied in spatial domain by other researchers to extract the phase from fringe patterns with carrier, it can only process the high-quality fringe patterns obtained by fringe projection or moiré. Due to the random spatial noise in speckle interferometry, either Fourier or wavelet is not as effective when they are applied spatially to a fringe pattern.

The main contribution of this project is the development of a new temporal phase analysis approach based on time-frequency analysis and wavelet transform. The outcome is a robust technique that permits processing of a series of interferograms and reconstructing the temporal phase evolution precisely. This is the first time that wavelet has been studied and applied to temporal phase analysis, and generally the results from wavelet analysis are much better than those from Fourier analysis and have equivalent quality as the phase-shifting method.

The second contribution is the introduction of a temporal carrier in dynamic problems so that the phase ambiguity problem can be avoided in temporal phase analysis techniques by the use of a high speed camera.

Lastly, the combination of the two techniques mentioned above results in a more complete and robust processing method which can be applied to a much broader area in engineering. This important extension can particularly benefit researchers and engineers who are carrying out research in time varying behavior, for example, continuous warpage of a PCB board under thermal loading, crack propagation, instantaneous shape, displacement and velocity of a vibrating objects, etc.

Furthermore, the proposed temporal wavelet method is more suitable as an automatic process without human intervention.

A list of publications arising from this research work is included in Appendix D.

6.2 Future work

The wavelet transform proposed in this work has demonstrated a high potential for the processing of a sequence of images. A complex Morlet wavelet is selected as the mother wavelet because of its phase properties. Although the effects of some parameters have been discussed in this thesis, more explorations such as system analysis of errors in wavelet transform for different types of signals, warrant further investigations. Furthermore, although complex Morlet wavelet is proved to be have the highest overall resolution in time and frequency domain, it is appropriate to look at other possible choices of mother wavelets. Some might provide more efficient algorithms or more robustness for signal processing. One can also think of the endless possibilities of combining different types of wavelet analysis for different physical quantity measurements. A good example is shown in this thesis. Haar wavelet has been applied spatially on the transient phase maps obtained by temporal wavelet analysis. Instantaneous curvature and twist of a continuously-deforming plate are obtained. It shows the possibilities for measurement of transient stress changes experienced in a plate.

At present, phase analysis techniques are used either in spatial or temporal domains. Generally, analyses in spatial domain are applied to two-dimensional problems, while analyses in temporal domain are applied to one-dimensional

problems. However, in many cases, the algorithms will be more robust if we consider them in the temporal-spatial plane, or a combination of techniques in both domains. For example, the temporal phase evolution of neighboring pixels can be combined in a weighted average using measured interferogram modulation as weights. The result is that the phase of some ill-behaved pixels can be interpolated from their neighbors when its modulation is too low to permit a successful temporal phase extraction. This is normally essential in speckle interferometry.

More applications with different optical techniques, such as continuous in-plane displacement measurement using moiré interferometry or ESPI, can be explored. The temporal carrier technique can also be possibly applied to fringe projection and projection moiré for vibration measurement. Further exploration of different temporal phase analysis techniques will broaden the applications in optical, non-destructive testing area and offer more accurate results and bring forward a wealth of possible research directions. Hopefully, the results of such investigations, through improved robustness of processing algorithms, should increase the applicability of whole-field interferometric methods outside of the controlled laboratory environment.

REFERENCES

1. Abbate, A., C. M. DeCusatis and P. K. Das. Wavelets and Subbands: Fundamental and Applications. Boston, Birkhauser, 2001.

2. Afifi, M., A. Fassi-Fihri, M. Marjane, K. Nassim, M. Sidki, S. Rachafi. Paul wavelet-based algorithm for optical phase distribution evaluation. Opt. Communi. 211 pp47-51. (2002).

3. Arai, Y. S. Yokozeki and T. Yamada. Fringe-scanning method using a general function for shadow moiré. Appl Opt. **34**(22). pp4877-4882. 1995.

4. Asundi, A. and J. Wang. Strain contouring using Gabor filters: principle and algorithm. Opt. Eng. 41(6). pp1400-1405. 2002.

5. Berger, E. W. V. D. Linden, V. Dose, M. W. Ruprecht and A. W. Koch. Approach for the evaluation of speckle deformation measurements by application of the wavelet transformation. Appl. Opt. 36(29). pp7455-7460. 1997.

6. Bone, D. J. Fourier fringe analysis: the Two-dimensional phase unwrapping problem. Appl Opt. 30(25). pp3627-3632. 1991.

7. Brown, G. M. Dynamic computer aided video holometry, in Laser Interferometry Quantitative Analysis of Interferograms: Third in a Series, ed by R. J. Pryputniewicz, Proc. SPIE 1162, pp36-45. 1989.

8. Chau, F. S. and J. Zhou, Direct measurement of curvature and twist of plates using digital shearography. Opt. Laser Eng. 39. pp431-440. 2003.

9. Chen, F., G. M .Brown and M. Song. Overview of three-dimensional shape measurement using optical methods. Opt. Eng. 39(1). pp10-22. 2000.

10. Cherbuliez, M., P. Jacquot and X. Colonna de Lega, Wavelet processing of interferometric signal and fringe patterns. Proc. SPIE, **3813**, pp692-702. 1999.

11. Cherbuliez, M. and P. Jacquot, Phase computation through wavelet analysis: yesterday and nowadays. Fringe 2001, W. Osten and W. Juptner Ed. pp154-162, Elsevier, Paris, 2001.

12. Cherbuliez, M. Wavelet analysis of interference patterns and signals: development of fast and efficient processing techniques. Theses n° 2377, Swiss Federal Institute of Technology Lausanne, 2001.

13. Chui, C. K. An introduction to wavelets. Academic Press, 1992.

14. Cloud, G. L. Optical Methods of Engineering Analysis, Cambridge University Press, 1995.

15. Colonna de Lega, X. Continuous deformation measurement using dynamic phase-shifting and wavelet transform. in Applied Optics and Optoeletronics 1996. K. T. V. Grattan, Ed. Institute of Physics Publishing, Bristol. pp261-267. 1996.

16. Colonna de Lega, X. Processing of non-stationary interference patterns: Adapted phase shifting algorithms and wavelet analysis. Application to dynamic deformation measurements by holographic and speckle interferometry. PhD Theses n° 1666, Swiss Federal Institute of Technology Lausanne, 1997.

17. Creath, K., K. M. Crennell and K. J. Gasvik Interferogram Analysis: Digital Fringe Pattern Measurement Techniques" Bristol, Philadelphia. Institute of Physics, 1993.

18. Daubechies, I. Ten lectures on wavelets. Society for industrial and applied mathematics. Philadelphia 1992.

19. Delprat, N., B. Escudie, P. Guillemain, R. Kronland-Martinet, P. Tchamitchian and B. Torresani, Asymptotic wavelet and Gabor analysis: extraction of instantaneous frequencies. IEEE Transactions on Information Theory. 38(2). pp644-664. 1992.

20. Dureli, A. J. and V. J .Parks. Moiré analysis of strain. Prentice-Hall, Englewood Cliffs, NJ. 1970.

21. Dursun, A., N. ECEVIT and S Ozder. Application of wavelet and Fourier transform for the determination of phase and three-dimensional profile. IJCI Proceedings of International Conference on Signal Processing. ISSN 1304-2386. 1(2). pp168-172. 2003.

22. Engelhardt, K. and G. Haausler. Acquisition of 3D data by focus sensing. Appl. Opt. 27. pp4684-4689. 1988.

23. Fang, J., C. Y. Xiong, H. H. Li, M. Li and J. Zhang. Wavelet transform based digital image processing of photomechanics. Third International Conference on Experimental Mechanics. X. Wu, Y. Qin, J. Fang and J. Ke ed. Proc. SPIE 4537. pp53-58. 2001.

24. Fang, J., C. Y. Xiong and Z. L. Zhang. Digital transform processing of carrier fringe patterns from speckle-shearing interferometry. J. Mod. Opt. 48. pp507-520. 2001.

25. Farrant, D. I., G. H. Kaufmann, J. N. Petzing, J. R. Tyrer, B. F. Oreb, and D. Kerr. Measurement of transient deformations with dual-pulse addition electronic speckle pattern interferometry. Appl. Opt. 37, pp7259-7267. 1998.

26. Federico, A. and G. H. Kaufmann. Phase retrieval in electronic speckle pattern interferometry using the continuous wavelet transform. Proc. SPIE 4419. pp162-165. 2001.

27. Federico, A. and G. H. Kaufmann. Comparative study of wavelet thresholding methods for denoising electronic speckle pattern interferometry fringes. Opt. Eng. 40(11). pp2598-2604. 2001.

28. Federico, A. and G. H. Kaufmann. Evaluation of the continuous wavelet transform method for phase measurement in digital speckle pattern interferometry. Proc. SPIE 4777. pp279-287, 2002.

29. Federico, A. and G. H. Kaufmann. Evaluation of the continuous wavelet transform method for phase measurement of electronic speckle pattern interferometry fringes. Opt. Eng. 41(12). pp3209-3216. 2002.

30. Fernandez, A., J. Blanco-Garcia, A. F. Doval, J. Bugarin, B. V. Dorrio, C. Lopez, J. M. Alen, M. Lopez-Amor and J. L. Fernandez, "Transient deformation measurement by double pulsed-subtraction TV holography and the Fourier transform method. Appl. Opt. 37, 3440-3446. 1998.

31. Flynn, T. J. Two-dimensional phase unwrapping with minimum weighted discontinuity. J. Opt. Soc. Am. A. 14(10). pp2692-2701. 1997.

32. Fujimoto, J. Determination of the vibrating phase by a time-averaged shadow moiré method. Appl. Opt. 21(23). pp4373-4376. 1982.

33. Gartner, H., P. Lehle, and H. J. Tiziani. New, high efficient binary codes for structured light methods. Proc. SPIE 2599. pp4-13. 1995.

34. Ghiglia, D. C., G. A. Mastin and L. A. Romero. Cellular-automata method for phase unwrapping. J. Opt. Soc. Am. A. 4. pp267-280 (1987).

35. Ghiglia, D. C. and M. D. Pritt. Two-dimensional phase unwrapping. John Wiley & Sons, Inc. 1998.

36. Guild, J. The interference systems of crossed diffraction gratings. Clarendon Press, Oxford, 1956.

37. Guild, J. Diffraction gratings as measuring scales. Oxford University Press, London. 1960.

38. Guillemain, P. and R. Kronland-Martinet. Characterization of acoustic signals through continuous linear time-frequency representations. Proc. IEEE. 84(4). pp561-585. 1996.

39. Hovanesian, J. D., Y. Y. Hung and L. Wang. A time-average scanning moiré technique for vibration studies. Proceedings of the Society for Experimental Stress Analysis, Spring Meeting, Dearborn, Michigan, pp209-212, 1981.

40. Huang, T. S. (ed). Picture processing and digital filtering. New York : Springer-Verlag, 1975.

41. Hung Y. Y., C. Y. Liang, J. D. Hovanesian and A. J. Durelli. Time-averaged shadow-moire method for studying vibrations. Appl Opt. 16(6), pp1717-1719. 1977.

42. Hung, Y. Y., C. Y. Liang, A. J. Durelli and J. D. Hovanesian. A shadow-moiré method with continuously variable sensitivity. Mech. Res. Comm. 4(3). pp157-162. 1977.

43. Hung, Y. Y. and A. J. Durelli. Simultaneous measurement of three displacement-derivatives using a multiple image shearing interferometric camera. Journal of Strain Analysis 14(3). pp81-88. 1979.

44. Hung, Y. Y. Shearography: a new optical method for strain measurement and nondestructive testing. Opt Eng. 21(3). pp391-395. 1982.

45. Hung, Y. Y. Shearography: a novel and practical approach for nondestructive testing. Journal of Nondestructive Testing. 8(2). Pp55-67. 1989.

46. Hung, Y. Y., W. D. Luo, Y. B. Zhang and H. M. Shang. Surface profilometry using projected fringe grating with continuously varying pitch. Proceeding of 2002 SEM Annual Conference on Experimental and Applied Mechanics, pp 284-287, June 10-12, Milwaukee, Wisconsin, 2002.

47. Huntley, J. M. and H. O. Saldner. Temporal phase-unwrapping algorithm for automated interferogram analysis. Appl Opt. 32. pp3047-3052. 1993.

48. Huntley, J. M. and H. O. Saldner. Shape measurement temporal phase unwrapping: comparison of unwrapping algorithms. Measurement Science & Technology. 8(9), pp986-992. 1997.

49. Huntley, J. M., G. H. Kaufmann and D. Kerr. Phase-shifted dynamic speckle pattern interferometry at 1kHz. Appl Opt. 38(31). pp6556-6563. 1999.

50. Jin, L. H., Y. Kodera, T. Yoshizawa and Y. Otani. Shadow moiré profilometry using the phase shifting method. Opt. Eng. 39(8). pp2119-2123. 2000.

51. Jin, L. H. Y. Otani and T. Yoshizawa. Shadow moiré profilometry by frequency sweeping. Opt Eng. 40(7). pp1383-1386. 2001.

52. Joenathan, C., B. Franze, P. Haible and H. J. Tiziani. Speckle interferometry with temporal phase evaluation for measuring large-object deformation. Appl. Opt. 37(13). pp2608-2614. 1998.

53. Joenathan, C., B. Franze, P. Haible and H. J. Tiziani. Large in-plane displacement measurement in dual-beam speckle interferometry using temporal phase measurement. J. Mod. Opt. 45(9). pp1975-1984. 1998.

54. Joenathan, C., B. Franze, P. Haible and H. J. Tiziani. Novel temporal Fourier transform speckle pattern shearing interferometer. Opt. Eng. 37(6). pp1790-1795. 1998.

55. Judge, T. R. and P. J. Bryanston-Cross. A Review of phase unwrapping techniques in fringe analysis. Opt. Laser Eng. 21(4). pp199-239. 1994.

56. Just, D., N. Adam, M. Schwabisch and R. Bamler. Comparison of phase unwrapping algorithms for SAR interferograms. Proc. of the 1995 International Geoscience and Remote sensing symposium. Firenze, Italy. July 10-14. 1995. IEEE. Piscataway, NJ.pp767-769. 1995.

57. Kadooka, K. K. Kunoo, N. Uda, K. Ono and T. Nagayasu. Strain analysis for moiré interferometry using the two-dimensional continuous wavelet transform. Expt. Mech. 43(1). pp45-51. 2003.

58. Kallmeyer, F., S. Krueger, G. Wernicke, H. Gruber, N. Demoli, W. Osten and D. Kayser. Optical processing for the detection of faults in interferometric patterns. Proc. SPIE. 4777. pp371-380. 2002.

59. Kaufmann, G. H. and G. E. Galizzi. Speckle noise reduction in television holography fringes using wavelet thresholding. Opt. Eng. 35. pp5-14. 1996.

60. Kaufmann, G. H., A. Davila and D. Kerr. Speckle noise reduction in TV holography. Proc. SPIE 2730. pp96-100. 1996.

61. Kayser, D., W. Osten, S. Kruger and G. Wernicke. Application of wavelet filters for feature extraction in interferometric fringe patterns. Proc. SPIE 3744. pp270-278, 1999.

62. Kong, I. B. and S. W. Kim. General algorithm of phase-shifting interferometry by iterative least-squares fitting. Opt. Eng. 34. pp183-187. 1995.

63. Kruger, S. G. Wernicke, W. Osten, D. Kayser, N. Demoli and H. Gruber. Fault detection and feature analysis interferometer fringe patterns by the application of wavelet filters in convolution processors. Proc. SPIE 3966. pp145-153. 2000.

64. Kruger, S. G. Wernicke, W. Osten, D. Kayser, N. Demoli and H. Gruber. The application of wavelet filters in convolution processors for the automatic detection of faults in fringe pattern systems. In the 4th International Workshop on Automatic Processing of Fringe Patterns, Fringe 2001, W. Osten and W. Juptner eds. pp193-198, 2001.

65. Kumar, R., I. P. Singh and C. Shakher. Measurement of out-of-plane static and dynamic deformations by processing digital speckle pattern interferometry fringes using wavelet transform. Opt. Lasers Eng. 41. pp81-93. 2004.

66. Kuwamura, S. and I. Yamaguchi. Wavelength scanning profilometry for real-time surface shape measurement. Appl. Opt. 36(19). pp4473-4481. 1997.

67. Li, X., G. Tao, and Y. Yang. Continual deformation analysis with scanning phase method and time sequence phase method in temporal speckle pattern interferometry. Opt. & Laser Tech. 33. pp53-59. 2001.

68. Ligtenberg, F. K. The moiré method. Proc. Soc. Exp. Stress Anal. (SESA), 12(2), pp83-98. 1955.

69. Liu, H, A. C. Cartwright and C. Basaran. Moiré interferogram phase extraction: a ridge detection algorithm for continous wavelet transforms. Appl. Opt. 43(4). pp850-857. 2004.

70. Liu, H, A. C. Cartwright and C. Basaran. Experimental verification of improvement of phase shifting moiré interferometry using wavelet-based image processing. Opt. Eng. 43(5). pp1206-1214. 2004.

71. Luo, W. D. Temporal phase measurement techniques with applications to dynamics deformation measurement, surface profilometry and strain determination. PhD Thesis, Oakland University, 2001.

72. Mallat, S. A wavelet tour of signal processing. Academic Press. San Diego. 1998.

73. Mauvoisin, G., F. Bremand and A. Lagarde. Three-dimensional shape reconstruction by phase-shifting shadow moiré. Appl. Opt. 33(11). pp2163-2169. 1994.

74. Meadows,D. M., W. O. Johnson and J. B. Allen. Generation of surface contours by moire patterns. Appl Opt. 9(4). pp942-947. 1970.

75. Miao, H., Z. Jiang, K. Qian and X. Wu. Advanced image processing method applied to speckle fringe pattern based on wavelet transform. Proc. SPIE 4537. pp370-373. 2002.

76. Morimoto, Y. and Y. Imamoto. Application of wavelet transform to displacement and strain measurement by grid method. Proc. of 1995 SEM Spring Conference on Experimental Mechanics, pp893-903. 1995.

77. Morimoto, Y., M. Fujigaki and S. Yoneyama. Shape, stress and strain measurement using phase analysis of grating or fringe patterns. Proc. SPIE 4537. pp47-52. 2002.

78. Muller, E. Fast three dimensional form measurement system. Opt. Eng. 34(9), pp2754-2756. 1995.

79. Oppenheim, A. V., R. W. Schafer and J. R. Buck. Discrete-time signal processing. Upper Saddler River, NJ: Prentice Hall, 1999.

80. Pawlowski, M. E., M. Kujawinska and M. G. Wegiel. Shape and motion measurement of time-varying three-dimensional objects based on spatiotemporal fringe-pattern analysis. Opt. Eng. **41**(2). pp450-459. 2002.

81. Post D., B. Han, P. G. Ifju. High Sensitivity Moiré: Experimental Analysis for Mechanics and Materials. New York: Springer-Verlag. 1994.

82. Press, W., S. Teukolsky, W. Vetterling and B. Flannery, Numerical Recipes in FORTRAN, 2nd Ed. Chap. 13. Cambridge University Press. Cambridge. 1992.

83. Priti, C., M. Giali, and N. Leuratti. SAR interferometry: A2-D phase unwrapping technique based on phase and absolute values information. Proc. of the 1990 International Geoscience and Remote Sensing Symposium. IEEE. Piscataway. NJ. pp2043-2046. 1990.

84. Qian, K., H. S. Seah and A. Asundi. Phase-shifting windowed Fourier ridges for determination of phase derivatives. Opt. Letters. 28(18). pp1657-1659. 2003.

85. Qian, K., H. S. Seah and A. Asundi. Instantaneous frequency and its application to strain extraction in moiré interferometry. Appl. Opt. 42(32). pp6504-6513. 2003.

86. Quan, C. H. M. Shang and P. J. Bryanston-Cross. Application of the holographic carrier fringe and FFT technique for deformation measurement. Opt. Laser Tech. 28(1). pp7-13. 1996.

87. Quan, C., X. Y. He, C. J. Tay and H. M. Shang. 3D surface profile measurement using LCD fringe projection. Proc. of SPIE Vol. 4317. pp511-516. 2000.

88. Recknagel, R., R. Kowarschik and G. Notni. High resolution defect detection and noise reduction using wavelet methods for surface measurement. J. Opt. A: Pure Appl. Opt. 2. pp538-545. 2000.

89. Roberge, D. and Y. Sheng. Optical wavelet matched filter. Appl. Opt. 33. pp5287-5293. 1994.

90. Robinson, D. W. and G. T. Reid. (ed). Interferogram analysis: digital fringe pattern measurement techniques. Bristol, Philadlphia. Institute of Physics. 1993.

91. Sandaz, P. Wavelet transform as a processing tool in white-light interferometry. Opt. Letters. 22(14). pp1065-1067. 1997.

92. Sansoni, G. S. Corini, S. Lazzari, R. Rodella and F. Docchio. Three dimensional imaging base on gray-code light projection: characterization of the measuring slgorithm and development of a measuring system for industrial application. Appl. Opt. 36. pp4463-4472. 1997.

93. Serra, J. P. Image analysis and mathematical morphology. New York, Academic Press. 1988.

94. Shakher, C., R. Kumar, S. K. Singh and S. A. Kazmi. Enhancement of contrast in digital speckle pattern interferometry fringes using wavelet transform. SPIE 4416. pp94-99. 2001.

95. Shakher, C., R. Kumar, S. K. Singh and S. A. Kazmi. Application of wavelet filtering for vibration analysis using digital speckle pattern interferometry. Opt. Eng. 41(1). pp176-180. 2002.

96. Shang, H. M., C. Quan, C. J .Tay and Y. Y. Hung. Discerning holographic and sharographic carrier fringes using the hyperboloids in holodiagrams. In Proc. of the SPIE. Vol.4317. pp573-578. 2001.

97. Sirnivasan, V. H. C. Liu and M. Halioua. Automated phase measuring profilometry of 3D diffuse objects. Appl Opt. 23. pp3105-3108. 1984.

98. Sirohi, R. S. and F. S Chau. Optical methods of measurement: wholefield techniques. New York: Marcel Dekker. 1999.

99. Sitnik, R. M. Kujawinska and J. Wznicki. Digital fringe projection system for large-Volume 360-deg shape measurement. Opt. Eng. 41(2) pp443-449. 2002.

100. Steel, W. H. Interferometry, 2nd ed. New York: Cambridge University Press. 1986.

101. Suganuma M and T. Yoshizawa. Three-dimensional shape analysis by use of a projected grating image. Opt Eng. 30(10). pp1529-1533. 1991.

102. Takasaki, H. Moiré topography. Appl Opt. 9(6). pp1467-1472. 1970.

103. Takeda, M. H. Ina, S. Kobayashi. Fourier-transform method of fringe-pattern analysis for computer-based topography and interferometry. J. Opt. Soc. Am. Vol 72. pp156-160. 1982.

104. Takeda, M. and H. Yamamoto. Fourier-transform speckle profilometry: three-dimensional shape measurements of diffuse objects with large height steps and/or spatially isolated surfaces. Appl. Opt. 33. pp7829-7837. 1994.

105. Tan, S. M., L. R. Watkins and T. H. Barnes. An alternative to phase stepping: profile extraction using wavelets. Proc. of the 1997 Pacific Rim Conference on Lasers and Electro-Optics. pp273-274. 1997.

106. Theocaris, P. S. Moiré Fringes: A Powerful Measuring Device. Applied Mechanics Surveys. Spartan Books, Washington DC. pp613-626. 1966.

107. Theocaris, P. S. Moiré Fringes in Strain Analysis. Pergamon Press. Oxford. 1969.

108. Tiziani, H. J., B. Franze and P. Haible. Wavelength-shift speckle interferometry for absolute profilometry using a mode-hop free external cavity diode laser. J. Mod. Opt. 44. pp1485-1496. 1997.

109. Tiziani, H. J. Spectral and temporal phase evaluation for interferometry and speckle applications. In Trends in Optical Nondestructive Testing and Inspection. Ed by P. Rastogi and D Inaudi. pp 323-343. 2000.

110. Vest, C. M. Holographic Interferometry. New York: Wiley. 1979.

111. Vikhagen, E. Nondestructive testing by use of TV holography and deformation phase gradient calculation. Appl Opt. 29. pp137-144. 1990.

112. Wang, J. and A. Asundi. A computer vision system for wineglass defect inspection via Gabor-filter-based texture feature. Information Science. 127. pp157-171. 2000.

113. Wang, J. and A. Asundi. Strain contouring with Gabor filters: filter bank design. Appl. Opt. 41(34). pp7229-7236. 2002.

114. Wasowski, J. Moire topographic maps. Opt. Communi. 2(7). pp321-323. 1970.

115. Watkins, L. R., S. M. Tan and T. H. Barnes. Interferometer profile extraction using continuous wavelet transform. Electronics Letters. 33. pp2116-2117. 1997.

116. Watkins, L. R., S. M. Tan and T. H. Barnes. Determination of interferometer phase distributions by use of wavelets. Opt. Lett. 24(13). pp905-907. 1999.

117. Wickerhauser, M. V. Adapted wavelet analysis from theory to software. Wellesley MA: A. K. Peters. 1994.

118. Xie, X., M. J. Lalor, D. R. Burton and M. M. Shaw. Four-map absolute distance contouring. Opt. Eng. 36(9). pp2517-2520. 1997.

119. Xiong, C. Y., J. Fang and W. C. Chen. A wavelet transform analysis of the concentration boundary layer in crystal growth. J. of Materials Science Letter. 19. pp619-622. 2000.

120. Yoshizawa, T. and T. Tomisawa. Shadow moiré topography by means of the phase-shift method. Opt. Eng. 32(7). pp1668-1674. 1993.

121. Zhong, J. and J. Weng. Dilating Gabor transform for the fringe analysis of 3-D shape measurement. Opt. Eng. 43(4). pp895-899. 2004.

APPENDIX A   WAVELET RIDGES

We start from the definition of analytic instantaneous frequency. A cosine modulation

$$f(t) = I_M \cos(\omega t + \varphi_0) = I_M \cos \varphi(t) \tag{a.1}$$

has a frequency ω that is the derivative of the phase $\varphi(t) = \omega t + \varphi_0$. To generalize this notion, real signals f are written as an amplitude I_M modulated with a time-varying phase φ:

$$f(t) = I_M(t) \cos \varphi(t) \quad \text{with} \quad I_M(t) \geq 0 \tag{a.2}$$

The instantaneous frequency is defined as a positive derivative of the phase:

$$\omega(t) = \varphi'(t) \geq 0 \tag{a.3}$$

The derivative can be chosen to be positive by adapting the sign of $\varphi(t)$. One must be careful because there are many possible choices of $I_M(t)$ and $\varphi(t)$, which implies that $\omega(t)$ is not uniquely defined relative to f.

In windowed Fourier transform, the spectrogram $P_S f(b, \zeta) = |Sf(b, \zeta)|^2$ measures the energy of f in a time-frequency neighborhood of (b, ζ). The ridge algorithm computes instantaneous frequencies from the local maxima of $P_S f(b, \zeta)$. The windowed Fourier transform is computed with a symmetric window $g(t) = g(-t)$ whose support is equal to [-1/2, 1/2]. The Fourier transform $\hat{g}$ is a real symmetric

function and $|\hat{g}(\omega)| \leq \hat{g}(0)$ for all $\omega \in R$. The maximum $\hat{g}(0) = \int_{-1/2}^{1/2} g(t)dt$ is on the

order of 1. Generally, the window g is normalized so that $\|g\| = 1$. For a fixed scale a,

$g_a(t) = a^{-1/2} g(t/a)$ has a support of size a and a unit norm. The corresponding

windowed Fourier atoms are

$$g_{a,b,\zeta}(t) = g_a(t-b)e^{i\zeta t} \tag{a.4}$$

and the windowed Fourier transform is defined by

$$Sf(b,\zeta) = \langle f, g_{a,b,\zeta} \rangle = \int_{-\infty}^{+\infty} f(t)g_a(t-b)e^{-i\zeta t}dt \tag{a.5}$$

The following theorem relates $Sf(b,\xi)$ to the instantaneous frequency of f.

<u>Theorem</u>

Let $f(t) = I_M(t)\cos\varphi(t)$. If $\zeta \geq 0$ then

$$\langle f, g_{a,b,\zeta} \rangle = \frac{\sqrt{a}}{2} I_M(b) \exp(i[\varphi(b) - b\zeta])(\hat{g}(a[\zeta - \varphi'(b)]) + \varepsilon(b,\zeta)) \tag{a.6}$$

The corrective term satisfies

$$|\varepsilon(b,\zeta)| \leq \varepsilon_{I,1} + \varepsilon_{I,2} + \varepsilon_{\varphi,2} + \sup_{|\omega| \geq a\varphi'(b)} |\hat{g}(\omega)| \tag{a.7}$$

with

$$\varepsilon_{I,1} \leq \frac{a|I_M'(b)|}{|I_M(b)|} \; ; \qquad \varepsilon_{I,2} \leq \sup_{|t-b| \leq a/2} \frac{a^2|I_M''(b)|}{|I_M(b)|} \tag{a.8}$$

and if $a|I'_M(b)|\,|I_M(b)|^{-1} \le 1$ then

$$\varepsilon_{\varphi,2} \le \sup_{|t-b| \le a/2} a^2 |\varphi''(t)| \tag{a.9}$$

if $\zeta = \varphi'(b)$ then

$$\varepsilon_{I,1} = \frac{a|I'_M(b)|}{|I_M(b)|} |\hat{g}'(2a\varphi'(b))| \tag{a.10}$$

The proof of above theorem is presented by Mallat (1998). Delprat et al. (1992) give a different proof of a similar result when $g(t)$ is a Gaussian, using a stationary phase approximation. If the corrective term $\varepsilon(b,\zeta)$ can be neglected, Eq. (a.6) enables us to measure $I_M(b)$ and $\varphi'(b)$ from $Sf(b,\zeta)$. This implies that the decomposition $f(t) = I_M(t)\cos\varphi(t)$ is uniquely defined. By reviewing the proof of the theorem mentioned above, one can verify that I_M and φ' are the analytic amplitude and instantaneous frequencies of f. Equations (a.8) and (a.9) show that the three corrective terms $\varepsilon_{I,1}$, $\varepsilon_{I,2}$ and $\varepsilon_{\varphi,2}$ are small if $I_M(t)$ and $\varphi'(t)$ have small relative variations over the support of the window g_a. Let $\Delta\omega$ be the bandwidth of $\hat{g}$ defined by

$$|\hat{g}(\omega)| << 1 \quad \text{for} \quad |\omega| \ge \Delta\omega. \tag{a.11}$$

The term $\sup_{|\omega| \ge a\varphi'(b)} |\hat{g}(\omega)|$ of $\varepsilon(b,\zeta)$ is negligible if

$$\varphi'(b) \ge \frac{\Delta\omega}{a} \tag{a.12}$$

Ridge Points of Windowed Fourier transform

Let us suppose that $I_M(t)$ and $\varphi'(t)$ have small variations over intervals of

size a and $\varphi'(b) \geq \dfrac{\Delta \omega}{a}$ so that the corrective term $\varepsilon(b, \zeta)$ can be neglected. Since

$|\hat{g}(\omega)|$ is maximum at $\omega = 0$, Eq. (a.6) shows that for each b the spectrogram

$|Sf(b, \zeta)|^2 = |\langle f, g_{a,b,\zeta}\rangle|^2$ is maximum at $\zeta(b) = \varphi'(b)$. The corresponding time-

frequency points $(b, \zeta(b))$ are called *ridges*. At ridge points, Eq. (a.6) becomes

$$Sf(b,\zeta) = \frac{\sqrt{a}}{2} I_M(b) \exp\left(i[\varphi(b) - b\zeta]\right)\left(\hat{g}(0) + \varepsilon(b,\zeta)\right) \qquad \text{(a.13)}$$

Theorem above proves that the $\varepsilon(b, \zeta)$ is smaller at a ridge point because the first

order term $\varepsilon_{I,1}$ becomes negligible in Eq. (a.10). This is shown by verifying that

$|\hat{g}(2a\varphi'(b))|$ is negligible when $a\varphi'(b) \geq \Delta\omega$. At ridge points, the second order term

$\varepsilon_{I,2}$ and $\varepsilon_{\varphi,2}$ are predominant in $\varepsilon(b, \zeta)$.

The ridge frequency gives the instantaneous frequency $\zeta(b) = \varphi'(b)$ and the

amplitude is calculated by

$$I_M(b) = \frac{2|Sf(b, \zeta(b))|}{\sqrt{a}|\hat{g}(0)|} \qquad \text{(a.14)}$$

Let $\Phi_S(b, \zeta)$ be the complex phase of $Sf(b, \zeta)$. If we neglect the corrective term, the

Eq. (a.13) proves that ridges are also points of stationary phase:

$$\frac{\partial \Phi_S(b, \zeta)}{\partial b} = \varphi'(b) - \zeta = 0 \qquad \text{(a.15)}$$

Testing the stationarity of the phase locates the ridges more precisely.

Wavelet Ridges

Windows Fourier atoms have a fixed scale and thus cannot follow the instantaneous frequency of rapidly varying events such as hyperbolic chirps. In contrast, an complex wavelet transform modifies the scale of its time-frequency atoms. The ridge algorithm of Delprat et al. (1992) is extended to complex wavelet transforms to accurately measure frequency tones that are rapidly changing at high frequencies.

An approximately complex wavelet is constructed by multiplying a window g with a sinusoidal wave:

$$\Psi(t) = g(t)\exp(i\omega_0 t) \tag{a.16}$$

As in the previous section, g is a symmetric window with a support equal to [-1/2, 1/2], and a unit norm $\|g\| = 1$. Let $\Delta\omega$ be the bandwidth of $\hat{g}$ defined in Eq. (a.11). if $\omega_0 > \Delta\omega$ then $\forall \omega < 0$, $\hat{\Psi}(\omega) = \hat{g}(\omega - \omega_0) << 1$. The wavelet Ψ is not strictly analytic because its Fourier transform is not exactly equal to zero at negative frequencies.

Dilated and translated wavelets can be rewritten as

$$\Psi_{ab}(t) = \frac{1}{\sqrt{a}}\Psi\left(\frac{t-b}{a}\right) = g_{a,b,\zeta}(t)\exp(-ib\zeta) \tag{a.17}$$

with $\zeta = \omega_0 / a$ and $g_{a,b,\zeta}(t) = \sqrt{a}\, g\left(\frac{t-b}{a}\right)\exp(i\omega_0 t)$.

The resulting wavelet transform uses time-frequency atoms similar to those of a windowed Fourier transform [Eq. (a.5)] but in this case the scale a varies over R^+ while $\zeta = \omega_0/a$:

$$Wf(a,b) = \langle f, \Psi_{ab} \rangle = \langle f, g_{a,b,\zeta} \rangle \exp(i\omega_0 b) \qquad \text{(a.18)}$$

The above-mentioned theorem computes $\langle f, g_{a,b,\zeta} \rangle$ when $f(t) = I_M(t)\cos\varphi(t)$, which gives

$$Wf(a,b) = \frac{\sqrt{a}}{2} I_M(b) \exp[i\varphi(b)] \big(\hat{g}(a[\zeta - \varphi'(b)] + \varepsilon(b,\zeta)) \big) \qquad \text{(a.19)}$$

The corrective term $\varepsilon(b,\zeta)$ is negligible if $I_M(t)$ and $\varphi'(t)$ have small variations over the supports of Ψ_{ab} and if $\varphi'(b) \geq \Delta\omega/a$.

The instantaneous frequency is measured from ridge defined over the wavelet transform. The normalized scalogram defined by $\dfrac{\zeta}{\omega_0} P_W f(b,\zeta) = \dfrac{|Wf(a,b)|^2}{a}$, for $\zeta = \omega_0/a$, it can be calculated as

$$\frac{\zeta}{\omega_0} P_W f(b,\zeta) = \frac{1}{4} I_M^2(b) \left| \hat{g}\left(\omega_0 \left[1 - \frac{\varphi'(b)}{\zeta} \right] \right) + \varepsilon(b,\zeta) \right|^2 . \qquad \text{(a.20)}$$

Since $|\hat{g}(\omega)|$ is maximum at $\omega = 0$, if $\varepsilon(b,\zeta)$ can be neglected, this expression shows that the scalogram is maximum at

$$\zeta(b) = \varphi'(b) \qquad \text{(a.21)}$$

The corresponding points $(b, \xi(b))$ are called wavelet ridges. The analytic amplitude is given by

$$I_M(b) = \frac{2\sqrt{\omega_0^{-1} P_W f(b, \zeta) \zeta}}{|\hat{g}(0)|} \tag{a.22}$$

When $\zeta = \varphi'(b)$, the first order term $\varepsilon_{I,1}$ calculated in Eq. (a.10) becomes negligible. Similar as windowed Fourier transform, the corrective term is then dominated by $\varepsilon_{I,2}$ and $\varepsilon_{\varphi,2}$. To simplify their expression, we approximate the sup of I_M'' and φ'' in the neighborhood of b by their value at b. Since $a = \omega_0 / \zeta = \omega_0 / \varphi'(b)$, Eqs. (a.8) and (a.9) imply that these second order terms becomes negligible if

$$\frac{\omega_0^2}{|\varphi'(b)|^2} \frac{|I_M''(b)|}{|I_M(b)|} << 1 \tag{a.23}$$

and

$$\omega_0^2 \frac{|\varphi''(b)|}{|\varphi'(b)|} << 1 \tag{a.24}$$

The presence of φ' in the denominator proves that I_M' and φ' must have slow variations if φ' is small but may vary much more quickly for large instantaneous frequencies.

APPENDIX B RESULTS

B.1 Temporal phase analysis using Micro-ESPI

Figure 4.10 shows a tiny steel cantilever beam being tested. The length, width and thickness of the beam are 2.5 mm, 0.25 mm and 0.25 mm, respectively. The beam is continuously loaded with a linear displacement by a PZT stage. During deformation of the beam, a series of speckle patterns is captured by a high speed CCD camera (KODAK Motion Corder Analyzer, SR-Ultra) with a long working distance microscopic lens (OPTEM 100). Figure A.1 shows a typical speckle pattern captured at intervals of 0.008 s with imaging rate of 125 fps. Five hundred speckle patterns are captured during a four-second period. Among them, two hundred and fifty six consecutive images are selected for processing.

(b)
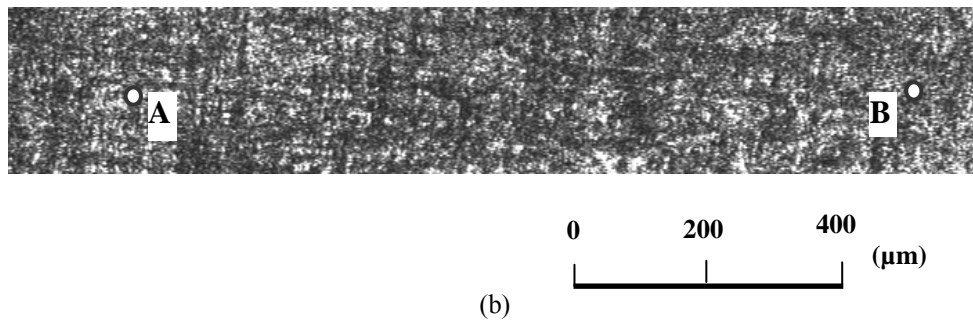
Figure A.1 typical speckle patterns on micro-beam captured by CCD camera.

Figure A.2 shows the gray value variation of points A and B (indicated in Fig. A.1). A difference in amplitude is observed, however, only temporal frequencies are considered as they contain information on velocity and displacement. The temporal frequency of point A is lower than that of point B. This implies that Point B deforms faster than point B. The modulus of the Morlet wavelet transform of intensity variation of points A and B are shown in Figs. A.3(a) and A.3(b) respectively. The dashed line shows the ridge of the wavelet transformation where the maximum

modulus are found. Little variation of a_{rb} is observed on the ridge, which implies the velocities are almost constant along time axis. Figure A.4(a) shows the velocities on points A and B where the transient velocities at each pixel can be retrieved. Integration of $\dfrac{2\pi}{a_{rb}}$ is carried out on each pixel to generate a continuous temporal phase change $\Delta\varphi_{xy}(t)$. In an ESPI setup as shown in Fig. 4.8, a 2π phase change represents a displacement of $\lambda/2$ (=316.4 nm) in the z direction. The transient displacements of points A and B are shown in Fig. A.4(b). Figure A.5(a) shows a 3-D plot of the out-of-plane displacement of the beam between two instants $T_1 = 0.4s$ and $T_2 = 1.2s$. A 3×3 median filter has been used on the phase map to remove several ill-behaved pixels.

For comparison, temporal Fourier analysis is also applied on the same speckle patterns. Bandpass filters with different width are applied. A one-dimensional phase unwrapping is then applied along the time axis, as all phase values obtained by inverse Fourier transformation are within [0, 2π). Figure A.5(b) shows the 3-D displacement plot from temporal Fourier analysis. Similar as in wavelet transform, a 3×3 median filter is also applied on the phase map. Figure A.6 shows a comparison of displacement on central line of the cantilever beam at different instants. A smoother spatial distribution of displacement is observed using wavelet analysis. The maximum displacement fluctuation due to noise is around 0.06 μm in Fourier transform, but only 0.02 μm in wavelet analysis.
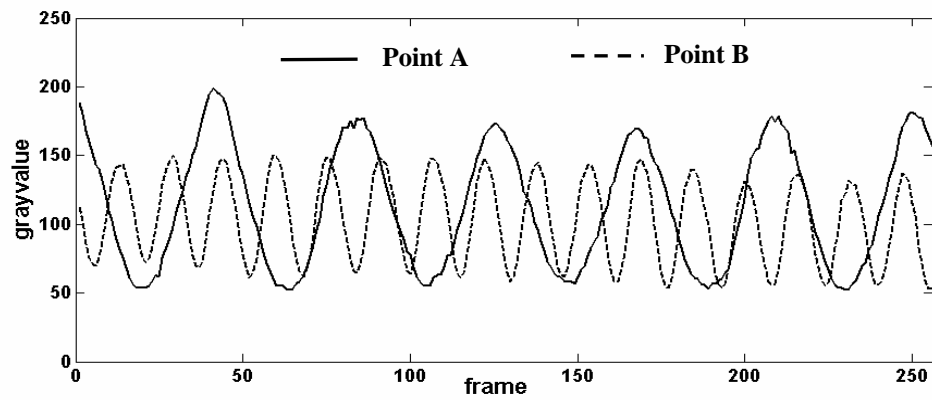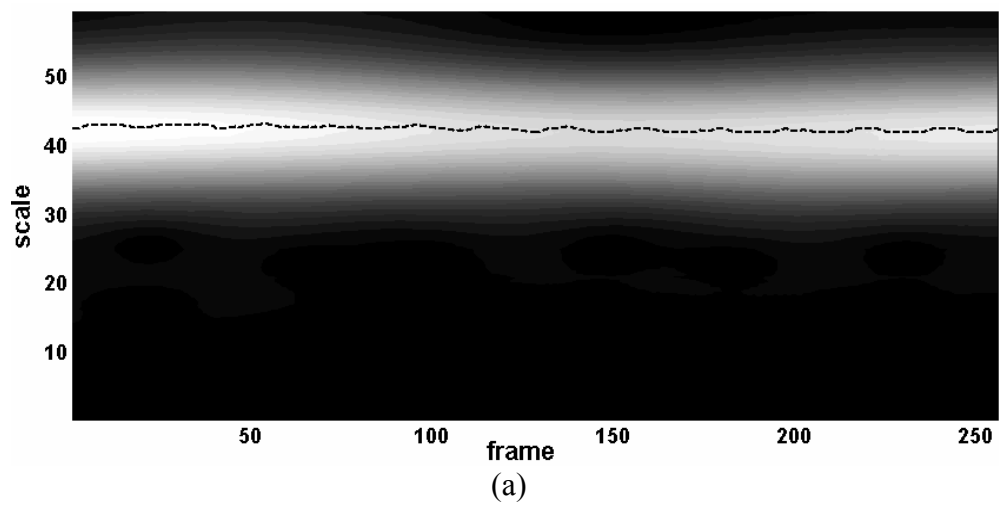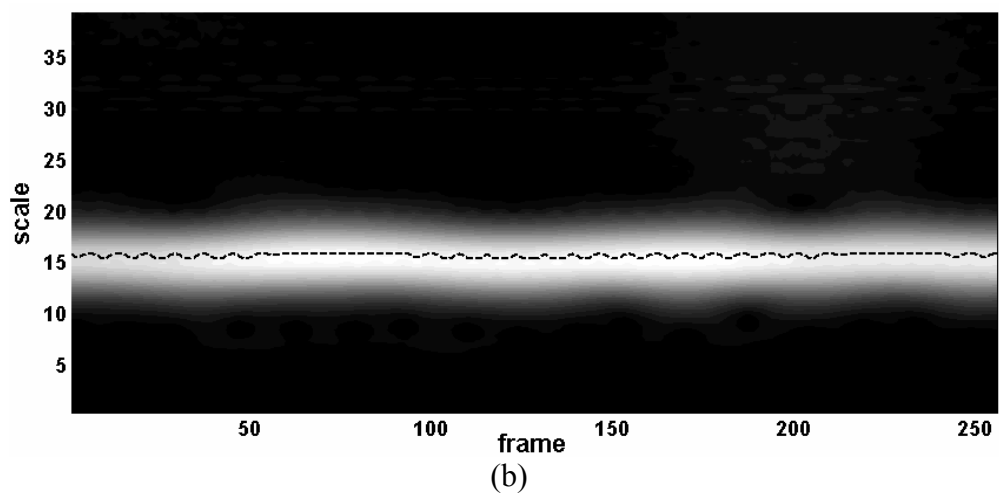
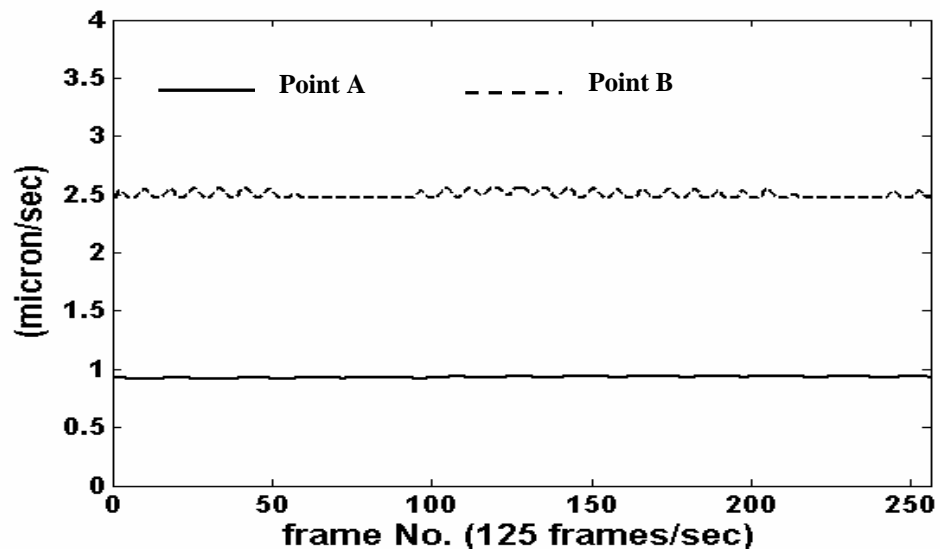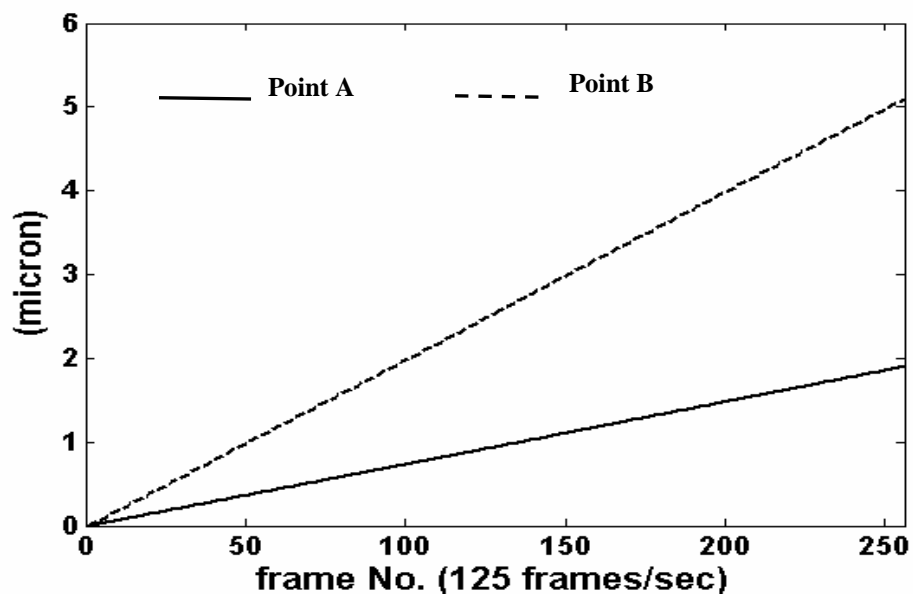Figure A.2 Gray values of points A and B.

(a)

(b)

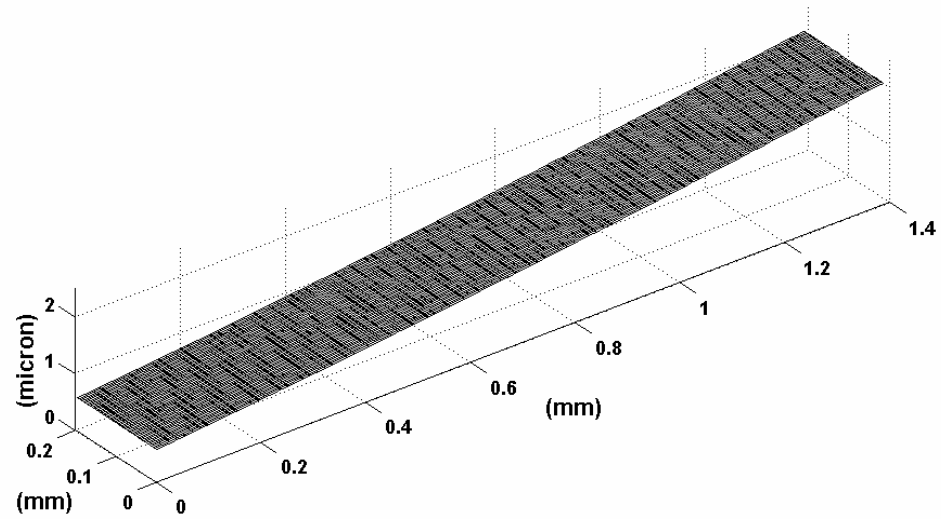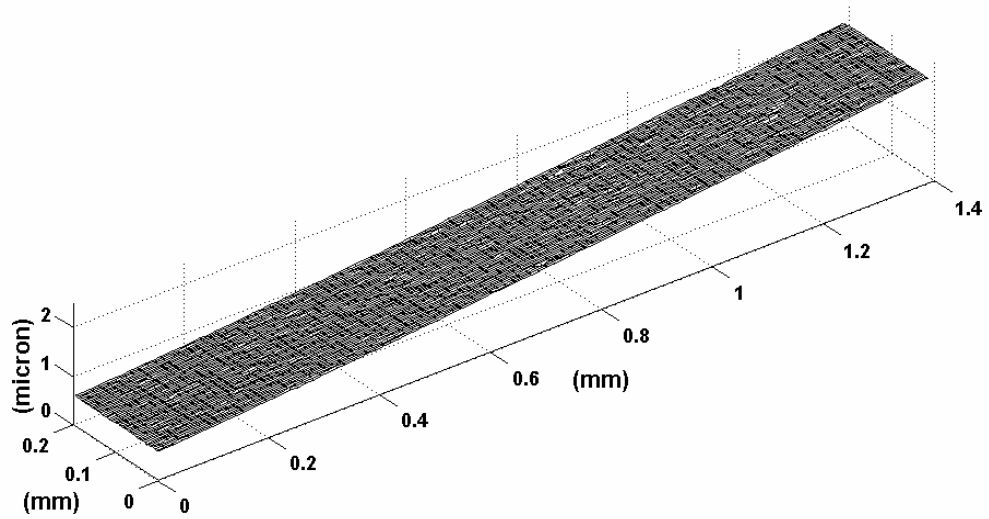Figure A.3 Modulus of the Morlet wavelet transform at (a) point A and (b) point B.

(a)

(b)

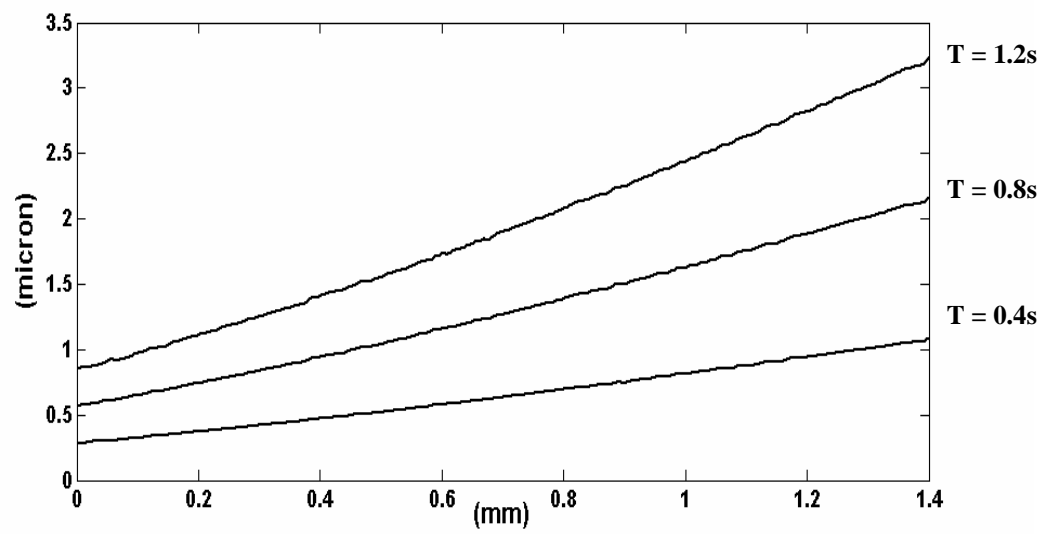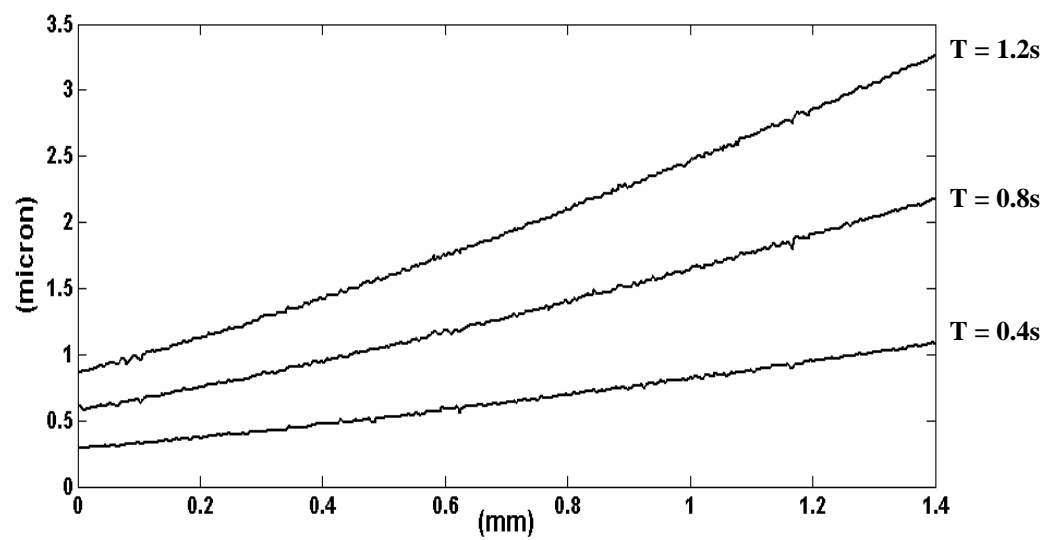Figure A.4 (a) Instantaneous velocity and (b) displacement at points A and B.

(a)

(b)

Figure A.5 Displacement of the beam between two instants $T_1 = 0.4s$ and $T_2 = 1.2s$ by use of (a) temporal wavelet analysis and (b) temporal Fourier analysis.

(a)

(b)

Figure A.6 Comparison of displacements at central line of the cantilever beam
between (a) wavelet and (b) Fourier analysis.

B.2 Results on phase scanning method using shadow moiré

The phase scanning method is also applied on a vibrating coin of 24.5 mm diameter and having a diffuse surface (shown in Fig. A.7). A small area of interest containing 256×256 pixels (also indicated in Fig. A.7) is cropped. A grating with difference pitch (6 lines/mm) is used to increase the resolution. The distance d_S and l_S (shown in Fig. 2.3) are respectively 245 mm and 250 mm. The test object is subjected to a triangular wave vibration with a frequency of approximately 5 Hz. The camera recording rate remains at 250 fps. Figures A.8(a) and A.8(b) show two typical fringe patterns recorded by high speed CCD camera at different moments. Carrier fringes are also introduced on the images by rotating the grating. First one hundred consecutive images are processed. The process is similar with the spherical cap mentioned in Chapter 6. Figures A.8(c) and A.8(d) are typical fringe patterns after filtering. As the surface profile of the coin is much smaller than the spherical cap, it is found that increasing the carrier fringe frequency improves the quality of the phase map. However, it is observed that the contrast of the moiré fringes changes with the distance between the object and grating. High contrast fringes are generated when the distance is small. This is due to the diffraction effect of the grating. From Figs A.8(a) and A.8(b) it is observed that the fringe contrast increases from left to right, which implies the distance between the coin and grating decreases in this direction. Higher sensitivity can also be obtained by increasing the distance d_S, but this will also generate shadow on the object.

Figure A.9 shows the vibration amplitude of Point C (indicated in Fig. A.7). The frequency and the amplitude of vibration are evaluated as 4.8 Hz and 0.258 mm respectively. Figures A.10(a) and A.10(b) show the wrapped phase map and

continuous map after unwrapping. Subsequently the 3-D profile of the interest area is obtained as shown in Fig. A.10(c). Figure A.11 shows a comparison of profile plot on cross-section D-D (indicated in Fig. A.7) using proposed phase scanning method and mechanical stylus method. The average discrepancy is 4.7%. The maximum difference is around 10μm which is same order of the error using phase shifting method where at least three images are required.
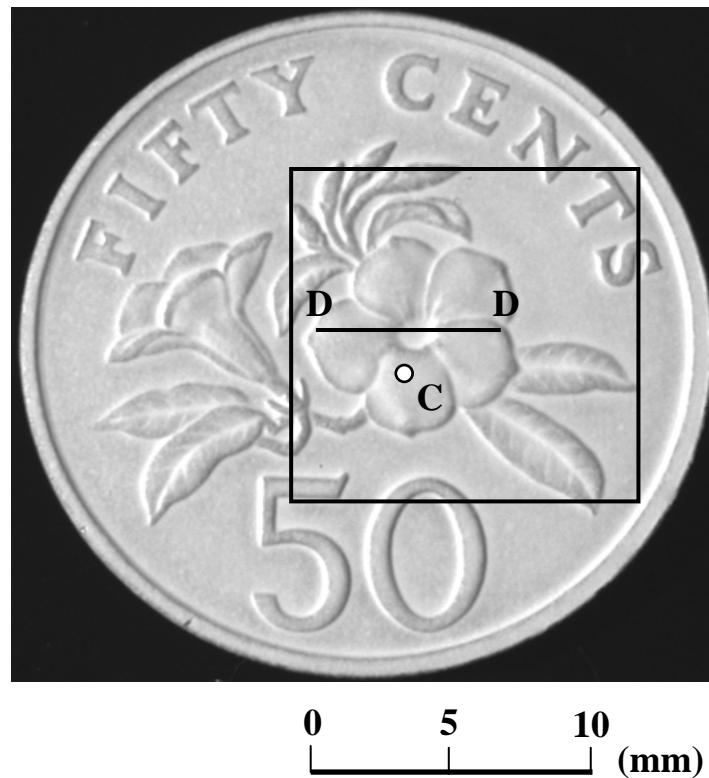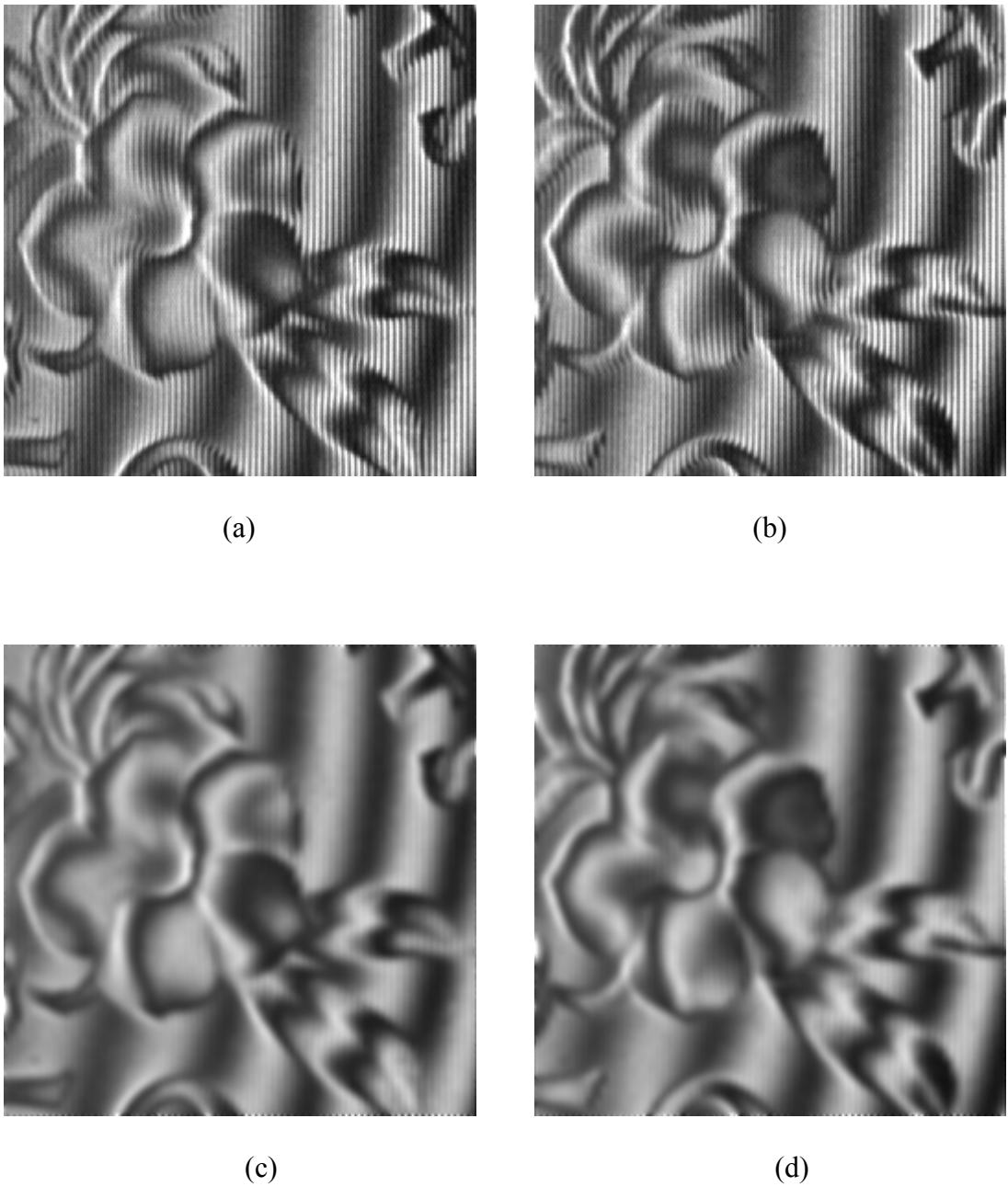

Figure A.7 Specimen 2: a 50-cent coin and area of interest.

(a)

(b)

(c)

(d)

Figure A.8 Typical moiré fringe patterns of interest area captured at different instants (a) 0s (before filtering); (b) 0.04s (before filtering); (c) 0s (after filtering); (d) 0.04s (after filtering).
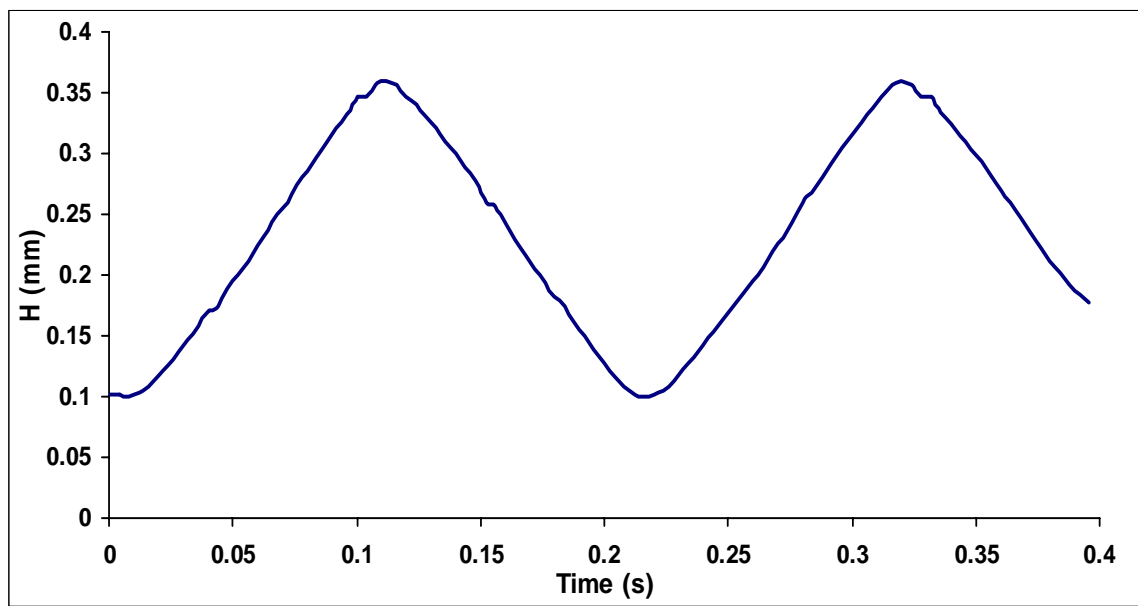
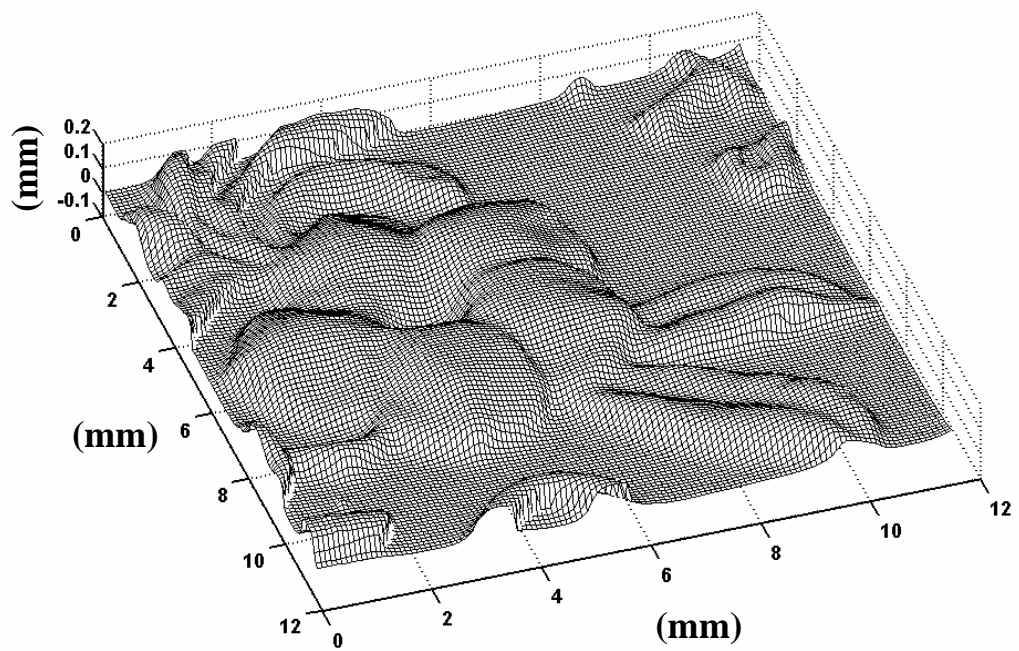Figure A.9   Displacement of Point C in z-axis
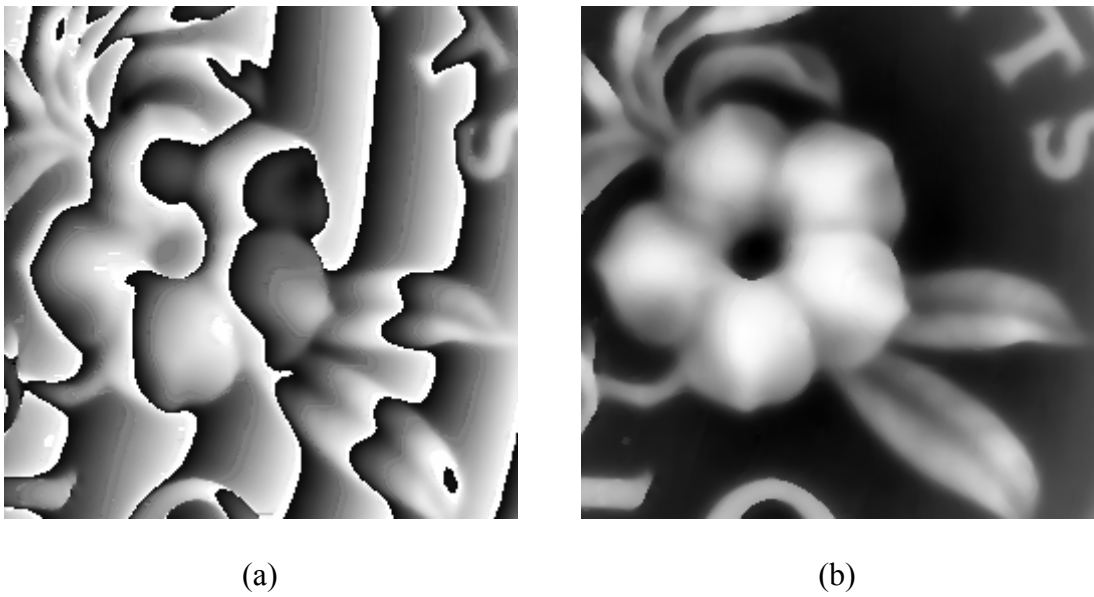
<center>(a)</center>

<center>(b)</center>

Figure A.10 (a) Wrapped phase in spatial coordinate at 0.04s; (b) continuous phase map obtained by phase scanning method; (c) reconstructed 3-D plot of surface profile.
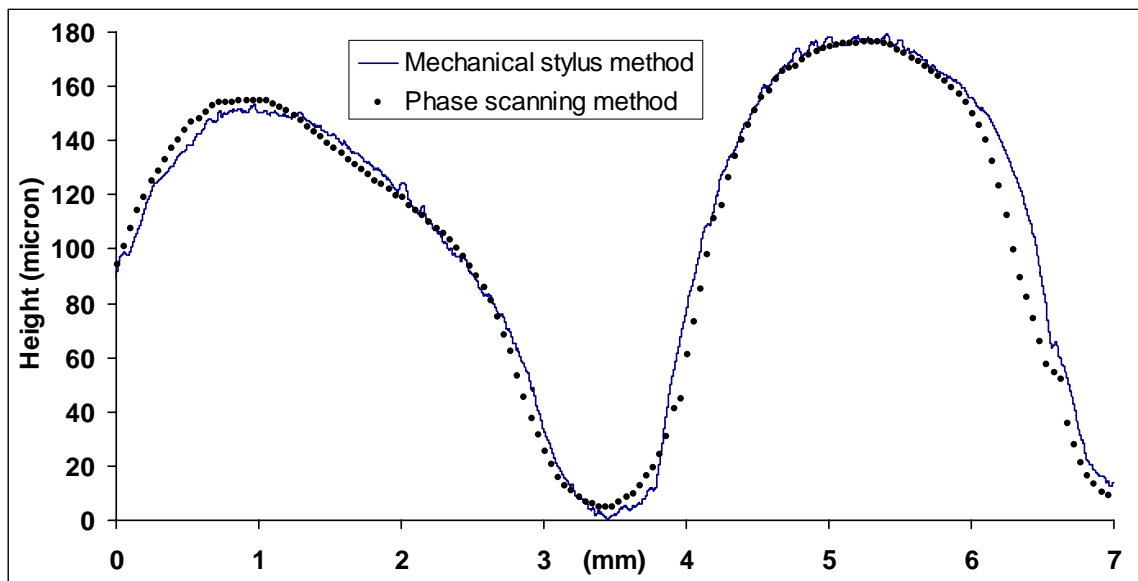
Figure A.11 A comparison of surface profile of 50-cent coin on cross-section D-D
between phase scanning method and mechanical stylus method.

APPENDIX C   HAAR WAVELET AS A DIFFERENTIATION OPERATOR

Haar wavelet is the simplest wavelet basis function. It has the shortest support among all orthonormal wavelets. It is not well adopted to approximating the phase of the smooth functions because it has only one vanishing moment. However, it is an effective function to extract the derivative from a signal with noise, depending on proper selection of scaling factors a. The mother wavelet is given in Fig. A.12(a).

$$\psi(t) = \begin{cases} 1, & if\ 0 \le t < 1/2 \\ -1 & if\ 1/2 \le t < 1 \\ 0 & otherwise \end{cases} \tag{a.25}$$
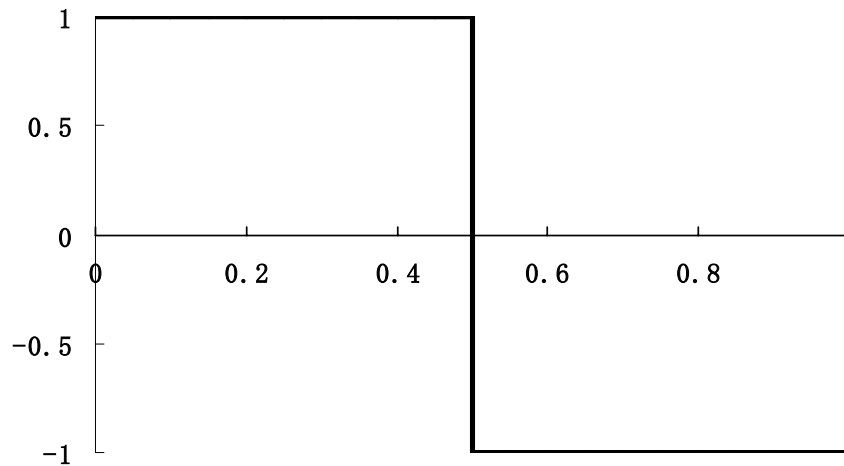
(a)
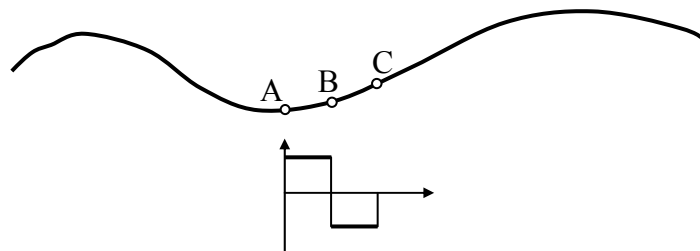
(b)

Figure A.12(a) Plot of Haar wavelet function; (b) Haar wavelet as a differentiation operator.

Figure A.12 (b) shows how Haar wavelet works as a differentiation operator. The wavelet coefficient of continuous Haar wavelet transform is an approximation of the negative value of the first derivative at point B. It is equivalent to calculate the average values on AB and BC sections, and obtain the first derivative at point B using these two values. Different values of scaling factor determine the various lengths of AB and BC. Obviously the wavelet coefficient obtained is insensitive to the noise that has higher frequencies than selected Haar wavelet.

Figure A.13(a) shows a simulated signal which is a sinusoidal curve extended smoothly at the beginning and the end. Figure A.13(b) is its theoretical first derivative which is obtained directly from numerical differentiation. Only two discontinuities are observed in the first derivative which are circled in Fig. A.13(b).
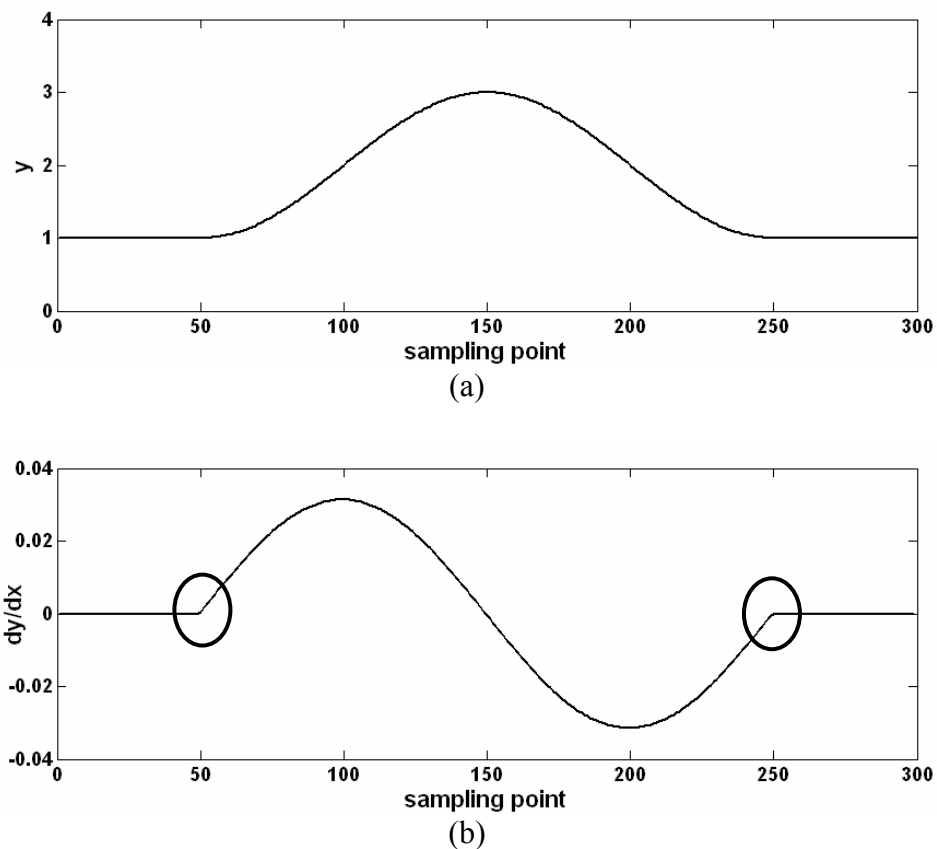
Figure A.13 (a) A simulated Signal and (b) its theoretical first derivative.

Figure A.14(a) shows the first derivative of the signal obtained by Haar wavelet when scaling factor $a = 20$. Figure A.14(b) shows the different in the derivatives when different scaling factor a are selected. It can be observed that last error occurs at the points that the derivative is not continuous (circled in Fig. A.13b).The increment of error is observed when the scaling factor a is increased.
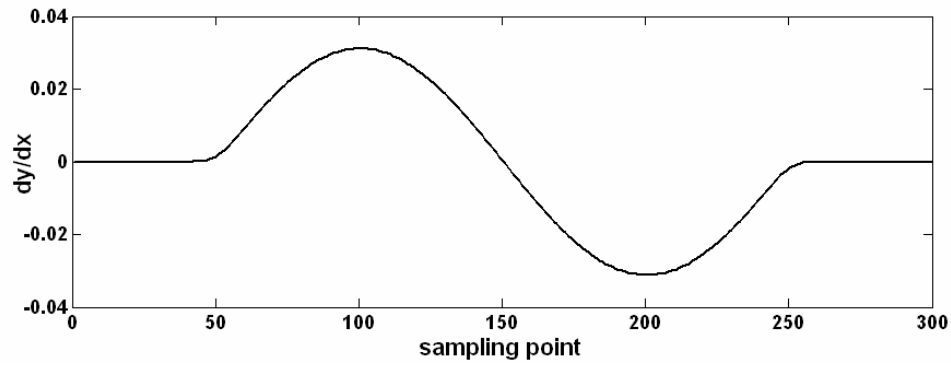
(a)
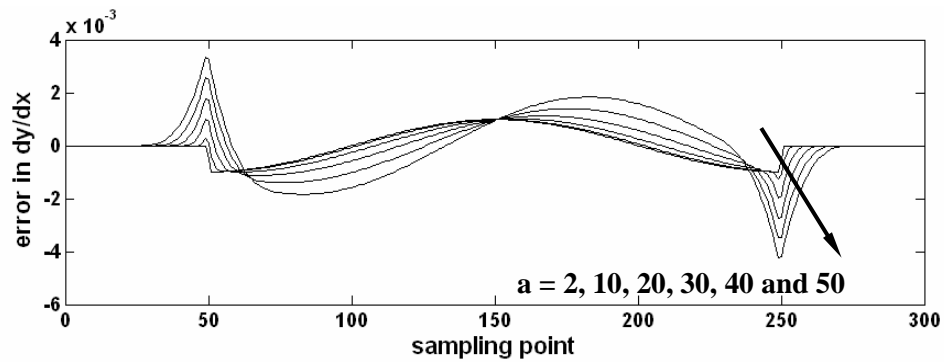
(b)

Figure A.14 (a) Derivative obtained by Haar wavelet when $a =20$; (b) The error in derivative when different values of a are selected.

When the noise is involved in signal, the differentiation directly obtained from two adjacent points will be failed. Due to the smooth effect mentioned above in Haar wavelet, it is a suitable tool to extract the derivatives from a noise signal. Figure A.15 shows a simulated signal with some random noise. Although the noise effect is not so serious in the signal, the numerical differentiation from two adjacent points [Fig.

A.16(a)] is still unsuccessful. Fig. A.16(b) shows the results from Haar wavelet when

a = 30. Besides the errors at the discontinuity points mentioned above, relative large

errors are found at the beginning and end of the signal due to the border effect of the

continuous wavelet transform. However, this error can be eliminated by extend the

signal properly with some linear prediction algorithms. The main problem involved in

continuous Haar wavelet transform is the proper selection of scaling factor a.

Evaluation of signal and noise frequencies is necessary. In our applications, the signal

to be processed is generally in very low frequency, such as displacement of a plate;

and the noise is caused by speckle noise, which is a high-frequency term. Selection of

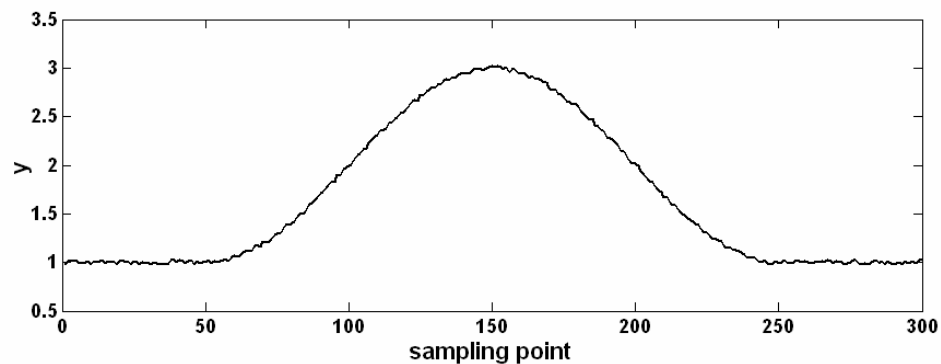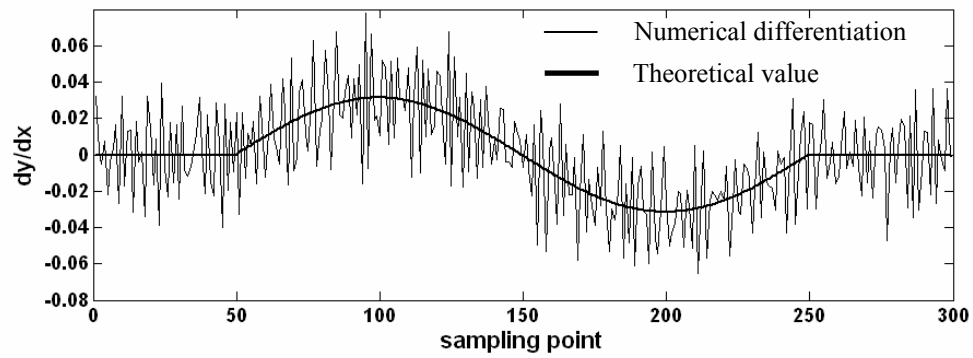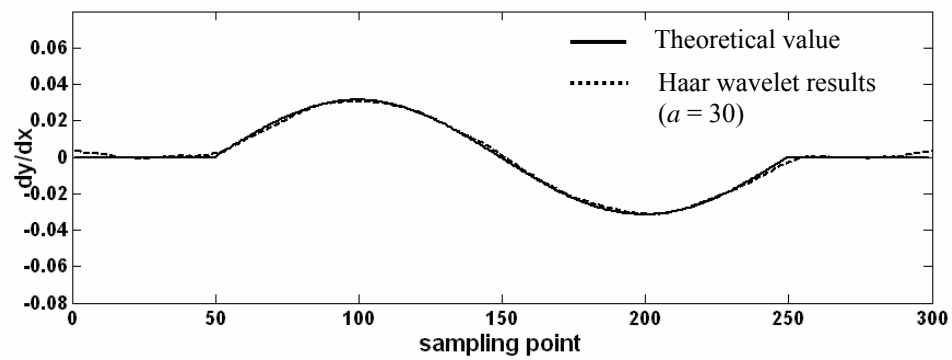the scaling factor a is not difficult in most of the cases.

Figure A.15 A simulated signal with random noise

(a)

(b)

Figure A.16 (a) Result from numerical differentiation directly from two adjacent sampling points; (b) Result from Haar wavelet when $a = 30$.

APPENDIX D   LIST OF PUBLICATIONS DURING PHD PERIOD

Journal papers

1. C. J. Tay, C. Quan, Y. Fu, L. J. Chen, H. M. Shang, "Surface profile measurement of low-frequency vibrating objects using temporal analysis of fringe pattern", Optics and Laser Technology, Vol. **36**(6), pp 471-476, 2004.

2. C. Quan, Y. Fu, C. J. Tay, "Determination of surface contour by temporal analysis of shadow moiré fringes", Optics Communications, Vol. **230**(1-3), pp 23-33, January, 2004.

3. Y. Fu, C. J. Tay, C. Quan and L. J. Chen，"Temporal wavelet analysis for deformation and velocity measurement in speckle interferometry" Optical Engineering, Vol. **43**(11), pp2780-2787, November 2004.

4. Cho Jui Tay, Chenggen Quan, Yu Fu and Yuanhao Huang, "Instantaneous velocity displacement and contour measurement by use of shadow moiré and temporal wavelet analysis", Applied Optics, Vol. **43**(21), pp 4164-4171, July 2004.

5. Yu Fu, Cho Jui Tay, Chenggen Quan and Hong Miao, "Wavelet analysis of speckle patterns with a temporal carrier", paper was accepted by Applied Optics for publication in November, 2004.

6. Chenggen Quan, Yu Fu , Cho Jui Tay and Jia Min Tan, "Profiling of objects with height steps by wavelet analysis of shadow moiré fringes", paper was accepted by Applied Optics for publication in January, 2005.

7. Chenggen Quan, Cho Jui Tay, Lujie Chen, and Yu Fu, "Spatial-fringe-modulation-based quality map for phase unwrapping", Applied Optics, Vol. **42**(35), pp7062-7065, December 2003.

8. C. J. Tay, C. Quan, L. Chen and Y. Fu, "Phase extraction from electronic speckle patterns by statistical analysis", Optics Communications, Vol. **236**(4-6), pp259-269. 2004.

9. Lujie Chen, Chenggen Quan, Cho Jui Tay, Yu Fu, "Shape measurement using one frame projected sawtooth fringe pattern", paper was accepted by Optics Communications for publication in October, 2004.

Conference papers

1. Y. Fu, C. J. Tay, C. Quan, "Determination of instantaneous velocity, displacement and surface contour by temporal phase analysis", ICEM12, International Conference on Experimental Mechanics, Bari (Italy) 29Aug – 2 Sep. 2004. ISBN: 88 386 6273-8. Edited by Carmine Pappalettere.

2. Y. Fu, C. J. Tay, C. Quan and L. J. Chen, "Temporal wavelet analysis for deformation measurement of small components using micro-ESPI", ICEM04, International Conference on Experimental Mechanics, Singapore, November, 2004.

3. L. J. Chen, C. Quan, C. J. Tay, and Y. Fu, "Phase shifting technique for closed-fringe analysis by Fourier transform method" International Conference on Advanced Technology in Experimental Mechanics, Nagoya, Japan. September, 2003.